

DISSERTATION ZUR ERLANGUNG DES DOKTORGRADES
DER FAKULTÄT FÜR CHEMIE UND PHARMAZIE
DER LUDWIG-MAXIMILIANS-UNIVERSITÄT MÜNCHEN

**Live-cell imaging elucidates cellular interactions
of gene nanocarriers for cancer therapy**

Frauke Martina Mickler (geb. König)

aus

Braunschweig, Deutschland

2013

Erklärung

Diese Dissertation wurde im Sinne von §7 der Promotionsordnung vom 28. November 2011 von Herrn Prof. Dr. Christoph Bräuchle betreut.

Eidesstattliche Versicherung

Diese Dissertation wurde eigenständig und ohne unerlaubte Hilfe erarbeitet.

München, den 10.6.2013

Frauke Martina Mickler

Dissertation eingereicht am: 11.06.2013

1. Gutachter: Prof. Dr. Christoph Bräuchle
2. Gutachter: PD Dr. Manfred Ogris

Mündliche Prüfung am: 18.07.2013

Summary

The nanocarrier-mediated delivery of therapeutic transgenes into human target cells is a promising approach to treat life-threatening diseases such as cancer.

For effective gene delivery, the nanocarrier has to meet a series of challenging requirements. First, high capacity loading of the genetic material and high stability of the formed nanoparticles in the blood circulation is required. Next, the gene carrier must specifically bind target cells of interest, e.g. cancer cells, and enter them. After uptake, trafficking towards the cell nucleus and destabilization of endosomal membranes has to be realized, followed by DNA release from particles and DNA import into the nucleus. Furthermore, ideal gene nanocarriers should be non-toxic and non-immunogenic and allow cheap and reproducible manufacturing.

In this work polymeric nanocarriers were studied that contained different functionalities to sense their environment and adapt dynamically to overcome cellular barriers for gene delivery. Highly-sensitive fluorescence microscopy was applied as a tool to dissect the interactions of functionalized gene nanocarriers on the single-cell level in real-time. To study the effects of polymer design on DNA condensation, cell binding and internalization, live-cell imaging experiments were combined with biological assays, new experimental setups and tailor-made image analysis routines. The influence of polyethylene glycol (PEG) shielding and receptor targeting on particle uptake was examined in detail and microscopy-based assays were applied to study endosomal release and nuclear import of biomolecules.

The results from live-cell experiments with PEGylated polymer particles demonstrate that fine-tuning of the PEG length is important to reduce non-specific interactions and maximize specific receptor-mediated uptake of targeted particles. The data additionally reveals that the applied particle dose can significantly affect the uptake characteristics. A second study with bioreducible PEGylated PDMAEMA polyplexes demonstrates that reversible PEG shielding is a promising approach to enhance the transfection efficiency of gene nanocarriers.

Furthermore, a study on EGF receptor targeted polyplexes is presented. Applied polyplexes were equipped either with natural full-length EGF or the alternative peptide ligand GE11. Presented data demonstrates that the ligands induce two distinct endocytosis mechanisms for particle uptake. The full-length EGF triggers accelerated endocytosis due to its dual active role in receptor binding and signaling. For GE11 an alternative EGFR signaling-independent, actin-driven pathway is proposed.

SUMMARY

In addition to optimization of the targeting ligand itself, a method is introduced that can be used to determine the optimal ligand density on the particle surface for efficient particle internalization.

Furthermore the setup of a microfluidic device is reported in this thesis that can be applied to screen the interactions of nanoparticles with cells and physiological surfaces. Experimental results on the cellular adhesion of targeted and untargeted polyplexes under flow conditions are presented.

In an additional study the gene delivery potential of novel four-arm PEG dendrimer hybrids as well as sequence-defined polymers from solid phase assisted synthesis was investigated using live-cell imaging. The results indicate a clear advantage of the four-arm construct in comparison to a two-arm dendrimer construct. Successful ligand installation and EGF receptor-mediated uptake of sequence-defined polymers was confirmed.

Furthermore, endosomal destabilization in cells was monitored by a calcein release assay proving the positive effect of histidine incorporation on endosomal escape of gene vectors.

Finally, successful nuclear import of biomolecules with nuclear localization sequences was visualized after direct microinjection into the cytoplasm.

In conclusion, our results demonstrate that the rational design of “intelligent” nanocarriers can lead to more specific, more efficient and safer gene delivery into cancer cells. Fluorescence live-cell imaging provides detailed insight into the cellular interactions of nanocarriers and can support the development of improved gene vectors for clinical application.

Contents

Summary	V
1 Introduction	1
2 Principles of gene therapy	5
2.1 Gene delivery systems	6
2.2. Cancer therapy	8
2.2.1 Strategies for tumor targeting	9
2.3 <i>In vivo</i> barriers for gene carriers	12
2.4 Cellular interactions of gene carriers	15
2.4.1 Attachment to the cell surface	15
2.4.1.1 Tumor-associated cell surface receptors	15
2.4.2 Endocytosis pathways and intracellular trafficking	19
2.4.3 Endocytosis-independent pathways	22
2.4.4 Endosomal escape	23
2.4.5 Decondensation and transport to the nucleus	24
2.4.6 Transgene expression	25
2.4.7 RNA interference	26
2.4.8 Toxicity	27
2.5 From <i>in vitro</i> studies towards clinical application	28
3 Fluorescence microscopy	31
3.1 Resolution and contrast	32
3.2 Principles of fluorescence	33
3.3 Fluorescence labeling	35
3.3 Special considerations for live-cell imaging	36
3.4 Wide-field and confocal scanning microscopy	37
4 Surface shielding of gene vectors	39
4.1 Interplay between PEG shielding and receptor targeting - live-cell imaging of integrin-targeted polyplex micelles	40
4.1.1. Particle design	40
4.1.2. Coincubation of RGD(+) and RGD(-) micelles at low concentration	41
4.1.3 Colocalization analysis of coincubated micelles at low concentration	42
4.1.4 Coincubation of micelles at high dose	43
4.1.5 Colocalization analysis at high dose	45

CONTENTS

4.1.6 Quantification of micelle uptake by flow cytometry	46
4.1.7 Identification of the uptake pathway	46
4.1.8 Luciferase reporter gene expression	50
4.1.9 Discussion	51
4.2 Reversible PEG shielding for improved intracellular DNA release.....	54
4.2.1 Particle design	54
4.2.2 Live-cell imaging of particle uptake and trafficking to late endosomes	55
4.2.3 Luciferase reporter gene expression	57
4.2.4 DNA release	58
4.2.5 Discussion	59
5 Receptor targeting of gene vectors	61
5.1 Tuning nanoparticle uptake: Natural and artificial EGFR targeting ligand mediate two distinct endocytosis mechanisms	63
5.1.1 Particle design	63
5.1.2 Uptake kinetics determined by quenching assay	64
5.1.3 Live-cell imaging of polyplex uptake	65
5.1.4 Uptake pathway	69
5.1.5 Receptor signaling activation	70
5.1.6 Correlation between receptor signaling and uptake kinetics	70
5.1.7 Effect of serum starvation	72
5.1.8 Discussion	73
5.2 Influence of ligand density and dual targeting	76
5.2.1 Particle design	76
5.2.2 Quantifying the uptake efficiency from confocal images	76
5.2.3 Discussion	79
5.3 Receptor targeting under flow.....	81
5.3.1 Microfluidic set-up.....	81
5.3.2 Influence of PEG shielding on polyplex adhesion under flow	84
5.3.3 EGF receptor-targeted polyplexes under flow	85
5.3.4 Discussion	86
6 Improved scaffolds for gene and drug delivery	89
6.1 Internally functionalized dendrimers with PEG core for gene therapy	90
6.1.1 Particle design	90
6.1.2 DNA binding and gene transfection	91
6.1.3 Discussion	92
6.2 Intrinsically functionalized dendrimers for drug delivery	94
6.2.1 Particle design	94
6.2.2 Live-cell imaging of loaded and unloaded dendrimers.....	95

6.2.3 Discussion	97
6.3 Sequence defined scaffolds from solid phase supported synthesis.....	98
6.3.1 Particle design	98
6.3.2 EGF ligand induces cell binding and uptake of STP polyplexes	98
6.3.3 Comparing gene transfer efficiency of EGF-PEG-STP and EGF-PEG-PEI polyplexes	99
6.3.4 Discussion	100
7 Endosomal escape and nuclear import.....	103
7.1 Histidine as endosomal escape agent	104
7.1.1 Particle design	104
7.1.2 Uptake efficiency and gene transfer	105
7.1.3 Endosomal escape monitored by calcein release assay	106
7.1.4 Discussion	107
7.2 Visualizing nuclear localization sequence (NLS) mediated import.....	109
7.2.1 Micromanipulators for direct cytoplasmic delivery	109
7.2.2 NLS mediated import of microinjected proteins	109
7.2.3 Discussion	110
8 Conclusion.....	111
9 Experimental Methods	113
9.1 Particle preparation	113
9.1.1 DNA labeling.....	113
9.1.2 Integrin-targeted polyplex micelles with different PEG lengths	113
9.1.3 Reversibly shielded PDMAEMA polyplexes.....	114
9.1.4 Receptor-targeted PEG-PEI polyplexes	115
9.1.5 Dendrimer hybrids for gene and drug delivery.....	116
9.1.6 Sequence defined STP Polymers from solid phase synthesis.....	117
9.2 Cell culture.....	118
9.3 Single-cell imaging	118
9.3.1 Particle addition	118
9.3.2 Particle quenching	119
9.3.3 Markers of cellular compartments.....	119
9.3.4 Dead cell staining	119
9.3.5 Inhibition of endocytic pathways	120
9.3.6 Receptor signaling assays.....	120
9.3.7 Fixation of cells.....	120
9.3.8 Calcein Release Assay.....	120
9.3.9 GFPnuc expression	121
9.4 Bulk cell assays.....	121
9.4.1 Flow cytometry	121

CONTENTS

9.4.2 Luciferase reporter gene expression	121
9.4.3 Western Blotting	122
9.5 Microscopical setup	122
9.5.1 Wide-field fluorescence microscopy	122
9.5.2 Spinning disk confocal microscopy	123
9.6 Microfluidic setup	123
9.6.1 SAW system	123
9.6.2 Syringe pump device	123
9.7 Micromanipulator for cytoplasmic injection	124
9.8 Data analysis	125
9.8.1 Image calibration and editing	125
9.8.2 Particle counting	125
9.8.3 Particle tracking	125
9.8.3 Colocalization analysis	126
9.8.4 Nano_In_Cell_3D	126
Appendix	127
Bibliography	131
List of Abbreviations	151
List of Publications	155
Curriculum Vitae	157
Acknowledgements	159

1 Introduction

“Gene Therapy Arrives in Europe“ was the headline of an article in the *Scientist Magazine* on the 6th of November 2012. After a turbulent history of clinical trials in gene therapy with major setbacks due to severe safety concerns, the European Commission approved the first gene therapy medicine for the European market, almost ten years after the first gene therapy of the world was introduced in China¹. The approved gene therapy medicine, called Glybera, uses a viral vector encoding for a lipid processing enzyme to treat patients lacking the functional enzyme.

Recent successes in gene therapy development were further reported from a number of clinical trials, highlighting the promising potential of gene vectors for the treatment of patients with severe, life-threatening diseases. In 2011 a study was published in the *New England Journal of Medicine* describing the effective treatment of four patients suffering from haemophilia B, an inherited bleeding disorder. After a single injection of a viral gene vector into the blood, the patients did not require blood clotting factors for up to 18 months². Also in 2011, Gaspar et al. released a study that showed recovered immune function of four from six children with severe combined immune deficiency that received hematopoietic bone marrow stem cells transduced with a retroviral vector³. A new promising gene therapy approach was also demonstrated for the treatment of cancer comprising the combination of gene therapy and immune therapy. In this approach genetically engineered T-cells that can attack cancer cells are introduced into the patients. Two patients suffering from leukemia showed complete remission of the disease after treatment with engineered T-cells⁴.

Despite encouraging data revealing the life-saving potential of gene therapies, the treatment with viral gene vectors remains risky and for each patient the potential benefits of the therapy have to be weighed up carefully against the risks. Lasting long time effects from gene therapy remain yet to be proven. One major risk when using retroviruses for gene delivery is the random integration of genes into functional sequences of the patients DNA, as shown in 2003 in a clinical trial in France where two of ten gene therapy patients developed leukemia⁵. Also, activation of undesired immune response against the viral vector has been repeatedly observed in clinical trials. Furthermore ethical and religious questions need to be solved. The concept of changing the DNA of a person is frightening to many people, and it has to be decided carefully which disorders and disabilities should be treated and which should not, to prevent abuse of the technology. Another concern is the high costs of gene therapy, which currently makes the therapy available for the wealthy only. According to the *Financial Times Deutschland* magazine (issue Nov 2nd, 2011), Glybera will be the most expensive medicine in the world, costing around 1.2 million euros for each patient.

INTRODUCTION

To improve the efficiency and persistence of gene therapy and at the same time reduce risks and costs of the treatment, novel gene vectors have to be designed. A promising strategy for the custom-designed production of gene vectors with reduced immune response is the development of artificial, non-viral gene nanocarriers. In this strategy synthetic polycationic molecules are used to complex therapeutic nucleic acids into small nanoparticles that can be internalized by cells and deliver their DNA.

In the present work polymer-based artificial gene nanocarriers were studied for their ability of gene delivery into cancer cells. Cancer is still one of the most threatening diseases worldwide that affects people of all ages. Available therapies are often effectless or patients suffer from severe side-effects due to the high systemic toxicity of conventional drugs. To provide a targeted gene therapy of diseased cancer cells might enhance the efficiency of treatment in the future with improved quality-of-life during therapy.

In this thesis, highly sensitive widefield and confocal fluorescence microscopy was applied as a tool to unravel the interactions of single gene nanocarriers with cells. This powerful method allows the observation of cellular processes in real-time with high spatial and temporal resolution. Live-cell imaging was combined with molecular biology assays such as selective inhibition of receptor phosphorylation to gain insights into the underlying cellular processes. Dual color colocalization experiments gave further insights on the pathway and fate of single particles inside the cell. To quantify the observed effects imaging experiments were combined with tailor-made digital image analysis procedures. Furthermore a microfluidic setup was designed and microinjection was used to dissect specific processes. All experiments were performed in close collaboration with interdisciplinary researchers from the Universities in Munich, Tokyo (Japan), Soochow (China) and Santa Barbara (U.S.A). The results from this thesis provide new detailed insights into the interaction of artificial gene vectors with cells, which might be used to improve the design of synthetic nanocarriers for more efficient gene delivery in the future.

The nanocarrier-mediated delivery of nucleic acids into target cells is a multi-step process and different functionalities of the particles are required to overcome different cellular barriers. First, after injection to the blood circulation the gene carriers are exposed to blood cells, serum proteins, ions and degradative enzymes that can mediate particle opsonization and degradation. To shield artificial gene carriers from undesired interactions and to enhance their circulation in the blood, hydrophilic polyethylene glycol (PEG) molecules can be attached to the particles. PEGylation also reduces uptake of the gene nanocarriers into healthy, non-target cells. To increase the specific binding and uptake into diseased cancer cells, targeting ligands can be coupled to the nanocarrier that recognize tumor-specific surface receptors. To deliver the DNA into the nucleus where transcription of the introduced gene takes place, the nanocarrier has to be internalized into the cell. For most particles uptake occurs via endocytosis into membrane-coated vesicles, called endosomes. Nanocarrier-filled endosomes can fuse with other compartments, mature by import of selective molecules and distribute inside the cell by

INTRODUCTION

passive and active transport processes. For successful transfection, the particle needs to escape from the endosomal compartment and the DNA has to be released from the particle. Next the nucleic acid has to be transported into the nucleus. The live-cell imaging experiment that will be described in the following chapters investigate a selection of nanocarriers with different functionalities to overcome these hurdles in gene delivery.

This thesis is structured into nine different chapters:

Following this introduction (chapter 1) two theory chapters are included that provide a general overview on the actual state of knowledge in the research fieldⁱ. In the first theory chapter, the biomedical principles of gene delivery, cancer therapy and tumor targeting are summarized (chapter 2). The design of artificial nanocarriers is introduced and the processing of gene vectors inside the organism and on the cellular level is explained. In chapter 3 the physicochemical basics of fluorescence live-cell imaging are described with an introduction into fluorescence, labeling strategies and the presentation of our microscope setups.

The experimental results and discussions are presented in chapter 4 to 8 in a partly cumulative manner.

Chapter 4 focuses on the effect of PEG shielding on cellular interactions of gene vectors. In a first part, integrin-targeted and untargeted polyplex micelles with different PEG length were studied to compare the effect of PEG shielding on the receptor-mediated and non-specific uptake of particles. The study was performed in collaboration with the group of Prof. Kazunori Kataoka from Tokyo University. Described results are published in the *Journal of Controlled Release*⁶.

In a second part of the chapter, reversibly PEG shielded PDMAEMA polyplexes with bioresponsive linkers were studied for their ability of enhanced intracellular DNA release. This study was initiated by Prof. Zhiyuan Zhong from Soochow University and presented results are adapted from our publication in *Biomacromolecules*⁷.

Chapter 5 describes three projects that deal with the question how receptor targeting of gene vectors can be optimized. In the first project EGF receptor-targeted polyplexes equipped either with a natural full-length ligand or a short peptidic ligand were compared in terms of uptake kinetics, endocytosis pathway and molecular mechanism of receptor-mediated endocytosis. This project was done in collaboration with PD Manfred Ogris and Prof. Ernst Wagner from the pharmacy department of the LMU and obtained results were published in *Nanoletters*⁸. In the second project the effect of ligand density and dual targeting on the uptake of integrin- and transferrin receptor-targeted polyplexes was investigated. The third project involved the establishment of a microfluidic setup to study the adhesion of targeted particles under flow conditions.

ⁱ The theory chapters summarize general information from actual publications, reviews, text books and the world wide web to put our experimental data into a broader context, they do not intend to describe our own data.

INTRODUCTION

In chapter 6, three novel scaffolds for gene and drug delivery with simplified production processes were examined on living cells. The first scaffold, a 4-arm PEG dendrimer hybrid was developed in the group of Prof. Craig Hawker at UC Santa Barbara. The obtained results on DNA complexation and gene delivery with the novel construct were included in a publication in *Biomacromolecules*⁹. Next to gene delivery, the dendrimers were also evaluated for drug delivery applications. In the second part of this chapter the effect of covalent drug loading on the cellular processing of the dendrimer was detected and the release of a model delivery unit into cells was monitored. The third scaffold analyzed in this chapter was produced in the group of Prof. Ernst Wagner by a recently developed solid phase assisted strategy. The sequence defined polymer for DNA complexation was equipped with EGF as targeting ligand, and the successful cellular internalization of formed polyplexes was determined by confocal microscopy.

Chapter 7 contains two studies on endosomal release and nuclear import. In the first study an endosomal escape assay was applied to monitor destabilization of endosomal membranes in the presence of histidines for improved endosomal buffering. This study was initiated in the group of Prof. Ernst Wagner and results are submitted for publication. In the second study cytoplasmic microinjection of samples was applied to visualize nuclear import mediated by the nuclear localization signal.

In chapter 8, a conclusion of the experimental part is given.

The experimental methods applied in this work are summarized in chapter 9.

2 Principles of gene therapy

The human body is composed of trillions of cells forming specialized tissues and organs. Each cell contains the same genetic material made of deoxyribonucleic acid (DNA) that encodes for around 25.000 genes¹⁰. The expression of these genes is highly regulated and the individual set of expressed genes determines the function and morphology of each particular cell. Inherited or acquired mutations in the DNA can lead to altered protein expression and cause severe diseases. Conventional medicine treats the symptoms of these diseases by administration of synthetic or natural product derived drugs. Gene therapy is a new approach that addresses the source of the disorder¹¹. In gene therapy a specific nucleic acid sequence is inserted into target cells in order to correct dysfunctional or missing gene function (e.g. treatment of monogenetic diseases such as cystic fibrosis¹²), to add additional gene function (e.g. enhanced immune response in cancer therapy¹³) or to suppress pathogenic gene expression. The transfection of cells with therapeutic genes can occur either directly *in vivo* or *ex vivo* after removal of tissue from the patient. Both, somatic cells as well as germ cells can be treated. Mostly, double-stranded DNA is transferred as genetic material, but short ribonucleic acid (RNA) molecules (such as microRNA (miRNA) or small interfering RNA (siRNA))¹⁴ or single-stranded antisense oligonucleotides¹⁵ can also be used to modify the protein expression in target cells. Since 1989 more than 1800 clinical studies on gene therapy have been approved. Most clinical trials focus on the treatment of cancer (65 %), monogenetic diseases (8,5 %), cardiovascular diseases (8,4 %) or infectious diseases (8 %).¹⁶

This work focuses on the application of synthetic gene nanocarriers for cancer therapy. The main aim of our experiments was to investigate how the molecular composition of gene carriers affects their interaction with cancer cells in order to gain knowledge on the future design of improved, more efficient delivery systems. In the following chapter, the fundamentals of gene carrier design as well as the current state of cancer therapy and tumor targeting are summarized. Furthermore the most important barriers for successful gene delivery in the organism and on the cellular level are explained and an overview about recent developments in clinical research is given.

2.1 Gene delivery systems

To deliver therapeutic genes to cells in the human body naked DNA can be used, which is directly injected into the target tissue¹⁷. However, the internalization efficiency of naked DNA into cells is low, the uptake is not cell-specific and DNA is easily degraded by nucleases in extracellular fluids. To achieve a more efficient and specific delivery of therapeutic nucleic acids to diseased cells a gene delivery system is required. The ideal gene delivery system should combine several properties: it should contain a high loading capacity for the genetic material, be easily administrable to the human body, be non-toxic and non-immunogenic, be targetable to specific sites and provide efficient long-term expression of the therapeutic genes. Viruses¹⁸ as well as synthetic, non-viral gene vectors¹⁹ are extensively investigated as gene delivery tools. More unconventional biological vehicles like bacteria²⁰, bacteriophages²¹, erythrocyte ghosts²² and exosomes²³ are additionally discussed for gene delivery to specific organs.

Viral gene vectors

Genetically modified viruses provide a powerful tool for gene delivery¹⁸. Viruses utilize the metabolism of host cells for production of viral proteins and have been optimized in many thousands years of evolution to efficiently infect cells and transfer their genetic material. For gene therapy, replication-deficient viruses are used whose harmful viral genes are removed and replaced by therapeutic ones. Most commonly used viruses in gene therapy are adenoviruses²⁴ and retroviruses²⁵. Adenoviruses contain double-stranded DNA which enters the nucleus but is not incorporated into the genome of the target cells (Fig. 2.1). Therefore the viral and therapeutic genes are transcribed but not replicated upon cell division. The adenovirus internalizes by receptor-mediated endocytosis. Penton and fiber proteins of the viral capsid interact with the coxsackie virus adenovirus receptor (CAR) surface protein on target cells resulting in clathrin-mediated uptake²⁶. Inside the endosome, proteins of the virus capsid are shed and at pH 6 the virus escape from the vesicle and its DNA is transported through nuclear pores into the nucleus.

Retroviruses contain an RNA genome which is transcribed into DNA inside the host cell using the reverse transcriptase enzyme. The DNA is then incorporated into the host's genome by the enzyme integrase. Upon cell division the viral genome is therefore replicated. Retroviruses bind to their host cells by specific interaction of glycoproteins in the virus envelope with cell surface receptors. Entry of virus capsids into the host cell cytoplasm is achieved by fusion of the virus envelope with host cell membranes either at the cell surface or in intracellular vesicles²⁷. Lentiviruses, a genus of the retroviridae family, are the favored system of choice for many gene therapy applications²⁸. They are able to transduce non-dividing and dividing cells and can accommodate large transgenes.

Despite the excellent transfection efficiency of these viruses, their application is limited due to safety issues. Major concerns are the high immunogenicity, induced by viral proteins and peptides, and in case of retroviruses the risk of random integration of the transferred genes into the patients DNA causing oncogenesis. Furthermore, the loading capacity of viruses is limited to the size of their endogenous genome, the production costs of viruses are high and the specific re-targeting of viruses is challenging.

Non-viral gene vectors

To overcome the limitations of viral gene vectors, research increasingly focuses on the development of artificial, non-viral gene carriers²⁹. Non-viral gene carriers are mostly cationic substances that form self-assembly complexes with negatively charged nucleic acids because of electrostatic interactions (figure 2.1). Cationic lipids (such as DOTAP, DOTMA and DOSPA)³⁰, peptides containing positively charged amino acids (polylysine, polyhistidine and polyglutamine)³¹ and polymers with a high charge density such as polyethylenimine (PEI), poly-L-lysine (PLL), polyamido-amine (PAMAM), polylactide (PLA), polylactic-co-glycolic acid (PLGA) and chitosan can be used as gene carriers³². The size of the assembled particles depends on the charge density and length of the complexing agent, the length of the nucleic acid sequence and the salt conditions in the buffer and can be adjusted from few nanometers to several hundred nanometers. Because of the lack of viral proteins, these artificial gene carriers exhibit low immunogenicity. They allow cheap and up-scalable production and provide a high gene loading capacity. Furthermore, the carrier design can be modified at will to add desired functions that are required for a specific and personalized therapy³³. For example targeting ligands can be attached to allow specific binding to diseased cells with altered surface receptor expression³⁴. To reduce unspecific, electrostatic interactions and enhance the circulation time in the body, the charged core of synthetic gene carriers can be shielded by hydrophilic molecules, such as polyethylene glycol (PEG)³⁵. To allow the programmed release of the genetic material in a defined environment, "intelligent" linkers can be introduced that sense pH, specific enzymes or temperature³⁶. Despite their promising potential, the clinical application of synthetic gene vectors is still hampered because of their low transfection efficiency. Therefore it is of great importance to understand the mechanism and cellular interactions of these gene carriers in more detail in order to optimize their design reduce undesired side effects and enhance their transfection efficiency.

2. PRINCIPLES OF GENE THERAPY

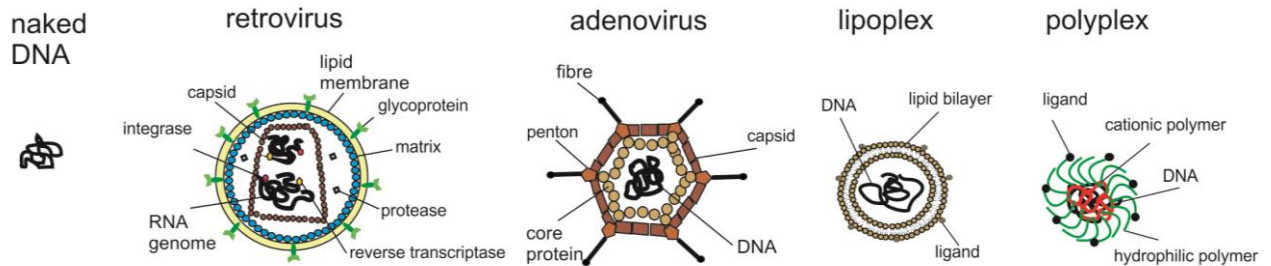


Figure 2.1 Gene carriers for nucleic acid delivery. To insert a therapeutic gene into human target cells naked DNA, viral vectors or synthetic gene vectors can be applied. Lipid enveloped retroviruses containing a capsid enclosed RNA genome and adenoviruses with a capsid enclosed DNA genome are the most commonly applied viral gene vectors. Synthetic cationic lipids or polymers are widely used to form self-assembly complexes with nucleic acid molecules (lipoplexes and polyplexes, respectively). Surface molecules can be attached to modify the cellular interactions of gene carriers.

2.2. Cancer therapy

Cancer is a prominent cause of death worldwide and deaths from cancer are predicted to continue rising in the future with 13.1 million deaths in 2030 estimated by the world health organization (WHO)³⁷. In cancer, abnormal cells divide and grow uncontrollably leading to the formation of malignant tumors. Cancer cells are able to invade nearby tissue and spread by the bloodstream or the lymphatic system to form metastasis in distant parts of the body. Cancer death is caused by the displacement of functional tissue by cancer cells impairing the function of an intact organ. Also, cancer cells can induce hemorrhages after invasion of blood vessels, compete with healthy cells for nutrients or restrict vital passages in the body.

The transformation of normal cells to abnormal cancer cells is caused by mutations in their DNA that alter the function of genes which regulate cell growth and differentiation³⁸. Affected genes are often classified as oncogenes and tumor suppressor genes¹⁰. Oncogenes induce cell survival, growth and proliferation. They encode for growth factors, growth factor receptors or downstream signaling molecules. Tumor suppressor genes encode for proteins that inhibit progression through the cell cycle, such as checkpoint-control proteins that arrest the cell cycle when the DNA is damaged, enzymes for DNA repair, and proteins that induce apoptosis.

Cancer is usually treated by surgery followed by radiation and chemotherapy. During radiation therapy ionizing radiation is exposed to the tumor tissue leading to DNA damage in exposed cells and cell death³⁹. Conventional cytostatic drugs that are used for chemotherapy prevent the growth and proliferation of cells and therefore predominantly affect rapidly dividing cells.

According to their mechanism of action cytostatic drugs can be divided into different classes⁴⁰. Alkylating agents, such as cyclophosphamide, induce DNA damage by alkylation of DNA bases. Platinum coordination complexes, such as Cisplatin, can bind two DNA bases causing cross-linking of DNA and are often classified as alkylating-like agents.

Antimetabolites, such as methotrexate or purine antagonist, are structural analogues that interfere with nucleic acid and nucleotide synthesis. Cytostatic antibiotics like doxorubicin intercalate into DNA. Mitotic inhibitors impair cell mitosis, e.g. by inhibiting topoisomerase (camptothecin) or stabilization of microtubules (paclitaxel). Hormones and hormone antagonist are applied in endocrine therapy. Immunostimulants such as interferon and immunosuppressants like interleukin inhibitors are also used in cancer therapy.

In gene therapy, instead of systemic administration of highly cytotoxic drugs, non-toxic DNA is administered which induces the expression of therapeutic proteins inside the target cells. The applied DNA can encode for pro-apoptotic proteins such as p53⁴¹, proteins that induce immune response (e.g. cytokines)⁴², antiangiogenic proteins that inhibit the formation of new blood vessels in the tumor⁴³ or prodrug converting enzymes that activate non-toxic precursors of cytotoxic drugs⁴⁴.

2.2.1 Strategies for tumor targeting

Conventional chemotherapeutic agents reach all parts of the body therefore systemic toxicity associated with severe side effects occurs during treatment. The aim of modern approaches is to design delivery systems that selectively target cancer cells, the tumor microenvironment or the tumor vasculature to enable cancer treatment with lower dosage and reduced side effects⁴⁵.

Biological targeting of cancer cells

Cancer cells differ from normal cells in many respect, they show altered gene expression, growth control, morphology, cell-to-cell interactions, membrane properties, cytoskeletal structure and protein secretion³⁸. The knowledge gained in tumor biology during the past years provides information for the design of novel, more specific anti-cancer therapies. For instance, a number of selective small molecule protein kinase inhibitors have been approved for clinical therapy⁴⁶. They suppress protein kinases which are known to play a major role in cancer progression.

A variety of surface receptors are overexpressed on the plasma membrane of cancer cells which can be targeted by selective ligands. Among these receptors are the epidermal growth factor (EGF) receptor⁴⁷, the transferrin receptor⁴⁸, the folate receptor⁴⁹ and a subset of integrins⁵⁰. Furthermore, cancer cells show altered glycosylation pattern of glycolipids, glycoproteins and proteoglycans that serve as recognition site for therapeutic agents⁵¹.

Targeting ligands can be used to directly block surface receptors (such as Herceptin, an EGFR binding antibody that is approved for the treatment of early stage breast cancer)⁵², or to promote binding and internalization of an attached drug or gene carrier⁵³. Molecules used for selective receptor binding are natural protein ligands, synthetic peptides, carbohydrates, antibodies, antibody fragments and aptamers (short DNA- or RNA strands)⁵⁴.

Targeting the tumor microenvironment

The microenvironment in which a tumor grows plays an important role for its progression⁵⁵. Cancer cells shape their environment. They recruit a number of stromal and non-malignant cells, such as

2.PRINCIPLES OF GENE THERAPY

fibroblasts, endothelial cells and inflammatory cells, to form a supportive microenvironment for tumor growth (figure 2.2). These cells secrete components of the extracellular matrix, growth factors, proteases and cytokines that promote angiogenesis (the formation of new blood vessels), proliferation and migration of cancer cells and support tumor malignancy. As the microenvironment has a crucial role in carcinogenesis and metastasis it represents a crucial target for cancer therapy as well⁵³.

A number of strategies have been developed that target tumor associated macrophages⁵⁵. These strategies include depletion of chemokines that are secreted by tumor cells to attract or polarize macrophages, targeting subsets of macrophages themselves or factors that tumor-associated macrophages produce⁵⁶.

Many stages in cancer progression depend on the expression of matrix-metalloproteinases (MMPs) that degrade various components of the extracellular matrix. Inhibitors of MMPs have been developed for cancer therapy, as well as activable drug- and gene carriers that contain cleavage sites for specific MMPs⁵⁷.

Targeting the tumor vasculature

The vasculature of solid tumors is fundamentally different from the vasculature in normal tissues offering an additional target for anti-cancer therapy. Tumor vessels are immature and hyperpermeable, they are poorly lined with smooth muscle cells and have a discontinuous endothelial cell layer⁵⁸ (Fig. 2.2). The vasculature in tumors is disorganized; the normal hierarchy of blood vessels is missing. The associated lymphatic vessels are dilated and discontinuous. The ability of tumor vessels to deliver nutrients and remove waste products is strongly reduced. The lack of normal vasculature in the tumor causes oxygen starvation resulting in acidosis of the tumor microenvironment. As lymphatic fluid and waste are inefficiently transported from the tumor microenvironment the interstitial pressure increases in the tumor.

The enhanced permeability and retention in the tumor (EPR effect) can be used for passive targeting of nano-sized materials⁵⁹. Nanocarriers with a hydrodynamic diameter above 5.5 nm (approximately 40 kDa) escape from renal clearance and are unable to pass through tight endothelial junctions in normal blood vessels⁶⁰. In the tumor tissue they extravasate from leaky tumor vessels resulting in accumulation of the administered drugs or genetic material in the tumor⁶¹.

It has been observed that tumors cannot grow beyond a size of 2 mm without neovascularization⁶². This knowledge has led to the development of a number of anti-angiogenic agents that inhibit the formation of new blood vessels. Most common among them are therapeutics that target the vascular endothelial growth factor (VEGF) and its receptor (VEGFR)⁶³.

The reduced pH in the extracellular space of tumors enables targeting strategies with pH sensitive nanocarriers⁶⁴. Polymeric micelles and liposomes have been established that destabilize at low pH, resulting in enhanced drug release in the tumor tissue⁶⁵. Also, pH-sensitive peptides like the TAT peptide can be attached to nanocarriers that promote specific cellular internalization at low pH⁶⁶.

Physical targeting strategies

Next to biological targeting strategies, physical targeting methods have been established to enhance drug and gene delivery at the tumor site. Electrical pulses (electroporation)⁶⁷ as well as ultrasonic waves (sonoporation)⁶⁸ locally destabilize membranes in exposed tissues leading to enhanced nanocarrier uptake. High magnetic fields can be used to accumulate superparamagnetic particles at a specific site (magnetofection)⁶⁹. Controlled heating (hyperthermia) enhances permeability of blood vessels and increases nanocarrier uptake in tumors⁷⁰. Photo-induced therapies rely on the local activation of photosensitizers after light-exposure resulting in photochemical damage of membranes and increased drug internalization⁷¹.

Various cancer therapeutics are currently examined in preclinical and clinical trials. A major challenge in cancer therapy remains the treatment of spread metastatic cells that are difficult to detect and to reach even with sophisticated, targeted therapeutics.

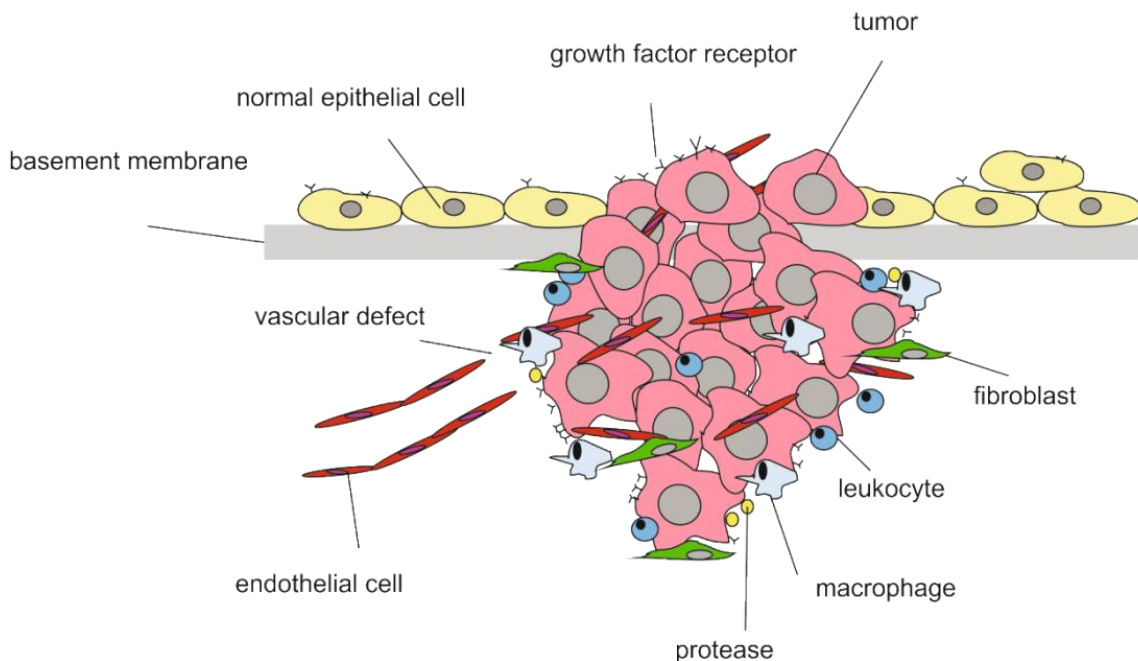


Figure 2.2 The tumor microenvironment. Malignant tumor cells displace normal epithelial cells and break through the basement membrane to reach the blood flow and form metastasis in distant organs. The tumor cells attract stromal and non-malignant cells like leucocytes, macrophages and fibroblasts to form a supportive microenvironment for tumor growth. Formed tumor blood vessels are discontinuous and hyperpermeable. Selective surface molecules like growth factor receptors are upregulated on tumor cells to promote cell proliferation and survival (figure adapted from⁷²).

2.3 *In vivo* barriers for gene carriers

The administration of therapeutic nanocarriers to the human body can occur by intravenous or non-intravenous (subcutaneous, intramuscular, intradermal, intratumoral) injection, by oral exposure or by inhalation. On their way to the target tissue, therapeutic nanocarriers face several barriers which they need to overcome for efficient gene delivery⁷³ (Fig. 2.3). The pharmacokinetics of nanoparticles is determined by their chemical and physical properties, such as size, charge and surface chemistry and differs significantly from small molecule drugs⁷⁴. The different barriers before reaching the target tissue are described in the following section.

Barriers in the gastrointestinal tract and the airway

When administered orally, particles first have to pass the gastrointestinal tract where they face degradation by digestive enzymes. Additional barriers before entering the blood circulation or the lymphatic system are the mucus and the epithelium of the gastrointestinal tract. The mucus renews continuously and carries trapped nanoparticles to the feces. Passage through the epithelium mainly occurs through Peyer's Patches in the wall of the small intestine⁷³.

After pulmonary administration, particles can be removed by ciliary movements in the mucus of the upper airway⁷⁵. The lower section of the airway is lined by immune cells that efficiently internalize and clear inhaled nanoparticles.

Interaction with blood components

When reaching the blood circulation, nanoparticles interact with serum proteins (e.g. laminin, fibronectin, c-reactive protein, collagen), immunoglobulins and complement proteins that adsorb on the particle surface, a process called opsonization⁷⁶. These adsorbed proteins are recognized by specialized receptors (Fc receptor, mannose/fructose receptor, scavenger receptor) on phagocytes that ingest large numbers of particles and remove them from circulation⁷⁷. High numbers of phagocytes are found especially in the liver (Kupffer cells), in lymph nodes, bone marrow and spleen (reticular cells). Therefore in general, high accumulation of nanoparticles is observed in these organs. Enhanced opsonization and clearance occurs for charged particles compared to particles with neutral surface charge⁷⁸. In addition, phagocytosis seems to be size and shape dependent⁷⁹. Particles with sizes from 250 nm to several microns exhibit higher opsonization and phagocytosis than smaller particles^{80, 81}. Positively charged particles furthermore tend to form large aggregates with serum proteins that can induce embolism in the lung⁸².

The opsonization and aggregation of particles can be significantly reduced by attachment hydrophilic, neutral polymers such as polyethylene glycol (PEG) resulting in elongated circulation times (several hours to days) in the blood^{20, 76}.

Passage through capillary walls

Nanoparticles are distributed to different tissues by the blood stream and the lymphatic system. Blood vessels are lined by a tight layer of endothelial cells. Small molecule drugs are able to diffuse through the capillary walls into the tissue. Nanoparticles are not able to penetrate by diffusion, they rely on gaps to pass through this barrier⁷³. Blood vessel endothelium is classified in three different categories, depending on its morphology: continuous, fenestrated and discontinuous⁸³. Most capillaries are formed by continuous epithelium in which neighboring cells are separated by tight junctions. Fenestrated endothelium contains pores of 50 nm size and is found in glands, digestive mucosa and kidney⁸⁴. Discontinuous endothelium with an incomplete basement membrane is present in liver, spleen, and bone marrow containing gaps of 50-100 nm size. Small nanoparticles with sizes below 60 nm have enhanced access to tissues with fenestrated or discontinuous endothelium (Fig. 2.3 B). Tumor vessels have a defective cellular lining with disorganized, loosely connected cells and openings between cells that can be passed by larger nanoparticles⁸⁵.

Internalization by non-target cells

During their passage in the blood circulation, nanoparticles can directly bind and internalize into non-target cells such as blood or endothelial cells. In general, particles with positive surface charge show higher endocytosis levels compared to negatively charged or uncharged particles^{86, 87}. Specific accumulation of nanoparticles in tumor tissue can be enhanced by passive targeting (EPR effect) or active targeting strategies³⁴.

Interaction with extracellular matrix components

Tissues are not only made of cells, a substantial part is extracellular space that is filled by a tight network of macromolecules (polysaccharides, glycosaminoglycans, fibrous proteins) forming the extracellular matrix¹⁰. The diffusion of charged nanoparticles is slowed down in the extracellular space due to electrostatic interactions with negatively charged matrix molecules, neutral particles show faster diffusion⁸⁸. One approach to increase the diffusion of therapeutic particles in the extracellular space is the controlled partial degradation of extracellular matrix components by enzymes like collagenase or hyaluronidase⁸⁹.

Degradation and excretion

Nanoparticles can be metabolized by hydrolytic or enzymatic degradation in extracellular fluids or inside cells in endo/lysosomes. Inorganic nanoparticles are usually difficult to metabolize⁹⁰. Polymers can be designed biodegradable or non-biodegradable⁹¹. Their rate of degradation can be controlled by composition and molecular weight. Nanoparticles can be excreted from the body in the bile via the liver and the kidney. Degraded particles are removed by renal clearance (cutoff for glomerular filtration = 5.5 nm)⁶⁰.

2. PRINCIPLES OF GENE THERAPY

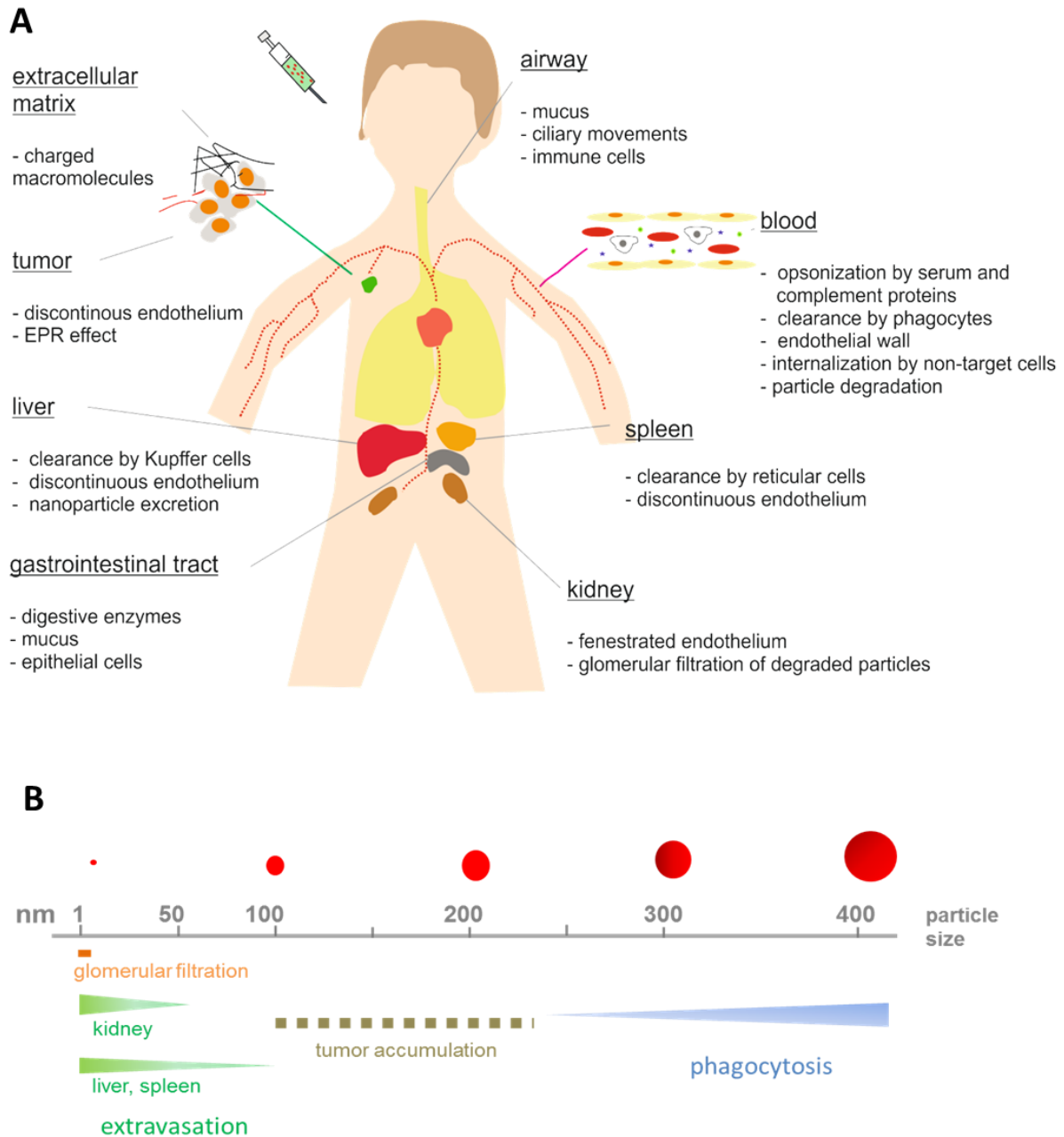


Figure 2.3 *In vivo* barriers for nanoparticle delivery.

A After injection, inhalation or oral exposure nanoparticles have to pass several barriers before reaching the target cells of interest. Physical barriers include mucus, epithelial cells in the gastrointestinal tracts, the endothelial cell layer and the extracellular matrix. Gaps in the endothelial layer enhance particle access to distinct organs like liver, spleen and kidney. Activated immune cells ingest nanoparticles and clear them from circulation. Immune activation is enhanced by opsonization of particles with serum proteins. Enzymatic or non-enzymatic degradation of particles can occur in biological fluids followed by renal clearance.

B Size dependency of nanoparticle clearance from the blood flow. Small nanoparticles can extravasate from the blood flow in organs with fenestrated or discontinuous endothelium. Phagocytosis increases for larger particles above 250 nm.

2.4 Cellular interactions of gene carriers

After reaching the tissue of interest, gene carriers need to be internalized and processed inside the target cells in order to achieve efficient expression of the therapeutic genes. The different steps of cellular interactions include attachment to the cell surface, uptake via endocytosis or non-endocytic pathways, trafficking inside the cell, release from endosomes, transport into the nucleus and gene expression (Fig. 2.5)⁹².

2.4.1 Attachment to the cell surface

The plasma membrane that encloses human cells consists of a lipid bilayer (made of phospholipids, glycolipids and cholesterol) with embedded proteins, glycoproteins and proteoglycans¹⁰. Endothelial cells are typically covered by a carbohydrate rich layer between 0.5 μm and 4.5 μm thickness, the glycocalyx⁹³. Gene carriers without shielding often exhibit a net positive charge. They supposedly bind to anionic cell surface proteoglycans such as heparin sulfate and syndecan which have been proposed as receptors for particle endocytosis⁹⁴. Consistently, improved cell surface binding and endocytosis has been demonstrated for positively charged nanoparticles compared to negatively charged or neutral nanoparticles^{95, 96}. However, molecules of the glycocalyx may also serve as a barrier for efficient particle internalization. Recently, it was demonstrated that syndecan-1 mediates fast internalization of PEI-polyplexes, whereas syndecan-2 has an inhibitory effect on gene transfer⁹⁷. The negative effect of certain cell surface glycosaminoglycans on the transfection of PEI polyplexes has also been described by Hanzlikova et al⁹⁸. They propose that free PEI in solution is essential to minimize the undesirable binding of particles to surface aminoglycans.

Shielding of particles with hydrophobic molecules such as polyethylene glycol reduces non-specific electrostatic interactions with the cell surface³⁵. Targeting ligands on the particle surface can mediate binding to selective cell surface molecules and induce receptor mediated particle internalization⁵⁴. After their passage through biologic fluids, nanoparticles are typically covered by a large number of biomolecules, forming the particle corona⁹⁹. These bound molecules can modify the surface charge and can be recognized by cellular receptors, changing the cellular attachment and uptake of the nanoparticles¹⁰⁰.

2.4.1.1 Tumor-associated cell surface receptors

As mentioned before, cancer cells often exhibit upregulated or mutated surface receptors that promote cell proliferation and survival or transformation of epithelial cells into migrating metastatic cells. These receptors are promising targets for the selective delivery of therapeutic nanocarriers. In the experimental part of this thesis, different receptor targeting strategies are investigated; therefore the molecular mechanism of selected tumor-associated cell surface receptors is described in more detail in the following section.

2.PRINCIPLES OF GENE THERAPY

EGF receptor

The epidermal growth factor receptor (EGFR) belongs to the family of tyrosine kinases and controls proliferation, survival, differentiation and migration of cells. Deregulation of EGFR signaling contributes to tumorigenesis by inhibition of apoptosis, induction of angiogenesis, cell-cycle progression and promotion of cell mobility. The EGFR is known to be overexpressed in a variety of human tumors, including breast, lung, colorectal, prostate, kidney, pancreas, ovary, brain and bladder cancer^{101, 102}. The receptor is a transmembrane glycoprotein consisting of an extracellular ligand-binding ectodomain, a transmembrane domain and an intracellular tyrosine kinase domain¹⁰³ (figure 2.4). Binding of high-affinity ligands, such as EGF, to the ectodomain promotes receptor dimerization followed by activation of the intracellular kinase domain and phosphorylation of the C-terminal tyrosines^{104, 105}. Subsequently components of downstream signaling pathways are activated, including the Ras/MAPK, PLC1/PKC, PI3kinase/Akt and Stat pathway (see figure 5.7 A). To inactivate the receptor it is internalized by clathrin-mediated endocytosis and transported to lysosomal compartments¹⁰⁶. A number of adapter molecules, such as AP-2 and epsin, have been identified that mediate the formation of clathrin coated pits after receptor signaling activation^{107, 108}. For endocytosis, reorganization of the actin cytoskeleton is required¹⁰⁹. Downstream signaling molecules such the small G-proteins Rac and Rho are involved in the linkage of the EGF receptor to actin¹¹⁰. For low-affinity EGFR ligands, such as TGF α and epiregulin, different endocytic sorting of the EGF receptor has been reported leading to receptor recycling instead of lysosomal degradation¹¹¹. Apart from ligand-induced EGFR endocytosis, ligand-independent internalization of the EGF receptor has been observed¹¹². Recent studies suggest that ligand-independent receptor endocytosis correlates to Rab5 expression¹¹³, activation of p38 mitogen-activated protein kinase¹¹⁴ and phosphatidic acid signaling¹¹⁵. Strategies for EGFR-directed tumor therapy include the blockade of ligand binding by monoclonal antibodies¹¹⁶, the inhibition of receptor activation by small molecule tyrosine kinase inhibitors¹¹⁷ and the specific transfer of ligand installed drugs or gene delivery systems to diseased cells^{118, 119}.

Folate receptor

Folate receptors (FR) are N-glycosylated proteins with high binding affinities for folate, an essential vitamin with a central role in the cellular metabolism. Cancer cells require increased levels of folate to maintain DNA synthesis and repair. Folate receptors include at least four isoforms; FR α , β and δ are glycosylphosphatidylinositol (GPI) anchored membrane proteins, whereas FR γ is secreted by lymphoid cells¹²⁰. Functional folate receptor expression is low in most normal tissues but upregulated in carcinomas^{49, 121}. FR α expression is frequently amplified in epithelial cancers, whereas FR β overexpression is found in myeloid leukemia and tumor associated macrophages. After binding to the folate receptor, folate conjugates are endocytosed. Conflicting reports exist in the literature on the uptake pathway of folate receptors. First it was claimed that GPI anchored folate receptors are clustered in caveolin-rich domains and are internalized by caveolin-dependent endocytosis¹²². Later on it was shown that the sequestration of the folate receptor in caveolae was an effect of the cross-linking procedure with fluorescently labeled antibodies, whereas without cross-linking the receptors are diffusely distributed over the plasma membrane¹²³.

More recent studies give evidence that GPI coupled folate receptor α is internalized via a clathrin- and dynamin-independent mechanism to endocytic compartments termed GPI-anchored protein enriched endocytic compartment (GEEC)¹²⁴. After uptake into GEEC, the folate receptor is transported either to recycling compartments or late endosomes. Next to high-affinity folate receptors two additional folate carriers are ubiquitously expressed on cells that mediate folate transport from the blood stream into the tissues¹²⁰. The reduced folate carrier (RFC) is an organic anion antiporter that utilizes the high transmembrane phosphate gradient to achieve uphill folate transport into cells. The proton coupled folate transporter (PCFT) mediates folate import at low pH. However the *in vivo* distribution of folate receptor-targeted therapeutics is unlikely to be affected by the RFC and the PCFT, as the binding affinity of folate to the folate receptor is much higher¹²⁵.

Transferrin receptor

The transferrin receptor (TfR) is a membrane glycoprotein that mediates cellular uptake of iron from the plasma protein transferrin⁴⁸. Whereas the expression of TfR2 is largely restricted to hepatocytes, the TfR1 is ubiquitously expressed at low levels in most human tissues. Cancer cells rely on iron import for proliferation and many cancer cells show highly increased expression of transferrin receptor¹²⁶. The homodimeric receptor binds up to two iron-transferrin molecules and is constitutively internalized via clathrin coated pits¹²⁷ (Fig. 2.4). Acidification of the early endosome triggers conformational changes resulting in iron release and fast recycling of the receptor-apotransferrin complex to the cell surface¹²⁸. When the receptor-apotransferrin complex reaches the plasma membrane, apotransferrin dissociates from its receptor because of its low receptor affinity at neutral pH¹²⁹. In the absence of transferrin the transferrin receptor is susceptible to higher rates of proteolysis. Targeting experiments with the transferrin receptor have been performed with natural ligand transferrin, short peptides, monoclonal antibodies and antibody fragments⁴⁸.

Integrins

Integrins are heterodimeric cell surface receptors that bind components of the extracellular matrix (ECM) and counter receptors to promote cell adhesion and migration and control cell survival¹³⁰. At least 24 distinct integrin heterodimers are formed by the combination of 18 α -subunits and 8 β -subunits. Integrins possess the unique ability to dynamically modulate their adhesiveness by regulation of their affinity (binding affinity of monomeric integrins to their substrate ligands) and valency (changes in local cell surface receptor density and diffusivity)^{131, 132}. Integrin molecules can switch between a closed, bent state with low ligand affinity, an intermediate state and an open, stretched conformation with high ligand affinity (Fig. 2.4)¹³³. Conformational changes in integrins can be induced either by cytoplasmic events (such as cytoplasmic binding of talin and kindlin protein after activation of G-protein coupled receptor signaling (inside-out activation)) or by extracellular factors (outside-in activation)¹³⁰. Activating extracellular factors can be the high concentration of ECM ligands, integrin clustering or mechanical stress^{134, 135}. Ligand binding to integrins triggers integrin clustering in the membrane and the recruitment of several adapter and signaling proteins (src family kinases, focal

2.PRINCIPLES OF GENE THERAPY

adhesion kinases) leading to the formation of macromolecular adhesion complexes. Recruited proteins like talin, vinculin and paxillin couple activated integrins to the actin cytoskeleton mediating the reorganization of the cellular cytoskeleton¹³¹. Furthermore integrin-ligand interactions induce the activation of several signal transduction pathways that regulate proliferation, survival and gene expression. For focal adhesion disassembly and integrin redistribution, integrins need to be internalized and recycled. Integrins are endocytosed via clathrin-dependent and clathrin-independent mechanisms^{136, 137}. In cancer, integrins play an important role for tumor cell migration and invasion. Integrins $\alpha\beta3$, $\alpha5\beta1$ and $\alpha\beta6$ are usually expressed at low or undetectable levels in most adult epithelia but can be highly upregulated in some tumors⁵⁰. Unlike normal endothelium, tumor associated blood vessels express $\alpha\beta3$ and $\alpha\beta5$ integrins. Preclinical and ongoing clinical trials reveal that integrin antagonists, including monoclonal antibodies and RGD peptide mimetics have the potential to inhibit tumor growth¹³⁸.

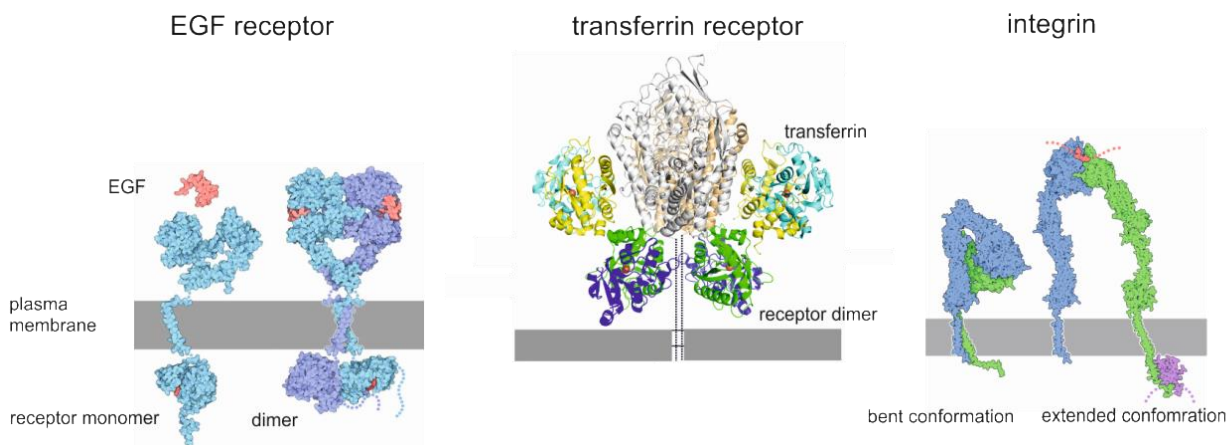


Figure 2.4 Tumor-associated cell surface receptors. Protein structures of the epidermal growth factor (EGF) receptor, the transferrin receptor and an integrin molecule are illustrated. **A** Binding of the EGF ligand to its receptor induces receptor dimerization, signaling activation and endocytosis (source: protein data base (PDB), doi 10.2210/rcsb_pdb/mom_2010_6). **B** Up to two transferrin molecules bind to the homodimeric transferrin receptor resulting in clathrin-mediated receptor endocytosis. (PDB, doi 10.2210/pdb1suv/pdb) **C** Integrins can change between a bent conformation with low ligand affinity and an extended conformation with high affinity. Activation of integrins can be induced by intracellular or extracellular factors resulting in integrin clustering and recruitment of adapter and signaling proteins. (PDB, doi 10.2210/rcsb_pdb/mom_2011_2)

2.4.2 Endocytosis pathways and intracellular trafficking

Cells are able to internalize molecules from the surrounding medium by endocytosis. In this process the extracellular material is surrounded by plasma membrane which buds off to form an intracellular vesicle. Endocytosis is the main pathway for therapeutic nanoparticles to cross the plasma membrane, either caused by specific interactions with target receptors or after unspecific attachment to the cell surface¹³⁹. Generally, endocytosis can be divided into two categories: phagocytosis and pinocytosis.

Phagocytosis (“cell eating”) is done explicitly by specialized immune cells (macrophages, monocytes, neutrophils and dendritic cells) that ingest large molecules such as pathogens and cell debris⁷⁷. During phagocytosis foreign particles in the blood stream are recognized by opsonization, bind to the surface of phagocytes via specific receptor ligand interactions and are then internalized into large vesicles.

Pinocytosis (“cell drinking”) is present in all cell types and can be classified based on the proteins involved in the endocytic pathway into clathrin-mediated endocytosis, caveolin-mediated endocytosis, clathrin- and caveolin-independent endocytosis and macropinocytosis¹⁴⁰.

Clathrin-mediated endocytosis (CME) is the “classical route” that is responsible for the uptake of essential nutrients (e.g. cholesterol bound to LDL, or iron bound to transferrin), the down-regulation of cell-signaling (by uptake of surface receptors) and the maintenance of cellular homeostasis¹⁴⁰. Best described is the mechanism of clathrin mediated endocytosis after specific receptor-ligand interactions, but non-specific endocytosis via clathrin coated pits also exists¹⁴¹. CME typically occurs in membrane regions enriched in clathrin-1¹⁴². Clathrin is a cytosolic protein with a typical three leg structure, called triskelion. These triskelia assemble in a polyhedral lattice on the cytosolic surface of the cell membrane which helps to deform the membrane into a coated pit. The pit formation requires additional assembly proteins such as AP2 and AP180¹⁴³. The assembled vesicle is pinched off from the plasma membrane by a small GTPase dynamin¹⁴⁴. Various accessory proteins like intersectin and eps15 connect the endocytic machinery with the actin cytoskeleton. Actin is required for the movement of the endocytic vesicle towards the interior of the cell. Within the cell, the clathrin coat sheds off and the vesicle fuses with early endosomes. Early endosomes are the major sorting station in the cell. From this organelle material can be either recycled to the plasma membrane or directed to later endocytic compartments or secretory vesicles¹⁰. Early endosomes are acidified by ATP driven proton pumps (pH=6)¹⁴⁵. At this pH, some receptor-ligand complexes already dissociate enabling recycling of the internalized receptors. Recycling endosomes are less acidified (pH=6.4-6.5)¹⁴⁶. The recycled cargo can be transported to the membrane from which they were internalized or cross the cell to be delivered to the opposite membrane (transcytosis). Early endosomes mature into late endosomes (p=5.0-6.0) where degradative enzymes are active. After fusion with prelysosomal vesicles, lysosomes containing acid hydrolases (pH=4.6-5.0) are formed¹⁴⁷. Biological molecules such as proteins and DNA can be degraded in this organelle. Several ligands are known to utilize clathrin-mediated endocytosis such as transferrin, LDL, EGF and mannose-6-P¹⁴⁸. Notably, the intracellular trafficking of ligand-modified nanomaterials can differ from trafficking of the unmodified ligand. For example, a study

2.PRINCIPLES OF GENE THERAPY

with transferrin-modified quantum dots revealed their transportation to perinuclear endosomes, whereas transferrin alone is usually recycled to the plasma membrane¹⁴⁹.

Caveolae are characteristic flask-shaped membrane invaginations lined by the dimeric protein caveolin-1 and enriched with cholesterol and sphingolipids¹⁵⁰. Molecules that bind to the caveolae surface are engulfed into vesicles with the help of cavin, dynamin and VAMP-2¹⁵¹. After budding from the plasma membrane vesicles fuse with caveosomes or multivesicular bodies (MVB) that have neutral pH. Caveolin-mediated endocytosis seems to be slower than CME, but at least in some cases it avoids transport to lysosomes¹⁵². Because of the reduced lysosomal degradation of the internalized particles this pathway is believed to be beneficial for the delivery of biological molecules. Typical molecules that utilize caveolin-mediated endocytosis are shiga toxin and cholera toxin B (CT-B)¹⁵³. Also some viruses enter the cell via this pathway¹⁵⁴.

Clathrin- and caveolin-independent endocytosis is subclassified into Arf-6-dependent, flotillin-dependent, Cdc42-dependent and RhoA-dependent pathways¹⁵⁵. Up to now, not many details are known about the uptake mechanism, but all pathways seem to depend on cholesterol and require specific lipid composition. Internalized molecules seem to bypass Rab5 positive early endosomes. Not many nanomaterials are documented to utilize these pathways. Examples include folate-modified nanoparticles and polymers¹⁵⁶.

Macropinocytosis is a special case of clathrin-, caveolin-, and dynamin-independent endocytosis¹⁵⁷. It is a nonspecific uptake pathway that can be utilized by large particles. Macropinocytosis can be initiated by transient activation of receptor tyrosine kinases by growth factors. The transient receptor activation triggers changes in the actin cytoskeleton that induce the formation of membrane ruffles. These membrane ruffles engulf extracellular fluids and molecules and form vesicles (macropinosomes) that are usually larger (0.5-10 μm) than other pinocytosis vesicles. Bacteria, viruses and cell debris can also induce the membrane ruffling independent of transient activation by growth factors¹⁵⁸.

In all endocytosis pathways, vesicles are transported over long distances in the cytoplasm to defined target organelles. Whereas early endosomes and recycling endosomes are mainly located in the cellular periphery, late endosomes and lysosomes show accumulation in proximity to the nucleus. For efficient gene expression in the cell, it is favorable to bring the therapeutic DNA in close proximity to the nucleus to shorten its residence time in the cytoplasm where nucleases are active. Studies with microinjected circular DNA revealed that both single and double-stranded DNA disappear with an apparent half-life of 50-90 minutes from the cytosol¹⁵⁹. The cytoplasm of cells is highly crowded with cytoskeleton, organelles and soluble macromolecules. Therefore passive transport by free diffusion is strongly limited for large DNA molecules and vesicles (confinement diameters 0.1-2 μm)¹⁶⁰. To achieve directed transport of vesicles with sufficient velocity (0.5-0.7 $\mu\text{m/s}$), active transport mechanisms are required. During active transport vesicles are bound by ATP-driven motor proteins (kinesin and dynein) that transport their cargo along the microtubule network of the cell¹⁶¹.

Most nanoparticles exploit more than one endocytosis pathway to enter the cell¹⁴⁸. The uptake pathway seems to be affected by the charge, size and shape of the particles as well as the attached surface ligands. Also the cell type plays an important role as well as the cell phenotype depending on the growth conditions of the cells (e.g. cell density, available growth factors). The majority of reports suggest that positively charged nanoparticles predominantly internalize via CME, whereas negatively charged nanoparticles are more likely to use caveolae-mediated endocytosis¹⁴⁸. To dissect the intracellular trafficking pathway of a nanoparticle, colocalization studies with specific endocytosis markers can be performed or specific pathways are excluded by utilizing cell mutants or inhibitors. Unfortunately, many endocytosis markers and inhibitors are not selective. Therefore, and due to the multiple parameters that affect cell endocytosis, many conflicting reports on nanomaterial trafficking pathways exist in the literature and generalizations are difficult to make.

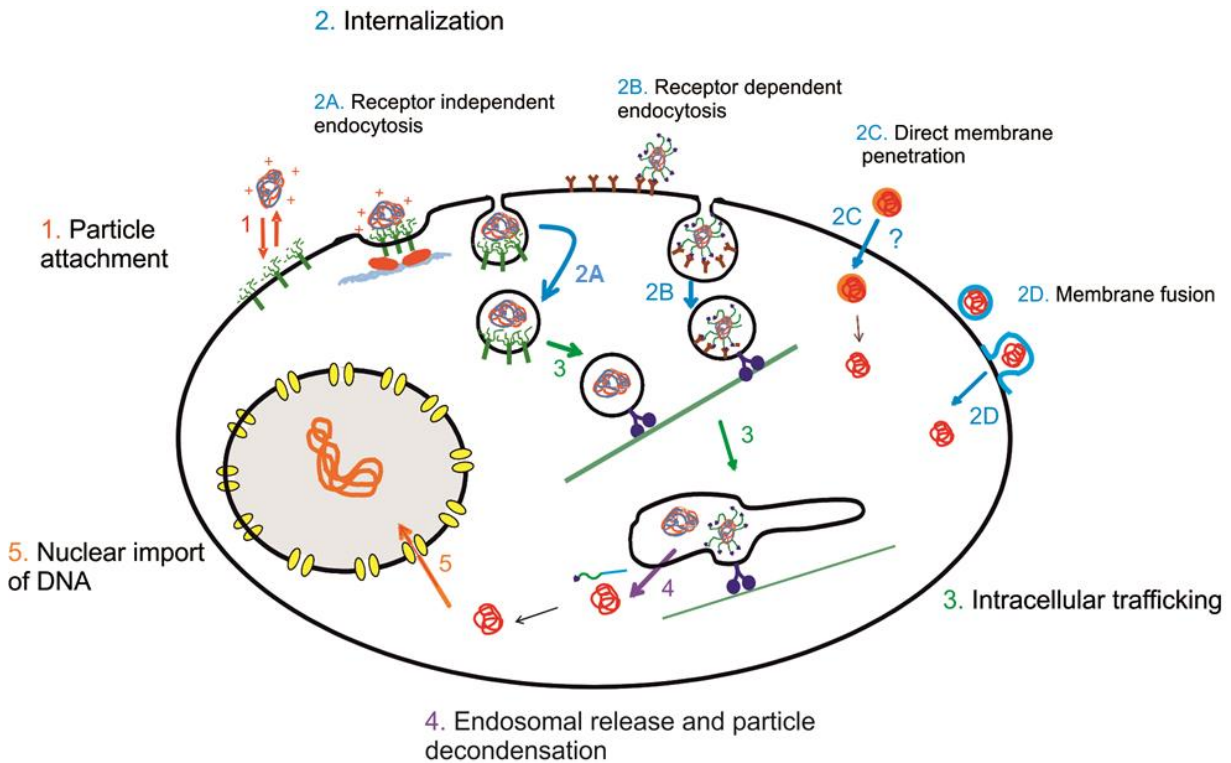


Figure 2.5 Cellular interactions of gene carriers. To express the therapeutic DNA, gene carriers need to be processed by the target cells. After attachment of the particle to the cell membrane (1) it can be internalized either by receptor-dependent (2A) or receptor-independent endocytosis (2B), by membrane fusion (2C) or by direct membrane penetration (2D). Nanoparticle filled endosomes are sorted inside the cell and are actively transported by motor proteins along the cytoskeleton to specific organelles (3). Release of gene carriers from endosomes and decondensation of the particle are critical barriers for gene delivery (4). Cytoplasmic DNA can be delivered to the nucleus by the nuclear import machinery or after breakdown of the nuclear envelope during cell division (5). Adapted from a figure provided by Dr. Nadia Ruthardt.

2. PRINCIPLES OF GENE THERAPY

2.4.3. Endocytosis-independent pathways

Next to endocytosis, additional endocytosis-independent uptake pathways exist for the cellular entry of nanoparticles.

Some lipid enveloped particles are able to enter the cell via direct lipid bilayer fusion¹⁶². During this process, the lipid bilayer of the particle merges with the lipid bilayer of the plasma membrane resulting in direct delivery of the uncoated particle core to the cytosol. To achieve fusion in an aqueous environment, counteracting electrostatic forces first need to be overcome to bring the membranes in close proximity. Next, the boundary between the hydrophilic and hydrophobic portion of the bilayer have to be destabilized locally to form an aqueous fusion pore¹⁶³. Cations, such as Ca and Mg play a critical role in the fusion process by binding negatively charged lipids and reducing electrostatic repulsion¹⁶⁴. Fusion is also affected by the nature of lipid headgroups in the bilayer. It was shown that the presence of uncharged phosphatidylethanolamine (PE) enhances membrane fusion¹⁶⁵. A number of enveloped viruses, such as HIV¹⁶⁶ or Herpes simplex¹⁶⁷, utilize lipid bilayer fusion to enter the cell. They contain specialized fusion proteins that undergo conformational changes upon activation and induce the fusion process. It was initially thought that synthetic lipoplexes, consisting of cationic lipids and DNA, deliver their DNA by fusion with the plasma membrane. However, more recently, it has been established that the major entry pathway for lipoplexes is endocytosis instead of fusion^{168, 169}.

Another endocytosis-independent entry mechanism has been proposed for cell-penetrating peptides (CPP)¹⁷⁰. These are short, water soluble and partly hydrophobic, and/or polybasic peptides (30-35 aminoacids) with net positive charge, which are able to penetrate the membrane without using any receptor. The first CPP discovered was the tat peptide of HIV¹⁷¹. CPPs are able to efficiently transport covalently bound cargos such as drugs into the cell. There is evidence, that CPPs directly penetrate the membrane in an energy-independent process. Different models have been suggested including pore formation, carpet-like perturbations or inverted micelle formation in the plasma membrane¹⁷⁰. However, at least at low concentration, CPP also utilize endocytosis as predominant pathway for cell entry. Direct penetration of the plasma membrane has also been described for monolayer coated gold nanoparticles with alternating anionic and hydrophobic groups^{172, 173}.

Recently, a new synthetic peptide called pHLIP (pH(low) integrating peptide) has been discovered that undergoes conformational changes at low pH resulting in its membrane insertion into acidic tissues, such as tumors or sites of inflammation¹⁷⁴. After insertion the c-terminal, inserting end of the peptide comes in contact with the inner leaflet of the lipid bilayer. When coupling a cargo, like a short nucleic acid, via a cleavable, redox-sensitive disulfide linker to the C-terminal end of the peptide, the cargo can be delivered directly to the cytoplasm circumventing endocytosis¹⁷⁵.

2.4.4. Endosomal escape

As described before, most therapeutic nanoparticles are internalized via endocytosis and remain entrapped in endosomes during intracellular trafficking. To deliver therapeutic nucleic acids to the cell nucleus or into the cytoplasm, the internalized material has to escape from endosomes. Endosomal escape is believed to be one of the main limiting steps for efficient transfection and much effort is done to improve the endosomal release properties of artificial gene vectors¹⁷⁶.

To achieve enhanced endosomal escape, one can learn from escape mechanisms developed by pathogens. Viruses and bacteria often contain specialized peptides that transit into an alpha-helical conformation at low pH, leading to integration in the endosomal membrane and membrane destabilization¹⁶³. Examples are the pH sensitive hemagglutinin protein¹⁷⁷ of influenza A virus or the gp41 subunit¹⁷⁸ of the HIV envelope protein that induce fusion of the endosomal membrane and the virus envelope. Bacteria derived toxins such as diphtheriatoxin¹⁷⁹ and shigatoxin or melittin¹⁸⁰, the active component of the bee venom, induce the formation of pores in lipid membranes and can function as endosomal escape agents as well. Based on biological models, several synthetic endosomolytic peptides have been designed, such as the cationic KALA peptide¹⁸¹ that can be coupled to gene carriers to enhance their transfection efficiency.

For endosomal escape of cationic lipoplexes, a flip-flop mechanism is proposed¹⁸². Negatively charged lipids from the endosomal membrane may laterally diffuse into lipoplexes resulting in charge neutralized ion pairs and release of the incorporated nucleic acids. Neutral helper lipids such as dioleoyl-phosphatidylethanolamine (DOPE) are known to enhance the release. It is thought that the ethanolamine headgroup of DOPE converts from lamellar to hexagonal phase at low pH resulting in destabilization of the endosomal membrane¹⁸³.

Another mechanism to facilitate endosomal escape is the so-called proton-sponge effect¹⁸⁴. Substances with a high buffering capacity, such as histidine-rich molecules and polyamidoamine-polymers, induce ion and water inflow after protonation resulting in swelling of the endosome and subsequent rupture or local destabilization¹⁸⁵ of the endosomal membrane. Next to their high buffering capacity, amine-containing polymers also show direct interactions with lipid membranes inducing substantial membrane permeability¹⁸⁶.

Additional chemical and physical strategies for endosomal escape have been developed recently. One example is the photo-induced release of molecules¹⁸⁷. A number of photosensitizers, including TPPS, AIPcS and dendrimer-based photosensitizer (DP) localize preferentially in endosomal membranes. After exposure to light they induce the formation of singlet oxygen, which destroys the endosomal membrane and causes release of the entrapped material^{71, 188}.

Plasmon-resonant gold nanoparticles can induce endosomal release by controlled hyperthermia. They absorb at near infrared frequencies and efficiently convert light energy into heat resulting in local heating and membrane destabilization¹⁸⁹.

2.PRINCIPLES OF GENE THERAPY

2.4.5. Decondensation and transport to the nucleus

Intracellular DNA release from condensed particles and access to the transcription machinery is regarded as another main rate-limiting step for gene therapy.

The balance between stability and instability has to be fine-tuned in condensed DNA complexes to protect the DNA from nucleases in extracellular fluids and intracellular compartments and allow DNA unpacking inside the cytoplasm. It has been suggested that cytosolic DNA release from polyplexes is induced by competitive interaction with negatively charged RNA molecules and cytosolic proteins¹⁹⁰. One approach to facilitate intracellular DNA release is the introduction of chemosensitive cross-linkers that stabilize particles outside the cell and are cleaved in the intracellular environment³⁶. For example disulfide bridges are formed in physiological fluids but are cleaved in the reductive environment of the cytosol. Protease-sensitive linkers which are recognized by selective cytosolic proteases can be used for triggered intracellular release as well.

The transcription machinery of cells that transcribes the genetic information on DNA into messengerRNA (mRNA) is located in the cellular nucleus, which is enclosed by two concentric membranes. Therapeutic DNA molecules have to enter the nucleus, either by transport through nuclear pore complexes (NPC) or after nuclear disassembly during mitosis.

The diameter of the aqueous channels in the nuclear pore is approximately 9 nm, only small molecules with a molecular weight below 40 kDa can pass by passive diffusion¹⁰. During active transport the pore can be dilated to a size of 26 nm. Active transport through nuclear pores is mediated by cytosolic importins that bind to nuclear localization sequences (NLS) on proteins and connect them to nucleoporins of the pore complex. Nuclear import of DNA strands can be enhanced by conjugation with NLS containing peptides or proteins¹⁹¹. Furthermore, DNA import can be improved by specific sequence elements on the DNA, such as the SV40 enhancer or NFkB binding sites. The enhancer sequence has binding sites for numerous transcription factors that promote transport into the nucleus¹⁹². Small ligands such as dexamethasone which binds to the glucocorticoid receptor for nuclear import can be attached to DNA as well¹⁹³.

Transfections are cell-cycle dependent, fast-dividing cells show high transfection efficiencies whereas differentiated and growth-arrested cells are difficult to transfect¹⁹⁴. During mitosis the nuclear envelope breaks down permitting the access of cytosolic DNA to the nucleus. This results in increased target gene expression after mitosis.

2.4.6 Transgene expression

Once inside the nucleus, the genetic information encoded on the DNA is transcribed into mRNA with the help of a complex machinery of proteins including the RNA polymerase, helicase and transcription factors¹⁰. Transcription is a highly regulated process and various activators and repressors modulate the transcription level. The newly synthesized mRNA strand is post-processed and transported through the nuclear pore complex to ribosomes, where translation of the mRNA into proteins takes place. To improve the transcription levels of therapeutic transgenes, the plasmid DNA design can be optimized. Strategies for vector design are summarized in the following section.

By adjusting the codon usage in the expressed genes to codons most commonly used human cells an increase in transgene expression can be observed¹⁹⁵.

Furthermore the CpG content of the plasmid can be reduced to achieve prolonged transgene expression¹⁹⁶. Unmethylated CpG dinucleotides in DNA are known to induce immune response resulting in cytokine induction¹⁹⁷.

Strong, ubiquitously expressed viral promoters such as the CMV promoter are often used to induce high-level transgene expression. However the usage of strong promoters results in rapid loss of expression due to epigenetic silencing of the promoter region (methylation of CpG sequences). The combination of weaker promoters with strong transcriptional activators has shown to result in enhanced, prolonged expression¹⁹⁸. In addition, tissue-selective promoters can be used to achieve transgene expression in selective cell-types.

For many clinical therapies it is of interest to regulate the expression level of a transgene in the patient to allow a tailored, individual treatment. Therefore, regulated expression cassettes have been developed that can be switched on or off in response to an externally administered controlling agent¹⁹⁹. For regulated expression, artificial transcription factors are used that are activated or deactivated by selective effector molecules. These transcription factors recognize specific DNA-binding sequences from non-mammalian genomes, which are not recognized by endogenous transcription factors. Examples for regulated expression systems are the rapamycin based regulation system, or the tet on/off system, where transgene expression is controlled by externally administered Tetracycline, an FDA approved antibiotic drug²⁰⁰.

2.PRINCIPLES OF GENE THERAPY

2.4.7 RNA interference

Gene delivery systems can not only be applied to introduce additional gene function, but also to suppress specific target genes. For this purpose, double-stranded RNA (dsRNA) molecules are used that initiate an RNA-dependent gene silencing process, called RNA interference²⁰¹.

When molecules of long dsRNA – either of endogenous or exogenous origin – reach the cytoplasm, they trigger activation of the ribonuclease enzyme dicer that cleaves the dsRNA into small fragments, called small interfering RNAs (siRNAs)²⁰². These fragments are separated into single strands and the guide strand is incorporated into the RNA-induced silencing complex (RISC). The guide strand pairs with a complementary messenger RNA resulting in cleavage of the messenger RNA by Argonaut, the catalytic subunit of the RISC complex.

Short 21bp siRNAs can be produced synthetically to induce post-transcriptional knock-down of disease causing target genes. Other dsRNAs, such as microRNA or short hairpin RNA can also be used for gene therapy approaches, however siRNA is the most commonly used molecule²⁰³. Another option is the selective inhibition of the gene silencing process by the application of antagomirs, which block the activity of endogenous microRNAs²⁰⁴.

By chemical modification the stability of siRNAs against nucleases in biological fluids can be improved. For instance, an oxygen atom in the backbone phosphate can be replaced by sulfur, or the 2' hydroxyl group of ribose can be methylated, or replaced by a 2' fluoro group²⁰⁵. Furthermore extremely stable peptide nucleic acids with a pseudopeptide backbone can be used as antisense agents for RNA interference²⁰⁶.

One major advantage of siRNA delivery compared to pDNA delivery is the improved release of siRNA from condensed particles and the bypass of nuclear import as the target of siRNAs, the RISC complex, is located the cytoplasm²⁰⁷.

2.4.8 Toxicity

For clinical application, synthetic gene carriers with low systemic toxicity are desired. Therefore cationic lipids and polymers are screened for adverse side effects *in vitro* and *in vivo*.

Some lipids such as derivatives of cholesterol are known to inhibit protein kinase C, which seems to be associated with their toxicity²⁰⁸. Furthermore the toxicity of lipids is associated to the cationic nature of their headgroup. The quaternary amine headgroup shows higher toxicity than the tertiary amine. By substituting linear amine headgroups by heterocyclic rings, the toxicity can be reduced significantly²⁰⁹. Cationic lipids with ester bonds are more biodegradable and less toxic than lipids with ether linkers; however they are liable to decompose in the blood circulation. Recently, carbamate linked lipids with low toxicity have been developed that are stable at neutral pH and are hydrolyzed under acidic conditions²¹⁰. The incorporation of neutral lipids, such as DOPE, DOPC and cholesterol into cationic liposomes can mediate to lower toxicity and improved transfection efficiencies.

One of the most potent and most studied cationic polymers for gene delivery is polyethylenimine (PEI), which exists in linear or branched morphology¹⁸⁴. In cell culture, free PEI causes several changes to cells including cell shrinking, reduced number of mitosis and vascularization of the cytoplasm²¹¹. *In vivo* experiments revealed that PEI with low molecular weight is better tolerated than high molecular weight PEI. Complexes with linear PEI showed reduced toxicity compared to branched PEI. Acid-labile PEIs with imine linkers have been developed that can be degraded in acidic endosomes into low molecular weight PEI reducing its toxicity²¹². The attachment of polyethylene glycol (PEG) to the surface of PEI-complexes can further reduce their toxicity²¹³.

Poly-L-lysine (PLL) polymers possess a biodegradable nature. However PLL complexes are more likely to be cleared from circulation and show low endosomal release²¹⁴. In the last years cationic polysaccharides such as chitosan²¹⁵ and dextran-spermine²¹⁶, which are water soluble, biodegradable and exhibit low toxicity gained more and more attention as gene delivery agents. Furthermore promising degradable acrylates and dendrimers have been developed²¹⁷⁻²¹⁹.

2.5 From *in vitro* studies towards clinical application

Before a new drug or gene carrier is approved for the market its safety and efficacy has to be confirmed in preclinical and clinical trials. Despite well-defined criteria for the identification of promising drug candidates, only 1 of every 5000 to 10000 potential formulations reaches approval by the U.S. Food and Drug administration (FDA)²²⁰.

Preclinical characterization of a medical substance involves the determination of physicochemical parameters, *in vitro* experiments and *in vivo* assays in a clinically relevant animal model. The characterization of multi-component nanocarriers is significantly more challenging than the characterization of conventional small-molecule drugs, as each component within the formulation needs to be analyzed. Additional data on the purity of the nanocarrier sample (residual bound or free drug components), the particle size distribution, particle shape, surface ligand density, and surface charge are required²²⁰. The stability of therapeutic nanoparticles has to be tested as a function of time, storage, temperature, pH, centrifugation and lyophilization. Predictive characterization assays need to be identified to ensure reproducible synthesis and batch-to-batch consistency. During preclinical assessment, interactions of the nanomaterial with blood components should be tested to identify pro-inflammatory effects or the induction of coagulation and hemolysis. *In vitro* characterization includes mechanistic information on particle uptake, subcellular localization and intracellular drug delivery. Pharmacological characterization in an animal model (accumulation in different tissues, plasma concentration, persistence, tumor distribution) should include drug-free nanoparticles and non-nanoparticle formulations of the drug.

After satisfactory information from preclinical trials, a clinical trial with volunteering human patients is initiated. Clinical trials are commonly classified into four classes. In phase I, the pharmacology and pharmacokinetics as well the maximum tolerated dose of the drug is determined in a small group of patients. Next, in phase II the effectiveness of the drug and side effects are determined. In phase III additional information about the effectiveness and the overall risk-benefit ratio is evaluated over several years in a large, demographical diverse group (hundreds to thousands of patient with target disease). After approval to the market, the safety of the drug is further monitored and additional uses of the drug are identified (phase IV). Most clinical trials are designed as randomized, double-blind studies with placebo-controls.

More than 50 companies worldwide develop nanoparticle based cancer therapeutics. In the beginning, simple constructs like PEGylated drugs, protein-drug conjugates or targeted antibody-drug conjugates were studied, next generation nanomedicines are more complex. The first approved nanotechnology-based drug was Abraxane in 2005, which consists of paclitaxel linked to albumin for enhanced solubility and increased circulation time and is applied in the treatment of breast cancer²²¹. Several PEGylated proteins have also reached market application, such as PEGylated asparaginase for the treatment of acute lymphoblastic leukemia³⁵. 11 different therapeutic antibodies used as active agents

or to deliver drugs to the tumor are approved until today including Herceptin (EGF Receptor targeting)²²², Zevalin (CD20 targeting)²²³ and Avastin (VEGF Receptor targeting)²²⁴. Liposomal nanocarriers used for the packaging of cytotoxic anticancer drugs were successfully developed and are currently applied in antineoplastic cancer therapy, examples include Doxil (liposomal doxorubicin)²²⁵ and Daunoxome (liposomal anthracycline)²²⁶. Currently, around 500 clinical trials are investigating additional liposomal anticancer formulations²²⁷. Polymeric drug carriers with biodegradable polymers have not been approved by the FDA so far but are on their way through clinical trials^{32, 228}. For example, PEGylated cyclodextrin nanoparticles that embed camptothecin into a sugar shell are in phase II for various cancer applications. Self-assembly particle built from PEGylated polyaspartate that incorporate Paclitaxel reached phase III in clinical trials (status June 2013)²²⁹.

Besides nanocarriers for drug delivery, a large number of gene therapies have entered clinical trials. Worldwide, there are over 800 open clinical trials for gene therapy based cancer treatment and more than 30 trials reached phase III¹⁶. Mostly, adenoviruses, adeno-associated-viruses and naked DNA are applied in these trials. Lipid formulations are used in more than 40 open trials on cancer therapy. Polymeric gene vectors are strongly investigated as promising tools for next-generation gene carriers; however their design has to be optimized before entering clinical trials.

The first gene therapy clinical trials were carried out in the late 1980s and at that time it was expected that gene therapy would become a treatment for serious genetic diseases in just a matter of years²³⁰. However, in the following two decades the enthusiasm for gene therapy diminished, because of the death of an 18 year old patient with ornithine transcarbamylase deficiency during a clinical trial and the development of leukemia-like conditions in two SCID-patient after gene therapy²³¹. Also, little progress has been made in experimental clinical trials during that time. More recently some technical barriers have been solved and first promising results have been reported from clinical and preclinical trials of specific diseases encouraging the expansion of gene therapy trials. Recent successes include the effective therapy of patients with chronic myelogenous leukemia (CML)⁴, SCID²³² and Parkinson's-disease²³³. Patients with Leber's congenital amaurosis, a genetic retinal disease that is a common cause for blindness in children, showed improved vision in response to treatment²³⁴. In 2012 Glybera⁸⁷, a gene delivery vector derived from adeno-associated virus encoding for the lipoprotein lipase (LPL) gene, became the first gene therapy product that gained approval in Europe and the U.S.A. In all clinical studies the therapy was well tolerated without material safety concerns and patients with lipoprotein lipase deficiency showed long-term presence of the LPL protein in the injected muscle.

The recent developments in clinical trials give hope that gene therapy may emerge as a meaningful treatment for severe diseases in the future. However, not all challenges are solved yet and the design of gene vectors requires further optimization to allow the application of multiple doses without immune response and long term benefits of the treatment.

3 Fluorescence microscopy

The technique of fluorescence microscopy has become an essential tool in biomedical and material science. Structures too small for conventional light microscopy can be visualized in fluorescence microscopy and dynamic processes can be monitored with high sensitivity at physiological conditions²³⁵. Fluorescence microscopy is widely used to study interactions of individual molecules with their environment^{236, 237}, to resolve conformational changes and short-living intermediate states of single proteins (using fluorescence resonance energy transfer, FRET)^{238, 239} or to study biological processes in living cells or organisms at the molecular level²⁴⁰⁻²⁴².

In this thesis highly-sensitive fluorescence imaging was applied to study the interaction of therapeutic gene carriers with living cancer cells in real-time on the single-cell level. By analyzing individual, labeled particles with different composition and functionalities in terms of membrane- and receptor binding, uptake kinetics, endocytosis pathways and intracellular trafficking, endosomal release properties and gene expression levels, detailed information on the underlying processes was gained. The understanding of the cellular interactions provides general information for the optimization of particle design for future applications.

In this chapter an introduction into the basic principles of fluorescence microscopy is given explaining the fundamentals of resolution, the photophysics of fluorescent dyes and labeling techniques. The two imaging techniques that were used in this work are described and special requirements for live-cell imaging are mentioned.

3.1 Resolution and contrast

In conventional light microscopy the absorption or diffraction of incoming visible light by a specimen is detected. As biological samples are mostly transparent and contain few substances that absorb or scatter the incoming light the signal-to-noise ratio of these images is low and contrast-enhancing techniques are required. In fluorescence microscopy the emission of red-shifted light from illuminated fluorophores which are attached to a molecule or particle of interest is detected and the background light from illumination is filtered, enabling imaging with optimal contrast²³⁵.

The spatial resolution in microscopy is defined as the shortest distance between two points that can be distinguished as separable. Due to the wave nature of light the resolution in optical microscopy is diffraction limited²⁴³. Light waves converge and interfere at the focal point of optical lenses and produce a diffraction pattern of concentric rings surrounding a bright central region (airy disks). When two point emitters are in too close proximity their diffraction patterns interfere and cannot be detected separately. The resolution limit of an optical setup is given by the Rayleigh criterion in which d is the minimum distance between two resolvable points, λ the wavelength of the illumination light and the N.A. the numerical aperture of the objective lens²⁴⁴.

$$d = 0.61 \lambda / N.A.$$

The numerical aperture N.A. of a lens is determined by the maximum cone of light that can enter the lens and the medium of reflection in which the lens is placed. Best oil immersion objectives reach a numerical aperture of 1.45. When using excitation light in the visible range (400-700 nm), the resolution limit of the microscope lies around 200 nm. However, when the distance between two labeled molecules or particles exceeds this limit, their position can be determined with higher accuracy using an algorithm that identifies the center of the diffraction limited spot²⁴⁵. Recognition algorithms have been developed that allow the positioning of fluorescent molecules with 2 nm accuracy and 10 ms temporal resolution²⁴⁶. By tracking the position of objects in a time-series of images, their motion can be analyzed. By single molecule or particle tracking e.g. the diffusion characteristics of receptors in the membrane or transport processes of viruses inside cells can be unraveled²⁴⁷. Recently an emerging number of super-resolution techniques have been developed²⁴⁸ that allow the reconstruction of structures below the diffraction limit by sequential activation and time-resolved localization of fluorophores (e.g. in stochastic optical reconstruction microscopy STORM²⁴⁹ or photo-activated localization microscopy PALM²⁵⁰) or by selectively deactivating excited fluorophores by stimulated emission (stimulated emission depletion microscopy STED²⁵¹).

3.2 Principles of fluorescence

The photophysics of common fluorophores can be described by the Jablonski-diagram (Fig. 3.1). When electromagnetic light with sufficient energy hits a fluorophore, the molecule can absorb this light and is excited from its electronic ground state S_0 into a transient, higher energy state S_n ($n \geq 1$). After absorption, the molecule typically populates a higher vibrational level of the excited state²⁵². The excited molecule emits the absorbed energy in successive steps. First it can reach a lower electronic state by internal conversion. In this process electronic energy is transformed into vibrational energy. This transformation is feasible because high vibrational states of lower electronic states overlap with low vibrational states of higher electronic states. The vibrational energy is then transferred to nearby molecules by collision (vibrational relaxation)²³⁵. As a result the molecule usually reaches the lowest vibrational level of the first excited state S_1 . Vibrational relaxations occur quickly at a timescale of 10^{-12} s. From the lowest electronic excited state the molecule can return to the ground state S_0 by emission of a photon (fluorescence) or by radiationless decay. After photon emission the molecule undergoes additional vibrational relaxation to reach the lowest energy level of the ground state. Fluorescence occurs on a timescale of 10^{-9} s. Because of the energy loss during vibrational relaxation, the emitted fluorescence light is typically shifted to higher wavelengths compared to the excitation light (Stokes shift). This phenomenon permits the separation of the much weaker emitted fluorescence light and the excitation light in fluorescence microscopy resulting in specific detection of the fluorescent specimen with high contrast.

Besides the process of fluorescence there is certain probability that the fluorophore in the excited state undergoes spin conversion and reaches a triplet state T, a process called intersystem crossing. Molecules in the triplet state contain an electron with parallel spins and can return to the ground state either by radiationless decay or by emission of a phosphorescence photon with longer wavelength compared to fluorescence. Phosphorescence is a much slower process than fluorescence occurring on a timescale of 10^{-6} s or longer. The overall phenomenon of photon emission through excitation of a molecule by ultraviolet or visible light photons (including both fluorescence and phosphorescence) is termed photoluminescence²⁵². Most fluorophores repeat the excitation-emission cycle hundreds to thousand times before they photobleach and can repeatedly be excited and detected. The fact that one fluorophore emits many thousands of detectable photons is fundamental to the high sensitivity of fluorescence microscopy techniques²⁴⁸.

3.FLUORESCENCE MICROSCOPY

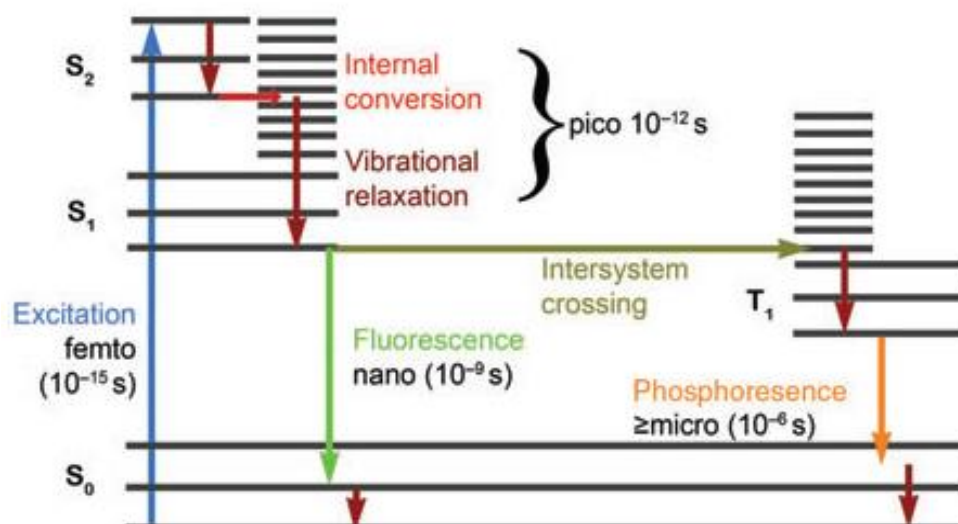


Figure 3.1 Jablonski diagram. Typical energy level scheme revealing the photophysics of common dyes. The following electronic states are depicted: S_0 = ground singlet state, S_1 = first excited singlet state, S_2 = second excited singlet state, T_1 = triplet state. Different vibrational energy levels are shown for each electronic state. Arrows indicate the energy transitions and time scales for excitation, fluorescence, phosphorescence, internal conversion, vibrational relaxation and intersystem crossing (figure taken from Lichtman et al.²³⁵).

Fluorescent molecules are characterized by their individual absorption and emission spectra that describe their likelihood to absorb and emit photons as a function of wavelength. Commercially available fluorophores offer a broad range of excitation wavelengths, Stokes shifts and spectral bandwidths to permit flexible experimental designs and multicolor imaging.

For single molecule or single particle fluorescence microscopy, fluorophores with high quantum yield and photostability are required. The fluorescence quantum yield is defined as the ratio of the number of photons emitted to the number of photons absorbed and can reach a maximum of 1.0, where every absorbed photon is emitted as fluorescence²⁵².

Photobleaching, blinking and quenching limit the fluorescence signal. Photobleaching is defined as the irreversible transformation of a dye to a non-radiative state that occurs after a limited number of excitation-emission cycles and is thought to be associated with photo-oxidation or other degradative reactions in the dye after high-intensity illumination²⁵³. Quenching is a reversible process in which the fluorophore either in its excited or ground state is transformed to a non-radiative state by noncovalent interactions with environmental molecules (e.g. paramagnetic molecules such as oxygen, heavy ions or proteins)²⁵⁴. After removal of the quenching substance the fluorescence of the dye is recovered. At high labeling density, self-quenching of the fluorescent dyes can occur. Photoblinking, the random switching of a molecule between a bright "on" and a dark "off" state, can be induced by transitions to the triplet state or other effects²⁵⁵.

3.3 Fluorescence labeling

To visualize a non-fluorescent biomolecule or nanoparticle in fluorescence microscopy, it needs to be linked to an organic dye²⁵⁶, a fluorescent protein²⁵⁷ or a nanocrystal (quantum dot)²⁵⁸.

Intrinsically fluorescent proteins enable the permanent labeling of selected molecules in living cells. They derive from the green fluorescent protein (GFP) which was originally isolated from the jellyfish *Aequorea victoria*²⁵⁹. By genetic engineering, a number of mutants with improved fluorescence quantum yield (eGFP) and shifted spectral characteristics (red fluorescent protein RFP, yellow fluorescent protein YFP, cyan fluorescent protein CFP) have been developed²⁶⁰. For labeling, the fluorescent protein encoding DNA sequence is fused to the DNA sequence of the protein of interest. Next, the fusion gene is introduced into cells that subsequently express the fluorescent fusion protein. Organic fluorescent dyes can be covalently coupled to biomolecules like proteins, peptides or nucleic acids e.g. by amine-reactive or thiol-reactive linkers²⁶¹. Labeling of the biomolecules with reactive dyes is usually performed *in vitro*, followed by purification and subsequent application of the labeled construct to the cell. A relatively new labeling technology is the copper-catalyzed azide alkyne cycloaddition in which the biological molecule of interest is first linked to an azide or alkyne and then reacts with a fluorescent dye with a complementary azide or alkyne in the presence of copper (Click-iT label technology)²⁶². As the reaction partners do not have endogenous representation in biomolecules, the Click-iT label technology can be applied to specifically label azide or alkyne-tag containing molecules inside living cells at defined time points. Because copper can harm cells, additional copper-free click chemistry has been developed²⁶³. Additional procedures exist for the noncovalent or covalent labeling of selective proteins in living cells with fluorophores. The general strategy entails genetically fusing the target protein of interest to a receptor protein²⁶⁴. A small molecule probe consisting of a receptor-binding ligand coupled to fluorophore is then added to the cell for labeling. The ligand–receptor pairs include hapten–antibody, biotin–avidin, various enzyme–inhibitor combinations, nitrilotriacetate-oligohistidine sequence, and biarsenical fluorophores that bind cysteine-rich peptide sequences.

Semiconductor quantum-dots contain some excellent characteristics for imaging applications²⁶⁵. They show a size-tunable absorption and emission, contain broad absorption and narrow emission bands and are very bright and photostable. A major drawback is their low stability in biosolutions and their potential cellular toxicity that can be reduced by polymer coating. Conjugated quantum dots are commercially available containing linkers such as biotin, streptavidin or protein A for binding to target molecules.

To stain selective subcellular structures or organelles (such as the plasma membrane, the cytoskeleton, lysosomes, mitochondria or the nucleus) a variety of selective fluorescent dyes and fluorophore-conjugates are commercially available²⁶¹. For example, the fusion of a fluorescent protein or dye with Rab5, a small GTPase that localizes to early endosomes²⁶⁶, results in staining of these endosomal compartments. To follow specific uptake pathways, conjugates like fluorescent dye-labeled

3.FLUORESCENCE MICROSCOPY

transferrin are typically utilized that internalize via a selective endocytosis mechanism. Ph-sensitive or ion-sensitive dyes serve as sensors to monitor the conditions in different cellular compartments²⁶⁷.

3.3 Special considerations for live-cell imaging

When imaging live cells with fluorescence microscopy some challenges need to be taken into account²⁶⁸. During excitation with visible light, cells exhibit a significant intrinsic fluorescence (autofluorescence) that enhances the background signal and complicates the imaging of target molecules with low fluorescence intensity²⁶⁹. Cellular autofluorescence often arises from the excitation of NAD(P)H, flavins, proteins of the extracellular matrix medium components or fixation additives²⁷⁰. Autofluorescence varies between different cell lines and is affected by cell density and environmental conditions. Furthermore imaging with high energy excitation can induce photodamage in cells leading to changes in morphology, excessive vacuole formation and cell cycle arrest²⁷¹. To reduce photodamage and autofluorescence, cell imaging should be performed with low laser power and red-shifted fluorophores with high quantum yield and photostability whenever possible²⁷². Careful control experiments are required to optimize cell growth, experimental conditions (e.g. reduction of oxygen and phenol red in the sample), the imaging protocol (selection of excitation mode, excitation time, intensity of illumination, acquisition speed, binning) and the microscope setup (selection of laser lines, objective, excitation and emission filters, beam splitters and detectors) for each individual set of experiments. To ensure the cells' health on the microscope stage, imaging has to be done at physiological conditions, at convenient temperature, pH, CO₂ level and supply of nutrients. To reduce drift of the cells in time-lapse experiments, the cell slide can be fixed on the stage, air circulation by air conditioning units may be reduced and autofocus routines may be applied²⁷³. Transmission light images can be recorded in addition to fluorescence images to provide additional information on the cell shape, morphology and position. Fluorescence imaging in living organisms should be performed with excitation wavelength in the deep red of near infrared range because of the improved tissue penetration and reduced autofluorescence at higher wavelengths. Two-photon microscopy is a new technology that allows penetration of thicker specimens and imaging with high resolution *in vivo*²⁷⁴.

3.4 Wide-field and confocal scanning microscopy

In this work two different microscopy techniques were applied, widefield-fluorescence microscopy and spinning disk confocal microscopy, which will be introduced briefly in the following.

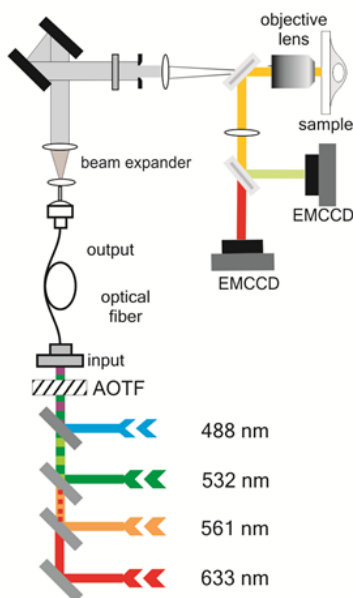
In a widefield microscope with epi-illumination the microscope objective serves as a condenser to vertically illuminate a distinct area of the specimen and to collect the fluorescence light emitted by excited molecules in this area²³⁵. In this mode only the small percentage of exciting light that is reflected from the sample needs to be separated from the emission by dichroic mirrors and optical filters. The ideal objective has a high numerical aperture, few lens elements to reduce losses of fluorescence light and a low intrinsic fluorescence of the lens elements. Light sources for illumination can be laser beams that provide high excitation intensities at single wavelength or mercury and xenon arc lamps. The filtered fluorescence light is focused onto an array detector, which is usually a charge coupled device (CCD) chip. In this thesis a custom-build widefield-microscope was set up with four different laser lines, an acousto-optic tunable filter (AOTF) for precise adjusting of excitation intensities and the switching of laser lines, and two highly-sensitive EMCCD cameras allowing fast multi-color imaging and alternating laser excitation experiments. A schematic figure of the setup is depicted in figure 3.2. Major advantages of epi-fluorescence widefield microscopy are the simultaneous imaging of several individual molecules in a large micro-sized area with high sensitivity and the high imaging velocity. Single molecule detection and frame rates of 30 frames per second are realized by modern EMCCD technology. Limitations of this technique are the missing information in the third z-dimension of the cell and the collection of fluorescence from excited molecules outside the focal plane (out-of-focus light) that contribute to background fluorescence.

To achieve 3-dimensional information of a specimen and reduce out-of focus light, confocal scanning microscopy can be applied. In confocal microscopy a collimated laser beam is focused by the objective to the smallest possible, diffraction limited spot on the sample plane²⁷⁵. The fluorescence emitted from the small excited confocal volume is collected and recollimated by the same objective and separated from residual laser light by optical elements. By placing a pinhole aperture in front of the detector, light from out-of focus sources is eliminated and the depth of the confocal spot is adjusted. The sample is scanned point by point in xy direction to acquire two-dimensional images of thin slices of the specimen. By computationally combining the image data from a number of different two-dimensional slices 3D information is gained. The main limitation of confocal microscopy techniques is the slow velocity of the image acquisition. Spinning disk confocal microscopy is a modern technique that enables confocal imaging with increased velocity²⁷⁶. A spinning disk microscope contains a fast-rotation disk with multiple concentrically arranged lenses and pinholes allowing the simultaneous imaging of different spots resulting in faster image acquisition. The spinning disk microscope applied in this work is commercially available from Andor technology (Fig. 3.2) and was based on a Nikon TE2000E microscope corpus with a Plan Apo 100x oil immersion objective and the Yokogawa CSU10 spinning disk unit. For excitation four different laser lines could be chosen and combined individually by an acousto-optic tunable filter (AOTF). The sample position could be

3.FLUORESCENCE MICROSCOPY

controlled by a motorized stage in xy-position and by piezo-stage in z-position. Emission light was split into two channels by an appropriate dichroic mirror and detected with an EMCCD camera after passage through emission filters.

A Widefield microscope



B Spinning disk confocal microscope

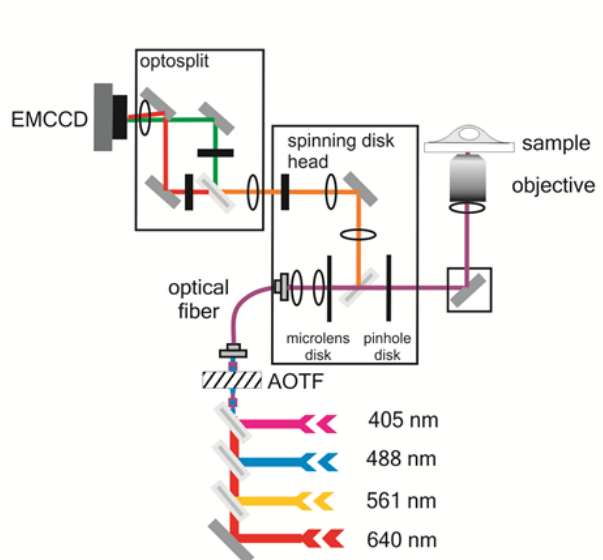


Figure 3.2 Widefield microscope and spinning disk confocal setup. **A** For widefield imaging, four different laser lines (488 nm, 532 nm, 561 nm, 633 nm) were coupled into an acousto-optical tunable filter and passed a multimode fiber. By optical lenses the laser beam was expanded and focused to the backfocal plane of an objective to permit vertical widefield-illumination of the biological sample. Emission light was separated from excitation light by dichroic mirrors and split into two emission channels. After passage through adequate filters the signal was detected on two EMCCD cameras. **B** For spinning disk confocal imaging the laser light (four lines: 405 nm, 488 nm, 561 nm, 640 nm) passed through an AOTF and an optical fiber. The expanded and collimated laser beams illuminate an upper disk containing about 20,000 microlenses (microlens disk). Each microlens focuses the laser beam onto its corresponding pinhole on the pinhole disk (Nipkow disk). About 1,000 laser beams fill the aperture of the objective lens, and are then focused on the focal plane. Fluorescence generated from the specimen is captured by the objective lens and focused back onto the pinhole disk, transmitted through the same holes to eliminate out-of-focus signals and deflected by a dichroic mirror located between microlens array disk and the Nipkow disk to split fluorescence signal from reflected laser. Fluorescence light was then split into two channels, filtered by adequate emission filters and detected by an EMCCD camera. Adapted from figures kindly provided by Dr. Sergey Ivanchenko and Dr. Yoshihiko Katayama.

4 Surface shielding of gene vectors

The attachment of hydrophilic, neutral polymers to therapeutic nanocarriers is commonly applied to increase their stability in serum, avoid opsonization by macrophages and reduce electrostatic interactions of nanocarriers with non-target components³⁵. The best studied polymer for shielding is polyethylene glycol (PEG) that is approved by the FDA for several clinical applications. PEGylation of nanocarriers has proven to reduce nanocarrier toxicity *in vivo* and to enhance the circulation time of nanocarriers in the blood stream²⁷⁷. The shielding properties of a particle can be adjusted by variation of the PEG length and the PEG density on the surface²⁷⁸. To achieve specific uptake of PEGylated nanocarriers into target cells, they can be equipped with selective molecular ligands that recognize upregulated target receptors on diseased cells²⁷⁹. However, besides favorable surface shielding properties, negative influences of PEGylation on the efficiency of gene and drug delivery have to be considered. The flexible PEG polymer may sterically hinder targeting ligands and block their receptor binding. Furthermore, the uptake kinetics of passively tumor-targeted nanocarriers can be reduced by PEGylation and the endosomal release and decondensation of gene carriers is complicated with increasing PEG shielding (PEG dilemma)²⁸⁰. To find the right balance between efficient and safe gene delivery, the PEG shielding of a particle needs to be fine-tuned and the underlying cellular processes have to be elucidated.

In a first part of this chapter we evaluate how PEG shielding can be tuned to optimize the receptor targeting of RGD-ligand equipped polyplex micelles (4.1). Therefore the effect of the RGD ligand on particle uptake and intracellular trafficking was monitored by highly-sensitive fluorescence microscopy for two particle compositions with different PEG length. Their uptake pathway was determined by colocalization assays and inhibitor experiments and their transfection efficiency was studied by reporter gene expression. Furthermore we were interested in the question if the applied particle dose affects the uptake mechanism of integrin-targeted nanoparticles and therefore compared particle internalization at two different particle concentrations. The project was performed in collaboration with the research group of Prof. Kazunori Kataoka from the University of Tokyo. Particle synthesis, flow cytometry and reporter gene expression experiments were performed by Yelena Vachutinski and Dr. Makoto Oba in Tokyo. Parts of this chapter are taken from our publication in the *Journal of Controlled Release*⁶. In a second part of this chapter we describe how the undesired side effects of PEG shielding can be circumvented by applying bioresponsive PEG linkers that are cleaved in the intracellular environment (4.2). This project was initiated by the group of Prof. Zhiyuan Zhong from Soochow University in China and described results are adapted from our publication in *Biomacromolecules*⁷.

4.1 Interplay between PEG shielding and receptor targeting – live-cell imaging of integrin-targeted polyplex micelles

This chapter is adapted from:

F.M. Mickler, Y. Vachutinsky, M. Oba, K. Miyata, N. Nishiyama, K.Kataoka, C.Bräuchle and N.Ruthardt; "Effect of integrin targeting and PEG shielding on polyplex micelle internalization studied by live-cell imaging.", *J Control Release*, (2011), 156(3),364-73.

4.1.1. Particle design

To study the interplay between PEG shielding and receptor targeting we used polyplex micelles that are composed of cationic block copolymers (ligand-PEG-poly(lysine-SH)) and plasmid DNA (Fig. 4.1)²⁸¹. These particles have the potential for clinical application as they possess a suitable size of approximately 100 nm for systemic delivery^{29, 282}. By incorporation of disulfide-crosslinks into the micellar core, their stability in extracellular fluids is enhanced²⁸³. These redox-sensitive cross-links are disrupted in the reducing environment of the cytosol, triggering the controlled liberation of plasmid DNA after endosomal release. Targeted micelles were equipped with a cyclic RGD peptide (RGD(+ micelles) that binds to $\alpha_v\beta_5$ and $\alpha_v\beta_3$ integrins on tumor cells, control micelles were left without targeting ligand (RGD(- micelles)²⁸¹. $\alpha_v\beta_5$ and $\alpha_v\beta_3$ integrins are highly investigated target structures for cancer therapy because they are overexpressed in solid tumors as well as the angiogenic tumor vasculature, which facilitates the accumulation and extravasation of the therapeutic gene vectors at the tumor site^{284, 285}. For visualization in fluorescence microscopy, the plasmid DNA was labeled with fluorescent dyes. To evaluate the influence of surface shielding on the selectivity of integrin targeting, two micelle types with differently sized PEG shell layers were compared: PEG12 micelles were equipped with a 12 kDa PEG, whereas PEG17 micelles contained an elongated 17 kDa PEG resulting in enhanced shielding of the positively charged micelles core²⁸⁶.

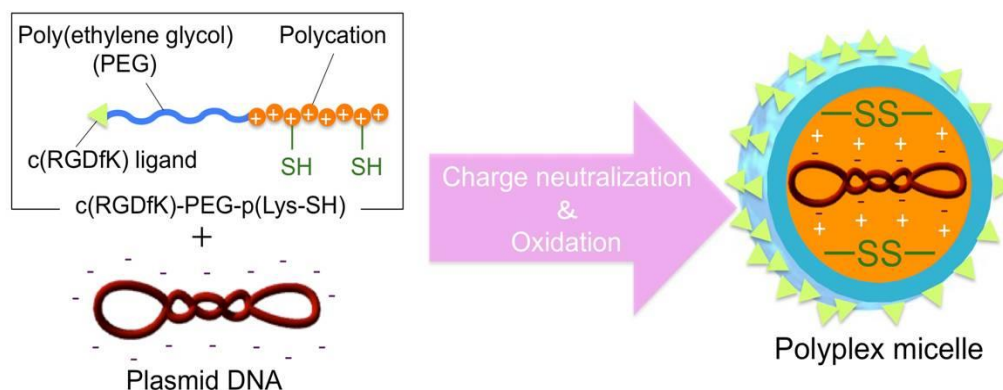


Figure 4.1 Schematic illustration of micelle formation between plasmid DNA and c(RGDfK)-PEG-p(Lys-SH)-polymer. Micelles are formed through polyion complex formation between positively charged polylysine segments and negatively charged DNA. The charged micellar core is shielded by a PEG shell layer (12 kDa PEG for PEG12 micelles, 17 kDa PEG for PEG17 micelles) to which a cyclic RGD-peptide is attached as a targeting ligand. Covalent cross-linking of polylysine segments by disulfide bonds causes high stability of micelles. For the formation of integrin targeted RGD(+) micelles 100 % ligand-quipped c(RGDfK)-PEG-p(Lys-SH)-polymer was applied, RGD(- micelles contained PEG-p(Lys-SH)-polymer without ligand. Light scattering revealed a cumulant diameter of 112 nm for PEG12 micelles and 104 nm for PEG17 micelles (see 9.1.2).

4.1.2. Coincubation of RGD(+) and RGD(-) micelles at low concentration

In order to directly compare the internalization of integrin-targeted (RGD(+)) and untargeted (RGD(-)) micelles, we simultaneously applied both micelle types with different fluorescent labels onto HeLa cells and analyzed their cellular localization over time. Due to cross-linking of the polymer chains by disulfide bonds, micelles are highly stable and mixing of RGD-positive and RGD-negative polymer between different micelles should rarely occur²⁸². To evaluate the importance of surface shielding for effective receptor targeting, experiments were performed in parallel with PEG12 micelles and PEG17 micelles. For the measurement, HeLa cells were incubated with a low dose of premixed micelles (2.5 ng of DNA per 10.000 cells) allowing the detection and subsequent quantification of single micelles on the cell surface by highly sensitive wide-field microscopy. Short movies of single cells were recorded 0, 2, 4 and 6 hours after micelle addition.

As reference, a mixture of Cy3 and Cy5 labeled RGD(-) PEG12 micelles (identical micelles differing only in their fluorescence label) was added to the cells (Fig 4.2 A). As shown in the fluorescence overlay images in figure 4.2, separate, non-aggregated micelles were uniformly distributed all over the cell during the first minutes post micelle addition. After two hours, we observed a shift of micelle distribution from the cell periphery towards the center of the cell. The total number of detected fluorescent spots was reduced while their intensity was increased, indicating the enrichment of multiple micelles in endosomal compartments. In addition, colocalizing spots represented by the white label in the overlay images appeared. Within two to six hours of incubation, the fraction of colocalizing spots and the accumulation in the nuclear proximity further increased.

Unexpectedly, the same pattern was observed when targeted RGD(+) and untargeted RGD(-) micelles with PEG12 shielding were coincubated (Fig. 4.2 B). We observed accumulation of both micelle types in the cell center and increasing colocalization over time, indicating transport of targeted and untargeted micelles to the same endocytic compartments. In contrast, after coincubation of RGD(+) and RGD(-) micelles with PEG17 shielding, we detected a separation in localization of targeted and untargeted micelles during the measurement (Fig. 4.2 C). After six hours, in the majority of the cells, PEG17 RGD(-) micelles were retained in peripheral section of the cell, whereas PEG17 RGD(+) micelles accumulated in the nuclear proximity.

4. SURFACE SHIELDING OF GENE VECTORS

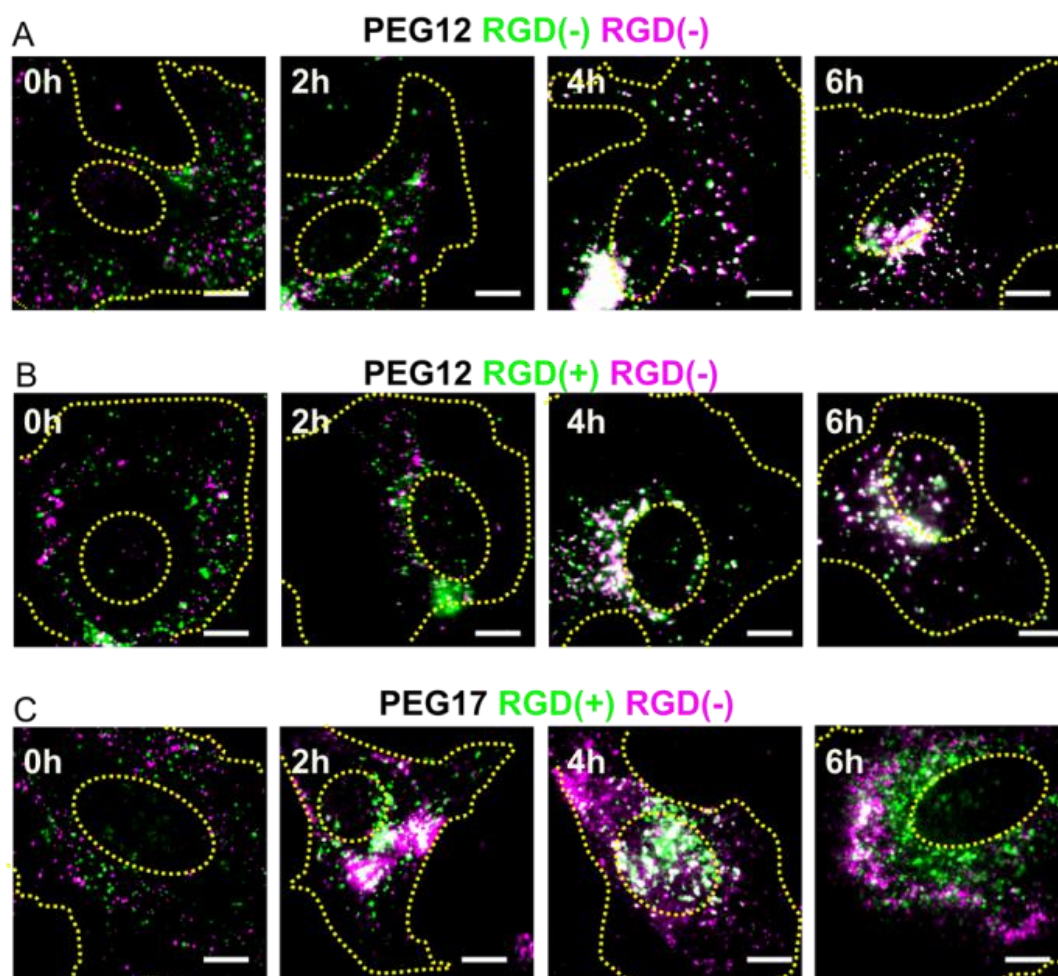


Figure 4.2 Cellular localization of coincubated RGD(+) and RGD(-) micelles with different PEG shielding. Cy3 and Cy5 labeled micelles were simultaneously applied at low concentration (2.5 ng DNA per 10.000 cells) onto HeLa cells and imaged by wide-field-microscopy after 0, 2, 4 and 6 hours with alternating laser excitation. Fluorescence overlay images were obtained by superposition of the Cy3 and the Cy5 channel. Colocalizing endosomes appear in white. The regions of the cell nucleus as well as the cell membrane are both marked with a dashed, yellow line. **(A)** Cy3 and Cy5 labeled PEG12 micelles without a targeting ligand (= reference cells) were transported into the same endocytic compartments, resulting in increasing colocalization over time. **(B)** RGD(+) (green) and RGD(-) (magenta) PEG12 micelles show a similar time-dependent localization compared to the reference. **(C)** Coincubation of PEG17 shielded RGD(+) (green) and RGD(-) (magenta) micelles resulted in a separated cellular distribution. RGD(+) micelles were transported to the nuclear proximity, whereas RGD(-) micelles were predominantly retained in the cell periphery. Scale bar: 10 μ m.

4.1.3 Colocalization analysis of coincubated micelles at low concentration

To validate our data, we quantified the degree of colocalization for the various micelle combinations using custom-designed software. As displayed in figure 4.3, calculated colocalization values were plotted over time and were best approximated by linear regression. The reference measurement revealed a constant increase of the colocalization degree over time with an R-Squared value of 0.85 for the linear fit. In the first 30 minutes after addition, between 5 % and 20 % colocalizing micelles were detected. After four hours the colocalization value increased to 50 % and reached 90 % after six hours of incubation. Coincubated RGD(+) and RGD(-) micelles with PEG12 shielding showed a similar time-dependent progression of the colocalization degree as the reference measurement (R-Squared

value of 0.94 for the linear fit). The uptake and intracellular trafficking of PEG12 micelles seemed not affected by the targeting ligand. A different colocalization behavior was determined for simultaneously applied RGD(+) and RGD(-) micelles with PEG17 shielding. Compared to the reference, significantly lower colocalization values were reached after four to six hours of incubation. Furthermore, we observed a broad spread of the data points and a low R-Squared value of 0.2 for the linear regression of the plotted data. The obtained colocalization values support the described cellular distribution of micelles in the overlay images, demonstrating that only with the longer 17 kDa PEG an effect of the RGD ligand on the subcellular distribution of micelles can be observed.

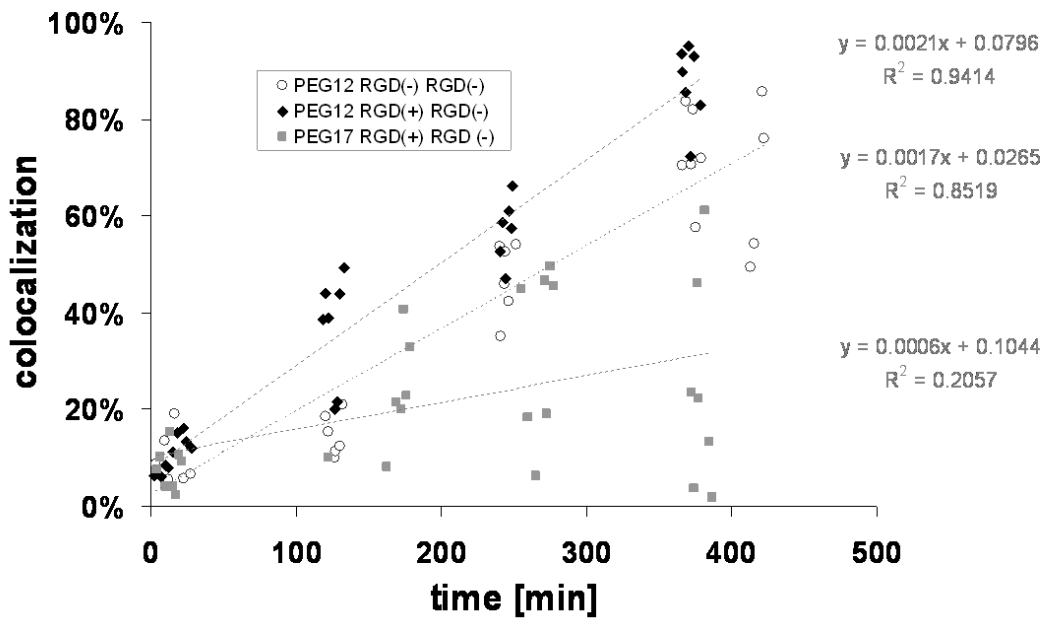


Figure 4.3 Quantification of the time-dependent colocalization degree of coincubated micelles. HeLa cells were coincubated with different combinations of fluorescently labeled micelles and imaged by wide-field fluorescence microscopy at the indicated time points. Obtained movies were analyzed for colocalizing endosomes using custom-written software. Each data point represents the calculated colocalization degree in one camera section corresponding to one or two HeLa cells. Plotted data points were approximated by linear regression (grey, dashed line). White circle: reference cells coincubated with Cy3 and Cy5 labeled PEG12 micelles without a targeting ligand for determination of normal distribution of colocalization, black diamond: cells coincubated with targeted (RGD(+)) and untargeted (RGD(-)) PEG12 micelles, grey square: cells coincubated with RGD(+) and RGD(-) PEG17 micelles.

4.1.4 Coincubation of micelles at high dose

Next, we were interested in the question whether the applied particle dose influences the internalization behavior. To answer this question, the previously described colocalization experiment was repeated with a 53 fold increase in micelle concentration (132 ng DNA per 10000 cells). Treated HeLa cells were imaged four to six hours post application by wide-field fluorescence microscopy. Again, as a reference, untargeted PEG12 micelles labeled either with Cy3 or Cy5, were simultaneously applied in a 1:1 mixture. In figure 4.4, images of representative cells are presented showing the two individual emission channels as well as the overlay images of both fluorescence channels. The images illustrate that a subset of the applied reference micelles accumulated in nuclear

4. SURFACE SHIELDING OF GENE VECTORS

proximity, whereas another subset remained in the cell periphery (Fig. 4.4 A). The peripheral rim of PEG12 RGD(-) micelles was not observed in the experiments at low micelle concentration. A trypan blue quenching assay with Cy3 labeled, untargeted PEG12 micelles revealed that the peripheral fraction mainly consisted of extracellularly attached micelles, whereas the micelles in the nuclear proximity were in intracellular compartments (Fig. 4.5). This suggests that the internalization of untargeted micelles is saturated at high concentration resulting in the retention of a certain fraction of micelles on the plasma membrane. In the microscopic images, we observed varying amounts of peripheral micelles between different cells, indicating that the cell population is heterogeneous in their level of internalization. Interestingly, after cocubation of PEG12 RGD(+) and RGD(-) micelles a separated localization of targeted and untargeted micelles was observed, which did not appear at low micelle concentration (Fig. 4.4 B). Whereas RGD(-) micelles showed a distribution comparable to the reference micelles, the RGD(+) micelles were predominantly found in the nuclear proximity. As a consequence, in the overlay images a higher degree of green label encoding for RGD(+) micelles appears in the central section of the cell, whereas the magenta label, representing the RGD(-) micelles, is dominating in the periphery. This separated distribution of targeted and untargeted micelles was even more pronounced for cocubated PEG17 RGD(+) and RGD(-) micelles. Here, a strong accumulation of RGD(+) micelles was observed in the nuclear proximity, whereas untargeted micelles were almost completely retained in the cellular periphery (Fig. 4.4 C).

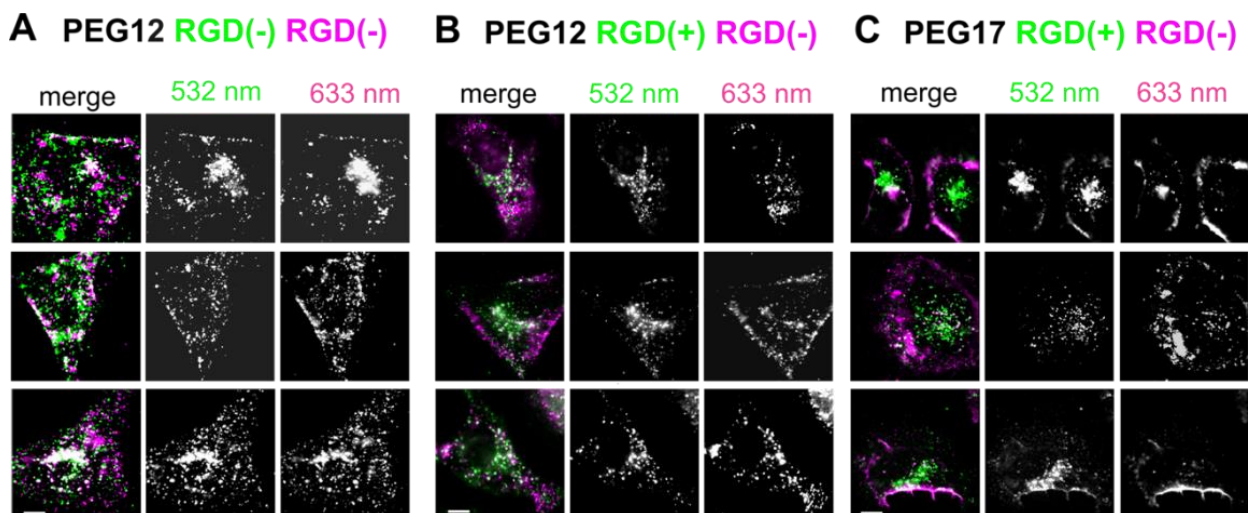


Figure 4.4 Effect of dosage on micelle internalization. HeLa cells were cocubated with a high concentration (132 ng DNA/ 10.000 cells) of micelles and imaged after four to six hours by wide-field fluorescence microscopy. (A) Overlay images of reference cells cocubated with Cy3 and Cy5 labeled RGD(-) micelles reveal high degree of colocalizing endosomes. (B) Cocubated PEG12 RGD(+) (green) and RGD(-) (magenta) micelles show a different distribution compared to the reference. RGD(+) micelles accumulate in the inner part of the cell, whereas RGD(-) micelles remain in the outer cell region. (C) A more pronounced separated distribution is observed for cocubated PEG17 RGD(+) (green) and RGD(-) (magenta) micelles. Scale bar: 10 μ m.

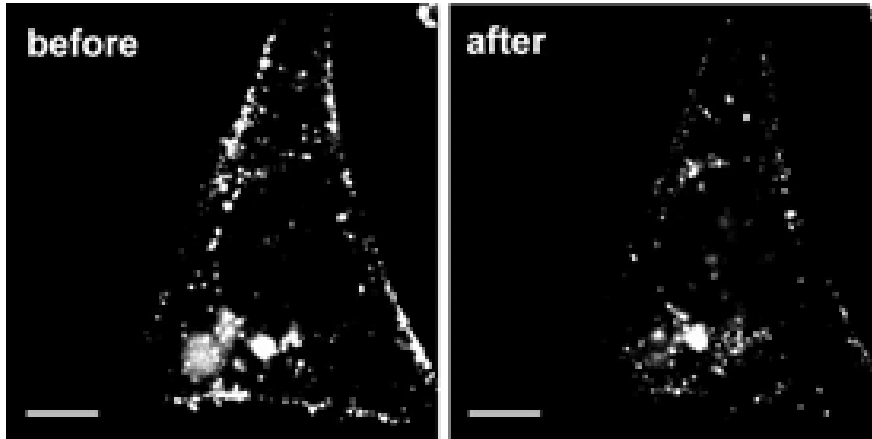


Figure 4.5 Discrimination of extra- and intracellular micelles by trypan blue quenching. HeLa cells were incubated for six hours with Cy3 labeled RGD(-) PEG12 micelles at high concentration followed by treatment with trypan blue under microscopical observation. A representative cell is shown before and after treatment. After addition of the quencher the peripheral rim of micelles vanished, indicating the extracellular localization of the peripheral micelles. Scale bar: 10 μ m.

4.1.5 Colocalization analysis at high dose

To determine the colocalization degree of the micelle combinations at high concentration, the mean colocalization value from cells, incubated for four to six hours, was calculated and normalized to the reference measurement with untargeted micelles (Fig. 4.6). Interestingly, for coincubated PEG12 RGD(+) and RGD(-) micelles the colocalization degree was comparable to the reference, although a partly separated cellular localization of the micelles was observed in the respective microscopical images. This high colocalization value indicates that a considerable amount of PEG12 RGD(-) micelles was still internalized and transported to the same cellular compartments as RGD(+) micelles. In contrast, for coincubated PEG17 RGD(+) and RGD(-) micelles, the colocalization was significantly reduced to 34 % of the reference value suggesting that in the presence of enhanced shielding solely integrin targeted micelles are efficiently transported to the nuclear proximity.

Our data revealed that both the applied particle dose as well as the PEG length has a significant effect on the distribution of targeted and untargeted micelles

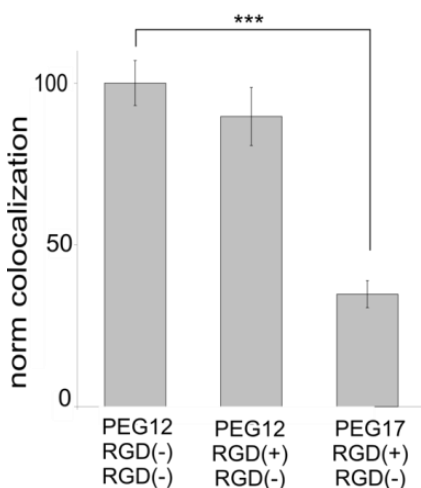


Figure 4.6 Quantification of micelle colocalization at high concentration. HeLa cells were coincubated with the indicated combinations of fluorescently labeled micelles and imaged by wide-field fluorescence microscopy after four to six hours. Obtained movies were analyzed for colocalizing endosomes using custom-written software. Mean colocalization values of the imaged cells were determined for the micelle combinations and normalized to reference cells that were coincubated with Cy3 and Cy5 labeled PEG12 micelles without a targeting ligand. The standard error of the mean (SEM) is represented by error bars (N=24 for PEG12 RGD(-)RGD(-), N=26 for PEG12 RGD(+)RGD(-), N=32 for PEG17 RGD(+)RGD(-)).*** P<0.0001 for PEG17 RGD(+)RGD(-) compared to the reference).

4. SURFACE SHIELDING OF GENE VECTORS

4.1.6 Quantification of micelle uptake by flow cytometry

Live-cell imaging is a powerful tool to study the detailed mechanisms of particle internalization and to visualize the cellular localizations in single cells. In the present study, the transfection experiments were performed with PEGylated polyplexes at extraordinarily low DNA concentrations, compared to conventional transfection conditions e.g. 2.5 ng / 10.000 cells. Such low micelle concentrations cannot be detected in standard bulk experiments. However, as considerable heterogeneity between cells exists, the quantification of nanoparticle internalization is challenging with microscopical methods and should be verified by standard bulk experiments such as flow cytometric analysis under conventional transfection conditions. Therefore, we performed a cellular uptake study of PEG17 RGD(+) and RGD(-) micelles by a flow cytometric analysis at 1 μ g DNA per 10.000 HeLa cells after 24 hours of incubation (Fig. 4.7). The obtained result clearly revealed that the uptake of PEG17 RGD(+) micelles into HeLa cells was significantly increased compared to the RGD(-) ones. In contrast, for PEG12 shielded micelles, the uptake was not significantly increased by introduction of the RGD ligand as revealed by a previous flow cytometry study under the same transfection conditions (1 μ g DNA per 10.000 cells and 24 hour of incubation)²⁸³.

These results demonstrate the superior effect of the targeting ligand on the uptake of micelles when combined with the longer 17 kDa PEG, consistent with our results from the microscopic observation.

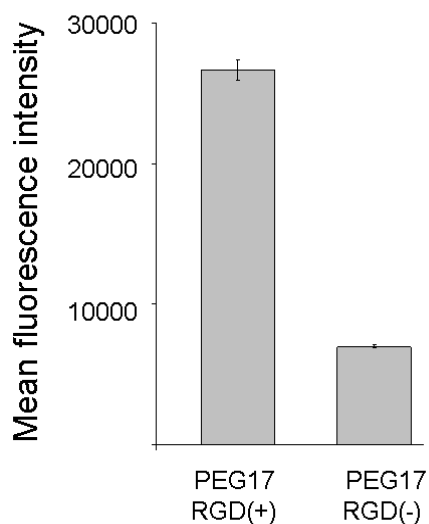


Figure 4.7 Uptake efficiencies of PEG17 RGD(+) and RGD(-) micelles, obtained by flow cytometric analysis. Each micelle sample containing 1 μ g of Cy5-labeled plasmid DNA was incubated with HeLa cells (10,000 cells) for 24 hours. The standard error of the mean (SEM) is represented by error bars (N=3).

4.1.7 Identification of the uptake pathway

To specify the uptake pathway used by integrin-targeted and untargeted micelles, we performed spinning disk confocal microscopy colocalization studies with pathway specific markers. RGD(+) micelles with PEG17 shielding were used to determine the pathway of targeted micelles. PEG12 RGD(-) micelles served as reference system for the internalization pathway of receptor-independent uptake. In a previous study it was suggested that integrin targeting with the cyclic RGD ligand leads to

4.SURFACE SHIELDING OF GENE VECTORS

caveolin-dependent internalization of micelles²⁸³. This conclusion was based on colocalization experiments with labeled cholera toxin B, a specific marker for caveolin-dependent endocytosis in several cell types. Singh et al reported that the uptake mechanism of cholera toxin B is highly cell type dependent and seems to occur predominantly via clathrin mediated endocytosis in HeLa cells²⁸⁷. Therefore we decided to use HeLa cells expressing caveolin-GFP as a more specific marker for caveosomes compared to cholera toxin B. As a marker for clathrin mediated endocytosis, transferrin 488 was applied to HeLa cells. According to the literature, transferrin is efficiently incorporated into clathrin coated vesicles, followed by transport to early, sorting, and recycling endosomes¹²⁹. After one hour coincubation of untargeted micelles and transferrin on cells, most micelles were located in the cell periphery whereas transferrin was localized in the central part of the cell and little colocalization was detected. This observation indicates that no direct interaction of micelles and marker occurred in the cell medium (data not shown). Coincubation of both targeted as well as untargeted micelles with transferrin 488 for four hours resulted in a high colocalization degree as demonstrated in figure 4.8 A by the distinct white signal in the fluorescence overlay image. Concerted movements of spots in both emission channels were observed, proving that transferrin and micelles were in fact entrapped in the same endosomal compartments. This result suggests that the uptake of integrin-targeted as well as untargeted micelles occurs via clathrin mediated endocytosis resulting in transportation to early, sorting or recycling endosomes during the first four hours of incubation. In contrast, after application of micelles to caveolin-GFP expressing cells, only a low number of colocalizing caveosomes were detected for the targeted as well as untargeted micelles, indicating that caveolin-dependent endocytosis is not the dominant internalization pathway for both micelle types (Fig. 4.8 B).

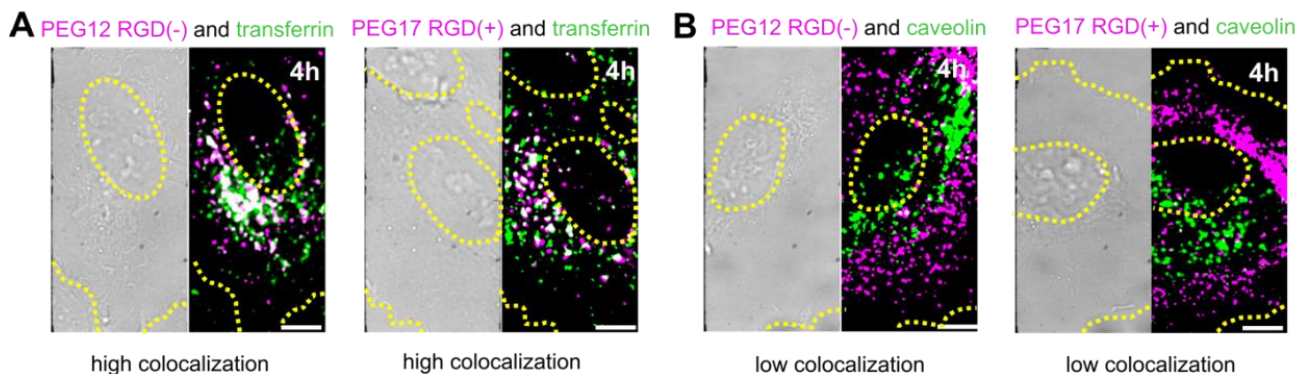


Figure 4.8 Colocalization analysis of micelles and endocytosis pathway specific markers. Single z-slices of representative cells, imaged by spinning disk confocal microscopy, are shown. The regions of the cell nucleus and the plasma membrane are marked in the transmission light and fluorescence image (left side) with a yellow, dashed line. **(A)** Coincubation of Cy5 labeled PEG12 RGD(-) or PEG17 RGD(+) micelles (magenta) with transferrin 488 (green) on HeLa cells for four hours. Both targeted as well as untargeted micelles show high colocalization with transferrin as indicated by white endosomes in the overlay image. **(B)** Incubation of Cy5 labeled PEG12 RGD(-) or PEG17 RGD(+) micelles (magenta) on caveolin-GFP expressing (green) HeLa cells for four hour results in a low colocalization degree. Scale bar: 10µm.

4. SURFACE SHIELDING OF GENE VECTORS

To verify the predominant uptake of targeted and untargeted micelles via clathrin-mediated endocytosis additional inhibitor experiments with chlorpromazine, a specific inhibitor of clathrin-mediated endocytosis, were performed. Inhibitor studies on the single cell level require careful controls²⁸⁸. Therefore we first proved the integrity of the cell membrane in the presence of 10 $\mu\text{g}/\text{ml}$ chlorpromazine by applying a trypan blue exclusion assay (Fig. 4.9). Additionally, we tested the successful uptake of lactosylceramide, a marker for caveolin-dependent endocytosis, into chlorpromazine treated cells to exclude inhibition effects caused by cell damage and unspecific inhibition effects. Significant amounts of lactosylceramide were internalized into HeLa cells at the applied chlorpromazine concentration. This indicates that the caveolin-dependent uptake pathway was not inhibited under the applied conditions (Fig. 4.10). Only cells that exhibited moderate changes in their cell shape in the bright field image were considered for evaluation. As a positive control for effective clathrin inhibition, we simultaneously applied fluorescently labeled transferrin with the micelles. Three to four hours post application, transferrin was absent in the cytoplasm of chlorpromazine treated cells, whereas untreated cell showed efficient uptake of transferrin. This verifies the effective inhibition of clathrin-mediated uptake by chlorpromazine addition. Incubation of the chlorpromazine treated cells with either PEG17 RGD (+) or PEG12 RGD(-) micelles resulted in a distinct accumulation of both micelle types on the cell membrane. Confocal z-slices of the treated cells revealed a narrow rim of micelles in the membrane region. Neither targeted nor untargeted micelles were detected in the central section of the cell. This result gives further evidence that in HeLa cells clathrin-mediated endocytosis is the predominant uptake pathway for integrin targeted as well as untargeted micelles (Fig. 4.11).

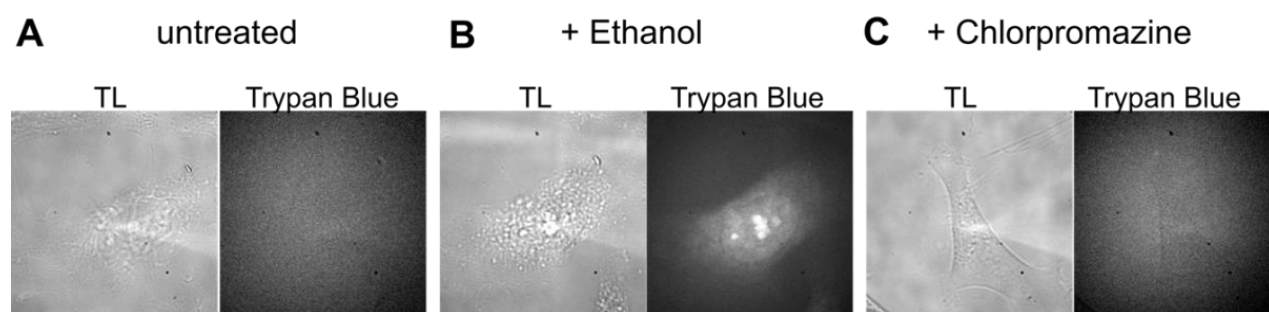


Figure 4.9 Trypan Blue exclusion assay to confirm cell viability. HeLa cells were incubated with trypan blue as a dead cell stain and imaged at 633 nm excitation with wide-field fluorescence microscopy. Transmission light (TL, left) as well as fluorescence images (right) of representative cells are shown. (A) Trypan blue staining was absent in untreated control cells proving high cell viability before inhibitor addition. (B) Control cells treated with ethanol (25% vol in cell medium) were efficiently stained revealing the cytotoxic effect of ethanol. (C) HeLa cells preincubated in 10 $\mu\text{g}/\text{ml}$ chlorpromazine for 4 hours are not stained by trypan blue proving sufficient cell viability in the presence of chlorpromazine.

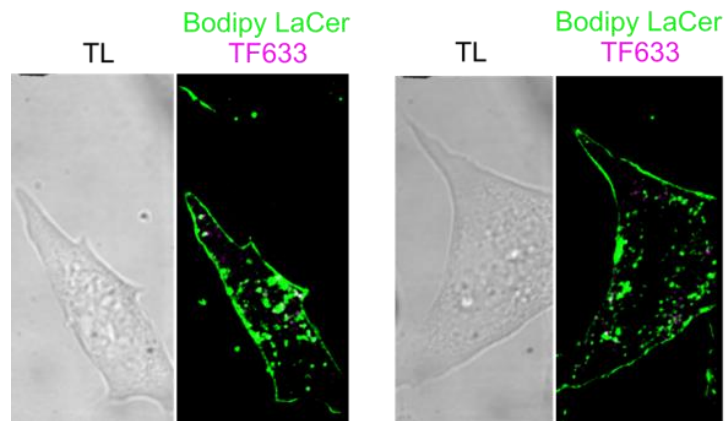


Figure 4.10 Functional caveolin-dependent endocytosis in the presence of chlorpromazine. HeLa cells were preincubated with 10 $\mu\text{g/ml}$ chlorpromazine for 30 minutes before simultaneous addition of BodipyFL Lactosylceramide (LaCer, green) and transferrin 633 (magenta). 2.5 hours after addition of the fluorescently labeled markers, cells were imaged by spinning disk confocal microscopy with alternating laser excitation. Fluorescence and transmission light images of two representative cells are shown revealing efficient uptake of LaCer and retention of transferrin in the presence of chlorpromazine. Thus caveolin-dependent endocytosis is functional in the presence of clathrin inhibition.

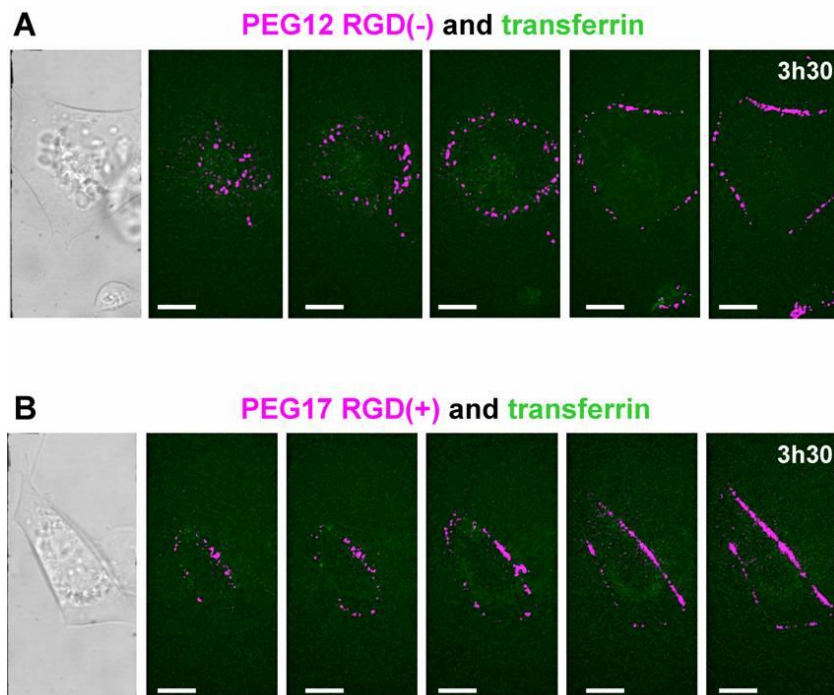


Figure 4.11 Polyplex micelles on chlorpromazine treated cells. HeLa cells were preincubated with 10 $\mu\text{g/ml}$ chlorpromazine for 30 minutes before addition of Cy5 labeled PEG12 RGD(-) (A) or PEG17 RGD(+) (B) micelles to the cell medium. Cells were evaluated 3.5 hours after micelle addition by spinning disk confocal microscopy. Representative z-stacks of treated cells are shown together with the transmission light image of the cell. The uptake of targeted and untargeted micelles is inhibited by the chlorpromazine resulting in extracellular accumulation of micelles on the cell membrane. Transferrin 488 that was coincubated with the micelles as a control for effective clathrin inhibition was not detected in the cytoplasm as well. Scale bar: 10 μm .

4. SURFACE SHIELDING OF GENE VECTORS

4.1.8 Luciferase reporter gene expression

After the detailed studies on micelle internalization, the influence of PEG shielding and integrin targeting on the reporter gene expression of micelle treated cells was determined by standard luciferase expression assay. HeLa cells were incubated with the different micelle types and luciferase expression was determined 24 hours post incubation (Fig. 4.12). Integrin targeting of PEG17 shielded micelles resulted in a 27 fold increase in gene expression compared to untargeted PEG17 micelles. The effect of integrin targeting was less prominent for micelles with PEG12 shielding and resulted in only 8 fold increase of gene expression. Notably, the transfection efficiency of PEG17 RGD(+) micelles exceeded the efficiency of PEG12 RGD(+) micelles by factor two. In addition, the transfection efficiency of untargeted micelles was reduced in the presence of enhanced PEG shielding by 40 percent. These results indicate that the PEG17 shielding reduces the probability for transgene delivery by unspecifically internalized untargeted micelles and enhances the ligand mediated transgene delivery induced by integrin-targeted micelles.

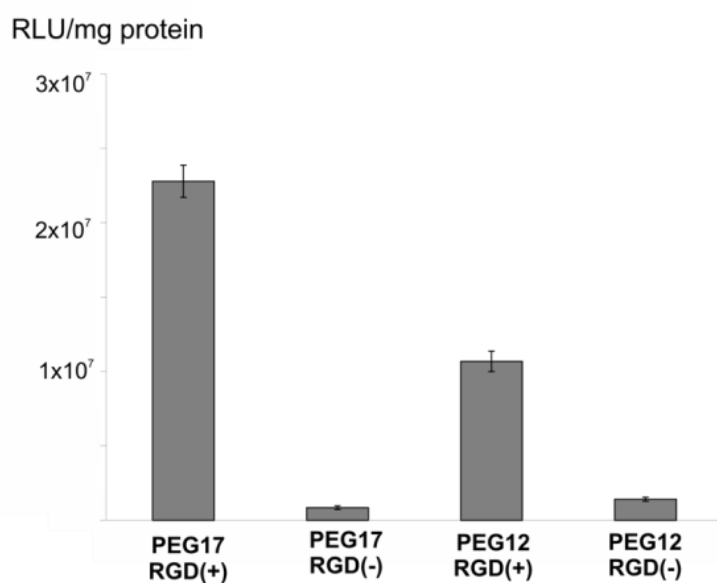


Figure 4.12 Luciferase expression. Cells were transfected with RGD(+) or RGD(-) micelles with PEG12 or PEG17 shielding, respectively. Each well was transfected with 1 μ g of DNA and analyzed for luciferase expression after 48 hours by photoluminescence detection. The experiment was performed in triplicates, the standard error of the mean (SEM) is represented by error bars. PEG17 RGD(+) micelles show enhanced reporter gene expression compared to PEG12 RGD(+) micelles.

4.1.9 Discussion

In this study, we show that the RGD ligand leads to accelerated and preferential internalization of micelles into HeLa cells when combined with proper 17 kDa PEG shielding. Simultaneous addition of fluorescently-labelled targeted and untargeted PEG17 shielded micelles to HeLa cells resulted in specific accumulation of RGD(+) micelles in the nuclear proximity and retention of RGD(-) micelles in the cell periphery. As a consequence, low colocalization of PEG17 shielded RGD(+) and RGD(-) micelles was observed. In presence of 12 kDa PEG shielding, we observed internalization characteristics dependent on the applied micelle dose. At low dose application, targeted and untargeted PEG12 shielded micelles showed comparable internalization. At high dose application, we observed split cellular localization reminiscent of PEG17 shielded micelles. However, a high colocalization of targeted and untargeted micelles in the nuclear proximity was maintained indicating the persistent internalization of untargeted micelles. Targeted as well as untargeted micelles were internalized by clathrin-mediated endocytosis portending that the RGD ligand alters the kinetics of micelle internalization without changing the uptake pathway. In addition, targeted micelles with PEG17 shielding induced the highest transgene expression.

The superior internalization characteristics of RGD-equipped PEG17 shielded micelles at all concentration demonstrate the positive effect of ligand installation on micelle uptake and emphasize the careful testing of proper shielding at several concentrations. Although PEG12 and PEG17 shielded micelles had a difference in zeta potential of only 1 mV in Tris-buffer (+ 1.5 mV for PEG12 micelles and + 0.5 mV for PEG17 micelles), they showed significant differences in internalization. It has been described before that the self-assembly of polymeric particles is considerably affected by the composition of the polymer²⁸⁹⁻²⁹¹. A different arrangement of the PEG and the RGD ligand might appear on the micelle surface dependent on the length of the applied PEG. The fact that PEG12 micelles are well internalized also in absence of the RGD ligand suggests insufficient shielding of the positively charged micelle core. Due to electrostatic interactions, the PEG12 RGD(-) micelles may bind to negatively charged plasma membrane components such as proteoglycans^{160, 292, 293} resulting in receptor-independent micelle uptake. Consistently, PEG17 shielding resulted in reduced internalization of untargeted micelles.

We further propose that in the presence of the longer PEG, the flexibility of the RGD ligand might be enhanced, improving the receptor binding properties of the micelles. We assume that the kinetics of integrin-dependent endocytosis depends on the local concentration of RGD ligands that are available to activate receptor signalling and clustering. Sancey et al. demonstrated that multimeric RGD is required to induce efficient integrin clustering and fast endocytosis²⁹⁴. The local concentration of RGD ligands that are available for receptor binding supposedly depends on the number of ligands per particle, the particle concentration on the cell and the flexibility of the ligand. The specific binding of RGD(+) micelles to integrins may additionally be hindered in the presence of electrostatic interactions with membrane components. Therefore, at the applied low micelle dose the local concentration of accessible RGD ligands of PEG12 shielded micelles might lie below the critical level that is required to induce efficient integrin mediated uptake.

4. SURFACE SHIELDING OF GENE VECTORS

At high dose of RGD(+) micelles, enhanced integrin clustering might occur, enforcing the integrin mediated endocytosis of the targeted micelles²⁹⁴. Additionally, negative charges on the cell membrane might be completely covered by positively charged micelles. In this scenario, excess micelles that diffuse in the cell medium, weakly interact with membrane components, resulting in preferential interaction of the RGD ligand with accessible integrins.

The fact that untargeted PEG12 micelles were partly retained in the cellular periphery at high micelle dose, suggests the saturation of the receptor-independent micelle internalization at high concentration. Accordingly, a quenching assay revealed that the peripheral rim of RGD(-) micelles observed in the microscopic images, consisted mainly of extracellularly bound micelles that were not internalized yet. In contrast, RGD(+) micelles were well internalized also at high concentration and saturation effects were not observed. Activated integrins are recycled to the plasma membrane after their endocytosis²⁹⁵⁻²⁹⁷. They may then serve as receptors for further endocytosis of micelles and promote increased internalization after activation.

The enhanced perinuclear accumulation of RGD(+) micelles at high concentration may be promoted by two mechanisms. First, the integrin mediated endocytosis may induce faster uptake kinetics, and second, an earlier onset of endosomal transportation of targeted micelles towards the cell nucleus may be possible. Previous studies on integrin uptake revealed that integrin heterodimers can be endocytosed via different internalization routes such as clathrin-dependent endocytosis^{136, 298}, caveolin-dependent endocytosis^{299, 300} and macropinocytosis¹³⁷. Our results from the colocalization experiments with markers for clathrin- and caveolin-dependent endocytosis as well as inhibitor studies suggest that clathrin-dependent endocytosis plays the major role for the uptake of integrin-targeted as well as untargeted micelles. The colocalization of RGD(-) and RGD(+) micelles at later time points demonstrates that untargeted micelles end up in the same cellular compartments as targeted micelles, but with slower kinetics. The RGD ligand therefore seems to accelerate the perinuclear accumulation of micelles without changing the uptake pathway. Lakadamyali et al. demonstrated that different endocytic ligands for clathrin-mediated endocytosis are sorted into distinct populations of dynamic, rapidly maturing or static, slowly maturing early endosomes³⁰¹. Interestingly, the sorting already starts at the plasma membrane and is ligand dependent. As the maturation rate of endosomes is highly correlated with their mobility along microtubules³⁰¹, cargo in dynamic endosomes can reach the nuclear proximity faster than static ones and may explain the fast transfer of RGD-equipped micelles to the nuclear proximity.

Within six hours of microscopical observation of micelle internalization, we did not observe significant DNA release into the cytosol or nucleus. However, successful luciferase expression after 24 hours reveals that certain amounts of DNA have been released and reached the nucleus. As few plasmids are sufficient to induce significant levels of gene expression^{302, 303}, the endosomal release of micelle DNA may have been below the detection limit of our microscopical set-up. Alternatively, the effective release may occur at later time points. The highly increased transgene expression of ligand-equipped micelles with proper PEG17 shielding suggests that the RGD ligand also induces alterations in the intracellular processing in addition to accelerated uptake kinetics.

Effects of the RGD ligand on intracellular processes have been reported. Shayakhmetov et al. revealed that the RGD motif triggers the enhanced endosomal release of adenovirus³⁰⁴. Chavez et al. described membrane destabilizing properties of the RGD ligand at low pH³⁰⁵. The RGD ligand may therefore account for enhanced transfection in later stages of transfection besides the accelerated and preferential internalization.

To conclude, our results give mechanistical insights into the interplay of shielding and receptor targeting. Surface shielding of integrin-targeted micelles has a significant effect on their targeting specificity. This effect is expected to be a general phenomenon for the targeting of charged polyplexes to all kinds of membrane receptors and has to our knowledge has not been investigated on single cell level so far. Solely in the presence of proper shielding, integrin targeting had a significant effect on internalization and transgene expression, which is an important feature for the selective targeted therapy of cancer cells. Our results emphasize that highly sensitive microscopy on the single cell level provides additional information on the cellular localization which cannot be resolved in bulk experiments. Furthermore, as shown for the coincubation experiments at low micelle dose, microscopical observations can be performed at extraordinary low particle concentrations and on a single particle level which is not feasible with standard cytometric analysis. Previous studies revealed that micelles built from block copolymers are promising candidates for gene therapy because they have a uniform size and are stable over a long time period^{281, 283, 286}. We propose that PEG17 shielded micelles equipped with a cyclic RGD ligand are the favoured system of choice for clinical therapy as they exhibit higher transfection efficiencies, a higher specificity for integrin-dependent endocytosis compared to PEG12 shielded micelles, and are functional at low doses as well. This gained knowledge enables the improved design of future gene vectors in order to maximize their therapeutic benefit for clinical application.

4.2 Reversible PEG shielding for improved intracellular DNA release

This chapter is adapted from:

C. Zhu, M. Zheng, F. Meng, F.M. Mickler, N. Ruthardt, X. Zhu and Z. Zhong, "Reversibly Shielded DNA Polyplexes Based on Bio-reducible PDMAEMA-SS-PEG-SS-PDMAEMA Triblock Copolymers Mediate Markedly Enhanced Nonviral Gene Transfection." *Biomacromolecules*, (2012), 13(3), 769-78

4.2.1 Particle design

To improve the intracellular delivery of DNA from PEGylated particles bio-reducible triblock copolymers (PDMAEMA-SS-PEG-SS-PDMAEMA, Mw=6.6-6-6.6 kDa) were designed. Poly-dimethylaminoethyl methacrylate (PDMAEMA) copolymers are conveniently synthesized by living radical polymerization providing controlled macromolecular structure and composition. The introduced reduction-responsive disulfide-bond (S-S) is stable in extracellular fluids but can be cleaved in the reductive environment of intracellular compartments, such as the cytoplasm or the nucleus^{282, 306}. Like their non-reducible analogues (PDMAEMA-PEG-PDMAEMA), the bio-reducible copolymer effectively condensed DNA into small nanoparticles with an average diameter less than 120 nm and close to neutral zeta potential (Fig. 4.13). In contrast, the 6.3 kDa PDMAEMA homopolymer was not able to efficiently condense DNA. In the presence of 10 mM dithiothreitol (DTT) the reducible particles showed rapid deshielding *in vitro*, as confirmed by a significant increase in particle surface charge from +0.7 mV to +11 mV. Furthermore the size of reversible shielded polyplexes rapidly increased in the presence of DTT, most likely due to aggregation of the cleaved homopolymer. Release of DNA in response to 10 mM DTT was further detected in gel retardation assays. DNA release occurred when using the reducible polymer, whereas no disassembly was observed for polyplexes with the non-reducible analogue proving selective cleavage and disassembly of the disulfide-bond equipped polyplexes in a reductive environment.

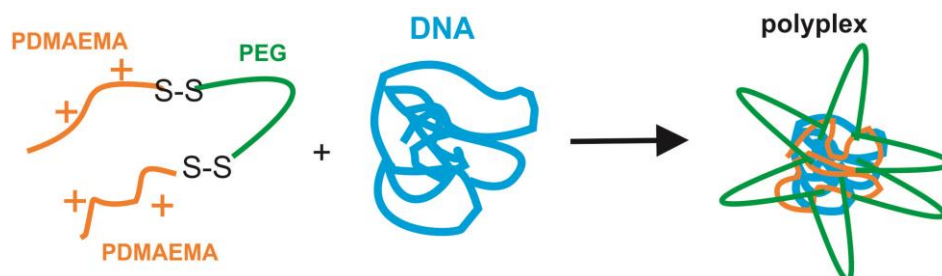


Figure 4.13 Design of reversibly PEG-shielded Poly-dimethylaminoethylmethacrylate (PDMAEMA) polyplexes. PDMAEMA-SS-PEG-SS-PDMAEMA triblock copolymers (Mw = 6.6-6-6.6 kDa) effectively condense DNA into partially shielded nano-sized particles with high colloidal stability. The cleavage of the reduction-responsive disulfide bond results in particle deshielding and DNA release. Non-reducible particles consisting of PDMAEMA-b-PEG-b-PDMAEMA triblock copolymers (Mw= 6.4-6-6.4 kDa) and DNA serve as reference.

4.2.2 Live-cell imaging of particle uptake and trafficking to late endosomes

In order to compare the cellular uptake and intracellular trafficking of the non-reducible PDMAEMA-b-PEG-b-PDMAEMA (6.4 kDa) and the bioreducible PDMAEMA-SS-PEG-SS-PDMAEMA (6.6 kDa) polyplexes fluorescence live-cell imaging experiments were performed on a single cell level. For the imaging experiments polyplexes with fluorescent dye-labeled plasmid DNA were prepared. To evaluate polyplex uptake into endocytic compartments, Cy5 labeled polyplexes were incubated on HuH7 cancer cells expressing Rab9-GFP as a marker for late endosomes. Z-stacks of single cells were recorded by spinning disk confocal microscopy in a time interval of 0-30 hours after polyplex addition. Z-projections of the recorded image sequences were analyzed for colocalization of polyplexes with Rab9-GFP labeled endosomes. By quantifying the time-dependent colocalization degree of both polyplex types, information on their uptake kinetics and intracellular processing could be gained.

Our microscopical images indicate that both polymer types form uniformly sized, non-aggregated particles that efficiently bind to the plasma membrane of the cell. After 1 hour of incubation similar particle numbers were monitored on the cells for the non-reducible and the bioreducible particles. During the first four hours of incubation low colocalization with Rab9 positive endosomes was observed for both polyplex types as indicated in the overlay images of the GFP and the Cy5 channel (Fig. 4.14). Most polyplexes were retained in the plasma membrane region during this time period indicating slow internalization of both PDMAEMA-SS-PEG-SS-PDMAEMA as well as PDMAEMA-b-PEG-b-PMAEMA polyplexes. In contrast, at later time points (17 – 30 hours post polyplex addition) both polyplex types showed intracellular localization and fast directed motion indicating active transport along the microtubule network. Enrichment of particles was detected in the perinuclear region of the cell. At this time points, a high percentage of polyplexes showed colocalization with Rab9 positive endosomes as demonstrated by the white spots in the overlay image of the green and the magenta channel, revealing polyplex transport to late endosomal compartments.

4. SURFACE SHIELDING OF GENE VECTORS

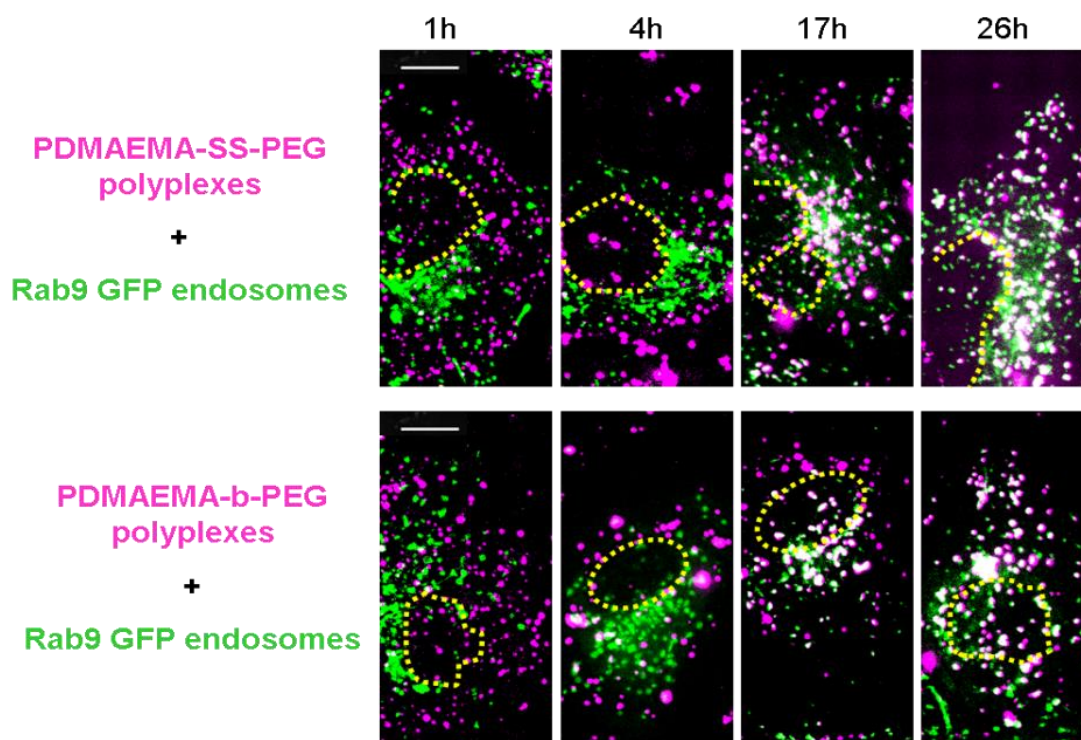


Figure 4.14 Uptake and trafficking of PDMAEMA polyplexes to late endosomes. Cy5 labeled polyplexes (PDMAEMA-SS-PEG-SS-PDMAEMA = upper row, PDMAEMA-b-PEG-b-PDMAEMA = lower row) were applied to Rab9-GFP expressing HuH7 cells and imaged by spinning disk confocal microscopy after 1, 4, 17 and 26 hours. Fluorescence overlay images were obtained by superimposing z-projections of the GFP and the Cy5 channel. Polyplexes colocalizing with Rab9-GFP labeled late endosomes appear in white. The region of the cell nucleus is marked with a dashed yellow line. Both polyplex types show increasing colocalization with Rab9-GFP labeled endosomes over time. Scale bar = 10 μ m.

Quantification of the time-dependent colocalization degree with custom-written analysis software revealed a linear increase of the colocalization degree in the first 25 hours post polyplex application, reaching similar levels for both polyplex types (Fig. 4.15). For both polyplex types, a broad spread of the data points was observed reaching from 50 to 95 % colocalization after 25 hours of incubation, indicating that a number of heterogenic cell-specific factors influence the polyplex internalization. However the mean colocalization values were similar for the two polyplex compositions.

These data suggest that the inserted disulfide bond does not disturb the particle formation, the uptake kinetics or intracellular trafficking of the polyplexes. Independently of the disulfide bond, both polyplexes were endocytosed and transported to late endosomal compartments in the same time interval.

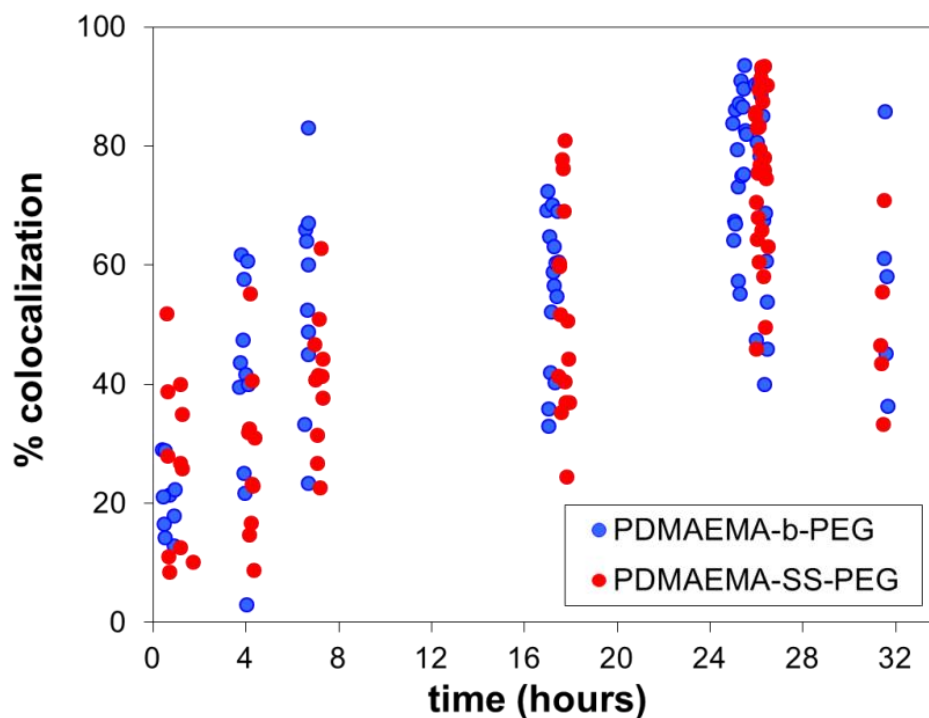


Figure 4.15 Quantification of the colocalization degree of polyplexes and late endosomes. Cy5 labeled polyplexes were incubated on Rab9-GFP expressing HuH7 cells for the indicated time periods before imaging with spinning disk confocal microscopy. Obtained movies were analyzed for colocalization of polyplexes with Rab9-GFP labeled late endosomes with custom-written software. Each data point represents the colocalization degree in a single cell. PDMAEMA-b-PEG-b-PDMAEMA and PDMAEMA-SS-PEG-SS-PDMAEMA polyplexes show a similar increase in the time-dependent colocalization degree indicating simultaneous uptake and transportation to late endosomes.

4.2.3 Luciferase reporter gene expression

To test if the transfection efficiency of the PDMAEMA polyplexes is improved by the bioresponsive linker luciferase expression experiments were performed at Soochow University. For the experiments, cells were plated at a density of $1.5 \cdot 10^5$ cells/well and treated with 100 μ l polyplex dispersion with pCMV Luc plasmid, equivalent to 1 μ g DNA per well. After 48 hours of incubation luciferase expression was determined using a commercial luciferase assay kit.

The results revealed a significant increase in transgene expression in the presence of the bioreducible linker (Fig. 4.16). PDMAEMA-SS-PEG-polyplex treated cells exhibited approximately 28-fold increased luciferase expression levels compared to PDMAEMA-b-PEG polyplex treated cells. This result suggests that the disulfide bond indeed facilitates the intracellular delivery of the DNA resulting in higher plasmid copies available for gene expression.

4. SURFACE SHIELDING OF GENE VECTORS

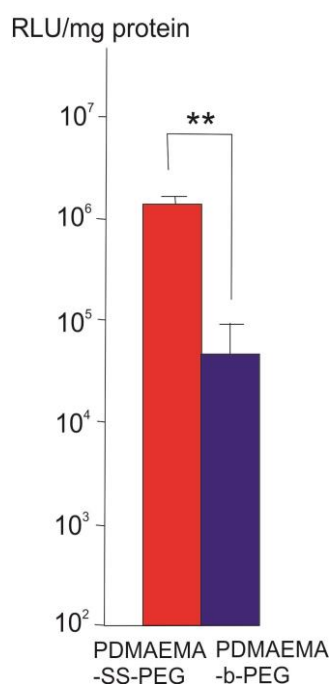


Figure 4.16 Luciferase reporter gene expression. Cells were transfected with PDMAEMA-SS-PEG-SS-PDMAEMA polyplexes and PDMAEMA-b-PEG-b-PDMAEMA polyplexes, respectively. Each well was transfected with 1 μ g of DNA and analyzed for luciferase expression after 48 hours by photoluminescence detection. Data are shown as mean \pm standard deviation (n=3, student's t-test, ** p < 0.01). PDMAEMA-SS-PEG-SS-PDMAEMA polyplex treated cells show enhanced reporter gene expression compared to PDMAEMA-b-PEG-b-PDMAEMA polyplex treated cells.

4.2.4 DNA release

To study if enhanced DNA release into the cytoplasm or the nucleus can be visualized for the reversibly shielded polyplexes, cells were incubated with the two polyplex types for 25 hours before imaging with spinning disk confocal microscopy. By digital image analysis, polyplex filled endosomes and the cytoplasmic region were identified in z-projections of recorded cells using an intensity threshold criterion. The mean fluorescence intensity of endosomes as well as the cytoplasm was determined and compared for both polyplex types (Fig. 4.17).

Our results show that the fluorescence intensity of polyplex filled endosomes is similar for both polyplex types. Furthermore no significant increase of the cytoplasmic fluorescence intensity could be detected for the disulfide-equipped polyplexes compared to the non-reducible polyplexes. Inside the nucleus which was identified by comparison with the transmission light image, no fluorescent spots were observed. In z-projections some spots appear in the nuclear region but they originate from endosomes in z-planes above or below the nucleus. These data suggest that the majority of polyplexes remains entrapped in late endosomes and endosomal release seems to be a main bottleneck in the transfection process. Nevertheless, our transfection experiments revealed that a certain number of plasmids had access to the transcription machinery of the cell, as significant

reporter gene expression was detected. The number of released plasmid DNA molecules though seems to lie below the detection limit of our imaging method.

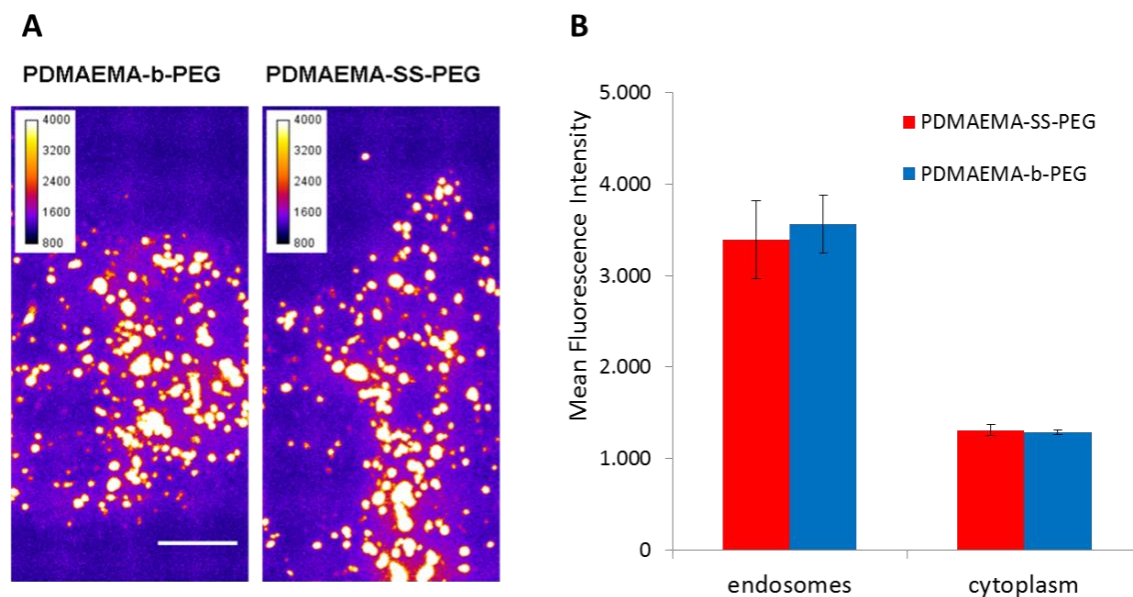


Figure 4.17 Polyplex fluorescence in endosomes and cytoplasm after 25 hours of incubation.

A Color coded confocal images of polyplex treated cells. Polyplexes were incubated on Rab9-GFP expressing HuH7 cells for 25 hours before imaging with spinning disk confocal microscopy. To visualize the fluorescence intensities of endosomes and the cytoplasm in treated cells, z-projections of confocal z-stacks were built and brightness and contrast settings were equalized for all recorded images. Fluorescence intensities were color coded according to the calibration bar in the upper left part of the images. Representative cells incubated with PDMAEMA-b-PEG-b-PDMAEMA (left image) or PDMAEMA-SS-PEG-SS-PDMAEMA (right image) are shown. Similar fluorescence intensity distributions are observed for both polyplex types. Low fluorescence intensities of the cytoplasm indicate low endosomal release of both polyplex types. Scale bar = 10 μ m.

B Quantification of mean fluorescence intensities. The fluorescence of polyplex containing endosomes and the cytoplasm was quantified by digital image analysis in z-projections of single cells. Median values were calculated and plotted in a histogram (N=18 cells for PDMAEMA-SS-PEG-SS-PDMAEMA polyplexes, N=17 cells for PDMAEMA-b-PEG-d-PDMAEMA polyplexes), the standard deviation is represented by error bars.

4.2.5 Discussion

Our experiments reveal favorable properties of the reversible shielded polyplexes for gene delivery. The bioreducible polymer forms stable complexes with DNA that bind to the surface of cancer cells and show similar uptake and intracellular trafficking to late endosomes like the non-reducible polyplexes. *In vitro* assays revealed successful deshielding and DNA release from bioreducible polyplexes in reductive environment. Enhanced reporter gene expression was induced in cancer cells by the reversible shielded polyplexes compared to the stably shielded polyplexes indicating that intracellular cleavage of the disulfide bridge facilitates the transfection process.

Our confocal images additionally revealed that endosomal escape is an important bottleneck in the transfection process as the majority of PDMAEMA-polyplexes remained entrapped in endosomes.

4. SURFACE SHIELDING OF GENE VECTORS

A recent study by Rehman et al suggests, that only a very limited number of polyplexes contribute to endosomal release of nucleic acids¹⁸⁵. The authors suggest the formation of transient pores in the endosomal membrane instead of complete membrane rupture. We therefore suppose that the number of DNA molecules released to the cytoplasm and the nucleus lies below the detection limit of our method for both polyplex formulations but is sufficient to induce transgene expression.

Conflicting reports can be found in the literature on the redox-potential of endocytic compartments. Experiments with redox-sensitive GFP suggested that late endosomes, lysosomes and recycling endosomes are oxidative³⁰⁷. However, more recently, Yang et al. performed experiments with a folate-FRET conjugate that changes fluorescence upon disulfide cleavage, showing that disulfide cleavage occurs with a half-time of 6 hours inside endosomes³⁰⁸.

Different scenarios can be envisioned how particle deshielding improves the transfection process. First, cleavage of the PEG molecule inside the endosome might enhance endosomal leakiness by increasing the proton sponge effect of the polymer or facilitating the interaction of cationic PDMAEMA with the endosomal membrane resulting in local endosome destabilization. Second, the cleavage of the polymer might enhance the particle decondensation inside the endosome or the cytoplasm resulting in enhanced DNA release. *In vitro* assays confirmed that the PDMAEMA homopolymer alone is not able to form stable particles; the linkage of two PDMAEMA molecules in the PDMAEMA-SS-PEG-SS-PDMAEMA polymer seems to be required for effective DNA complexation. After disulfide reduction the cleaved homopolymer tends to form aggregates, interactions with DNA are weakened and DNA release is triggered.

We conclude that bioresponsive deshielding is a promising strategy to overcome the PEG-dilemma. It allows the design of long-circulating particles with low toxicity and low nonspecific interactions combined with improved intracellular DNA delivery.

5 Receptor targeting of gene vectors

For efficient cancer therapy with low systemic toxicity “intelligent” delivery systems are desired that selectively target tumor cells or the tumor environment and do not affect healthy cells.

A variety of surface receptors are overexpressed on the plasma membrane of cancer cells providing promising target structures for specific binding and internalization of small molecule drugs, drug delivery nanocarriers or gene vectors equipped with selective targeting ligands. Among these receptors are the epidermal growth factor (EGF) receptor⁴⁷, the transferrin receptor¹²⁶, the folate receptor⁴⁹ and a subset of integrins⁵⁰. Molecules used for specific receptor binding include natural protein ligands, peptide ligands, antibodies, antibody fragments, carbohydrates and aptamers.

Many publications feature the positive effect of receptor targeting *in vitro* and *in vivo* and a number of antibody-drug conjugates are already approved for cancer treatment, such as Trastuzumab Emtansine³⁰⁹, a conjugate of an EGFR-directed antibody and the cytotoxic drug Mertansine that is applied for the treatment of breast cancer.

However, some challenges need to be taken into account when using targeting ligands. First, the ligand may modify the uptake pathway of the drug or gene carrier resulting e.g. in transport to degradative compartments. Second, the ligand can activate undesired cell signaling-cascades that promote cell proliferation and survival. Furthermore, hydrophobic targeting ligands might induce enhanced particle aggregation. Also, the production costs of receptor-targeted nanocarriers might significantly increase due to challenging synthesis and conjugation of the targeting ligand. Therefore the targeting ligand should be chosen carefully, the ligand density on the particle surface should be optimized and the effect of ligand installation on cellular interactions has to be elucidated in detail. As part of this thesis, different receptor targeting strategies were investigated with live-cell imaging. In a first project, we compared the cellular interactions of EGF receptor-targeted polyplexes that were equipped either with the natural full-length EGF ligand or a short synthetic peptide in terms of uptake kinetics, transfection efficiency, endocytosis pathway and molecular mechanism of ligand induced EGF receptor internalization (see section 5.1). This project was performed in collaboration with the groups of Prof. Ernst Wagner and PD Dr. Manfred Ogris from the pharmacy department of the LMU Munich. Described results are taken from our publication in Nanoletters⁸.

5. RECEPTOR TARGETING OF GENE VECTORS

In a second project the internalization efficiency of integrin-targeted polyplexes and transferrin receptor-targeted polyplexes was studied for different ligand densities on the particle surface. Additionally the strategy of combined integrin and transferrin receptor targeting of polyplexes (dual targeting) was evaluated (polyplexes for these experiments were provided by the group of Prof. Ernst Wagner, LMU Munich) (see section 5.2). Experiments from section 5.2 were performed by Leonhard Möckl under my instruction and results are adapted from his bachelor thesis.

In section 5.3 the development of a microfluidic device is described that was established to study interactions between nanoparticles and cells or physiological surfaces under flow conditions. Flow experiments were performed by the students Ellen Broda and Sophia Betzler under my supervision. Parts of the chapter are adapted from their master and bachelor thesis.

5.1 Tuning nanoparticle uptake: Natural and artificial EGFR targeting ligand mediate two distinct endocytosis mechanisms

This chapter is adapted from:

F.M. Mickler, L. Möckl, N. Ruthardt, M. Ogris, E. Wagner and C. Bräuchle,

“Tuning Nanoparticle Uptake: Live-Cell Imaging Reveals Two Distinct Endocytosis Mechanisms Mediated by Natural and Artificial EGFR Targeting Ligand.”

Nano Letters, (2012), 12, 3417-3423

5.1.1 Particle design

The epidermal growth factor (EGF) receptor is a promising target structure for cancer therapy as it is overexpressed on a broad variety of different tumors¹⁰¹. During the last years, *in vitro* and *in vivo* studies have demonstrated that recombinant full-length EGF can be coupled to gene and drug delivery systems providing their efficient and fast receptor mediated endocytosis^{119, 310}. Recent studies revealed that the full-length EGF ligand can be substituted by EGFR-directed antibodies¹¹⁸ or by short artificial peptides³¹¹, such as GE11^{312, 313}. This alternative ligand was identified by phage display and binds to the EGF receptor without mitogenic activity. The GE11 peptide allows cheap and up-scalable synthesis of EGF receptor-targeted nanocarriers for further preclinical or clinical investigations³¹⁴. The EGFR targeting with GE11 is receptor specific and gene carriers equipped with GE11 show transfection efficiencies similar to gene carriers with EGF^{314, 315}. Specific therapy of EGFR overexpressing tumors was achieved *in vivo* with GE11-equipped gene carriers³¹⁶.

Here, we compare the effect of the full-length EGF ligand and the short GE11 peptide ligand on the mechanism of nanocarrier endocytosis in detail by applying highly sensitive fluorescence live-cell microscopy. As a model system for therapeutic nanocarriers in gene delivery, we applied fluorescently labeled polyplexes – complexes of PEGylated polyethylenimine (PEI) and plasmid DNA - equipped with the respective targeting ligands³¹⁷.

Prior to each experiment, EGF polyplexes, GE11 polyplexes and untargeted polyplexes were generated freshly in HEPES buffered glucose (HBG, 20 mM HEPES pH 7.1, 5 % glucose w/v) at a molar N:P ratio of 6:1 (nitrogen in LPEI to phosphate in DNA), as described recently^{314, 318}. Briefly, dye-labeled plasmid DNA (final concentration 20 µg/ml) was complexed with positively charged polymer (EGF-PEG-PEI, GE11-PEG-PEI or PEG-PEI, respectively) containing a 2 kDa polyethylene glycol (PEG) linker conjugated to 22 kDa linear polyethylenimine (PEI) (Fig. 5.1). Recombinant 6 kDa murine EGF and GE11 (CYHWYGYTPQNVI), were used as targeting ligands. We confirmed specific EGFR targeting of the formed EGF- and GE11 polyplexes in previous studies using competition with free ligand and receptor negative control cell lines^{314-316, 319}. As EGF polyplexes tend to aggregate at high ligand concentration, 10 % of targeted EGF polymer was mixed with 90 % untargeted polymer in our experiments. The GE11 ligand exhibits lower aggregation properties and allows the formation of polyplexes with 100 % targeted polymer (see appendix, Fig. A1).

5. RECEPTOR TARGETING OF GENE VECTORS

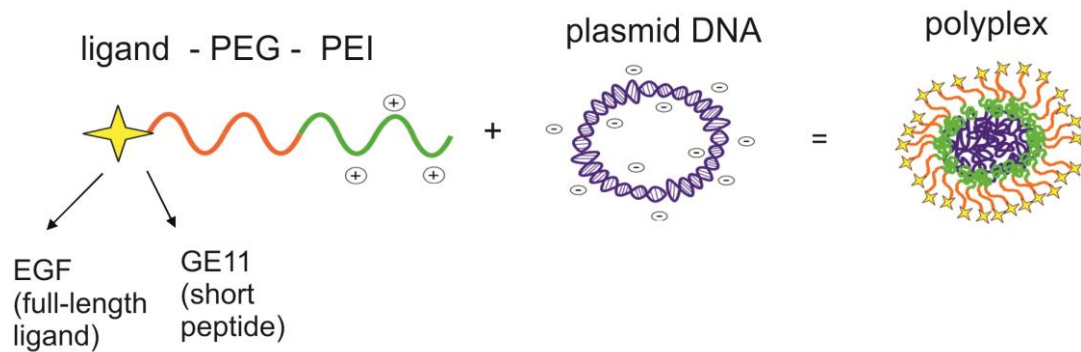


Figure 5.1 Design of EGF- and GE11 polyplexes. Targeting ligands (6 kDa full-length EGF ligand or peptidic GE11 ligand (13 amino acids)) were coupled to polyethylene glycol–polyethylenimine (PEG, 2kDa; linear PEI, 22 kDa) polymers. The resulting EGF-PEG-PEI and GE11-PEG-PEI polymers effectively condensed DNA into nanosized particles. For the formation of EGF polyplexes, 10 % targeted polymer was mixed with 90 % untargeted polymer; for GE11 polyplexes 100 % targeted polymer was applied. Untargeted polyplexes (PEG-PEI) served as reference for non-specific uptake.

5.1.2 Uptake kinetics determined by quenching assay

To compare the uptake kinetics of the different polyplex types, we performed a quenching analysis of Cy3 dye-labeled polyplexes on EGFR overexpressing HuH7 cells. For this purpose, polyplexes were incubated with cells for defined time periods before trypan blue was added as a membrane impermeable fluorescence quencher under microscopical observation. Only the fluorescence of extracellular but not intracellular polyplexes is quenched. Our data reveal that EGF polyplexes were internalized with fast kinetics. Up to 80 % of the EGF-equipped polyplexes were endocytosed in the first 10 minutes post application (Fig. 5.2), consistent with previous studies on EGF polyplexes³¹⁰. Interestingly, internalization of GE11 polyplexes occurred with significantly slower kinetics reaching only 40 % internalization in the same time interval. However, GE11 polyplex uptake significantly exceeded the uptake of untargeted polyplexes, which showed less than 20 % internalization during the first 10 minutes of incubation. As expected for single cell experiments, a high statistical spread of the data points was observed, caused by the biological heterogeneity of single cells. However, a clear trend was detected. It should be noted that absolute internalization values might be overestimated in the quenching assay as membrane bound polyplexes, which are not yet internalized but are incorporated into membrane invaginations, might not be completely accessible for the fluorescence quencher.

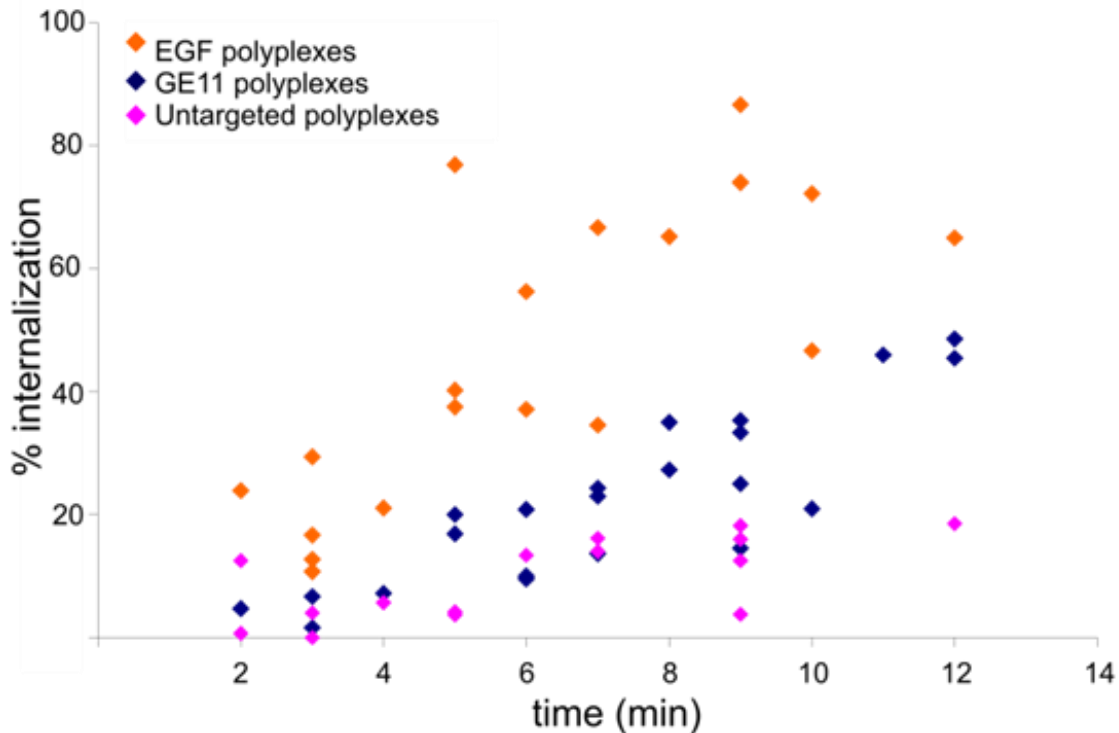


Figure 5.2 Uptake kinetics of EGF-, GE11- and untargeted polyplexes determined by quenching assay. Cy3-labeled polyplexes were incubated on HuH7 cells for the indicated time periods before addition of trypan blue as a fluorescence quencher of extracellular polyplexes. Each data point represents the calculated fraction of internalized polyplexes in a single cell measurement. (Orange square: EGF polyplexes, blue square: GE11 polyplexes, magenta square: untargeted polyplexes).

5.1.3 Live-cell imaging of polyplex uptake

To support the data from the quenching experiments, additional live-cell imaging of polyplexes was performed by spinning disk confocal microscopy on the single cell level (Fig. 5.3 A). For the experiments, HuH7 cells were incubated with Cy5-labeled EGF-, GE11- or untargeted polyplexes. Short movies of confocal z-slices of single cells were recorded in the first hour post polyplex addition. To illustrate the cellular motion of polyplexes, two-dimensional trajectories were generated by superimposing a time-series of 134 images (time projection), where each image was acquired at a frame rate of 330 ms. Endocytosed polyplexes can be identified by their central location within the cell and their characteristic intracellular motion, such as fast directed transport along microtubules, which is illustrated by long trajectories in the time-projection. Extracellular polyplexes are characterized by their location in the cellular periphery and their characteristic slow, concerted motion on the plasma membrane. Our data verified the fast endocytosis of EGF polyplexes. Within 30 minutes of incubation, the majority of EGF polyplexes was found in intracellular compartments that showed fast transportation towards the perinuclear region of the cell. Spots detected in proximity of the cell nucleus showed a clear increase in fluorescence intensity (6-10 times enhanced total integrated intensity of the fluorescent spots) indicating the fusion of several endosomal compartments during trafficking in the

5. RECEPTOR TARGETING OF GENE VECTORS

cytosol. In contrast, GE11 polyplexes as well as untargeted polyplexes showed considerable membrane retention during the first 30 minutes of incubation.

To quantify the internalization degree, cells were evaluated by digital image analysis using a novel custom-designed ImageJ macro (Nano_In_Cell_3D) (Fig. 5.3 B). This new analysis tool enables the selective quantification of particles in specific subcellular regions on the single cell level. Here we evaluated the internalization degree of particles by quantification of the fluorescence signal in the plasma membrane region and the cytoplasmic region.

For the analysis, cells were incubated with polyplexes for 20 minutes, fixed and the plasma membrane was stained with Wheat Germ Agglutinin (WGA)-AlexaFluor488. Z-stacks of single cells were imaged with dual laser excitation. By digital image analysis the membrane and the cytoplasmic region was identified and the polyplex fluorescence was subsequently quantified in both regions. The internalization degree was then calculated for each cell by dividing the fluorescence signal in the cytoplasm by the fluorescence signal of the entire cell (= cytoplasm + membrane region). As only polyplexes were examined that had already bound to the cell surface, effects due to different binding affinity were avoided and not considered.

For EGF polyplexes, a mean internalization degree of 70 % was determined after 20 minutes of incubation, indicating their fast receptor-mediated endocytosis consistent to our quenching data. Polyplexes without a targeting ligand showed only 9 % mean internalization, portending that unspecific receptor-independent internalization was successfully prevented by the implemented PEG shielding. GE11-equipped polyplexes reached a significantly higher mean internalization degree of 26 % in the same time period. Our results indicate that two different modes of EGFR mediated endocytosis exist: a fast uptake mode in case of EGF binding and a slow mode in case of GE11 binding to the receptor. The different uptake mode of EGF polyplexes and GE11 polyplexes was further confirmed by a coincubation experiment, in which Cy3-labeled EGF polyplexes and Cy5-labeled GE11 polyplexes were simultaneously added to the same cell chamber. Dual color movies affirmed that in the first hour of incubation, a large number of GE11 polyplexes remained extracellularly bound to the cell membrane, whereas EGF polyplexes were efficiently internalized in the first hour of incubation (Fig. 5.4).

The experiments described so far revealed the superior uptake characteristics of EGF polyplexes in the first hour of incubation. These results obtained by single cell imaging are in agreement with a recent study by flow cytometry showing enhanced EGF- versus GE11 polyplex levels after 30 minutes of incubation on cells³¹⁴.

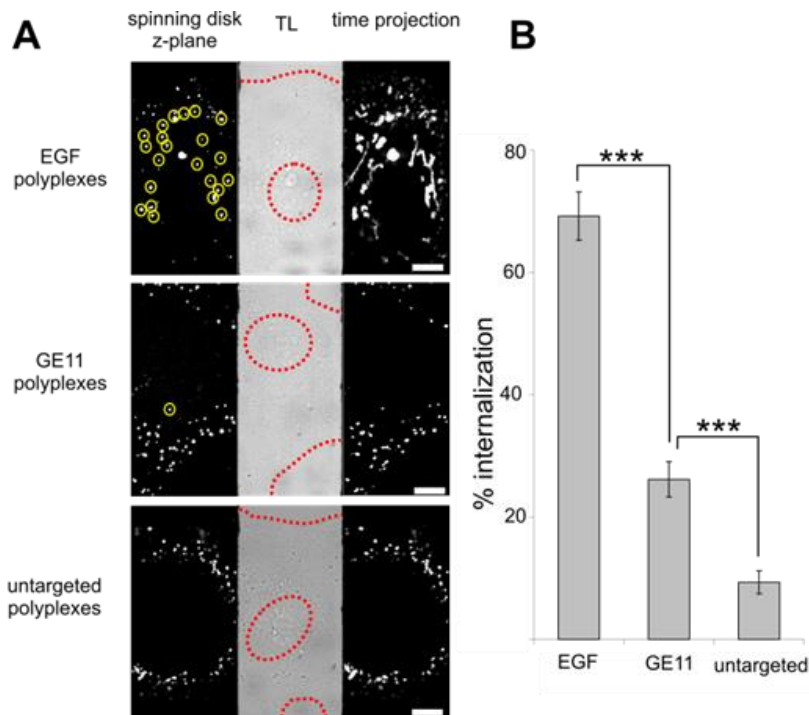


Figure 5.3 Different uptake kinetics visualized by spinning disk confocal microscopy. (A) Cy5-labeled polyplexes were incubated onto HuH7 cells for 30 minutes before imaging with spinning disk confocal microscopy. Confocal z-slices of representative cells (left image) are shown together with the transmission light image (TL, central image) of the respective cell. To display the characteristic intracellular motion of endocytosed particles, a sequence of 134 recorded images equivalent to a time interval of 45 seconds was superimposed (time projection, right image). Polyplexes identified as internalized are highlighted by yellow circles. The region of the cell nucleus and the cell membrane is marked in the transmission light image by a dashed red line. Scale bar: 10 μm . **(B)** Quantification of polyplex internalization after 20 minutes of incubation by digital image analysis. Mean internalization values are presented in the histogram. (N=14-17 cells for each data point). P-values were determined by student's t-test. (***) $P < 0.0001$ for EGF- compared to GE11 polyplexes, and GE11- compared to untargeted polyplexes). The standard error of the mean (SEM) is represented by error bars.

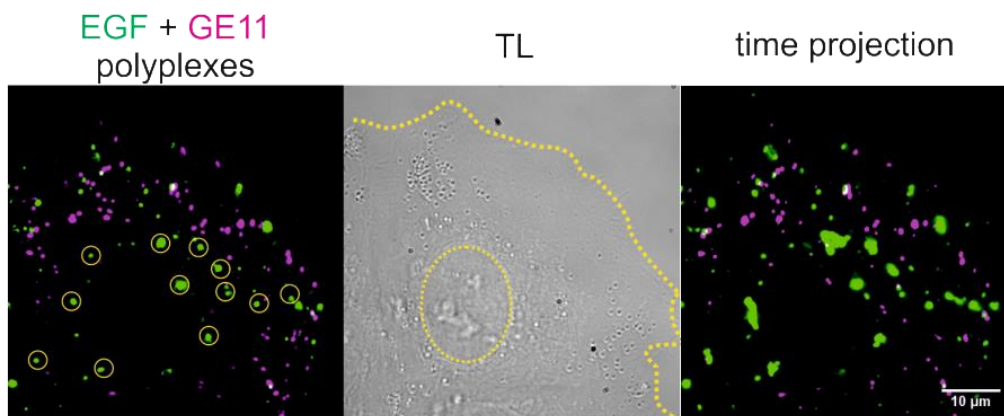


Fig. 5.4 Coincubation of differently labeled EGF- and GE11 polyplexes. Cy3-labeled EGF polyplexes (marked in green) and Cy5-labeled GE11 polyplexes (marked in magenta) were simultaneously applied onto HUH7 cells and imaged after 35 minutes by widefield fluorescence microscopy. An overlay image of the Cy3 and the Cy5 channel is depicted together with the transmission light image (TL) of the cell and a time projection (overlay of 134 images from a 45 seconds time interval). A significant number of EGF polyplexes show intracellular transport and are located in proximity to the cell nucleus. GE11 polyplexes remain bound in the peripheral membrane region of the cell.

5. RECEPTOR TARGETING OF GENE VECTORS

Next, to analyze the ligand effect on a longer time scale, polyplexes were incubated for four to six hours on HuH7 cells before imaging. In figure 5.5 A fluorescence widefield images of treated cells, incubated with EGF-, GE11- or untargeted polyplexes, are displayed together with the respective transmission light image of the cell. To visualize the cellular motion of the polyplexes, time-projections of the recorded movies are presented. Interestingly, our data revealed efficient internalization of GE11 polyplexes after four hours, comparable to EGF polyplexes. Both polyplex types showed distinct accumulation in perinuclear endosomes and characteristic intracellular motion. In contrast, untargeted polyplexes were predominantly retained in the cellular periphery. Internalization efficiencies of the polyplex types were quantified as described above. Mean values of internalization efficiencies obtained after four to six hours of incubation are displayed in figure 5.5 B. Quantification confirmed that GE11 polyplexes reached the same mean internalization levels as EGF polyplexes (65 % and 67 % of internalized polyplexes, respectively), whereas untargeted polyplexes showed a significantly lower mean internalization degree of 31 %. These data suggest continuous uptake of GE11 polyplexes, resulting in their efficient internalization within four hours.

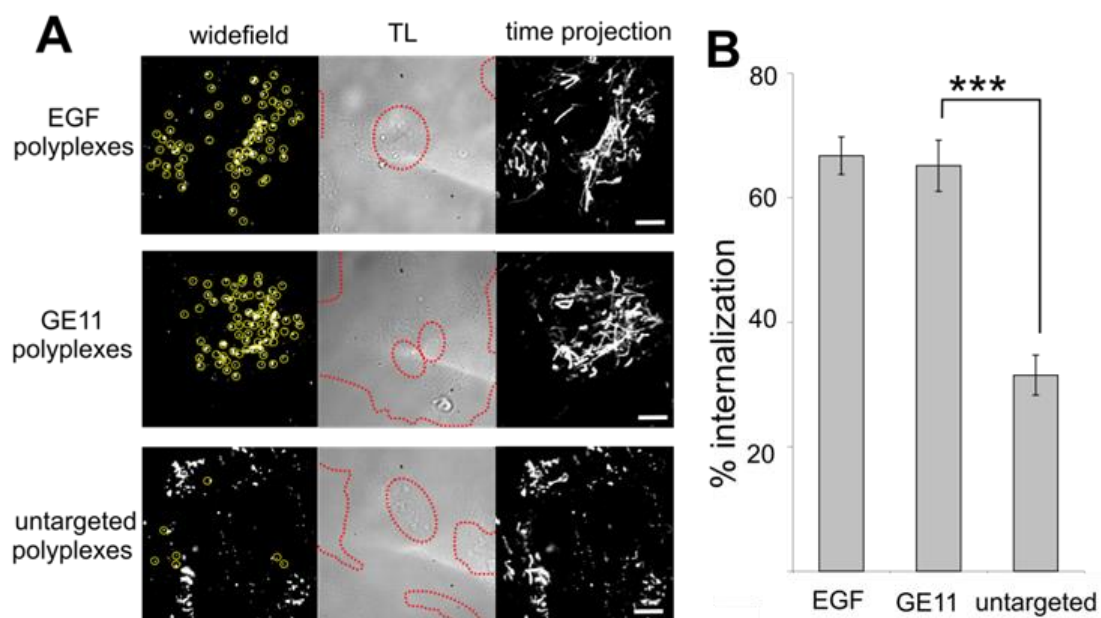


Figure 5.5 Efficient internalization of GE11 polyplexes on the long time scale. (A) HuH7 cells were incubated for four hours with Cy5-labeled EGF-, GE11- or untargeted polyplexes and imaged by widefield microscopy. Fluorescence (left image) and transmission light images (TL, central image) of representative cells are shown. Endosomal movements are visualized in time projections of 134 frames (right image, 45 seconds time interval). Polyplexes showing typical intracellular motion are marked with yellow circles. The region of the cell nucleus and the plasma membrane is highlighted by a dashed red line. Scale bar = 10 μ m. (B) Quantification of polyplex internalization after four to six hours of incubation by digital image analysis. Mean internalization values are presented. (N=17-19 cells for each polyplex type). The standard error of the mean (SEM) is represented by error bars. ***P < 0.0001 for GE11 polyplexes compared to untargeted polyplexes.

5.1.4 Uptake pathway

In addition to differences in the internalization kinetics, we evaluated details of the endocytic pathway for GE11- and EGF polyplexes. To this end, we performed colocalization experiments with pathway specific markers¹⁴⁰. Transferrin-Alexa488 was coincubated with Cy5-labeled polyplexes on HuH7 cells as a marker for clathrin-mediated endocytosis. Stably transfected Caveolin-GFP HuH7 cells were used to study the occurrence of caveolin-mediated uptake. Treated cells were imaged three hours post polyplex addition by spinning disk confocal microscopy with alternating laser excitation and dual channel detection to rule out spectral crosstalk of the two labeling dyes. Fluorescence overlay images of both emission channels are shown in figure 5.6 for representative cells. Both, EGF- and GE11 polyplexes showed high colocalization with transferrin as demonstrated by the distinct white signal in the overlay image. Low colocalization with Caveolin-GFP was observed for both polyplex types. Hence, EGF- as well as GE11 polyplexes are predominantly internalized via clathrin mediated endocytosis, seemingly not affected by the replacement of the full-length EGF ligand.

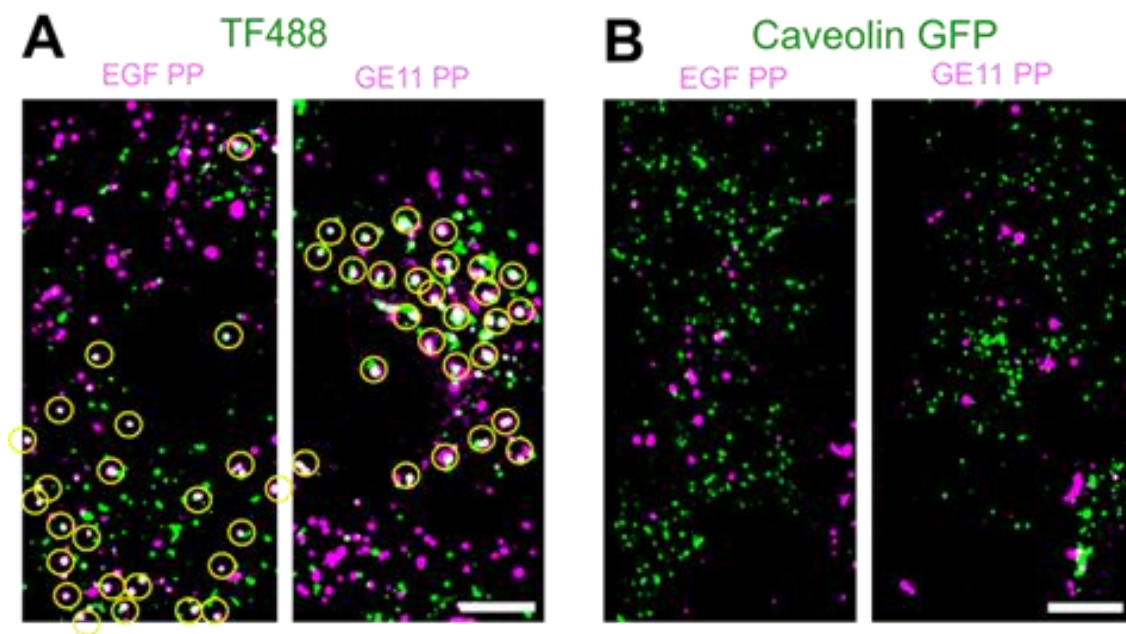


Figure 5.6 Colocalization with pathway specific marker proteins. (A) Transferrin-Alexa488 (green) was coincubated as marker for clathrin mediated endocytosis with EGF- (left side) or GE11 polyplexes (right side, both magenta) onto HuH7 cells. Three hours post polyplex addition z-planes of single cells were imaged by spinning disk confocal microscopy with alternating laser excitation. Fluorescence overlay images of both fluorescent channels are shown for representative cells. Colocalizing endosomes appear in white and are marked with yellow circles. (B) Incubation of polyplexes on HuH7 expressing Caveolin-GFP (green) as a marker for caveolae. Scale bar = 10 μm .

5. RECEPTOR TARGETING OF GENE VECTORS

5.1.5 Receptor signaling activation

It is well known that binding of the full-length EGF ligand to its receptor induces receptor dimerization, autophosphorylation and downstream signaling¹⁰⁵. An important signaling transducer which is stimulated during this cascade is the extracellular signal regulated kinase (ERK). To compare the extent of receptor signaling induced by GE11- and EGF polyplexes, we analyzed the phosphorylation degree of cytoplasmic ERK in polyplex treated cells by western blotting (Fig. 5.7). As positive control for EGFR signaling, cells were treated with free EGF. The resulting blots revealed a clear signal for phosphorylated ERK in the positive control and significantly lower phosphorylation levels in untreated cells and cells treated with untargeted polyplexes. GE11 polyplex treated cells showed less ERK phosphorylation compared to EGF polyplex treated cells. This indicates reduced activation of the EGF receptor signaling cascade after binding of GE11 polyplexes.

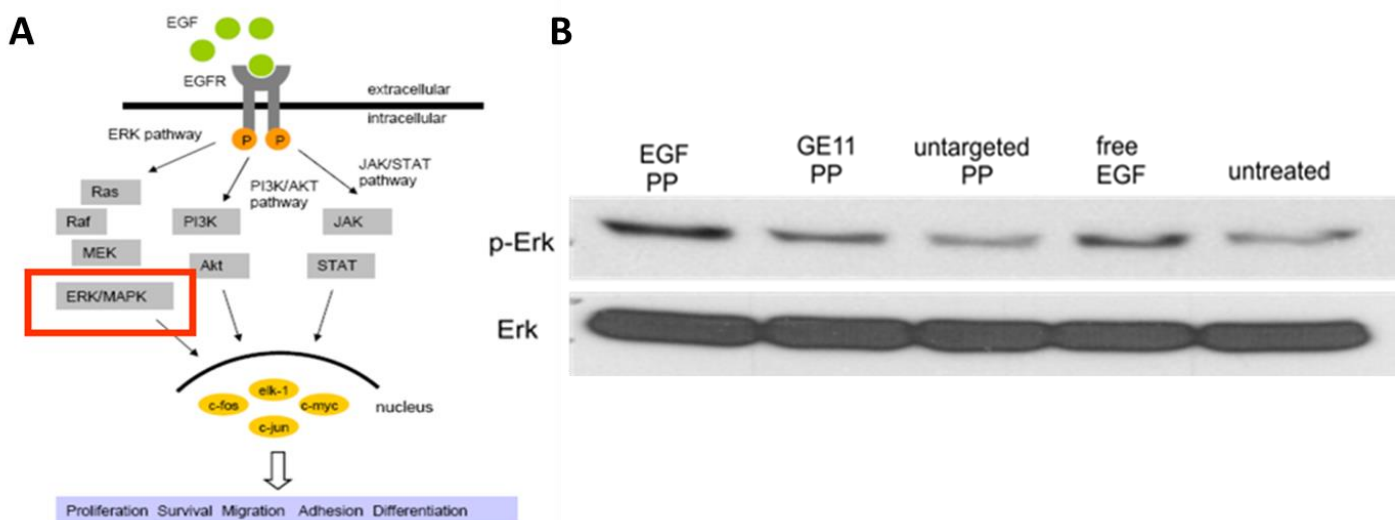


Figure 5.7 EGFR activation after polyplex binding. **A** Schematic illustration of the EGF receptor signaling cascade. **B** Phosphorylation of ERK protein monitored by Western Blotting. HuH7 cells were incubated with EGF- (lane 1), GE11- (lane 2) or untargeted polyplexes (lane 3) for one hour before lysis of the cells. EGF receptor activation was analyzed in the cell lysates using antibodies directed against the phosphorylated and unphosphorylated version of the ERK protein, respectively, which is activated during downstream signaling of the EGF receptor. As positive control, free EGF (lane 4) was incubated on the cells, whereas untreated cells were used as negative control (lane 5).

5.1.6 Correlation between receptor signaling and uptake kinetics

To examine the correlation between activation of receptor signaling and uptake kinetics of polyplexes, we performed an inhibitor assay with AG1478, a drug that specifically blocks the phosphorylation of the EGF receptor³²⁰. HuH7 cells were starved in serum free medium overnight to reduce background activation of the EGF receptor. The next day, cells were preincubated with AG1478 for one hour before addition of EGF-, GE11- or untargeted polyplexes.

5. RECEPTOR TARGETING OF GENE VECTORS

Control cells were kept in serum-free medium without inhibitor treatment. 20 minutes post polyplex addition to cells the internalization efficiency of polyplexes was analyzed. Most strikingly, a strong effect of the inhibitor on the internalization of EGF polyplexes was observed (Fig. 5.8 A). Without inhibitor, EGF polyplexes showed a mean internalization degree of 70 %, whereas in the presence of AG1478 only 22 % mean internalization was reached. Reduced uptake of EGF polyplexes in the presence of AG1478 was also visualized in living cells by widefield-fluorescence microscopy (Fig. 5.8 B). Time projections of the recorded movies clearly demonstrate enhanced retention of EGF polyplexes at the plasma membrane and reduced intracellular transport in presence of the inhibitor. This result reveals that the fast uptake kinetics of EGF polyplexes is coupled to activation of receptor signaling. In contrast, the uptake efficiency of GE11 polyplexes and untargeted polyplexes was not significantly affected by the inhibitor, portending uptake without EGFR activation. Remarkably, the uptake level of GE11 polyplexes without inhibitor matched the uptake level of EGF polyplexes in the presence of the inhibitor (mean internalization values of 24 % and 22 %, respectively) verifying that the internalization kinetics is determined by receptor signaling and not by the binding affinity of the particle.

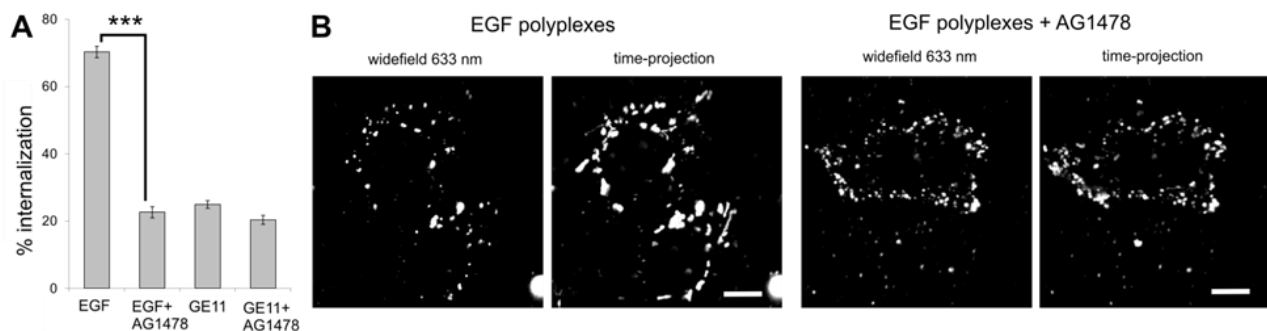


Figure 5.8 Tyrosine kinase inhibitor effect. (A) Serum starved HuH7 cells were treated with AG1478, a specific inhibitor of EGFR phosphorylation, or kept untreated before incubation of the indicated polyplex types for 20 minutes. Mean internalization levels were evaluated by digital image analysis. The standard error of the mean (SEM) is represented by error bars (N=54-63 cells for each data point). ***P <0.0001 for EGF polyplexes with inhibitor treatment compared to EGF polyplexes without inhibitor treatment. (B) Serum starved HuH7 cells were incubated with EGF polyplexes in the presence of AG1478 (right side) or without inhibitor (left side). Cells were imaged by widefield microscopy 35 minutes post polyplex addition. Single snapshots of representative cells as well as time projections of 100 frames (equivalent to a time interval of 33 s) are presented to visualize the localization and motion of the polyplexes. Scale bar = 10 μ m.

5. RECEPTOR TARGETING OF GENE VECTORS

5.1.7 Effect of serum starvation

As published by Song et al., serum starvation of cells interrupts connections between the EGF receptor and the actin cytoskeleton of the cell³²¹. We therefore additionally tested the effect of starvation on the uptake efficiency of EGF and GE11 polyplexes on a longer time scale. Cy5-labeled polyplexes were incubated on serum-supplemented or serum-starved cells for four to six hours prior to analysis. Surprisingly, we observed a significant effect on the uptake of GE11 polyplexes (mean internalization degree with serum 65 %, without serum 40 %) but not on the uptake of EGF polyplexes (Fig. 5.9 A, 5.9 B). Polyplexes without a targeting ligand were also not affected by the starvation. Remarkably, in starved cells GE11 polyplexes showed comparable internalization as untargeted polyplexes, whereas in non-starved cells GE11 polyplexes reached similar internalization levels as EGF polyplexes. These data suggest that GE11 induced uptake of polyplexes requires pre-existing connections of the EGFR to the actin cytoskeleton, whereas EGF is able to trigger new connections to the cytoskeleton after receptor binding, resulting in fast polyplex endocytosis. The different mechanisms proposed for the uptake of EGF- and GE11 polyplexes are summarized in figure 5.10.

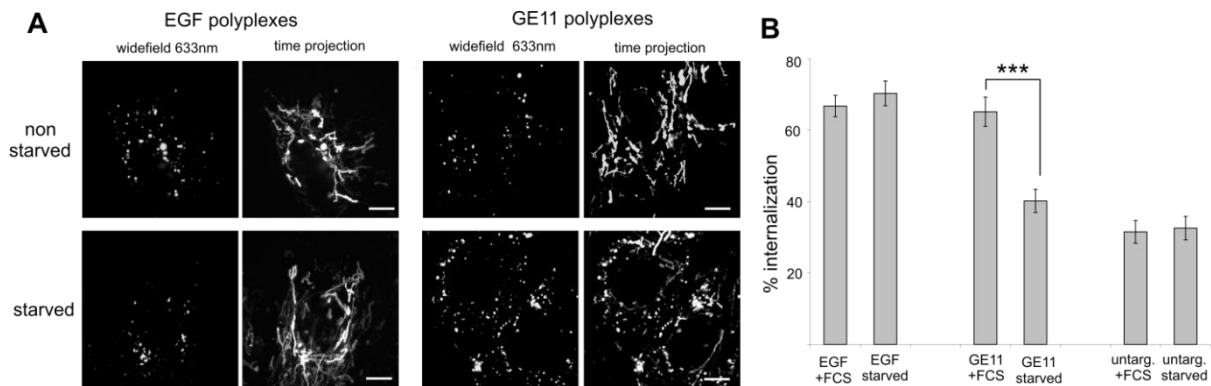


Figure 5.9 Effect of serum starvation. (A) EGF- and GE11 polyplexes were incubated on non-starved (upper row) or starved cells (FCS depletion for 16-18 hours, lower row) for four hours and imaged by widefield fluorescence microscopy. Single snapshots (left image) as well as time projections of 100 frames (right image, 33 seconds time interval) are shown. Scale bar = 10 μ m. **(B)** Quantification of the serum effect. EGF-, GE11- and untargeted polyplexes were incubated on starved (FCS depletion for 16-18 hours) and non-starved cells for 4-6 hours before imaging with spinning disk confocal microscopy. Mean internalization efficiencies were evaluated by digital image analysis. The standard error of the mean (SEM) is represented by error bars. (N=15-19 cells for each polyplex type), ***P < 0.0001 for GE11 polyplexes with FCS compared to GE11 polyplexes without FCS.

5.1.8 Discussion

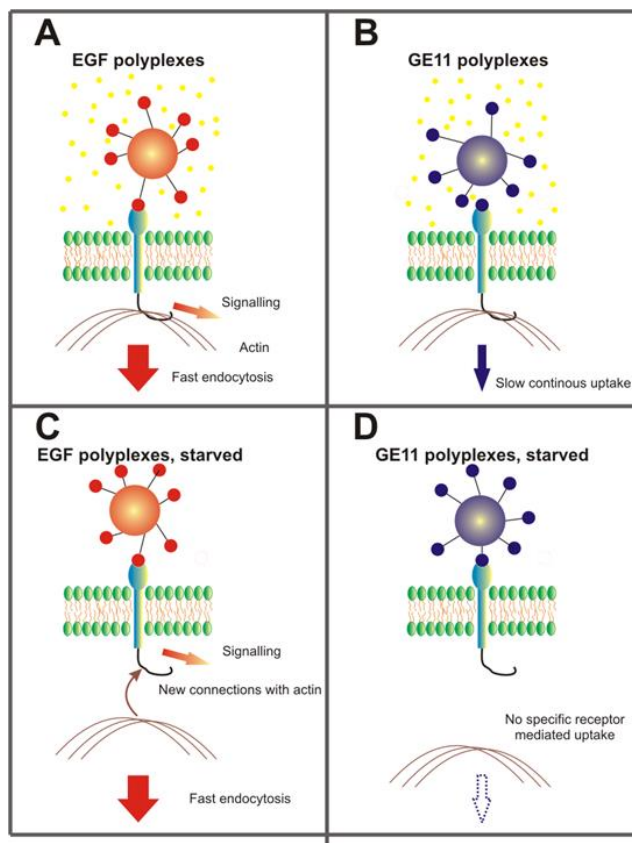


Figure 5.10 Schematic illustration of the proposed uptake mechanism of EGF- and GE11 polyplexes. (A, C) EGF polyplexes (red particle) bind to the EGFR (blue) on the plasma membrane. The EGF ligand induces downstream signaling triggering the fast clathrin-mediated endocytosis of the polyplex. In the absence of transient connections between the EGFR and actin (starved cells, **C**) new linkages are induced by signaling activation. **(B, D)** GE11 polyplexes (blue particle) bind the EGFR without subsequent signaling activation resulting in slower uptake compared to EGF polyplexes. The receptor-dependent uptake is mediated by transient connection between the EGFR and actin in serum-supplemented cells (**B**) and is inhibited in starved cells (**D**).

In the present study we unraveled the mechanism of EGF receptor mediated internalization of polyplexes decorated with different EGFR ligands. By applying highly sensitive fluorescence microscopy in combination with our recently developed digital image analysis method, we gained precise quantitative data on time-dependent polyplex internalization. Our data reveal that the uptake kinetics of polyplexes is strongly influenced by the applied targeting ligand. EGF polyplexes with natural full-length EGF showed extraordinary fast endocytosis reaching up to 80 % internalization in the first 10 minutes of polyplex incubation consistent with earlier studies³¹⁰. GE11 polyplexes equipped with an artificial peptide ligand reached 40 % internalization in the same time interval whereas without any targeting less than 20 % internalization was detected. Remarkably, after four hours of incubation, GE11 polyplexes reached same internalization levels as EGF polyplexes (mean internalization degree of 67 % and 65 %, respectively), whereas untargeted polyplexes showed

5. RECEPTOR TARGETING OF GENE VECTORS

significantly higher membrane retention (only 31% internalization). It should be noted that EGF polyplexes contained lower ligand density than GE11 polyplexes because of the higher aggregation tendency of full-length EGF, however the present EGF concentration was sufficient to mediate efficient receptor binding and uptake of the particles.

We demonstrate that the fast kinetics of EGF polyplex uptake is mediated by activation of receptor signaling, whereas the slow internalization of GE11 polyplexes occurs without considerable receptor activation. Inhibition of receptor phosphorylation by the specific tyrosine kinase inhibitor AG1478 reduces the uptake level of EGF polyplexes to the level of GE11 polyplexes. Furthermore, we observed a strong effect of serum starvation on the internalization of GE11 polyplexes, but not on the uptake of EGF polyplexes. These data suggest the existence of two different uptake modes for EGFR targeted polyplexes, regulated by the targeting ligand.

It is well known that binding of free EGF to the EGFR induces receptor dimerization, followed by subsequent receptor phosphorylation and activation of down-stream signaling promoting cell proliferation, survival, adhesion, migration and differentiation^{104, 105}. To terminate receptor signaling, the receptor-ligand complex is internalized into clathrin coated vesicles and transported to lysosomal compartments¹⁰⁶. Our data suggest that particle-conjugated EGF stimulates the same process involved in the internalization of free EGF, triggering the accelerated endocytosis of the conjugated payload (Fig. 5.10 A). This is supported by (i) our observation of ERK phosphorylation after incubation of cells with EGF polyplexes, (ii) the retarded uptake of EGF polyplexes in the presence of a tyrosine kinase inhibitor and (iii) the colocalization of EGF polyplexes with markers for clathrin-dependent endocytosis. The dual active role of the EGF ligand in EGFR docking and activation of receptor signaling as responsible event for accelerated uptake might present an added value in drug carrier design in a broader context for targeting of non-malignant cell types, but not in cancer applications because of the stimulation of undesired cell proliferation.

Much less is known so far about the uptake mechanism of artificial ligands for EGFR targeting such as antibodies and peptides. A number of studies have demonstrated the positive effect of artificial EGFR ligands on gene or drug delivery, however the underlying mechanism remained unclear^{311, 312, 322}. Here we show by combination of live-cell imaging with biological assays such as western blotting, tyrosine kinase inhibition and serum starvation that GE11 polyplexes are internalized via a clathrin-dependent uptake mechanism that occurs with slower kinetics, without EGFR signaling and depends on the presence of serum proteins (Fig. 5.10 B, D). It is known that in the absence of serum proteins, connections between the EGFR and the actin cytoskeleton are missing³²¹. New linkages between the EGFR are induced by receptor signaling¹¹⁰ and actin reorganization is postulated to be an important requisite for endosome formation¹⁰⁹. We therefore propose that the constant endocytosis of GE11 polyplexes is mediated by pre-existing linkages between EGF receptor and actin which are induced by stimulating agents in the serum supplement.

5. RECEPTOR TARGETING OF GENE VECTORS

A recent study with radiolabeled cetuximab, an EGFR-directed therapeutic antibody, described its slow internalization into cancer cells, similar to the uptake kinetics observed by us for GE11 polyplexes³²³. These results indicate that artificial EGFR binding ligands, such as antibodies and GE11 peptide, which are not evolutionary optimized for signal transduction, might utilize a common alternative uptake pathway mediated by non-activated EGF receptors as described above.

From our mechanistic study on the single cell level together with previously published ensemble data on GE11 polyplexes, several conclusions can be drawn on potential advantages of the peptide ligand GE11 for clinical application:

(i) GE11 polyplexes undergo efficient clathrin-mediated endocytosis and transport to the perinuclear region between one and four hours of incubation suggesting their high transfection potential. Consistently, we recently demonstrated high transgene expression induced by GE11 polyplexes in several cancer cell lines, comparable to expression levels induced by EGF polyplexes^{314, 315}. The retarded uptake of GE11- compared to EGF polyplexes thus does not seem to have a negative effect on transfection. The detected transgene expression correlated to EGFR levels on the cells, demonstrating specificity of GE11 polyplexes for EGFR targeting^{315, 316}.

(ii) We demonstrate that efficient uptake of GE11 polyplexes occurs without EGFR signaling activation using an alternative actin-dependent pathway. The reduced mitogenic signaling of the GE11 peptide displays a crucial benefit for cancer treatment *in vivo*, as the stimulation of cancer cell proliferation is circumvented.

(iii) Recently, we demonstrated that the EGFR level on the surface of cancer cells remains constant after treatment with GE11 polyplexes indicating a recycling process³¹⁴. In contrast after treatment with EGF polyplexes, the EGFR level is quickly reduced. Increased surface levels of the EGFR during treatment with GE11 polyplexes might enable prolonged receptivity of the cells for circulating polyplexes improving the targeting effect *in vivo*.

(iiii) Due to the small ligand size and the reduced hydrophobicity of the GE11 ligand, polyplexes with low aggregation properties and high ligand densities can be formed that are well-suited for up-scaled production and *in vivo* application. In fact, we obtained promising results with GE11 polyplexes in tumor bearing mice, showing successful gene therapy of solid tumors after systemic polyplex administration^{315, 316, 324}.

Taken together, we conclude from our mechanistical study that the alternative EGFR-mediated delivery of nanocarriers with artificial targeting peptides represents a promising strategy for efficient cancer treatment without side-effects from mitogenic signaling.

5.2 Influence of ligand density and dual targeting

5.2.1 Particle design

Targeting ligands on the surface of polyplexes encounter for receptor mediated uptake, but not much is known about the critical ligand concentration that is required for enhanced uptake. To enlighten the influence of ligand density on particle internalization, we quantified the uptake efficiency of transferrin receptor-targeted polyplexes and integrin-targeted polyplexes with different ligand densities by confocal microscopy combined with a digital image analysis routine.

For the experiments, PEGylated PEI polyplexes with covalently attached peptidic targeting ligands were applied to DU145 prostate cancer cells with high levels of integrin and transferrin receptor expression³²⁵. An arginine-glycine-aspartic acid (RGD) containing peptide was incorporated for integrin targeting, whereas the B6 peptide was applied for transferrin receptor targeting. To vary the ligand density on the particle surface, different ratios of untargeted and targeted polymer were mixed during the self-assembly process (e.g. 10 % RGD-PEG-PEI polymer was mixed with 90 % PEG-PEI polymer to obtain polyplexes with 10 % ligand density).

Motivated by the biphasic mechanism viruses enter the cell, a number of studies deal with the idea of using two different ligands for receptor targeting of polyplexes to enhance their specific binding and uptake efficiency³²⁵⁻³²⁷. These studies postulate that one ligand mediates cell attachment of the particles whereas the second ligand induces internalization. To additionally investigate the effect of dual targeting on the uptake efficiency, we incubated polyplexes carrying RGD- and B6 ligands in a 1:1 mixture on DU145 cells.

5.2.2 Quantifying the uptake efficiency from confocal images

The uptake efficiency of polyplexes was determined after an incubation time of 40 minutes on DU145 cells. To guarantee a defined incubation time, cells were fixed in 4 % paraformaldehyde. To identify the membrane region of the cell, the membrane was stained with CTB-488. Z-stacks of single cells were imaged by spinning disk confocal microscopy with alternating laser excitation. Next, nanoparticles in the membrane region and in the intracellular region were quantified using the ImageJ-macro "Nano-In-Cell-3D" developed by Adriano Torrano and Julia Blechinger³²⁸. The macro determines the cell volume by following the stained membrane from the top to the bottom of the cell using a masking strategy. In a next step an intensity threshold for particles and the width of the membrane region is entered. The macro then assigns whether identified particles are inside or outside the cell or in the membrane region by overlying the membrane and the particle images.

5. RECEPTOR TARGETING OF GENE VECTORS

By analyzing the integrated fluorescence intensity of particles/endosomes in the membrane region and inside the cell the uptake efficiency can be determined:

$$\text{Uptake efficiency} = \frac{\text{Integrated fluorescence intensity in intracellular region}}{\text{integrated fluorescence intensity (membrane region+intracellular region)}}$$

In figure 5.11 a color coded z-stack of a representative DU145 cell is presented, in which the membrane region is depicted by a yellow line, intracellular polyplexes are shown in green, membrane associated particles are marked in blue and extracellular particles appear in white.

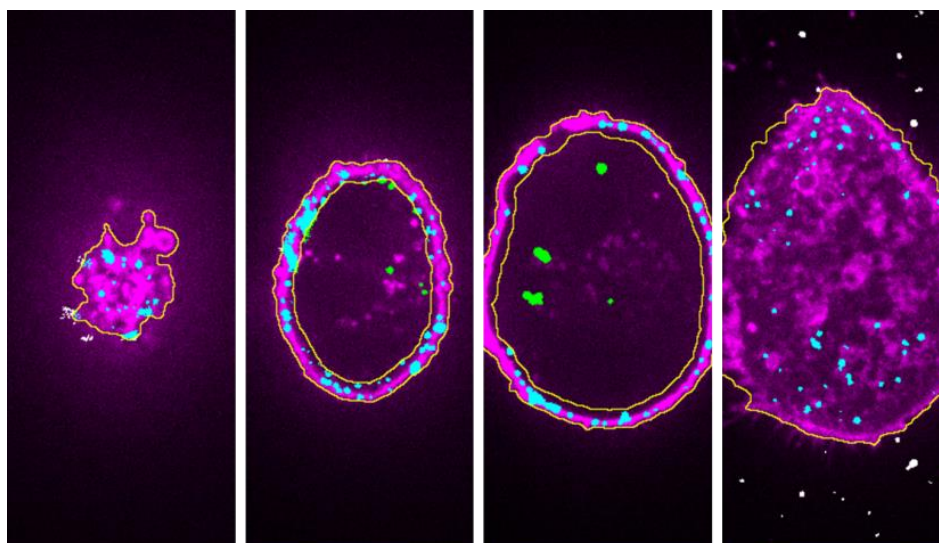


Figure 5.11 Analysis of spinning disk confocal images by the ImageJ macro Nano_In_Cell_3D. Z-slices of a representative DU145 cell treated with dual-targeted polyplexes are presented. The cell membrane was stained with CTB-488 after formaldehyde fixation (magenta label). By using the macro the membrane region of the cell was determined (yellow lines) and membrane bound particles (blue label), intracellular particles (green label) and extracellular particles (white label) were distinguished.

Results from quantification of polyplex uptake are shown in figure 5.12. The calculated uptake efficiencies were plotted against the ligand density on the particle.

For transferrin receptor-targeted polyplexes with B6 ligand a linear increase in the uptake efficiency was observed from 5 % to 30 % ligand density until saturation was reached and the uptake efficiency remained constant for higher ligand concentration (Fig. 5.12 A). Data were approximated by asymptotic fitting ($y = a - bc^x$). It should be noted that particle aggregation was induced when ligand concentrations exceeded 60 %; therefore these particles were not included in the analysis. Our data suggest that the optimal concentration of B6-equipped polymers for transferrin receptor targeting lies around 30 %.

For integrin-targeted polyplexes the dependency of the uptake efficiency on the ligand density did not

5. RECEPTOR TARGETING OF GENE VECTORS

seem to follow simple saturation but a more complex kinetics (Fig. 5.12 B). At low ligand concentration (5-20 %) the uptake efficiency was not significantly affected by increasing ligand densities. Between 20 % and 50 % ligand concentration the uptake efficiency of polyplexes increased reaching a plateau level. Data could be fitted using a hill-like function. Our data indicate that a critical number of integrins are required to induce endocytosis of the nanoparticles; around 50 % of targeted polymer should be applied to achieve optimum polyplex internalization.

For dual-targeted polyplexes, a saturation curve was observed similar to B6 targeted polyplexes. Notably, the maximum uptake efficiency of dual targeted polyplexes (25 % internalized particles) did not reach the level of single targeted polyplexes (35 % and 45 % uptake for B6 polyplexes and RGD polyplexes respectively) (Fig. 5.12 C).

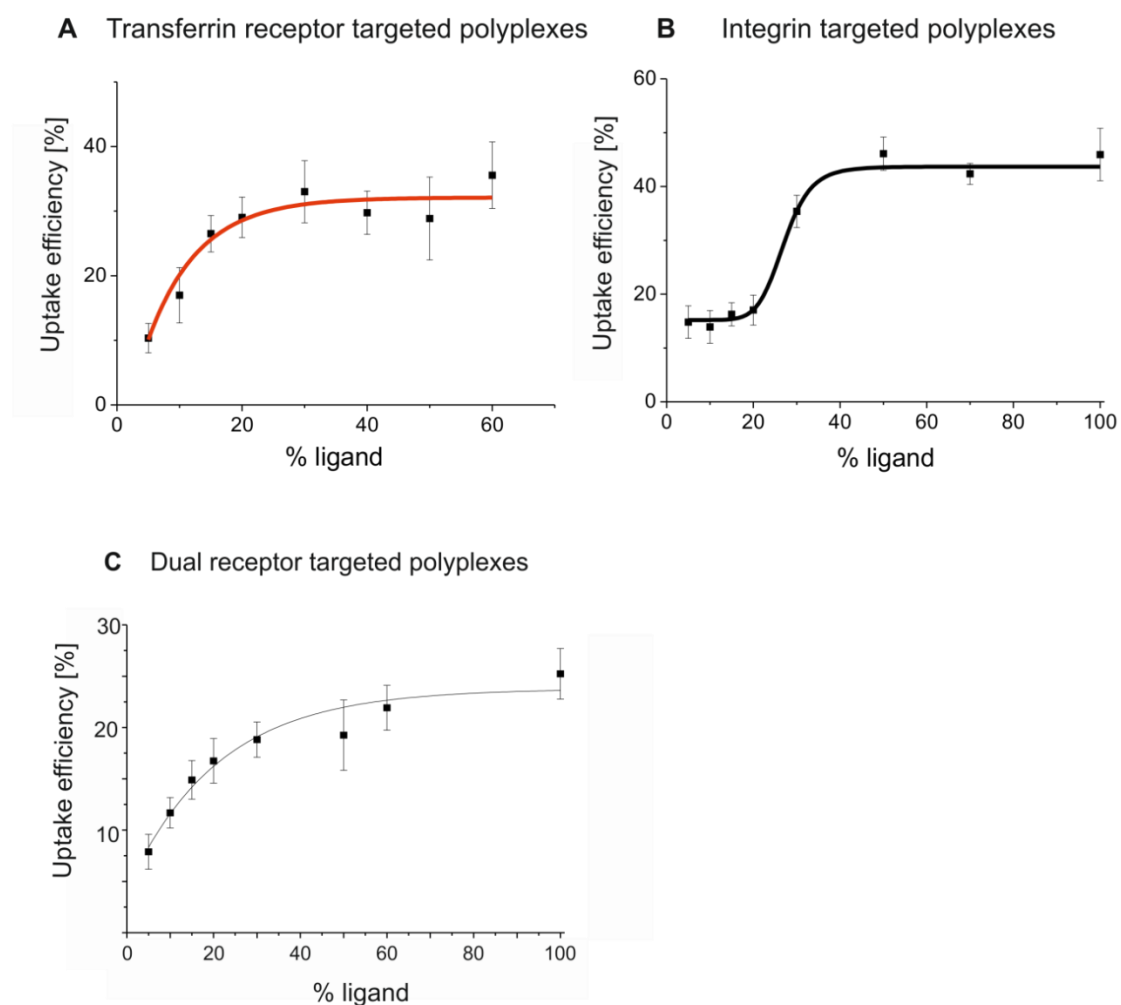


Figure 5.12 Internalization efficiencies of polyplexes dependent on ligand density. Polyplexes were incubated on DU145 cells for 40 minutes followed by formaldehyde fixation and membrane staining. Subsequently, cells were imaged by spinning disk confocal microscopy and polyplex internalization was evaluated by the digital image analysis routine Nano_In_Cell_3D. The percentage of internalized particles is plotted versus the ligand density for transferrin receptor-targeted polyplexes with B6 ligand (A), integrin-targeted polyplexes with RGD ligand (B) and dual-targeted polyplexes with a 1:1 mixture of RGD and B6 ligands (C). n= 9-15 cells per data point, mean values are presented; the standard error is presented in error bars.

5.2.3 Discussion

To create targeted polyplexes for specific gene delivery that provide high uptake efficiencies, moderate production costs and low aggregation, the ligand density on the particle surface should be optimized.

The uptake efficiency of targeted particles is most likely determined by the probability of receptor binding and the kinetics of receptor mediated particle endocytosis. When receptor-ligand interactions are weak, dissociation of the receptor-ligand complex can take place before endocytosis is induced. Furthermore, positively charged nanoparticles with insufficient shielding can exhibit additional interactions with negatively charged cell surface molecules and be internalized by alternative receptor-independent endocytosis pathways. We propose that by increasing the number of ligands the possibility of receptor binding is enhanced and thereby the probability of receptor mediated particle internalization increases. Above a certain ligand level, further elevation of ligand density does not lead to additional receptor-ligand interactions; therefore the uptake kinetics of particles with rather high ligand concentration is saturated. Using high ligand concentration above the saturation level can have negative side effects such as enhanced particle aggregation and increased production costs. We suggest that our method can be applied to determine the saturation level of ligands to optimize the concentration of targeted polymer in the production process.

Integrins are known to be activated by a clustering mechanism¹³¹. In this case, a higher ligand concentration on the particle surface might be required for multiple receptor binding. Sancey et al. revealed that single RGD fails to induce integrin internalization whereas tetrameric RGD constructs induce integrin clusters and efficient clathrin-dependent integrin endocytosis²⁹⁴. The low internalization of RGD polyplexes at low ligand density might therefore be explained by ineffective receptor clustering. The effect of integrin clustering on the endocytosis of gene vectors has to our knowledge not been investigated in detail so far. Therefore it might be of interest to further analyze the diffusion and localization of labeled integrins in the membrane and their interaction with RGD-equipped nanoparticles with more sensitive methods to gain improved mechanistical insights in the future. Our experiments with dual targeted polyplexes indicated reduced uptake efficiencies of membrane bound polyplexes with two targeting ligands compared to single targeted polyplexes. A recent study with dual targeted polyplexes by Nie et al. suggested that the RGD ligand mediates membrane binding of particles, whereas the transferrin receptor is responsible for particle uptake³²⁵. In this scenario the RGD ligand would enhance the number of membrane bound particles that are available for transferrin receptor mediated endocytosis. The uptake kinetics of the bound particles should resemble the kinetics of single targeted B6 polyplexes. In accordance to this hypothesis we observed a similar saturation curve for dual targeted polyplexes and transferrin receptor targeted polyplexes. The reduced uptake levels of dual targeted polyplexes observed in our measurement indicate that the RGD ligand might interfere with the transferrin receptor binding. However, more experiments are required to explain this effect.

5. RECEPTOR TARGETING OF GENE VECTORS

In our experiments we observed similar attachment of all particle types to the plasma membrane, few particles detached after membrane binding or were observed swimming in the cell medium. The cellular attachment of polyplexes with residual positive charge seemed to be dominated by electrostatic interactions rather than by receptor binding. However, when using particles with increased shielding or negative surface charge, an enhanced effect of dual targeting might be observed. We assume that the combination of two ligands may have additional positive effects on intracellular trafficking and endosomal release of particles. Previous studies described improved transfection efficiencies of dual-targeted polyplexes, however further experiments are required to dissect the underlying mechanism.

We suggest to perform additional live-cell imaging studies (e.g. cellular attachment under flow conditions, analysis of the uptake pathway, intracellular trafficking and endosomal release) to understand the mechanism by which the second ligand improves the gene delivery process.

5.3 Receptor targeting under flow

5.3.1 Microfluidic set-up

Most *in vitro* experiments on the adhesion and internalization of gene vectors are performed under static conditions. However *in vivo* many cells are subjected to perfusion, e.g. endothelial and smooth muscle cells in blood vessels, renal tubular cells³²⁹, osteocytes from bone canaliculi³³⁰, hepatic cells from bile canaliculi³³¹ or metastatic cancer cells.

Cells can experience different types of fluid flow. Cells from small arteries and veins are exposed to constant laminar flow. Pulsatile flow with periodically changing flow rates is induced by the heartbeat in large arteries. At branching sites of blood vessels non-uniform flow occurs.

The friction of liquid against the plasma membrane of cells induces shear stress. The shear stress ranges from 0.5 dyn/cm² in small arteries to 20 dyn/cm² in the aorta. The mechanical stimulus has large impact on the adhesion and physiology of cells. It can induce rearrangement of the cytoskeleton³³² as well as changes in metabolism and gene expression³³³.

To study nanoparticle-cell interactions under shear stress, cells can be grown in microfluidic channels that are commercially available with different geometries and coatings. Different pump systems can be applied to create a directed, laminar flow. Flow can also be induced by acoustic streaming on a surface acoustic wave device³³⁴.

Adhesion of nanoparticles under flow conditions can significantly alter to adhesion under static conditions. Dispersed nanoparticles in fluids are generally subjected to the gravitation field and drag forces. Particle deposition to cells depends on the diffusion velocity and the sedimentation of the particles and is determined by the density of the particle, the density of the medium and the particle size³³⁵. Hinderliter et al revealed that the transport of small nanoparticles below 10 nm is dominated by diffusion, whereas above 100 nm sedimentation plays an increasing role³³⁶.

Under flow conditions particles migrate with the induced stream; their local velocity depends on the applied flow rate and the channel geometry. A typical flow profile in a unilaminar channel is depicted in figure 5.13. The flow velocity shows a parabolic shape in z-direction, with low flow velocities close to the channel wall and maximum velocity in the center of the channel.

5. RECEPTOR TARGETING OF GENE VECTORS

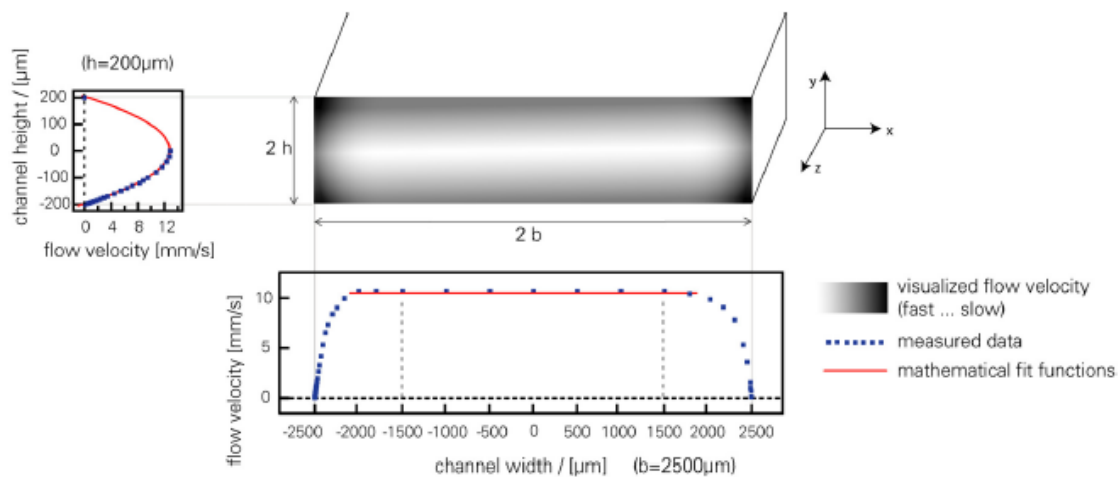


Figure 5.13 Flow profile of a unilaminar microfluidic channel with 0.4 mm height and 5 mm width. The flow profile in the channel is characterized by a parabolic shape in y-direction. (Source: Ibidi GmbH, application note 11)

We tracked the movement of fluorescently-labeled beads at different z-positions in a microfluidic channel. For the experiments a surface acoustic wave (SAW) driven microfluidic device was used, provided by the group of Prof. Achim Wixforth from Augsburg University. To detect an adequate number of steps for each particle, images were acquired at a frame rate of 35 ms and a maximum local flow velocity of 150 $\mu\text{m/s}$ (at 200 μm height) was set during the measurement. The obtained trajectories revealed that close to the channel wall the particles show typical Brownian, non-directed motion (2 μm height). 5 μm above the channel wall the random walk was superimposed by the external flow resulting in directed, but tumbling particle motion. 85 μm above the channel fast directed motion of the particles without tumbling was observed (Fig. 5.14).

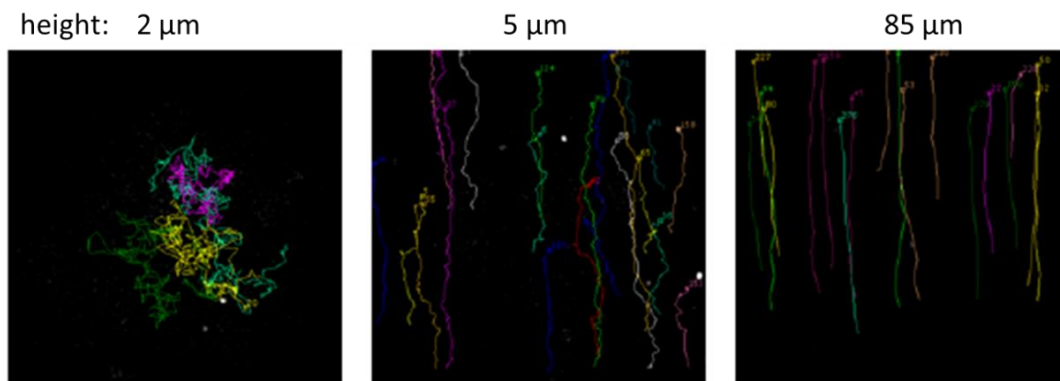


Figure 5.14 Particle trajectories in a microfluidic channel. The movement of fluorescent-dye labeled 0.17 μm beads under flow was recorded at a frame-rate of 35 ms by widefield-microscopy at different height in a surface-acoustic wave driven microfluidic channel (images from left to right: 2 μm , 5 μm and 85 μm above the bottom). Trajectories of single particles are presented. Image size = 61 μm x 61 μm .

5. RECEPTOR TARGETING OF GENE VECTORS

In addition to the surface acoustic wave driven (SAW) microfluidic device we set up a second syringe pump driven microfluidic device (with commercially available components) during our study. The syringe pump allows a broad range of flow rates and different operation modes (oscillating flow, constant unilaminar flow, pulsatile flow) and is more flexible compared to the SAW device. Furthermore the syringe pump can be connected to commercially available Ibidi Cell Culture Channels. These channels are easily assembled, show high stability and allow efficient cell growth and convenient exchange of medium. Furthermore multichannel systems are available for parallel screening experiments and the flow profile in the available channels is well characterized. Therefore the following flow experiments were performed with the syringe pump driven microfluidic system. The applied microfluidic setup is depicted in figure 5.15.

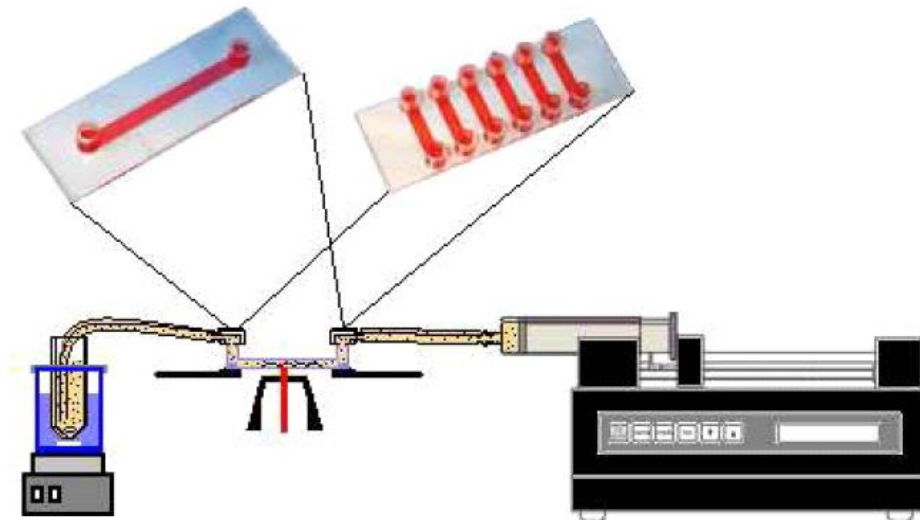


Figure 5.15 Schematic illustration of the syringe pump driven microfluidic system. Particles were suspended in cell medium and added to a heated reservoir on a magnetic stirrer. The flow chamber (single- or multi channel slides from Ibidi GmbH) was connected to the reservoir and an engine driven syringe pump by flexible tubes. By starting the pump a laminar flow with defined flow rate is generated and the particle solution passes through the microfluidic channel into the syringe. The picture was kindly provided by Ellen Broda.

To study nanoparticle adhesion to cells or physiological surfaces, fluorescent-dye labeled nanoparticles were added to a reservoir with cell medium that was heated to 37 °C and stirred to promote homogenous nanoparticle dispersion. Next the motor driven syringe pump was turned on to flush the nanoparticle solution through flexible tubes into the microfluidic channel with cultivated tumor cells or selected surface coating. Constant flow of 2 ml/minutes (equivalent to a shear stress of 2.6 dyn/cm² in the applied Ibidi Luer μ -slides l^{0.4} with 0.4 mm height and 5 mm width) was applied in our experiments. At defined time points selected regions were imaged by widefield fluorescence microscopy.

5. RECEPTOR TARGETING OF GENE VECTORS

In figure 5.16 exemplary images of representative cells are shown that reveal the time-dependent cellular adhesion of nanoparticles under flow. To quantify nanoparticle adhesion, particles were identified by digital image analysis using an intensity threshold criterion and size restriction.

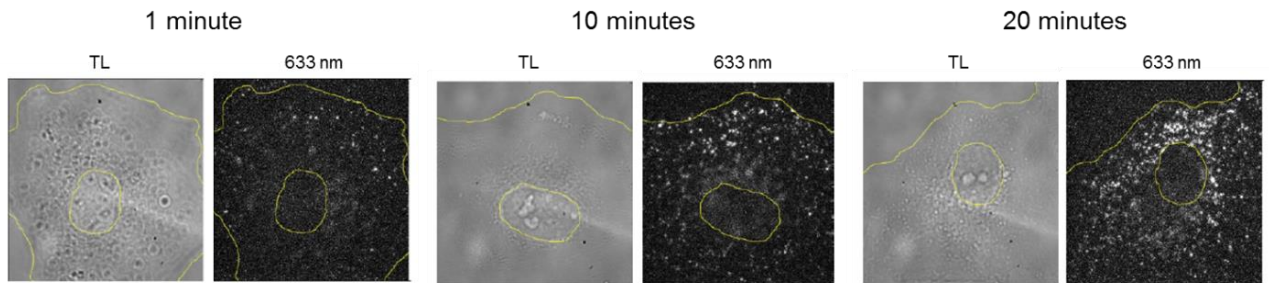


Figure 5.16 Cellular attachment of polyplexes under flow. HuH7 cells in a microfluidic channel were subjected to Cy5-labeled PEG-PEI polyplexes at flow rate of 2 ml/min (flow was generated by a motor-driven syringe pump). Polyplex attachment was detected at a given time by 633 nm laser excitation (from left to right: 1 minute, 10 minutes and 20 minutes incubation). Fluorescence images of representative cells are shown together with the transmission light image of the respective cell, the region of the nucleus and the plasma membrane is marked by a yellow line. Polyplex attachment clearly increases with time

5.3.2 Influence of PEG shielding on polyplex adhesion under flow

With the established microfluidic device we first studied the effect of PEGylation on the adhesion of untargeted polyplexes to collagen, the most abundant molecule of the extracellular matrix, as well as non-specific polyplex binding to HuH7 cancer cells.

In our experiments we compared PEI polyplexes with 2 kDa PEG (PEG2-polyplexes) and 20 kDa PEG (PEG20-polyplexes). Polyplexes were formed by self-assembly of negatively charged plasmid DNA and the cationic polymer prior to the experiment. The assembly process is influenced by many variables such as polymer composition, temperature and incubation time. We realized that the number, size and fluorescence intensity of formed polyplexes can vary significantly between different samples. Therefore careful controls are required to compare the adhesion of two different polyplex samples under flow. To estimate the number of polyplexes that were initially applied to the reservoir of the microfluidic channel, we took a control sample in each experiment: A defined volume of this control sample was pipetted into a collagen coated Labtek well and the number of sedimented particles on the coverslip was counted at a set time-point. According to the control number, the detected number of bound polyplexes in the microfluidic channel was the normalized.

In figure 5.17 our data on the time-dependent adhesion of PEG2- and PEG20- polyplexes to a collagen surface (A) and to HuH7 cells (B) is presented. Each data point corresponds to the normalized number of detected polyplexes from one field-of-view at a defined point of time. Our data reveal a clear effect of the implemented PEG shielding on polyplex adhesion under flow. At all times particles with 20 kDa PEG showed reduced adhesion to both collagen and HuH7 cells, compared to

particles with 2 kDa PEG. This result suggests that electrostatic interactions diminish in the presence of longer PEG, which would be advantageous for *in vivo* application of polyplexes. Next to electrostatic interactions, the size of the polyplexes might also influence their adhesion. Polyplexes with longer PEG showed reduced sizes in general which may contribute to reduced sedimentation in the flow channel and therefore reduced particle deposition to the cell surface or collagen. Notably for cell-binding a higher spread of the data-points was observed compared to collagen binding indicating that cell-specific factors such as the cell morphology or surface molecule expression, influence nanoparticle adhesion.

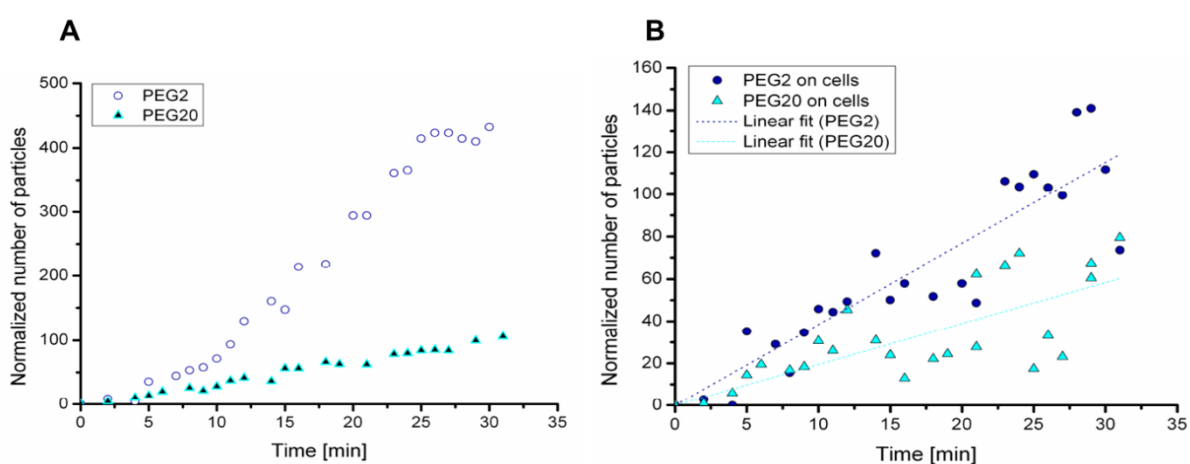


Figure 5.17 Adhesion of PEG2 and PEG20 polyplexes under flow. The adhesion of labeled PEG2 polyplexes and PEG20 polyplexes to (A) collagen and (B) HuH7 cells was monitored by widefield-fluorescence microscopy over 30 minutes (flow rate = 2 ml/min). Particles were quantified by digital image analysis using an intensity threshold and size restriction criterion and their number was normalized according to an external control. In the presence of longer PEG, particle adhesion to collagen and HuH7 cells was reduced.

5.3.3 EGF receptor-targeted polyplexes under flow

In chapter 5.1, we studied the internalization of EGF receptor-targeted polyplexes with 2 kDa PEG into HuH7 cancer cells under static conditions. We demonstrated that the full-length EGF ligand modifies the uptake kinetics of polyplexes, promoting fast receptor-dependent polyplex internalization, whereas untargeted polyplexes exhibit slow uptake. The positive effect of ligand installation on the transfection efficiency of EGF-PEG2-polyplexes was confirmed by other *in vitro* and *in vivo* studies.

To analyze if the EGF ligand promotes the adhesion of polyplexes to EGFR expressing cancer cells, we compared the binding of EGF-equipped and untargeted polyplexes in our microfluidic flow chamber. Experiments were performed analogue to the previously described flow experiments. Figure 5.18 depicts the adhesion kinetics of EGF-PEG2 and PEG2 polyplexes within 30 minutes under flow conditions (flow rate = 2 ml/minutes; shear stress = 2.6 dyn/cm²). Unexpectedly, similar normalized particle numbers were detected in the first 20 minutes of incubation. Within 20 to 30 minutes of incubation only a slight increase in particle adhesion could be observed for the EGF polyplexes.

5. RECEPTOR TARGETING OF GENE VECTORS

Additional experiments were performed after 1.5 hours of incubation, also here only a low effect of the EGF ligand within one magnitude was observed (data not shown). These results suggest that the cellular adhesion of PEG2-polyplexes is dominated by non-specific interactions and not by receptor-ligand interactions.

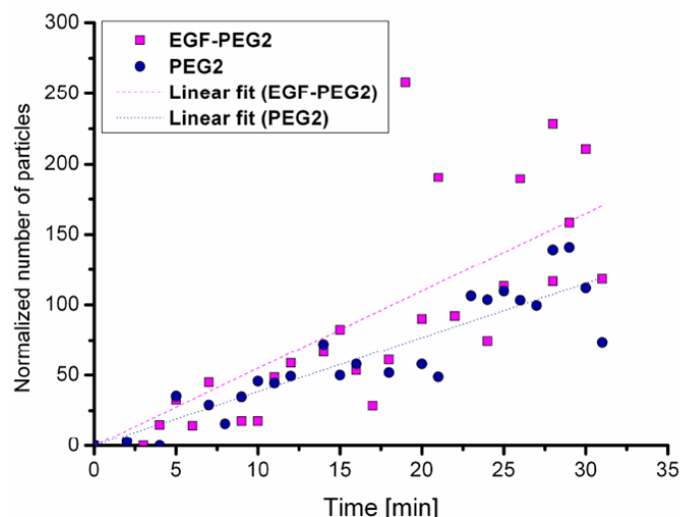


Figure 5.18 Cellular attachment of EGFR-targeted and untargeted polyplexes under flow. HuH7 cells in a microfluidic channel were subjected to EGF-PEG2 polyplexes (magenta squares) or untargeted PEG2 polyplexes (blue circles) for 30 minutes under flow conditions (2ml/min flow rate). The kinetics of particle attachment was followed by widefield-fluorescence microscopy. Each data point represents the normalized number of polyplexes bound to a single cell. Data were approximated by linear fitting.

5.3.4 Discussion

In this study a microfluidic device was successfully established that allows the detection of nanoparticle interactions with cells and physiological biomolecules at different shear rates.

In a first set of flow-experiments we evaluated the adhesion of untargeted polyplexes with different PEG shielding to collagen and to HuH7 cancer cells. We revealed that polyplexes with 2 kDa PEG show strong adhesion to collagen. *In vivo* this interaction may lead to strong retention of polyplexes in the extracellular matrix. The polyplex binding to collagen could be reduced by elongation of the PEG linker (20 kDa PEG). Polyplexes with 20 kDa PEG also exhibited reduced non-specific binding to HuH7 cancer cells compared to polyplexes with 2kDa PEG.

In a second set of experiments the adhesion of EGFR-targeted polyplexes and untargeted polyplexes with 2 kDa PEG to EGFR overexpressing HuH7 cancer cells was compared. Unexpectedly the EGF ligand had only low effect on the binding of polyplexes to HuH7 cells; the unspecific electrostatic interactions of the positively charged polyplex core seemed to dominate the adhesion process. Consequently, as a next step it would be of interest to monitor cell adhesion of targeted particles with

reduced surface charge under flow conditions. One possibility would be to use targeted polyplexes with long 20 kDa PEG linkers for these experiments.

However, we learned from our first microfluidic experiments that calibration of the experiments with self-assembly polyplexes is very challenging. The number and size of the polyplexes varies for each polyplex batch and aggregation of polyplexes can be induced over time in the cell medium. Implementation of longer PEG molecules or targeting ligands can affect the self-assembly process resulting in altered polyplex structure, DNA packaging and surface charge. The attachment of particles to cells under flow however is affected by each of these variables. The particle size and density determines the diffusion and sedimentation velocity of particles. The probability of cell surface binding increases with the number of deposited particles and additionally depends on various physico-chemical parameters such as hydrophobicity and surface charge. We tested different external and internal controls in our experiments to estimate the size and number of our particles in solution and particle deposition to the cells in the microfluidic channel, such as spin-coating of particles to a coverslip, particle sedimentation onto collagen under static conditions, fluorescence correlation spectroscopy (FCS) measurements in solution, and simultaneous multi-channel experiments with different cell-types and surface coatings. Nevertheless, exact quantification remained difficult. Therefore we decided to use commercially available model beads for future targeting experiments that should provide homogeneous size and defined composition. First experiments with PEGylated latex beads revealed a promising effect of installation of a B6 ligand on the specific binding to transferrin receptor overexpressing cancer cells. Another strategy would be to use stabilized polyplexes with internal cross-links for future experiments that should remain functional over longer time periods.

Despite some challenges, the microfluidic setup has great potential to elucidate interesting questions in the future. For example multiple microfluidic channels can be simultaneously flushed with a particle solution to screen the interactions of newly developed materials with selected molecules and cells in parallel. We are currently setting up a four-channel system in which the binding of particles to target cancer cells, non-target endothelial cells, extracellular matrix components and blood proteins can be evaluated at the same time. Furthermore, by combining highly-sensitive fluorescence imaging with particle tracking, the mechanisms of particle binding to targeting receptors, the glycocalyx or specific surface molecules can be enlightened. Next to adhesion studies, information on the effect of shear stress on the internalization kinetics of nanoparticles can be gained. Also the effect of residual molecules from the fabrication process of particles (e.g. free polymer, ions or surfactants) on particle binding, uptake and cell viability can be evaluated.

Furthermore, in the microfluidic flow chamber the effect of nanoparticles on circulating non-adherent metastatic cells or immune cells can be analyzed as well. Also, new types of gene or drug nanocarriers for the therapy of multiresistant bacteria cells in the blood flow, or for the therapy of cardiovascular diseases may be examined.

6 Improved scaffolds for gene and drug delivery

A plethora of polymer and dendrimer scaffolds with multiple modifications are available for the delivery of drugs and nucleic acids to cells and laboratories around the globe are working steadily on the design of improved molecules with high loading capacity, reduced aggregation, specific functionalities and low toxicity. When searching for publications dealing with “polymer and gene” in the U.S. library of medicine of the National Institutes of Health, almost 67.000 entries are displayed (status, May 2013). The production process of these scaffolds is often challenging due to complex, multi-step synthesis and purification. Furthermore lots of the produced scaffolds are polydisperse mixtures of molecules with a broad range of different sizes and conjugation sites.

Here we analyze two novel nanocarrier scaffolds with improved production process for their ability of gene and drug delivery.

In the first to part of this chapter we apply live-cell imaging to compare gene delivery by a new 4-arm-PEG dendrimer hybrid and a 2-arm PEG dendrimer hybrid that can be synthesized in only four steps with simple purification methods (section 6.1). The constructs were synthesized and characterized in the group of Prof. Craig Hawker at UC Santa Barbara and results described in this chapter are taken from our joint publication in the journal *Biomacromolecules*⁹.

In section 6.2 we study a similar internally functionalized dendrimer to which coumarin was attached as a model delivery agent via cleavable ester bonds³³⁷. The effect of coumarin loading to the dendrimer and intracellular coumarin delivery was monitored by confocal microscopy. Experiments with coumarin-loaded dendrimers were performed in collaboration with Dr. Roey Amir (UC Santa Barbara, since 2012 University of Tel Aviv) and Dr. Lorenzo Albertazzi (UC Santa Barbara, since 2012 University of Eindhoven) during the research visit of Lorenzo Albertazzi at our department.

In section 6.3 cellular interactions of a novel sequence-defined polymer with PEG shielding and EGF conjugation for EGFR targeting were monitored. The synthesis of this polymer with defined architecture and conjugation sites is based on the solid phase assisted coupling of artificial amino acid subunits published recently by Schaffert et al.³³⁸ Synthesis and characterization of the EGFR-targeted polyplexes was performed by Ulrich Lächelt, reporter gene expression assays were provided by Petra Kos (both from the group of Prof. Ernst Wagner, pharmacy department, LMU Munich).

6.1 Internally functionalized dendrimers with PEG core for gene therapy

This chapter is adapted from:

L. Albertazzi, F.M. Mickler, G.M. Pavan, F. Salomone, G. Bardi, M. Panniello, E. Amir, T. Kang, K. Killops, C. Bräuchle, R. J. Amir and C. J. Hawker.

*“Strong positive dendritic effects in the bioactivity of internally functionalized dendrimers with PEG cores”,
Biomacromolecules (2012), 13, 4089-4097*

6.1.1 Particle design

Dendrimers are appealing scaffolds for biomedicines because of their modular structure and the plurality of functional endgroups. However, their synthesis is still considered to be time-consuming requiring rigorous purification processes. To simplify the dendrimer preparation several groups have reported the use of polyethylene glycol (PEG) as difunctional core for dendrimer synthesis. These strategies rely on the solubility of the PEG core to simplify the purification by dialysis or precipitation. Additionally the introduced PEG core has shown to enhance the colloidal stability of particles and reduce toxicity.

In this study fourth-generation amine-terminated hybrid dendrimers were synthesized by our collaboration partners at the UC Santa Barbara based on a 4-arm PEG star core, in only four steps with precipitation and dialysis as the only means of purification. The prepared 4-arm dendrimer-PEG hybrid (4-arm PEG G4) contains 40 internal hydroxyl groups and 64 cationic amines at the chain ends (Fig. 6.1). Corresponding fourth-generation 2-arm dendrimers with 20 internal hydroxyl groups and 32 cationic amines (2-arm PEG G4) as well as second-generation dendrimers were synthesized for reference measurements. Viability of cells in the presence of the 4-arm PEG G4 dendrimer was assessed by a PI and calcein acetoxymethyl ester (AM) assay, confirming high cell viability up to a dendrimer concentration of 1 μ M. Only at 10 μ M concentration the 4-arm PEG G4 dendrimer showed toxicity. At this concentration the dendrimers' toxicity correlated to the number of end groups, the corresponding 2-arm PEG G4 hybrid dendrimer exhibited significantly lower toxicity. Live-cell imaging experiments performed by our collaboration partners with fluorescently labeled dendrimers revealed high cell-affinity and internalization of the 4-arm PEG G4 dendrimer as well as destabilization of endolysosomal vesicles in the presence of dendrimers. Furthermore molecular dynamic (MD) simulations were performed that suggest a much more dynamic behavior of the 4-arm PEG G4 dendrimer compared to the 2-arm PEG G4 dendrimer.

6. IMPROVED SCAFFOLDS FOR GENE AND DRUG DELIVERY

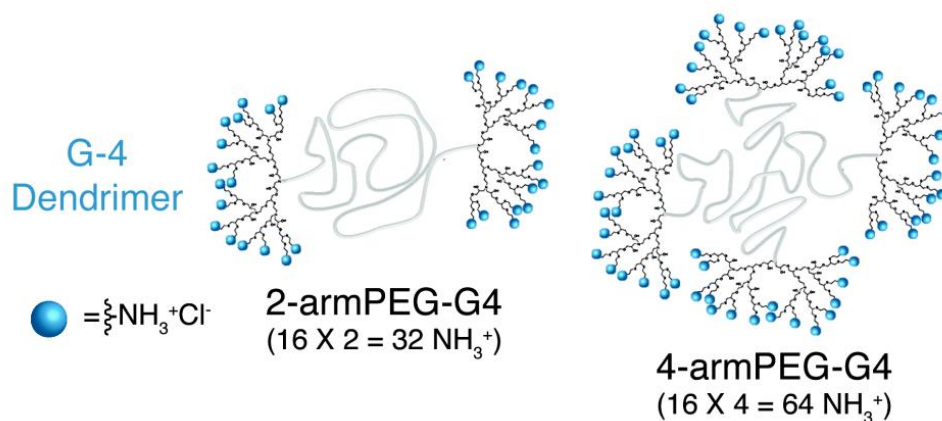


Figure 6.1 Dendrimer design. Schematic representation of the structures of fourth generation amine terminated hybrid dendrimers with two-arm PEG core (2-arm PEG-G4, left image) and four-arm PEG star core (4-arm-PEG-G4, right image). Cationic amine groups (blue spheres) can mediate DNA complexation.

6.1.2 DNA binding and gene transfection

The high structural dynamics of the 4-arm PEG G4 dendrimer coupled to numerous cationic surface groups, the cell-internalization ability and endosomal destabilization suggest that these hybrid dendritic systems may be attractive candidates for binding of negatively charged nucleic acids and subsequent delivery to the cytoplasm for gene delivery applications.

To compare the DNA binding ability of the 4-arm PEG G4 dendrimer and the 2-arm PEG G4 dendrimer an ethidium bromide (EB) exclusion assay was performed. EB emits red fluorescence upon intercalation into DNA. When a second molecule with higher affinity binds to the DNA and displaces the dye, a drop in fluorescence is observed. The assay revealed that the 4-arm-PEG-G4 dendrimer has significantly higher affinity for DNA than the 2-arm-PEG-G4 dendrimer (Fig. 6.2 A).

To analyze further the formation of 2- and 4-arm-based dendriplexes and study their ability to bind cell membranes, we mixed both types of dendrimers with Cy5-labeled DNA to form Cy5-labeled dendriplexes. The 2- and 4-arm dendriplexes were then incubated for one hour with HeLa cells and single particles were imaged using highly sensitive confocal spinning disk microscopy at the single cell level. Both 2- and 4-arm dendriplexes attached to the plasma membrane (Fig. 6.2 B); however, significantly lower fluorescence intensity per particle was detected in the case of the 2-arm dendriplexes (Fig. 6.2 C). This result supports the enhanced ability of 4-arm dendriplexes to bind DNA, as demonstrated in the EB intercalation assay. The amount of DNA delivered to HeLa cells after 22 h of incubation by the 2-arm and the 4-arm dendritic carriers was then quantified from the intensity of the fluorescence signal. Significantly, the amount of DNA that was delivered by the 4-armPEG-G4 was nearly an order of magnitude greater than that for the 2-arm dendriplex (Fig. 6.2 C). The enhanced DNA delivery by the 4-arm dendriplex can be attributed to numerous property enhancements driven by changes due to the 4-arm architecture and higher number of amine end groups, which leads to improved DNA-binding efficacy.

6. IMPROVED SCAFFOLDS FOR GENE AND DRUG DELIVERY

To verify the formation and internalization of intact dendriplexes, additional experiments were performed with dual labeled particles prepared from Cy3-labeled DNA and Atto647-labeled dendrimer. Dual color images confirmed colocalization of DNA and dendrimers in membrane bound particles as well as in intracellularly transported and perinuclear endosomes (data are shown in the appendix, Fig. A2). Next to the dual-labeled particles, an excess of free dendrimer was detected. Incorporation of free dendrimer in endosomes together with complexed particles might facilitate endosomal release and enhance transgene expression.

To evaluate the actual transfection potential of the dendriplexes, we then used a plasmid encoding for green fluorescent protein bearing a nuclear localization signal (EGFPNuc) in combination with either the 2- or 4-arm dendrimer. The fluorescence arising from GFP expression allows the transfection efficiency to be quantified by widefield-fluorescence microscopy. Figure 7.1b,c shows the overlay of transmission light images for treated cells coupled to the green fluorescence signal for GFP expression, followed by quantification of the GFP fluorescence signals, respectively. It is particularly noteworthy that the 2-armPEG-G4 shows no apparent transfection, whereas a strong fluorescence signal from GFP expression following transfection with the 4-arm dendriplexes was observed.

6.1.3 Discussion

Our results clearly show an enhanced ability for DNA delivery for the 4-armPEG-G4 platform compared with the corresponding 2-armPEG-G4 derivative.

The improved gene delivery by the 4-arm dendrimers is most probably attributed to a combination of different effects. First, 4-arm dendrimers provide significantly improved DNA complexation, as demonstrated by the enhanced DNA fluorescence per particle and the ethidium bromide exclusion assay. The enhanced ability of the 4-arm dendrimer for DNA condensation can be easily explained by the availability of higher numbers of cationic amines and the enhanced dynamic flexibility of the 4-arm compared to the 2-arm construct. Secondly, 4-arm dendriplexes seemed to exhibit higher membrane affinity than the 2-arm dendriplexes, as higher particle numbers were counted on cells for the 4-arm construct. However this observed effect might also be attributed to the reduced fluorescence intensity of 2-arm polyplexes, the fluorescence intensity of some 2-arm polyplexes might lie below the detection limit. The uptake kinetics of 4-arm and 2-arm constructs detected during live-cell imaging was quite similar. However as higher amounts of DNA were packed into particles, higher DNA levels reached the interior of the cell when using the 4-arm construct. Because of higher dendriplex loading inside endosomes, we suggest that proton sponge induced endosomal release is additionally facilitated for the 4-arm construct.

The main drawback of the 4-arm dendrimer is its enhanced toxicity. The removal of residual free dendrimer from the dendriplex solution might significantly reduce the toxicity of dendriplexes. Furthermore in the future internal cleavable linkers may be introduced to enhance the biodegradability of the dendrimers. Also, targeting ligands might be used to provide application for targeted therapy.

6. IMPROVED SCAFFOLDS FOR GENE AND DRUG DELIVERY

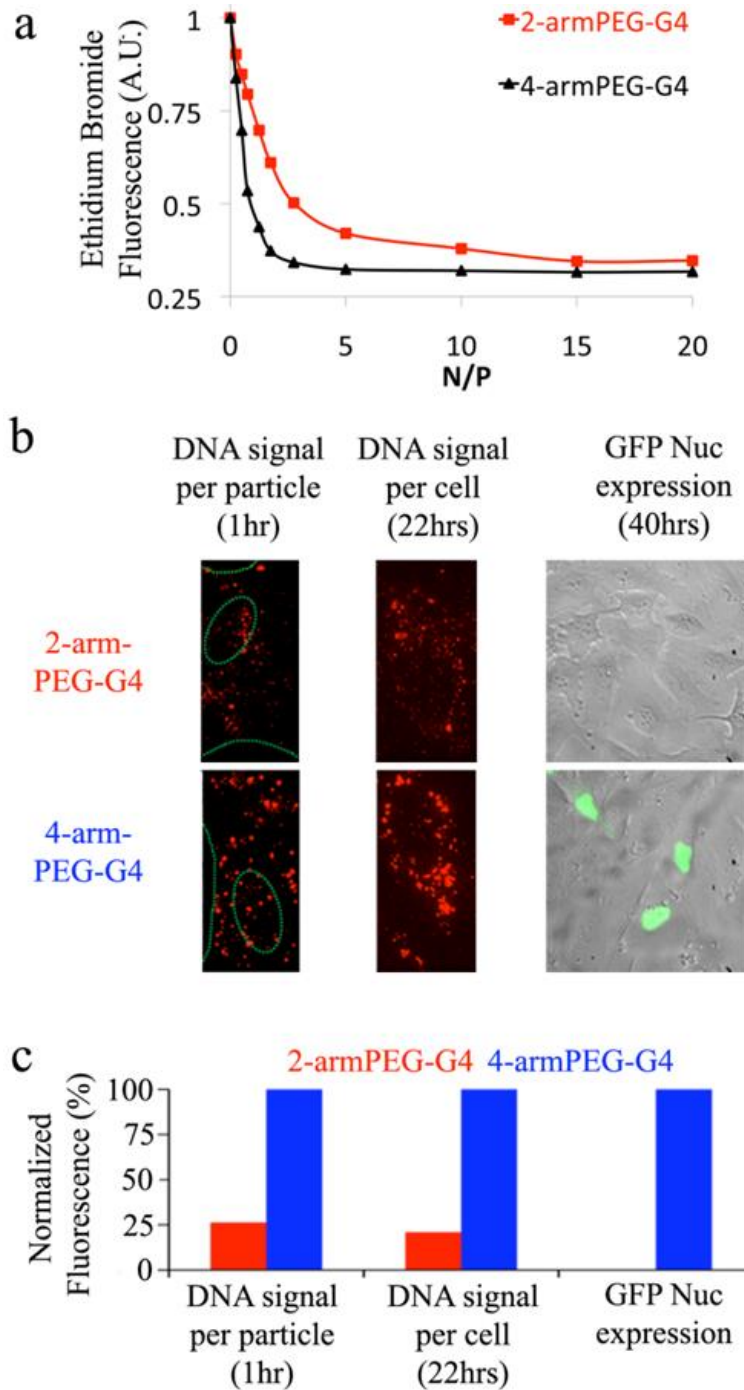


Figure 6.2 Dendrimer-mediated gene delivery. (a) EB intercalation assay and (b) confocal imaging (images widths are 30 μm for the left and center images and 205 μm for the image on the right) show dendriplex formation (left), cellular accumulation of dendriplexes (center), and the nuclear accumulation of the expressed GFP Nuc (green) overlaid on a transmission light image of treated cells (right). (c) Quantification of fluorescence signal (400 ng of DNA, N/P = 4, 240 μL).

6.2 Intrinsically functionalized dendrimers for drug delivery

6.2.1 Particle design

A number of dendritic architectures have been developed for the delivery of therapeutic biomolecules to diseased cells. Two major strategies for dendrimer mediated drug delivery are non-covalent drug encapsulation³³⁹ and covalent attachment of drugs to the dendritic chain end³⁴⁰.

Amir et al. published an alternative design in which the cargo molecule is covalently attached via cleavable ester bonds to the interior of a fourth generation 2-arm PEG dendrimer hybrid³³⁷ (Fig. 6.3). This strategy allows high and reproducible drug loading without significantly changing the surface structure of the dendritic scaffold and controlled intracellular drug release by enzymatic cleavage. In their study Amir et al. used coumarin dyes as model delivery unit. The dendrimer scaffold was additionally labeled by attachment of the Alexa Fluor dye AF647. Coumarin is often used as precursor for the synthesis of pharmaceutical compounds for anticoagulation. It can also be applied for the therapy of lymphedema³⁴¹. Coumarin fluorescence is quenched at high loading inside the particle and fluorescence increases after delivery to the cell. *In vitro* experiments confirmed that coumarins are released from the dendrimer in the presence of esterases. Imaging experiments on melanoma cells demonstrated that the coumarin loaded dendrimer carrier is successfully internalized into cells and coumarin is released to the cytoplasm. The published results suggest that internally functionalized dendrimers are promising candidates for drug delivery applications.

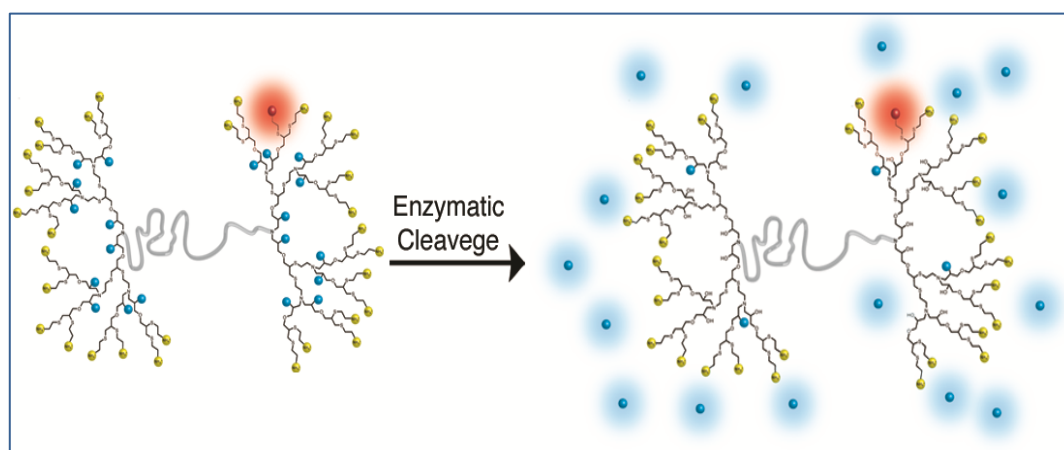


Figure 6.3 Internally functionalized dendrimers for drug delivery. Protonated amine groups at the chain ends (yellow) of fourth generation 2-arm PEG dendrimer hybrids mediate cellular uptake. Coumarin dyes (blue) were attached to the interior of the dendrimer via covalent ester-bonds and can be released by enzymatic cleavage. A non-cleavable dye (red) allows monitoring of the dendrimer itself. Figure taken from Amir et al.³³⁷

6.2.2 Live-cell imaging of loaded and unloaded dendrimers

Amir et al. observed in their study that the membrane binding and internalization kinetics of the dendrimer-coumarin complex seemed to differ from the unloaded dendrimer. To study this effect in more detail, we analyzed the cellular interactions of coumarin-loaded dendrimer and the unloaded dendrimer on our microscope setups with improved sensitivity. Analysis of the dendrimer solutions on a coverglass revealed that coumarin-loading of the dendrimer seemed to trigger a self-assembly process, as particles (single spots with increased fluorescence intensity) were observed in our microscopic images whereas the non-loaded dendrimer was homogeneously distributed on the coverglass without particle formation (Fig. 6.4). Particle formation in the presence of coumarin was confirmed by dynamic light scattering (DLS) measurements.

Our confocal images further revealed that the unloaded dendrimers display high affinity for the plasma membrane of cells. Shortly after addition of the dye-labeled dendrimer to HeLa cells homogeneous staining of the plasma membrane was detected. As expected, the cationic amine groups at the chain ends of the dendrimer seem to trigger efficient cell binding and uptake.

In contrast, for the coumarin loaded dendrimer only few fluorescent spots were detected on the plasma membrane of HeLa cells during the first hour of incubation, indicating that the formed particles exhibit reduced membrane affinity (Fig. 6.4). However, the number of membrane bound particles increased with time and distinct membrane accumulation was detected after four hours.

By following the movements of single coumarin-dendrimer particles and analyzing their time-dependent trajectories we could observe different effects: Particles sometimes detached from the plasma membrane after initial binding supporting our hypothesis of weak interactions between the dendrimer and cell surface molecules. Other particles showed directed, surfing motion along the plasma membrane. After particle internalization typical diffusive behavior of endosomes as well as active transport processes were detected. In the first 30 minutes post dendrimer addition few particles reached endocytic compartment, enhanced intracellular accumulation was observed between one and four hours of incubation.

Next, we studied the time-dependent increase of cytoplasmic coumarin fluorescence by spinning disk confocal microscopy with alternating laser excitation (Fig. 6.5). Unexpectedly, an increase in diffuse cytoplasmic fluorescence was observed in the first hour of incubation, before the majority of particles were internalized. At later time-points coumarin was also detected in endosomes colocalizing with the dendrimer. This result suggest that a subset of coumarin molecules are cleaved from the dendrimer and enter the cell circumventing endocytosis, whereas another subset of coumarin remain bound to the dendrimer and are internalized via endocytosis.

6. IMPROVED SCAFFOLDS FOR GENE AND DRUG DELIVERY

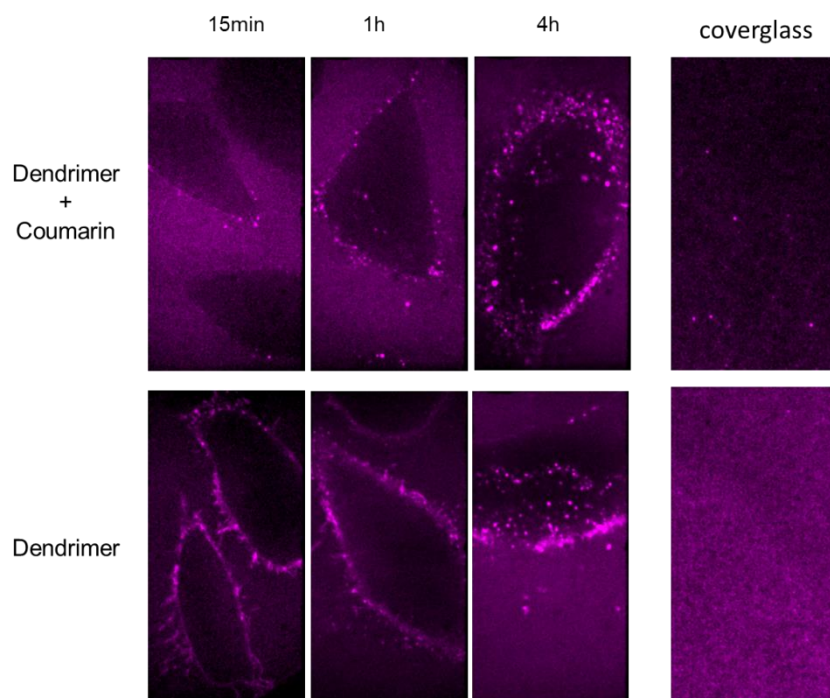


Figure 6.4. Different membrane affinity of coumarin-loaded (upper row) and unloaded dendrimer (lower row). AF647-labeled dendrimer solutions with covalently attached coumarin or without modification were applied to HeLa cells. Cellular adhesion and uptake was detected by spinning disk confocal microscopy. Confocal z-slices of representative cell are shown for different incubation times (15 minutes, 1 hour and 4 hours respectively). Dendrimer binding to the coverglass is additionally depicted. In the presence of coumarin particles are formed that exhibit reduced affinity to the plasma membrane compared to the unloaded dendrimer.

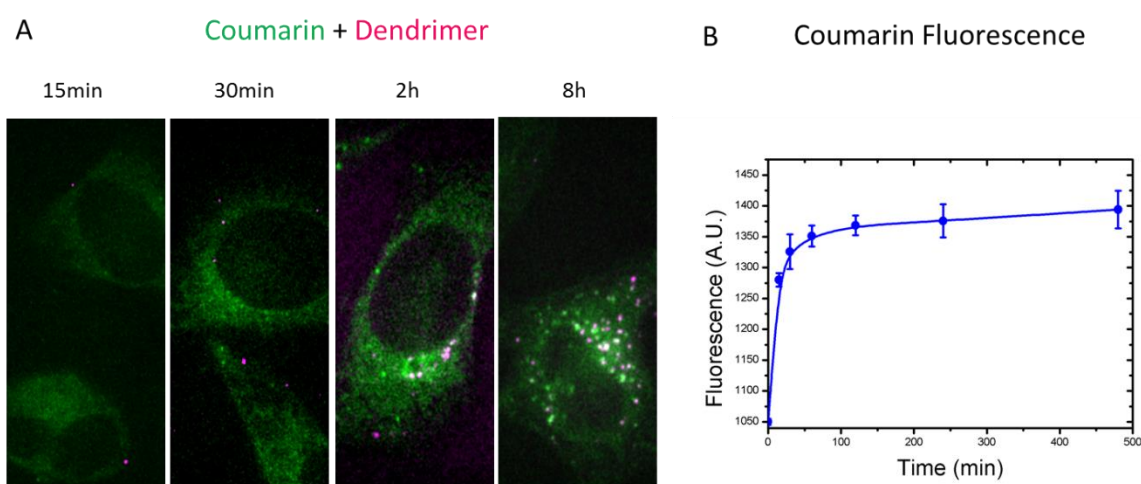


Figure 6.5 Coumarin release into cells. Coumarin loaded dendrimers were applied HeLa cells and the dendrimer signal (magenta) and the coumarin signal (green) was followed by spinning disk confocal microscopy with alternating laser excitation over eight hours. **A** Overlay images of both fluorescent channels are shown for confocal slices of representative cells after 15 minutes, 30 minutes, 2 hours and 8 hours of incubation. An increase of diffuse cytoplasmic coumarin fluorescence is observed over time. After 2 hours white spots appear in the cytoplasm indicating colocalization of dendrimers and coumarin in endosomes. **B** The fluorescence intensity of cytoplasmic coumarin was quantified by digital image analysis and plotted over time. Mean values are presented for n=8-10 cells. The standard deviation is presented in error bars.

6.2.3 Discussion

The application of dendrimers for the efficient and safe delivery of pharmaceutical compounds with low bioavailability and high systemic toxicity is a promising strategy. In this study an internally functionalized PEG-dendrimer hybrid was designed with high drug loading capacity, 20 coumarin molecules were attached as a model delivery unit to each dendrimer. The applied 7-(diethylamino)coumarin can be described by two resonance structures; a non-polar structure that is predominant in the ground state and a polar structure with positive and negative charge.

Our experiments from live-cell imaging indicate that loading of the coumarin dye to the dendritic carrier significantly alters the dendrimer-cell interactions. In the presence of coumarin the formation of particles with increased fluorescence intensity was observed, indicating the clustering of several coumarin-dendrimers. In contrast, the unloaded dendrimer remained homogeneously dissolved. The formed particle showed reduced binding to the cell membrane and the coverglass, which may be explained by exposure of PEG molecules to the particle surface. The reduced binding of the formed particles might be advantageous for future targeted delivery applications with additional targeting ligands. However, as the loaded molecules strongly changed the behavior of dendrimers, we encourage the testing of real drug candidates for dendrimer loading. It might be very interesting to compare the effects of drugs with different size and hydrophobicity on the dendrimer assembly.

In our experiments we observed a fast increase of coumarin fluorescence inside the cells, which was not expected and cannot be explained by the endocytosis and subsequent release of dendrimer-coumarin conjugates. The used dendrimer conjugates were purified systematically and should not contain free dye. Furthermore control experiments revealed that free coumarin does not pass the plasma membrane of cells, only at very high concentration of free dye an increase in cytoplasmic fluorescence was observed. The mechanism of this interesting effect remains unclear up to now. One could imagine local membrane destabilization induced by the dendrimer resulting in access of the molecules to intracellular esterases and membrane passage of the cleaved dye.

Again, it would be very interesting to repeat the release experiment with a real drug to monitor if the cytoplasmic increase is specific for coumarins or can be observed for other drugs as well.

The synthesis of new dendrimer conjugates with real drug candidates is currently under progress. We hope that live-cell imaging experiments can enlighten valuable mechanistic details on dendrimer mediated drug delivery in the future.

6.3 Sequence defined scaffolds from solid phase supported synthesis

6.3.1 Particle design

Synthetically engineered polymer conjugates are often polydisperse mixtures lacking the molecular precision of biological macromolecules. Schaffert et al. (group of Prof. Ernst Wagner, Pharmacy department, LMU) described a new solid phase supported method to synthesize sequence-defined polymer scaffolds with controlled topology and functionalities³³⁸. For the synthesis, artificial Fmoc/Boc protected amino acids with defined diaminoethane units were used. The diaminoethane motif is protonated at physiological pH and is known to be responsible for the high transfection efficiency of polyethylenimine, which has become the gold standard for gene delivery. With lysines as branching points and cysteines as disulfide forming stabilization units and various hydrophobic domains, Schaffert et al. created a library of more than 300 defined polymers with different shapes and modifications.

Based on the artificial aminoacid Succinoyl Tetraethylene Pentamine (STP, see figure 7.1 A), Ulrich Lächelt (group of Prof. Ernst Wagner, Pharmacy department) further developed sequence defined oligomers with PEG shielding and EGF ligand for EGF receptor targeting. Each polymer contained 24 protonable amines for DNA complexation. For reference measurements an untargeted PEGylated STP polymer was synthesized.

6.3.2 EGF ligand induces cell binding and uptake of STP polyplexes

To verify successful ligand installation and functional receptor targeting of the new polymers, we imaged their cellular interactions by spinning disk microscopy. In the experiments the polymers were complexed with Cy5-labeled plasmid DNA. The polymer contained cysteines for disulfide stabilization of the formed particles. We confirmed that functional particles with homogeneous size distribution were formed when mixing the reduced polymer with DNA. To prevent polymer oxidation before particle formation, particles should be assembled on ice and careful storage and handling of the polymer is required (see appendix, Fig. A3).

To study their cellular adhesion, EGF-equipped STP polyplexes (EGF-PEG-STP) and untargeted STP polyplexes (PEG-STP) were added to EGFR overexpressing HuH7 cells (Fig. 6.6 A). Interestingly, EGF STP polyplexes showed efficient binding to the cells whereas only few untargeted STP polyplexes were detected on the plasma membrane. This result suggests very specific binding of the STP polyplexes and low non-specific interactions of the particles, different to previous experiments with PEI polyplexes.

From our previous studies with EGF-PEI polyplexes (chapter 5.1) we learnt that the EGF ligand triggers exceptionally fast receptor mediated endocytosis of particles by signaling activation.

6. IMPROVED SCAFFOLDS FOR GENE AND DRUG DELIVERY

To detect if EGF-PEG-STP polyplexes are internalized with fast kinetics as well, we recorded short movies of single cells in the first hour post polyplex addition. In figure 6.6 B, two-dimensional trajectories of EGF-PEG-STP polyplexes after 40 minutes of incubation are presented, generated by superimposing a time-series of 100 images which were acquired at 330 ms frame rate. Displayed polyplexes show typical intracellular motion revealing successful receptor-mediated endocytosis.

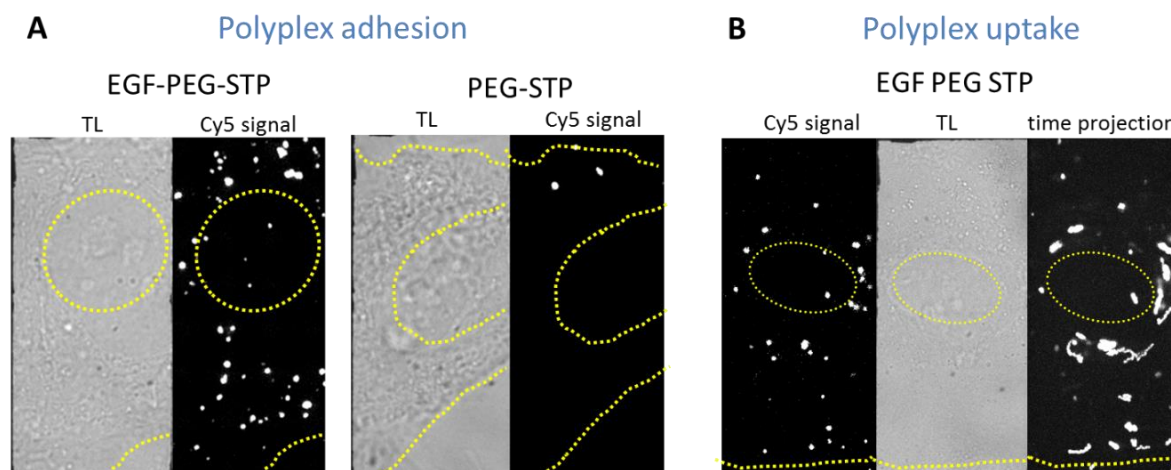


Figure 6.6 Adhesion and uptake of sequence defined STP polyplexes. Z-projections from confocal stacks are depicted (Cy5 signal) together with the transmission light image of the cell (TL). The region of the nucleus and the plasma membrane is marked by a dashed yellow line. **(A)** Sequence defined EGFR-targeted (EGF-PEG-STP) and untargeted (PEG-STP) polyplexes were dissolved in cell medium and added to HuH7 cells under microscopical observation. Whereas targeted polyplexes efficiently bound to the cells, few untargeted polyplexes were detected on the plasma membrane. **(B)** Efficient uptake of EGF-equipped polyplexes after 40 minutes of incubation. 2-dimensional trajectories of particles are displayed in a time-projection (right image), in which 100 frames with 330 ms frame rate were superimposed.

6.3.3 Comparing gene transfer efficiency of EGF-PEG-STP and EGF-PEG-PEI polyplexes

To compare the transfection potential of the newly developed sequence defined STP polymers and standard polydisperse PEI polymers, reporter gene expression assays were performed by Petra Kos (group of Prof. Ernst Wagner, Pharmacy department, LMU). For the experiments EGFR-targeted and untargeted PEG-STP- and PEG-PEI polyplexes with pCMV Luc plasmid were applied at same DNA concentration and N/P ratio to cells. One set of experiments was performed in the presence of chloroquine as enhancer of endosomal escape. Results are displayed in figure 6.7. The untargeted STP-PEG polyplexes did not induce gene expression above the background level, for both chloroquine treated and untreated cells. This result is in agreement with our imaging data revealing low PEG-STP polyplex binding to the cells. In contrast untargeted PEI-polyplexes mediated significantly higher gene expression, which can be explained by higher levels of non-specific particle internalization. Remarkably, the EGF-equipped PEG-STP polyplexes showed no significant transgene

6. IMPROVED SCAFFOLDS FOR GENE AND DRUG DELIVERY

expression in the absence of chloroquine, but strongly enhanced expression levels (more than 500 fold increase) in the presence of chloroquine. This result suggests efficient uptake but poor endosomal release properties of the new construct. In comparison, EGF-PEI polyplexes showed high reporter gene expression levels also in the absence of chloroquine, Results are displayed for mixtures with an N:P ratio of 6:1 but similar transfection data were achieved for N:P of 12:1.

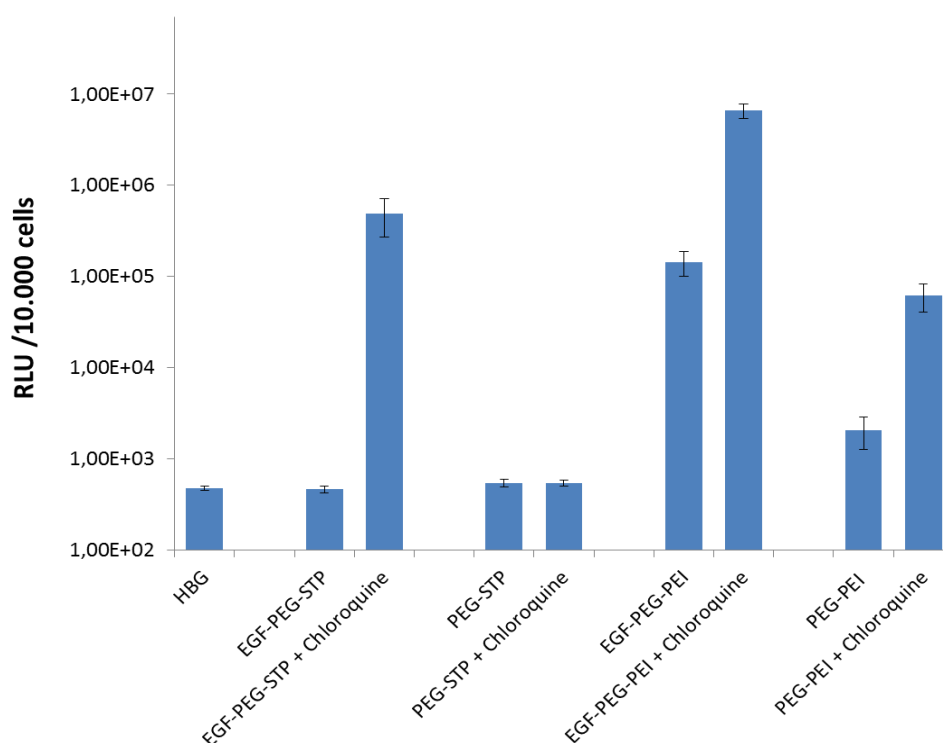


Figure 6.7 Luciferase reporter gene expression. 10.000 cells per well were transfected with targeted EGF-PEG-STP and EGF-PEG-PEI as well as untargeted PEG-STP and PEG-PEI polyplexes in the presence of chloroquine as enhancer of endosomal escape or without chloroquine. Reporter gene expression was detected after 24 hours of incubation, experiments were performed in triplicates. The standard deviation is shown in error bars. Buffer treated cells (HBG) served as reference.

6.3.4 Discussion

The recently published solid phase assisted synthesis is a potent method to produce defined polymers with high precision³³⁸. These polymers are very useful to analyze accurate structure-activity relationships. Furthermore the high precision of the method should maximize the yield of functional polymer and reduce side effects from non-functional molecules, which is an important requisite for their application in clinical therapy.

6. IMPROVED SCAFFOLDS FOR GENE AND DRUG DELIVERY

Here, we confirmed the successful coupling of an EGF ligand to PEGylated sequence defined STP polymers resulting in efficient membrane binding and fast uptake of the formed polyplexes into HuH7 cells. In comparison to polydisperse PEG-PEI polyplexes the untargeted PEG-STP polyplexes did not mediate significant membrane binding and uptake, portending superior shielding of the novel STP polyplexes. However, it should be noted that we observed altered cell binding and uptake as well as enhanced aggregation of the untargeted PEG-STP polyplexes in some polymer batches. We suspect that these effects are caused by oxidation processes in the stock solution, but further experiments are required to explain these observations.

Luciferase reporter gene expression assays suggested that EGF-PEG-STP polyplexes are efficiently internalized but do not as escape from endosomes, as the addition of chloroquine as an endosomal escape agent was required for successful gene expression. In contrast, polydisperse EGF-PEG-PEI polyplexes induced high gene expression also in the absence of chloroquine, demonstrating improved endosomal escape of the PEI polyplexes. The insufficient endosomal escape of sequence defined STP polyplexes was also observed in recent studies with integrin and transferrin receptor-targeted STP polymers³⁴².

To enhance endosomal escape of the EGF-PEG-STP polyplexes, additional molecules may be coupled during the solid phase assisted synthesis in the future; e.g. the pore-forming subunit of the hemagglutinin protein. Another strategy comprises the addition of histidines for enhanced endolysosomal buffering of the STP polyplexes. This strategy will be described in more detail in the next chapter (see 7.2).

7 Endosomal escape and nuclear import

Endosomal release and nuclear import are regarded as two major bottlenecks for gene delivery. Multiple strategies are currently investigated to improve the transfection efficiency of artificial gene nanocarriers by facilitating their escape from endosomal compartments and enhance the delivery of DNA to the nucleus.

Strategies for endosomal escape include membrane destabilization by pH sensitive fusogenic or pore forming peptides derived from viruses or bacteria¹⁷⁷⁻¹⁷⁹, or attachment of fusogenic lipids¹⁸³. Furthermore, molecules with high buffering capacity in the endolysosomal pH range can induce endosomes destabilization by promoting ion inflow and osmotic swelling of the endosomal compartment¹⁸⁴. Promising data were also published recently on light-induced release of photosensitizer-equipped particles³⁴³ or the local heating of membranes by plasmonic gold nanoparticles¹⁸⁹.

For enhanced nuclear import of DNA molecules, the attachment of nuclear localization sequences (NLS) or the incorporation of specific sequence elements for transcription factor binding are investigated¹⁹². Furthermore the coupling of small ligands that recognize specific molecules which are known to be transported from the cytoplasm to the nucleus can enhance nuclear accumulation of nucleic acids¹⁹³.

Because the portion of nucleic acids that are released from endosomes is usually very small and the majority of synthetic gene nanocarriers remain entrapped in endosomes over many hours, the subsequent processing of gene nanocarriers inside the cytoplasm or the nucleus is very difficult to detect by standard live-cell imaging routines.

In this chapter we introduce two strategies to visualize endosomal destabilization and nuclear import in living cells. In a first project we used a calcein release assay to monitor the effect of histidines on destabilization of endosomal membranes (chapter 7.1). For the study, targeted sequence-defined STP polymers with histidine modification were provided by our collaboration partners in the pharmacy department of the LMU (group of Prof. Ernst Wagner). Prior to our live-cell imaging experiments, they performed detailed experiments on the buffering capacity and transfection efficiency of the synthesized polymers. The described data from this chapter are included in a manuscript, which is currently in the revision process.

In a second project (chapter 7.2) we used microinjection as a tool to dissect nuclear import processes. Model protein constructs for the experiments were provided by Dr. Kevin Meier (group of Prof. Ernst Wagner, Pharmacy department, LMU).

7.1 Histidine as endosomal escape agent

This chapter is adapted from:

U. Lächelt, P. Kos, F.M. Mickler, E. Salcher, W. Roedl, N. Badgujar, Naresh, C.Bräuchle and E. Wagner, "Fine-tuning of proton sponges by precise diaminoethanes and histidines in pDNA polyplexes." Nanomedicine, 2013, accepted

7.1.1 Particle design

Polymers with highly basic groups are widely used as nanocarriers for gene delivery as they provide protonated polycationic structures at neutral pH that form complexes with negatively charged nucleic acids. Residual less basic groups, such as histidines, can provide additional buffering capacity in the endolysosomal pH range which may facilitate endosomal escape of the gene vectors.

In this study sequence defined oligomers with artificial succinoyl tetraethylene pentamine (STP) building blocks and histidines as protonable DNA-binding and buffering units were synthesized by Ulrich Lächelt (group of Prof. Ernst Wagner, LMU Munich) using a recently developed solid-phase assisted strategy (Fig. 7.1 A). To determine the basicity and buffering capacity of the synthesized oligomers at extracellular and intracellular pH (pH range = 5.0-7.4), potentiometric backtitrations of acidified samples with sodium hydroxide solution were performed. The titrations revealed that STP polymers without histidines show highest buffering capacity at extracellular pH (above pH=7.0) and lower buffering capacity in the endolysosomal range. Histidine incorporation led to an increase of the total buffering capacity and mediated a more homogeneous buffering distribution between pH=5.0 and pH=7.4 suggesting improved buffering in endolysosomal compartments.

To study if the transfection efficiency of targeted gene vectors is improved by histidine incorporation, well shielded PEGylated two-arm STP oligomers were generated for DNA complexation (Fig. 7.1). Alanines were used as non-functional substitutes for histidine. As branching points α,ϵ -amidated lysines were introduced, cysteines were additionally incorporated as disulfide forming polyplex stabilization units. For specific transferrin receptor targeting a B6 ligand was attached. Furthermore polymers with a new peptidic ligand (CMBP, c-Met binding peptide) for binding of the hepatocyte growth factor receptor were generated.

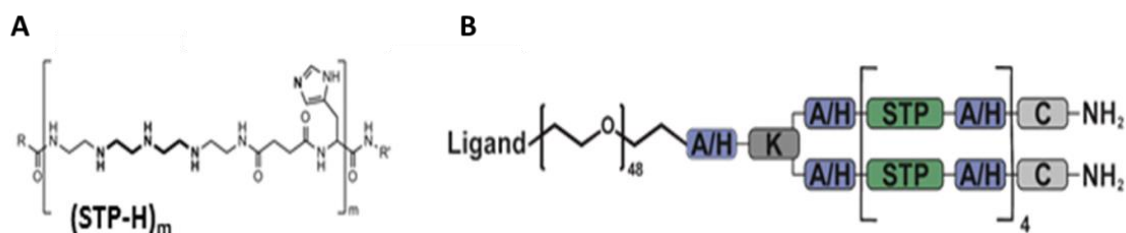


Figure 7.1 Design of targeted PEGylated STP oligomers with histidine for enhanced endosomal escape.

A Artificial succinoyl tetraethylene pentamine (STP) was used as protonable building block for DNA complexation. The chemical structure of an histidine-equipped STP unit (STP-H) is depicted. **B** Sequence defined oligomer with 2-arm topology. Histidines (H) were introduced for improved endosomal escape; alanines (A) were applied as non-functional substitutes in control oligomers. α,ϵ -amidated lysine (K) served as branching unit, cysteines (C) were incorporated for disulfide-crosslinking of oligomers after DNA complexation. For shielding, a polyethylene glycol (PEG) linker was attached. Targeting ligands were coupled for specific receptor targeting.

7.1.2 Uptake efficiency and gene transfer

First, the uptake efficiency of transferrin receptor-targeted STP polyplexes with histidine (B6-His polyplexes) or without histidine modification (B6-Ala polyplexes) was compared to the uptake of untargeted polyplexes (Ala-His polyplexes) by flow cytometry. The results obtained by our collaboration partners confirmed low non-specific uptake of the untargeted polyplexes and greatly enhanced uptake of the transferrin receptor-targeted polyplexes into transferrin receptor expressing DU145 cells, independently of alanine- or histidine modifications.

In a next step, the transfection efficiency of the respective polyplex formulations was determined in luciferase gene expression assays. To study the effect of endosomal escape on gene transfer, one set of cells was coincubated with the lysosomotropic reagent chloroquine. The untargeted polyplexes lacking B6 did not mediate signals above the background level in chloroquine treated as well as untreated cells, consistent to the low uptake determined by flow cytometry. In contrast the targeted B6-equipped polyplexes with or without histidine induced high transfection levels when chloroquine was added to enforce endosomal escape. In the absence of chloroquine, the histidine-analogue showed 10-30 fold enhanced gene expression levels compared to the histidine-free analogue. This result suggests that endosomal escape of DNA is improved for the histidine-equipped polymer.

By live-cell imaging of fluorescent-dye labeled STP polyplexes on DU145 cells, we confirmed that homogenously sized, non-aggregated particles were assembled (see appendix, Fig. A4). Targeted polyplexes with and without histidine showed similar affinity to transferrin receptor overexpressing DU145 cells. An uptake study by spinning disk confocal microscopy revealed that both polyplex types were efficiently endocytosed and transported to perinuclear endosomes between one and four hours of incubation (Fig. A4).

7. ENDOSOMAL ESCAPE AND NUCLEAR IMPORT

7.1.3 Endosomal escape monitored by calcein release assay

The previous results from reporter gene expression suggested enhanced destabilization of the endosomal membrane due to the incorporated histidines. To monitor if endosomal destabilization can be detected in the presence of histidine, we applied a calcein release assay on living DU145 cells. Upon coincubation with STP-polyplexes, fluorescent calcein dyes are internalized into polyplex filled endosomes. When the endosomal membrane is destabilized the small calcein molecules can diffuse into the cytoplasm. Calcein fluorescence is partly self-quenched at high concentration reducing the fluorescence signal from endosomes and allowing improved detection of dequenched calcein fluorescence after endosomal release.

In our experiments we passively coincubated 0.5 mg/ml calcein with B6 STP-His or B6 STP-Ala polyplexes for 3.5 hours on DU145 cells. Afterwards cells were washed several times to remove background fluorescence from the medium. Single z-slices of cells were imaged in CO₂-independent medium by spinning disk confocal microscopy. In figure 7.2 the calcein fluorescence of representative cells is depicted. Whereas for the alanine analogue the calcein fluorescence is mainly restricted to endosomes (spotty staining), an increase of the cytoplasmic calcein fluorescence was observed for the histidine analogue. The calcein fluorescence in the cytoplasm was quantified by digital image analysis in ImageJ. For the quantification mean grey values of background pixels and endosomal compartments were determined and two thresholds were set to exclude those regions from quantification. The integrated intensity of cytosolic pixels above the lower background threshold and below the upper endosomal threshold was then calculated (integrated intensity = number of selected pixels × mean grey value of selected pixels). Mean values of all evaluated cells are presented in figure 8.2 C demonstrating significantly increased calcein release to the cytoplasm in presence of the histidine analogue compared to the alanine analogue.

Next to transferrin receptor-targeted STP polyplexes, we additionally evaluated the endosomal release properties of histidine-equipped STP polyplexes with a new targeting ligand for hepatocyte growth factor binding. Also for these polyplexes improved endosomal calcein release was observed in the presence of histidine (data are shown in the appendix, figure A5). The new construct is currently tested in additional *in vitro* and *in vivo* experiments to determine its potential for *in vivo* gene delivery.

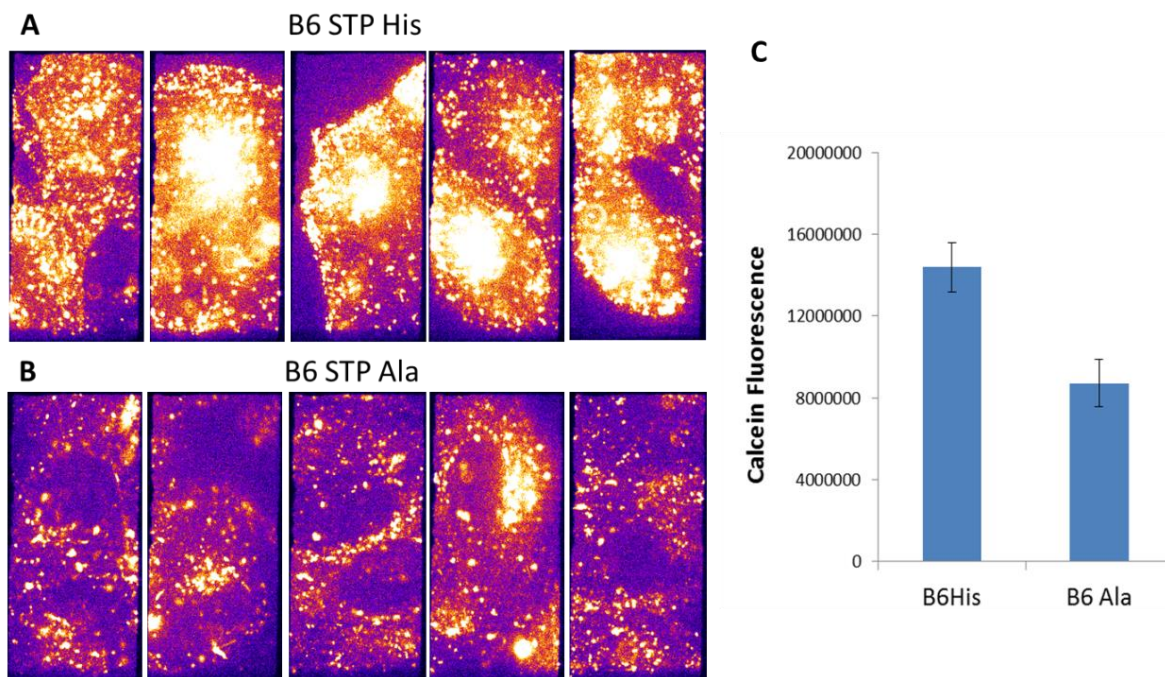


Figure 7.2 Calcein Release assay with transferrin receptor-targeted STP polyplexes. B6-equipped polyplexes with **(A)** histidine as endosomal escape agent (B6-STP-His) or with **(B)** alanine substitution (B6-STP-Ala) were coincubated with 0.5 mg/ml calcein on transferrin receptor overexpressing DU145 cells. Calcein release from endosomes was imaged with 488 nm laser excitation after 3.5 hours of incubation of spinning disk confocal microscopy. Images of five representative cells are depicted, the fluorescence intensity is color coded with orange and white regions exhibiting highest calcein fluorescence. **(C)** Calcein fluorescence in the cytoplasm was quantified by digital image analysis. Mean values of all evaluated cells are presented (N=20 for B6 SP Ala, N=22 for B6-STP-His), the standard error is depicted by error bars. A significant increase in calcein release from endosomes is observed for the histidine analogue.

7.1.4 Discussion

During their journey into cells, gene nanocarriers are exposed to a range of different pH values from pH=7.4 at the plasma membrane to pH=5.0 in lysosomal compartments. To change their properties dynamically in different compartments can be advantageous for the transfection process. Strong bases that are protonated at extracellular pH promote efficient complexation of nucleic acids. Functional groups with lower basicity that are protonated at endolysosomal pH can induce enhanced ion influx into endosomal compartments which according to the proton sponge hypothesis results in osmotic endosome swelling and membrane rupture. Cationic molecules might also directly induce defects in membranes.

Our experimental results support the positive effect of histidine incorporation on polymer mediated gene delivery. The imidazole side chain of the histidine molecule has a pKa of approximately 6.0. This suggests that ion influx is triggered after trafficking of the polyplexes to late endosomes.

In our experiments we detected a clear increase of calcein fluorescence in the cytoplasm after 3.5 hours of B6-STP-His polyplex incubation. Noteworthy at this point of time the DNA signal was still restricted to endosomes and colocalization of DNA and calcein was observed.

7. ENDOSOMAL ESCAPE AND NUCLEAR IMPORT

This result suggests local and temporal destabilization of the endosomal membrane rather than complete endosomal rupture. In this scenario, a subset of calcein molecules may leave the endosome via a small pore or defect together with a low number of DNA molecules, whereas the majority of the material remains entrapped in the endosome. The release of calcein is probably much easier to detect by fluorescence microscopy than the release of DNA, because of the dequenching effect and the small size of the calcein that allows fast distribution in the cytoplasm. In contrast the diffusion of large DNA molecules is strongly limited in the crowded cytoplasm.

Of course it would be of high interest to enlighten the process of endosomal DNA release in more detail. To allow the improved detection of released DNA molecules in the cytoplasm, it would be useful to apply constructs which show low fluorescence in endosomes and increased fluorescence after cytoplasmic delivery. For this purpose we are currently developing a DNA sensor, in which a donor and a quencher dye are connected via a bioreducible bond. In the cytoplasm the quencher should be cleaved and the fluorescence of the DNA construct should appear. With this sensor the effect of different lysogenic substances might be quantified in the future. Also the effect of DNA structure and size on endosomal release can be investigated. Mechanistic insights into the endosomal release process might then help to design more efficient artificial gene nanocarriers in the future.

7.2 Visualizing nuclear localization sequence (NLS) mediated import

7.2.1 Micromanipulators for direct cytoplasmic delivery

One method to dissect the nuclear import behavior of biomolecules is to circumvent endosomal accumulation by direct injection of the material into the cytoplasm of the cell. For this approach programmable micromanipulators are commercially available that provide the semi-automated microinjection of small volumes into single cells under microscopic observation. The molecules of interest are loaded into a thin microcapillary which is precisely located to the target cell and mechanically penetrates the cell membrane. The injection substance is then delivered from the capillary upon a pressure pulse.

7.2.2 NLS mediated import of microinjected proteins

We examined the approach using a model eGFP protein construct with a nuclear localization sequence for nuclear import. The GFP construct was provided by Kevin Meier (Pharmacy department, LMU) and contained an additional pH-sensitive linker (azidomethyl-methylmaleic anhydride (AzMMMan)) for subsequent coupling of the protein to a nanocarrier device³⁴⁴. In our experiments the nlsGFP construct was either microinjected into the cytoplasm of HeLa cells or applied extracellularly to the cell medium. Imaging of single cells by spinning disk confocal microscopy revealed that the fluorescent protein showed relatively low cell affinity and was retained at the plasma membrane or in endosomes after extracellular application; no fluorescent signal was detected in the cytoplasm or the nucleus (Fig. 7.3 A). In contrast, injection into the cytoplasm resulted in fast accumulation of the fluorescent protein inside the nucleus (Fig. 7.3 B). This result demonstrates that nls-equipped proteins can be efficiently transported to the nucleus after release to the cytoplasm. Furthermore, our results indicate that the attached linker does not disturb the nuclear import process of the protein and can be applied for the bioreducible coupling of biomedical substances to nanocarriers.

7. ENDOSOMAL ESCAPE AND NUCLEAR IMPORT

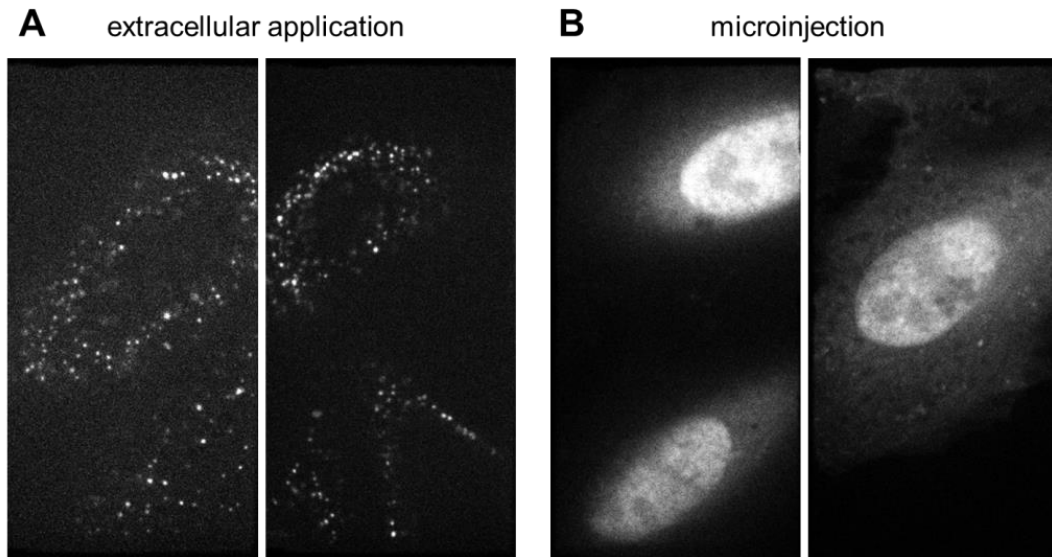


Figure 7.3 NLS-mediated protein import after cytoplasmic exposure. A NLS-GFP construct was placed either in the cell medium (**A**) or microinjected directly into the cytoplasm of HeLa cells (**B**). Detection of the GFP signal by spinning disk confocal microscopy revealed endosomal or membrane retention of GFP after extracellular exposure, whereas microinjected GFP was efficiently transported to the nucleus.

7.2.3 Discussion

Our first experiments with a model protein construct demonstrate that microinjection is a powerful tool to dissect the nuclear import characteristics of biomedical substances. The combination of microinjection and highly-sensitive fluorescence imaging may provide interesting data on the cytoplasmic fate and the kinetics of nuclear import of drugs and nucleic acids in the future. The gained knowledge can help to improve the design of gene and drug delivery vectors to achieve e.g. more efficient decondensation inside the cell or improved interaction with the nuclear import machinery. Also cytoplasmic interaction of microRNAs or siRNAs with selective cytoplasmic molecules, e.g. ribosomes or the RISC complex might be elucidated with the help of microinjection.

8 Conclusion

The results from this thesis clearly demonstrate that rational design of “intelligent” gene nanocarriers can be used to overcome the multiple cellular barriers for gene delivery. We show that the implementation of targeting ligands in combination with PEG shielding can be applied to mediate enhanced uptake of nanocarriers into diseased cancer cells. By selecting between different ligand molecules the signaling activation inside the cell as well as the uptake kinetics of the particle can be modulated. We also reveal the high potential of bioresponsive elements, such as enzyme-cleavable linkers for intracellular drug release, redox-sensitive linkers for intracellular particle deshielding or pH-sensitive histidines for endosomal destabilization. However, next to rational design additional fine-tuning of the polymers in cell-based assays is required to balance benefits and drawbacks of each modification. We show that it is not easy to predict from theory the best polymer composition for efficient nucleic acid complexation but low toxicity, the exact PEG linker length for sufficient shielding but high transfection as well as the optimum ligand concentration for efficient uptake but affordable synthesis; however these parameters can be experimentally determined.

Live-cell imaging is a powerful tool to support both, the identification and confirmation of novel concepts for rational gene delivery as well as the improvement of existing nanocarriers. This thesis was performed in close collaboration and with constant feedback from research groups with chemical and pharmaceutical expertise. This interdisciplinary approach is of great importance for the design of safe and effective gene vectors in the future with cheap, reproducible synthesis and excellent *in vivo* pharmacokinetics. Single cell imaging can provide valuable mechanistical insights into the cellular processing of gene vectors with different functionalities. In the future highly-sensitive fluorescence microscopy may also serve as tool to study the interaction of nanocarriers in more complex systems, such as artificial blood vessels or three-dimensional tissues.

9 Experimental Methods

9.1 Particle preparation

All gene vectors used throughout this thesis were formed by self-assembly from plasmid DNA (equipped with fluorescent-dyes for imaging experiments) and cationic polymers with different functionalities. Polymers were synthesized, purified and characterized by our collaboration partners. Particle assembly was performed, in general, shortly before the experiments in our laboratory. The production of the different polymer-based gene vectors that were studied in this work will be described in the following.

9.1.1 DNA labeling

Plasmid DNA encoding for Luciferase under the CMV promoter (pCMV-Luc, size=6400 bp) was covalently labeled with Cy5 and Cy3 by the Label IT Nucleic Acid Labeling Kit (Mirus, Madison, WI) according to the manufacturer's protocol. The DNA was purified by precipitation with sodium acetate (0.3 M) in ethanol at -80°C overnight. By centrifugation in a refrigerated microcentrifuge at full speed, the DNA was pelleted. The pellet was washed several times with sterile water followed by centrifugation. The purified DNA was resolved in sterile water and stored at -20°C. The concentration of the DNA and the labeling degree was determined in a Nanodrop spectrometer (Thermo Scientific, Wilmington, USA).

9.1.2 Integrin-targeted polyplex micelles with different PEG lengths

Polymer synthesis

Cyclo[RGDfK (CX-)] (c(RGDfK)) peptide (X=6-aminocaproic acid: ϵ -Acp) was purchased from Peptide Institute (Osaka, Japan). Thiolated block copolymers, poly(ethylene glycol)-block-poly(L-lysine-SH) (= PEG-p(Lys-SH)) for RGD(-) micelles and c(RGDfK)-poly(ethylene glycol)-block-poly(L-lysine-SH) (= c(RGDfK)-PEG-p(Lys-SH)) for RGD(+) micelles, were synthesized as previously reported^{281, 282}. The block copolymers used for the formation of PEG17 micelles consisted of a 17000 g/mol PEG, a polylysine segment with a polymerization degree of 73 and a thiolation degree of 15 %. Block copolymers of PEG12 micelles were equipped with a 12000 g/mol PEG and a thiolation degree of 11 %. The number of repeated lysine units and thiolation degree in PEG-p(Lys-SH)s were determined

9. EXPERIMENTAL METHODS

from the peak intensity ratio of the assigned protons to PEG protons in ¹H NMR spectra, according to a previous publication²⁸³. In detail, the lysine unit was calculated from the peak intensity ratio of beta-gamma-delta methylene protons in lysine to methylene protons in PEG. Also, the thiolation degree was calculated from the peak intensity ratio of methylene protons in 3-mercaptopropionyl moiety to methylene protons in PEG. The narrow molecular weight distribution (Mw/Mn~1.12) of the synthesized polymers was confirmed by gel permeation chromatography.

Micelle assembly:

Micelles were generated as reported in^{283, 286}. Briefly, plasmid DNA was ion complexed with thiolated block copolymers (PEG-p(Lys-SH) for RGD(-) micelles or c(RGDfK)-p(Lys-SH) for RGD(+) micelles) at a molar N:P ratio of 2:1 (nitrogen in lysine to phosphate in DNA) in 10 mM Tris-HCl buffer (pH 7.4) supplemented with 10 % volume of 100 mM DTT. Disulfide linkages were formed during dialysis of micelles against 10 mM Tris-HCl buffer. As determined by Ellman's method, more than 90 % of thiol groups were converted to disulfide linkages. Cumulant diameters analyzed by light scattering (Nano SZ zetasizer, ZEN3600, Malvern Instruments, Worcestershire, UK) were approximately 112 nm for PEG12 micelles and 104 nm for PEG17 micelles. Zeta-Potentials measured in 10 mM Tris-HCl, pH 7.4 by laser Doppler electrophoresis using Nano ZS with a He-Ne laser (633 nm) were approximately +1.5 mV for PEG12 and +0.5 mV for PEG17 micelles.

9.1.3 Reversibly shielded PDMAEMA polyplexes

Polymer synthesis

PDMAEMA-SS-PEG-SS-PDMAEMA triblock copolymers were prepared in four steps⁷. Briefly, poly(ethylene glycol) (HO-PEG-OH, 6 kDa, Alfa Aesar) was activated by addition of p-Nitrobenzyl chloroformate (NPC). The resulting NPC-PEG-NPC was mixed with cysteamine-2HCl and triethylamine (Et3N) to achieve Cys-PEG-Cys. Next, a solution of 4-cyanopentanoic acid dithionaphthalenoate (CPADN) and N-hydroxysuccinimide (NHS) was reacted with dicyclohexyl carbodiimide (DCC) to yield NHS-CPADN. Cys-PEG-Cys and NHS-CPADN were mixed to achieve CPADN-SS-PEG-SS-CPADN. For polymerization of the PDMAEMA-SS-PEG-SS-PDMAEMA copolymer, CPADN-SS-PEG-SS-CPADN was incubated with 2-N,N-Dimethylaminoethyl methacrylate (DMAEMA, Alfa Aesar), AIBN and THF.

The non-reducible PDMAEMA-b-PDMAEMA polymer was synthesized in two steps: HO-PEG-OH was reacted with CPADN and DCC to yield CPADN-PEG-CPADN, followed by polymerization with DMAEMA, AIBN and THF.

Polymer characterization was performed by ¹H-NMR spectra and gel permeation chromatography.

Polyplex assembly

The polyplexes were prepared by mixing a HEPES buffer solution (20 mM, pH 7.4) of triblock copolymer to a HEPES buffer solution of plasmid DNA (37.5 µg/mL) at a molar N:P ratio of 12:1. The dispersions were incubated at room temperature for 30 min before cell experiments were carried out. For particle characterization the ξ -potentials and hydrodynamic diameters of polyplexes in HEPES buffer (20 mM, pH 7.4) were determined at 25 °C using a Zetasizer Nano ZS instrument (Malvern) equipped with a standard capillary electrophoresis cell and dynamic light scattering (DLS, 10 mW He-Ne laser, 633 nm wavelength).

9.1.4 Receptor-targeted PEG-PEI polyplexes

Ligand-equipped PEG-PEI polyplexes for EGF receptor targeting, transferrin receptor targeting, integrin targeting and dual receptor targeting were prepared using the same strategy:

Polymer synthesis

Targeted polymers (EGF-PEG-PEI, GE11-PEG-PEI, B6-PEG-PEI) and untargeted polymers (OPSS (orthopyridyl-dithio)-PEG-PEI or Cys-PEG-PEI) contained a 2 kDa polyethylene glycol (PEG) linker conjugated to 22 kDa linear polyethylenimine (PEI) and were synthesized as described recently^{314, 318}. Briefly, linear PEI with an average molecular weight of 22 kDa was synthesized according to Brissault et al.³⁴⁵ and purified by gel filtration. The linear PEI was then incubated for 20 hours with a surplus of OPSS-PEG-NHS spacer (Ortho-Pyridyldithio (OPSS)-polyethylene glycol (PEG(2kDa)) -N-Hydroxylsuccinimide ester, Nektar, San Carlos, USA) to gain OPSS-PEG-PEI. Targeting ligands were activated by reaction with SPDP (N-succinimidyl 6-(3-(2-pyridyldithio)-propionate) resulting in ligand-PDP (ligand-(2-pyridyldithio) propionate). Reduction in DTT (dithiothreitol) was then performed to gain thiolated Ligand-SH. Thiolated ligands were reacted with OPSS-PEG-PEI followed by gel filtration to yield the targeted polymers ligand-PEG-PEI. RGD-equipped polymers were synthesized analogously but contained branching PEI (bPEI 25 kDa, Sigma, Germany) and 3.4 kDa PEG. The B6 peptide (Ac-CGHKAKGPRKNH₂, 1122 Da) and the RGD peptide (H- β A-C1DC2RGDC3FC4-NH₂, C1C4/C2C3-bicyclo, 955 Da) were obtained from IRIS Biotech (Marktredwitz, Germany), recombinant 6 kDa murine EGF from Prepro Tech EC (London, UK) and GE11 (CYHWYGYTPQNV_I) from Biosyntan (Berlin, Germany).

Particle assembly

Prior to each experiment, polyplexes were generated freshly in HEPES buffered glucose (HBG, 20 mM HEPES pH 7.1, 5 % glucose w/v) at a molar N:P ratio of 6:1 (nitrogen in LPEI to phosphate in pDNA) and a final pDNA concentration of 20 µg/ml (20 % of labeled DNA were mixed with 80 % unlabeled DNA). For the formation of EGF polyplexes 10 % of EGF-PEG-PEI was mixed with 90 % untargeted OPSS-PEG-PEI, for GE11 polyplexes 100 % GE11-PEG-PEI was applied. For B6-PEG-PEI, RGD-PEG-PEI and dual-targeted polyplexes, a series of particles with 5 to 100 % targeted polymer were prepared. Light scattering (Zetasizer 3000 HS, Malvern Instruments, Worcestershire, UK) revealed cumulant diameters in a range of 90 to 120 nm in HBG buffer of the formed polyplexes³¹⁴.

9. EXPERIMENTAL METHODS

9.1.5 Dendrimer hybrids for gene and drug delivery

Dendrimer synthesis

The 4-arm-PEG-G4 dendrimer hybrid was prepared in four steps. In step one, a tetra-amine PEG (10 kDa, Laysan Bio) was incubated with glycidyl propargyl ether (Santa Cruz Biotechnology) in MeOH to give the tetraalkyne dendrimer 4-arm-PEG-G1, which was precipitated into ether and collected by filtration. In step two, the product was mixed with cysteamine hydrochloride and DMPA (2,2-dimethoxy-2-phenylacetophenone, Sigma Aldrich) under UV-light in MeOH to give dendrimer 4-arm-PEG-G2. The solution was dialyzed and freeze dried. In a third step, glycidyl propargyl ether and DIPEA (N,N-diisopropylethylamine, TCI America) were added to give dendrimer 4-arm-PEG-G3, which was again purified by precipitation and filtration. In step four, cysteamine hydrochloride and DMPA were added to achieve the final 4-arm-PEG-G4.

The 2-arm-PEG-G4 dendrimer was prepared analogously with 10 kDa bis-amine PEG as starting material (for details see³³⁷). For internal coumarin loading, functionalization of the internal hydroxyl groups was performed at the terminal alkyne stage of the synthesis (2-arm-PEG-G3) by esterification with an excess of 7-(diethylamino)-coumarin-3-carbonyl chloride. The internally functionalized derivative, was dialyzed to remove excess coumarin, followed by thermal thiol-yne coupling with cysteamine hydrochloride in the presence of AIBN to give the hybrid dendritic structure (2-arm-PEG-G4-(coumarin)₂₀). For fluorescent dye-labeling, dendrimers were conjugated with Alexa647 fluorophores. Conjugation has been carried out via amide bond between the primary amine of the dendrimer and the N-hydroxysuccinimide activated carboxyl of the fluorophores.

Particle formation

Dendriplexes were generated by incubating DNA (Cy5-labeled pCMVLuc for single particle imaging experiments, unlabeled peGFPNuc for gene expression) with different dendrimers at N:P=4:1 for 30 minutes at room temperature in HBG buffer (20 mM Hepes pH 7.1, 5 % glucose w/v). DNA binding by the dendrimers was monitored by an ethidium bromide intercalation assay. Therefore, ethidium bromide (1 µg/ml) and DNA (3 µg/ml) were dissolved in 0.05 mol/l Tris-HCl buffer with 50 mmol/l NaCl (pH = 7.4). The fluorescence spectra of ethidium bromide (EB) in the presence of DNA before and after addition of dendrimers were taken with a Cary Eclipse fluorimeter. EB was excited at 477 nm and the emission spectra were recorded from 490 to 850 nm. A sample of EB with dendrimer was studied to check that no interaction of the macromolecule with the dye occurred.

9.1.6 Sequence defined STP Polymers from solid phase synthesis

Polymer synthesis

Sequence defined polymers with succinoyl tetraethylene pentamine (STP) building blocks were synthesized manually by Ulrich Lächelt (group of Prof. Wagner, LMU) under standard Fmoc solid phase peptide synthesis conditions using syringe microreactors as described recently³³⁸. Coupling of STP building blocks, PEG or aminoacids (histidines as endosomal escape agent, lysines as branching points, cyteines as stabilization units, alanines as non-functional substitutions) was carried out by using Fmoc protected versions of them. Deprotection was performed by incubation with piperidine. After each coupling and deprotection step a washing procedure was performed. As targeting ligands, B6 peptides (sequence: GHKAKGPRK), CMBP peptides, or 6kDa recombinant EGF were used.

All polymers were purified by size exclusion chromatography.

For calcein release assays receptor-targeted, PEGylated polymers with two-arm topology were used (B6-His = KRPGKAKHG-(dPEG24)₂-AK[A-(STP-A)₄-C]₂, B6-Ala = KRPGKAKHG-(dPEG24)₂-HK[H-(STP-H)₄-C]₂). EGF-STP polyplexes were synthesized analogously, with some modifications. By solid-phase synthesis an untargeted construct with an activatable linker was produced that subsequently was coupled to EGF in solution resulting in EGF-PEG-STP= EGF-Triazol-PEG24-K(STP4-C)₂.

Particle assembly

Prior to each experiment, STP polyplexes were generated freshly from frozen polymer stock and DNA stock. Mixing of polymer and DNA at a molar N:P ratio of 12:1 in HEPES buffered glucose (HBG, 20 mM HEPES pH 7.1, 5 % glucose w/v) was performed on ice with a final pDNA concentration of 20 µg/ml (20 % of labeled DNA were mixed with 80 % unlabeled DNA), followed by incubation for 40 minutes at room temperature.

9. EXPERIMENTAL METHODS

9.2 Cell culture

HeLa (cervical cancer cells), HuH7 (human hepatocellular carcinoma cells) and DU145 cells (human prostate cancer cells) were grown at 37 °C in 5 % CO₂ humidified atmosphere.

HeLa cells were cultivated in Dulbecco's modified Eagle medium (DMEM) (Gibco®, Invitrogen™ GmbH, Karlsruhe, Germany) supplemented with 10 % fetal bovine serum (FBS, Gibco®). Wild-type HuH7 cells (JCRB 0403, Tokyo, Japan), Rab9-GFP expressing HuH7 cells and Caveolin-GFP expressing HuH7 cells (plasmid Cav1-eGFP was kindly provided by Ari Helenius, ETH Zurich; stably transfected cells were prepared by Dr. Nadia Ruthardt) were cultivated in DMEM/F12 (Gibco®) with 10 % FBS. Before seeding of HuH7 cells, FBS was replaced by B27 supplement (Gibco®). DU145 cells were grown in RPMI 1640 medium (with glutamine, Gibco®) supplemented with 10% FBS. For live-cell imaging, cells were seeded at a density of 1.0×10^4 - 2.0×10^4 per well into a collagen coated 8 well-chambered Lab-Tek slide (Nunc, Rochester, NY) or 8-well chambered ibiTreat μ -Slides (Ibidi GmbH, Munich) 24-48 hours before particle addition. Ibidi Luer μ -slides I^{0.4} (Ibidi GmbH, Martinsried, Germany) treated with collagen A suspension (Biochrom AG) were used for experiments under flow. 4.0×10^5 cells were seeded per channel 48 hours before imaging. Cells were imaged in CO₂-independent medium (Invitrogen) supplemented with FBS on a heated microscope stage at 37 °C.

9.3 Single-cell imaging

9.3.1 Particle addition

For cell experiments, particles can either be diluted in cell medium followed by slow sedimentation and attachment of particles over time, or pipetted in a small volume on top of the cells to achieve immediate contact of particles with cells. For imaging experiments with a defined starting point (uptake kinetics, quantification of uptake efficiencies), we applied the second method; the cell medium was removed down to a thin fluid film followed by addition of suspended particles (volume 3-5 μ l). One minute post particle addition the removed medium was resupplied.

For experiments that should be performed analogue to bulk reporter gene expression experiments, larger volumes (100-400 μ l) were applied. For each set of experiments standardized concentrations of DNA, incorporated into polyplexes, were applied.

RGD polyplex micelles (chapter 4.1): low dose = 5 ng of DNA per well in 3 μ l volume (8-well slide), in case of colocalization 2.5 ng DNA per micelles type, high dose = 264 ng DNA per well in 100 μ l volume, for colocalization 132 ng per micelle type; PDMAEMA polyplex (chapter 4.2): 210 ng per well in 110 μ l volume, medium exchange after 5 hours, EGFR-targeted PEI polyplexes (chapter 5.1): 60 ng DNA per well for widefield microscopy, 120 ng per well for spinning disk microscopy (3 and 6 μ l volume); B6- and RGD PEI polyplexes (chapter 5.2): 80 ng DNA per well (4 μ l volume); dendriplexes (chapter 6.1 and 6.2): 400 ng DNA per well in 240 μ l, medium exchange after 5 hours; STP polyplexes (chapter 6.3); 60 ng of DNA in 200 μ l, STP His polyplexes (chapter 7.1): 400 ng DNA in 200 μ l medium.

9.3.2 Particle quenching

Fluorescence of Cy3-labeled ligand-PEG-PEI polyplexes (40 ng of DNA per well, added at defined starting point) was quenched at the indicating time-points by resuspending 2 μ l of 0.4 % trypan blue solution (Sigma-Aldrich, Germany) into 350 μ l medium of the observation chamber during image acquisition at the widefield microscope (frame rate 500 ms). As trypan blue is membrane impermeable only extracellular particles are quenched. To determine the internalization degree (= number of detected particles after quenching / number of detected particles before quenching), fluorescent polyplexes were counted with a custom-designed analysis software written in Matlab and Labview using an intensity threshold criterion and a defined size restriction. Prior to the analysis, the quenching behavior of particles in cell-free slides was examined and the concentration of trypan blue was adjusted to confirm successful fluorescence quenching and low increase of background fluorescence after trypan blue addition. These control measurements were also used to determine the parameters (intensity threshold and particle size) for the particle counting software. For quenching of Cy3-labeled RGD-equipped polyplex micelles, 3 μ l of trypan blue was added to 400 μ l cell medium.

9.3.3 Markers of cellular compartments

As a marker for clathrin-mediated endocytosis, 2.5 μ g/ml Alexa 488-labeled transferrin (Invitrogen, Karlsruhe, Germany) was coincubated with Cy5-labeled particles. Control experiments excluded direct interactions of transferrin and particles in the cell medium.

For detection of caveolin-mediated endocytosis, particles were incubated on stable caveolin-GFP expressing cells. Alternatively, caveolin-dependent endocytosis was imaged by addition of BodipyFL Lactosylceramide (Sigma-Aldrich, Germany) to cells.

Stable Rab9-GFP expressing cells were applied to detect transport into late endosomal compartments.

To stain the plasma membrane of cells, 2.5 μ g/ml Wheat Germ Agglutinin (WGA)-AlexaFluor488 conjugate (Invitrogen, Karlsruhe, Germany) was added prior to imaging.

9.3.4 Dead cell staining

A trypan blue assay was used for dead cell staining. Trypan blue (Sigma-Aldrich, Germany) is a commonly used dye that is membrane impermeable and therefore does not pass the membrane of viable cells. Control cells were treated with cytotoxic ethanol (25% vol in cell medium). Trypan blue treated cells (2 μ l of 0,4% trypan blue solution added to 400 μ l medium), were imaged by widefield microscopy with 633 nm laser excitation shortly after trypan blue addition.

9. EXPERIMENTAL METHODS

9.3.5 Inhibition of endocytic pathways

For inhibition of clathrin-mediated endocytosis, cells were preincubated with 10 µg/ml chlorpromazine (Sigma-Aldrich, Germany) in CO₂-independent medium supplemented with FBS for 30 minutes. RGD-equipped polyplex micelles were then added in the presence of chlorpromazine at a DNA concentration of 264 ng, together with 2.5 µg/ml Alexa Fluor 488 transferrin (Invitrogen) as a positive marker for clathrin inhibition. Treated cells were imaged 2-3 hours post micelle addition by spinning disk confocal microscopy. Cell medium was changed to fresh, chlorpromazine containing medium before imaging to reduce background fluorescence by non-internalized fluorophores. To prove the membrane integrity of cells in the presence chlorpromazine, a trypan blue exclusion assay was performed with cells treated with 10 µg/ml chlorpromazine for 4 hours. To prove functional caveolin-dependent endocytosis in chlorpromazine treated cells, control cells were coincubated with 0.8 µM Bodipy FL lactosylceramide (Invitrogen) and 2.5 µg/ml Alexa Fluor 633 transferrin (Invitrogen) for 2.5 hours, before imaging with spinning disk confocal microscopy using alternating laser excitation.

9.3.6 Receptor signaling assays

For inhibition of EGFR phosphorylation, serum containing cell medium was replaced by serum-free DMEM/F12, 16-18 hours before polyplex application. One hour before polyplex addition, cells were treated with 10 µM Tyrphostin AG1478 hydrochloride (N-(3-Chlorophenyl)-6,7-dimethoxy-4-quinazolinane hydrochloride, storage of stock solution 10 mM in DMSO), (Tocris Biosciences, Bristol UK), diluted in serum-free CO₂-independent medium with 0.2 % BSA. Reference cells were kept in serum-free medium without inhibitor treatment. Control experiments confirmed that polyplex internalization was not affected by DMSO at the applied concentration. To evaluate the influence of serum starvation, experiments were additionally performed with non-starved cells in the presence of 10 % FBS. We also used Erlotinib Hydrochloride for inhibition of EGFR expression, but some cells showed resistance to the drug.

9.3.7 Fixation of cells

To stop particle endocytosis at a defined point of time for subsequent quantification of the internalization degree, cells were fixed with paraformaldehyde (Electron Microscopy Sciences, Hatfield) in PBS. Cells were washed once in phosphate buffered saline buffer (PBS, Invitrogen) before addition of 4 % paraformaldehyde for 15 minutes. After fixation cells were kept in PBS.

9.3.8 Calcein Release Assay

For calcein release assay with B6-PEG-STP polyplexes, 10.000 DU145 cells per well were seeded on Ibidi µ-slides (Ibidi GmbH, Planegg/Martinsried, Germany) 48 hours prior to particle addition. 20 µl of polyplexes (400 ng DNA, N/P 16) were coincubated with 0.5 mg/ml calcein in 200 µl RPMI medium containing 10 % FCS for 3.5 hours on the cells. Afterwards cells were washed 4 times with PBS, and medium was replaced with 300 µl CO₂-independent medium containing 10% FBS. Z-slices of single

cells were imaged by spinning disk confocal microscopy with 488 nm laser excitation.

For CMPB-PEG-STP polyplexes, 400 ng DNA (N:P=12:1) were added to 200 µl fresh RPMI medium on DU145 cells. 40 minutes post particle addition the cell medium was removed and replaced by 300 µl fresh RPMI medium containing 0.5 mg/ml calcein. 20 hours post particle addition; cells were imaged with 488 nm laser excitation (calcein signal) after 2 washing steps with PBS in CO₂-independent medium containing 10% FCS by spinning disk confocal microscopy and z-projections of single cells were built.

To quantify the calcein signal in the cytoplasm, a lower threshold 1 was set to exclude background signal and a higher threshold 2 was set to exclude the calcein signal from endosomes. For selected pixels above threshold 1 and below threshold 2, the mean fluorescence intensity as well as the total integrated density (= mean fluorescence intensity of pixels x pixel area) was determined.

9.3.9 GFPnuc expression

To evaluate the transfection potential of dendriplexes, cells were seeded in 8-well chambered ibiTreat µ-Slides (Ibidi GmbH, Munich) and transfected with 400 ng peGFPnuc plasmid complexes by 4-arm and 2-arm PEG dendrimer hybrids. 5 hours post particle addition, medium was exchanged. GFPnuc expression was detected after 40 hours of incubation by widefield microscopy with a 10x or 20x objective. The total fluorescence signal per field of view was calculated in ImageJ by summing all pixel intensities above a set intensity threshold.

9.4 Bulk cell assays

9.4.1 Flow cytometry

Flow cytometry was applied by our collaboration partners to quantify cell-associated and internalized particles in a large number of cells. Therefore the cells of interest were plated into 24-well slides. Labeled particles were applied at a DNA concentration of 1 µg per well and incubated for the indicated time period (24 hours for RGD-polyplex micelles). Afterwards, cells were washed in PBS. To remove extracellular polyplexes, the washing buffer contained 100 I.U. of heparin in some experiments. Next, cells were detached with trypsin-EDTA solution and suspended in PBS. The fluorescence intensity from suspended cells was measured in a flow cytometer (BD LSR II flow cytometer, BD Biosciences for RGD micelles). DAPI (4',6-diamidino-2-phenylindole) was used to discriminate between viable and dead cells.

9.4.2 Luciferase reporter gene expression

To determine the transfection efficiency of the different polyplex types studied in this thesis, our collaboration partners performed standard luciferase reporter gene expression assays.

For the assay, the cells of interest were seeded on a multiwell plate 24 hours before particle addition. Particles containing luciferase encoding plasmid DNA were added at defined DNA concentration and

9. EXPERIMENTAL METHODS

incubation time. Following this incubation period the luciferase gene expression was evaluated by a Luciferase Assay Kit (Promega, Madison, WI) using photoluminescence detection in a plate reader (Berthold Technologies, Milbach, Germany). Transfection efficiencies were expressed as relative light units (RLU) per mg protein or per 10.000 cells. (For RGD+ polyplex micelles: 1 µg DNA per well in 24-well slide, 48 hours incubation; for STP polyplexes: 200 ng DNA per well in 96-well slide, 24 hours incubation (medium exchange after 40 minutes); for PDMAEMA polyplexes: 1 µg DNA per well in 12-well plate, 48 hours incubation).

9.4.3 Western Blotting

Western Blotting was performed to detect EGF receptor phosphorylation after polyplex binding to cells. For the assay, HuH7 cells were seeded at a density of 2×10^5 in 6 well plates. The next day, medium was replaced by 2 ml of fresh medium containing 100 µl of polyplexes, equivalent to 2 µg of DNA. As positive control, cells were treated with 108 pmol of free EGF; untreated cells were used as negative control. After 45 minutes of incubation at 37 °C, cells were washed with PBS followed by addition of 100 µl lysis buffer (Promega) supplemented with protease inhibitor cocktail (Roche, Germany) and phosphatase inhibitor cocktail I+II (Sigma-Aldrich, Germany). Cells were harvested with a cell scraper and incubated in lysis buffer for further 20 minutes on ice. Cell debris was removed by centrifugation for 15 minutes at 13.000 rpm and 4 °C. 40 µg of soluble protein (determined by Bradford assay) was separated by polyacrylamide gel electrophoresis and blotted onto a polyvinylidene fluoride membrane. Unspecific binding sites were blocked by incubation with 5 % non-fat milk for one hour. Immunostaining was performed over night at 4 °C with monoclonal mouse anti-phospho-ERK (dilution 1:2000) and polyclonal rabbit anti-ERK antibodies (dilution 1:5000) (New England Biolabs, Beverly, MA, USA). Horse radish peroxidase conjugated secondary anti-mouse and anti-rabbit antibodies (Vector Labs, Burlingame, CA, USA) chemiluminescence detection kit (ECL, Amersham, Arlington Heights, IL, USA) were used for visualization.

9.5 Microscopical setup

9.5.1 Wide-field fluorescence microscopy

Wide-field fluorescence microscopy was performed at the indicated time-points on a custom built setup based on the Nikon Ti microscope equipped with a Plan Apo 60x, 1.49 NA oil immersion objective and a heated microscope stage (37°C). Cy3- and Cy5-labeled particles were excited with 532 nm and 633 nm laser light, GFP with 488 nm laser light (300 or 500 ms per frame). For dual color imaging, alternating excitation was used. Fluorescence was collected in epifluorescence mode, split into two emission channels by a dichroic mirror (565 DCXR, Chroma) and passed through filter sets (Cy3 or GFP and 725/150, semrock). The green and red emission channels were projected onto two EMCCD cameras (DU-897 iXon+, Andor) with an image size of 61 µm x 61 µm for the 60x objective. Laser powers were optimized for each sample to receive maximum signal to noise ratio and low autofluorescence background. Overlay images were post-processed with ImageJ. To control the viability of cells, transmission light images of the treated cells were recorded.

The region of the nucleus and the plasma membrane were identified in the transmission light images and transferred to the fluorescence overlay images.

9.5.2 Spinning disk confocal microscopy

Spinning disk confocal microscopy was performed on a setup based on the Nikon TE2000E microscope and the Yokogawa spinning disk unit CSU10. The system was equipped with a Nikon 1.49 NA 100x Plan Apo oil immersion objective. 488 nm laser light was applied for the excitation of GFP, calcein, Alexa 488 and Atto 488 fluorophores, 640 nm laser light for the excitation of Cy5, Atto 633 and Alexa 647 fluorophores; coumarins were excited with 405 nm laser light. For two color detection, alternating laser excitation was used with a frame rate of 300 to 500 ms per frame. Confocal z-stacks of cells were imaged with a spacing of 166 nm between two planes. Fluorescence was split into two emission channels by a dichroic mirror (565DCXR chroma) and passed through appropriate filter sets (for 488 nm and 640 nm laser excitation: 525/50 and 730/140 filter, semrock). Image sequences were captured with an EM-CCD camera (iXon DV884; Andor), image size = 31 μm x 63 μm for each channel with 100x objective. Displayed images were post-processed with ImageJ.

9.6 Microfluidic setup

9.6.1 SAW system

The surface acoustic wave (SAW) driven microfluidic device used in the work was kindly provided by the group of Prof. Wixforth from Augsburg University. In the device, a loop channel without external fluid connections is equipped with an integrated acoustic micro pump^{346, 347}. The acoustic micropump, consisting of an interdigital transducer on a piezoelectric material, generates a surface acoustic wave after excitation with a high frequency signal. When the wave enters the water-filled channel a pressure-driven directed flow is induced (acoustic streaming effect). The loop channel with a volume of 180 μl is embedded in a PDMS chamber (produced with an Elastomer Kit (SYLGARD 184 Silicon Elastomer Kit, Dow Corning)) that is sealed with a coverglass. Before use, the PDMS chamber was cleaned in 0.5 % Helmanex followed by sonication. Assembled chambers were treated by plasma cleaning (20 kHz, 50 minutes; FEMTO, Diener) to enhance their stability. For cell seeding (2×10^4 cells per channel) the chamber was coated with collagen. To study particle movements under flow, tetraspeck Beads (FluoroSpheres, 0.17 μm , deep red fluorescent), were pipetted directly into the channel and the flow was generated under microscopical observation on the widefield microscope.

9.6.2 Syringe pump device

In the syringe pump microfluidic device, the flow is generated by an external engine driven syringe pump that is connected to a linear microfluidic channel via external tubings. The device was set up by Ellen Broda during her master's thesis. It contains a medium filled reservoir that is heated to 37°C and stirred continuously. For the measurements, polyplexes were added to the reservoir (20 μl polyplex solution equivalent to 400 ng DNA were applied to 56 ml medium). By starting the engine of the pump

9. EXPERIMENTAL METHODS

(PHD 2000 Programmable, Harvard Apparatus, Holliston, USA) the plunger of the mounted syringe (Terumo, 10 ml or 60 ml) mechanically drives backwards and the fluid from the reservoir is flushed through flexible tubes (Tygon, 1.6 mm diameter) into the microfluidic channels (Ibidi GmbH, Martinsried, Germany) generating a continuous flow. Flow chambers were coated with collagen or with cells. All compartments, syringe, flexible tubes, flow chamber and reservoir were filled with fluid prior to the experiments and were carefully assembled to prevent the formation of air bubbles in the system. A constant flow rate of 2 ml/min was applied in our experiments. Polyplex adhesion under flow was detected over 30 minutes by widefield microscopy with 633 nm laser excitation. To image the total amount of particles on a cell, the focus was adjusted manually along the z-axis during image acquisition from the top to the bottom of the cell. Subsequently z-projections of the obtained image sequences were built in ImageJ and particles were counted by custom-build software provided by Dr. Volodymyr Kydryavtsev, using a size-restriction of counted particles and an intensity threshold for particle identification. To compare different polyplex types with variable number of formed particles in solution, an external control was applied. For the control, a defined volume of polyplex suspension was pipetted into a collagen coated well (0.8 cm²) filled with 200 µl cell medium. After a set time-interval, sedimented particles on the collagen surface were detected, and the counted number from 10 pictures was averaged as control number. According to the calculated control number, the number of detected particles counted in the flow chamber was normalized. For cell measurements, only particles on top of the cell and not on the coverglass were counted and the number of particles was additionally normalized to the region of the cell.

9.7 Micromanipulator for cytoplasmic injection

For microinjection of proteins into the cytoplasm we used a commercially available InjectMan® NI micromanipulator (Eppendorf, Hamburg, Germany) equipped with a Femtojet® microinjector (Eppendorf). Samples were centrifugated at full speed in a microcentrifuge to remove aggregates and the supernatant was loaded into sterile femtotips (Eppendorf, Hamburg, Germany). Microinjection was performed according to the manufacturer's protocol with an injection pressure of $p_i = 150$ hPa and an injection time $t_i = 0.7$ s. The microinjector was set-up on the confocal spinning disk microscope, for phase contrast imaging of cells during microinjection a long working distance condenser and a 20 x and 40x dry objective were used. To relocate injected cells after exchange of the objective to higher magnification (100 x, oil immersion objective) for fluorescence imaging, cells were seeded on a 35 mm µ-dish with an integrated grid (Ibidi, Martinsried, Germany).

9.8 Data analysis

9.8.1 Image calibration and editing

To allow the comparison of signals from two emission channels, the channels need to be geometrically calibrated. Therefore, a reference image of Tetraspeck microspheres (fluorescent blue-green-orange-darkred, Invitrogen) spin-coated on a cover-glass was recorded for each set of experiments. A program which allows the calibration of one channel with respect to another was written in Labview and Matlab by Dr. Volodymyr Kydryavtsev. In the program, corresponding particles in each channel are selected and a transformation matrix is determined to correct linear and non-linear distortions of the channels.

For the processing of obtained raw images and movies (cutting images, overlay of images, selection of slices, thresholding, background subtraction, histogram analysis, formation of time-projections or z-projections, color coding, introduction of scale bars) the freely available ImageJ software was used. The ImageJ software was further applied to quantify the mean fluorescence intensity and total integrated density of particles or regions of interest above or below a set intensity threshold.

9.8.2 Particle counting

To count the number of particles on cells (e.g. in adhesion experiments under flow or quenching experiments) the software program "Count Colocalized Particles" written by Dr. Volodymyr Kudryavtsev was used.

Particles were identified by the following criteria: an intensity threshold that is adjusted dynamically, the particle size and the minimum distance between two neighbored particles to exclude aggregates. The dynamic intensity threshold was calculated for each image based on the intensity of each pixel in the image: A Gaussian fit of the pixel intensity distribution was performed, the center of the Gaussian fit I_{center} and the width of the distribution σ were determined. The corresponding threshold was given by $\text{threshold} = I_{\text{center}} + n \cdot \sigma$.

9.8.3 Particle tracking

To track particles in the microfluidic channel, the Manual Tracker Plugin from Image J was applied. During tracking the center of the particle has to be selected manually in each frame. The plugin then searches in a defined radius around the selected spot for the brightest pixel to improve the centering and calculates the particle velocity for each step.

9. EXPERIMENTAL METHODS

9.8.3 Colocalization analysis

For the quantification of the colocalization degree in the recorded movies, the green and the red channel were geometrically calibrated according to control measurements with 0.17 μm tetraspeck beads (Invitrogen, Karlsruhe, Germany). To enhance the signal to noise ratio in the images, median background subtraction was performed in ImageJ. (In case of colocalization of RGD(+) and RGD(-) polyplex micelles, widefield images were analyzed, in case of colocalization of PDMAEMA polyplexes with Rab9 GFP confocal z-projections (maximum intensity) were evaluated). Fluorescent spots were counted in both channels with custom-built software, written in Labview and Matlab by Dr. Volodymyr Kudryavtsev, using an intensity threshold criterion and a defined size restriction. Fluorescent spots were determined as colocalized in case the mean fluorescence intensities in both fluorescent channels were above the defined threshold. Optimized parameters were kept constant for all evaluated images. To calculate the degree of colocalization, the number of colocalized spots was divided by the total number of spots in the reference channel. For the histogram, the mean value of all analyzed cells was calculated. P-values were determined by Student's t-test.

9.8.4 Nano_In_Cell_3D

To quantify the degree of internalized Cy5 polyplexes in treated cells, acquired confocal cross-sections were evaluated using the custom-designed, semi-automated ImageJ macro "Nano_In_Cell_3D" published recently by Adriano Torrano and Dr. Julia Blechinger [<http://imagejdocu.tudor.lu>]³²⁸. On the basis of the membrane staining with WGA-AlexaFluor488, a three-dimensional image of the cell is reconstructed. For identification of the cell, the top and the bottom slide have to be selected in the acquired stack. The macro then creates a three dimensional mask of the cell, which can be corrected manually if required. In the following step, a background value and the threshold value for particles as well as the width of the membrane region is entered for analysis. The macro then assigns whether identified particles are inside or outside the cell or in the membrane region by overlying the membrane and the particle images. By analyzing the integrated fluorescence intensity of particles/endosomes in membrane region and inside the cell the uptake efficiency can be determined:

$$\text{uptake efficiency} = \frac{\text{integrated fluorescence intensity in intracellular region}}{\text{integrated fluorescence intensity (membrane region+intracellular region)}}$$

In addition to the report from quantification, a color coded image stack of the cell is displayed by the program.

Appendix

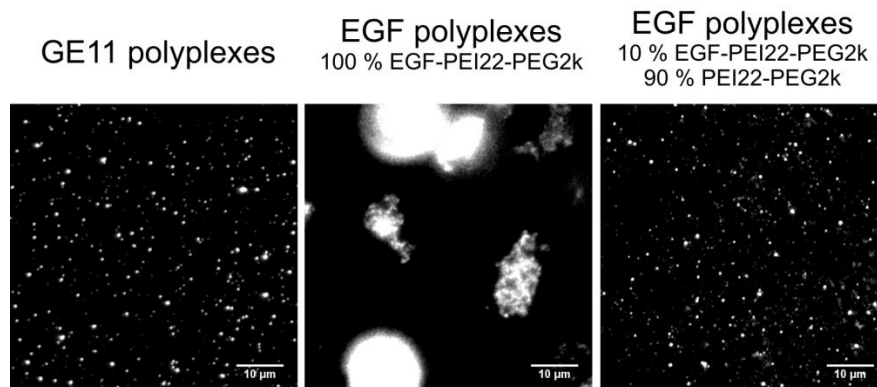


Figure A1. Reduced aggregation of polyplexes with GE11 ligand. EGF receptor-targeted polyplexes formed from Cy5-labeled plasmid DNA and 100 % GE11-equipped polymer (left image), 100 % EGF-equipped polymer (central image) or a mixture of 10 % EGF-equipped polymer and 90 % untargeted polymer (right image) were spincoated on a coverglass and imaged by widefield microscopy. Hydrophobicity of EGF induces particle aggregation at high ligand concentration. Therefore polyplexes with 10 % EGF ligand were applied in our experiments.

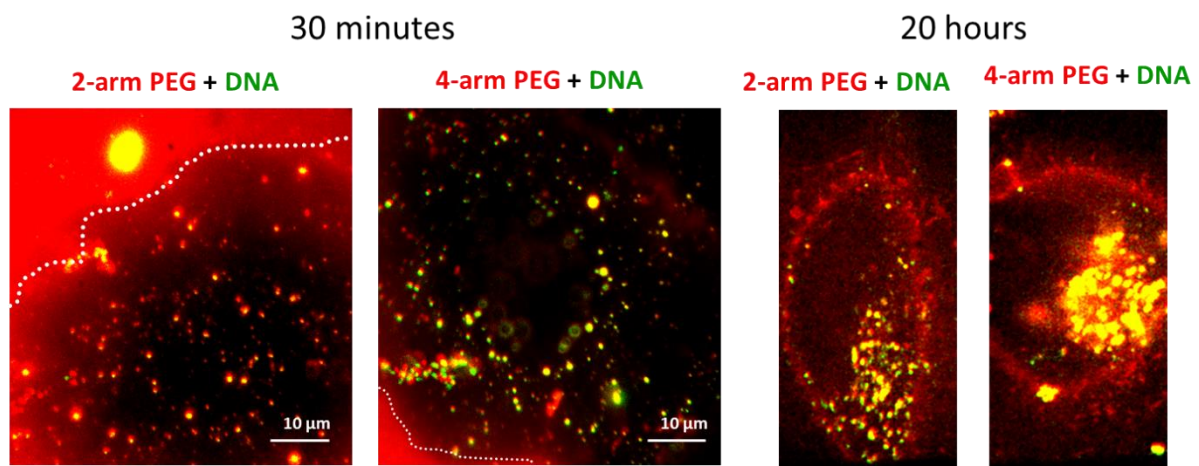


Figure A2. Integrity of dendriplexes confirmed by dual color imaging. Dendriplexes containing Cy3-labeled DNA (green signal) and AF647-labeled dendrimer (red signal) were imaged by alternating laser excitation after 30 minutes (left side) and 20 hours (right side) incubation on HeLa cells. Overlay images of both fluorescence channels are presented (widefield images are shown for 30 minutes incubation, whereas confocal images are depicted for 20 hour incubation). 4-arm PEG dendrimer hybrids and 2-arm PEG dendrimer hybrids are compared. Colocalization of DNA and dendrimer (yellow signal) reveals binding and internalization of intact dendriplexes. An excess of free dendrimer is observed in the samples with high affinity to the coverglass. To visualize the cell morphology the plasma membrane of cells was additionally stained in red after 20 hours of incubation.

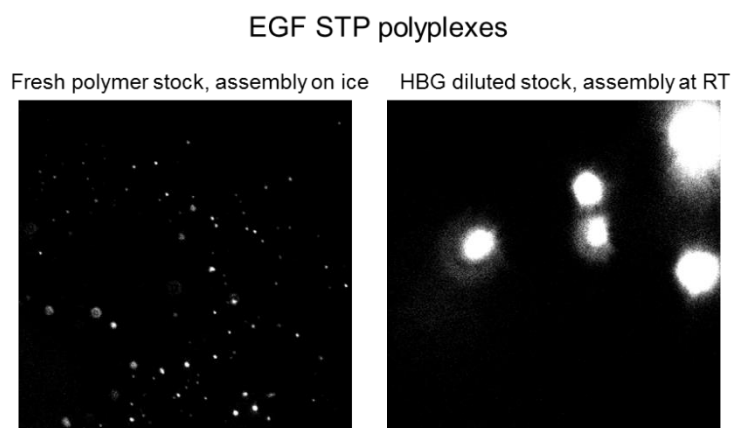


Fig. A3. Effect of polymer handling on the formation of STP polyplexes. Small particles with homogeneous size distribution are formed on ice when using fresh polymer solution (left image), whereas aggregated particles are observed for HBG diluted polymer stock and incubation at room temperature (right image). To prevent oxidation of cysteine equipped polymers prior to particle complexation, the stock polymer should be diluted in water, stored at -80 degrees and freeze-thawing cycles should be avoided. Mixture of polymer and DNA should be performed on ice.

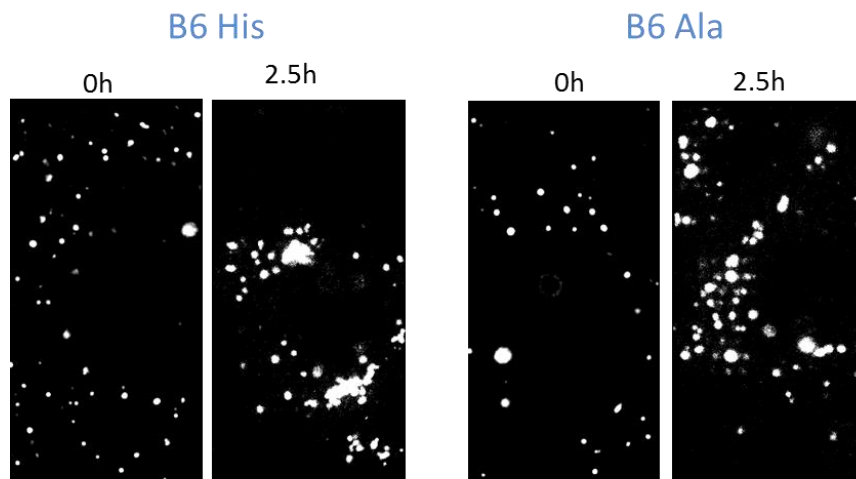


Fig A4. Comparable cell binding and uptake of B6-PEG-STP polyplexes with histidine (B6 His, left image) or alanine modification (B6 Ala, right image). Confocal images of single cells recorded by spinning disk confocal microscopy immediately after particle addition (0h) or after 2.5 hours of incubation are presented. Homogenously sized particles attached to the cell surface with high affinity. Both particle types were incorporated in intracellular compartments after 2.5 hours, as indicated by an intensity increase of the detected spots, their central localization close to the cell nucleus and typical intracellular motion (diffusion and directed transport) observed in the recorded movies.

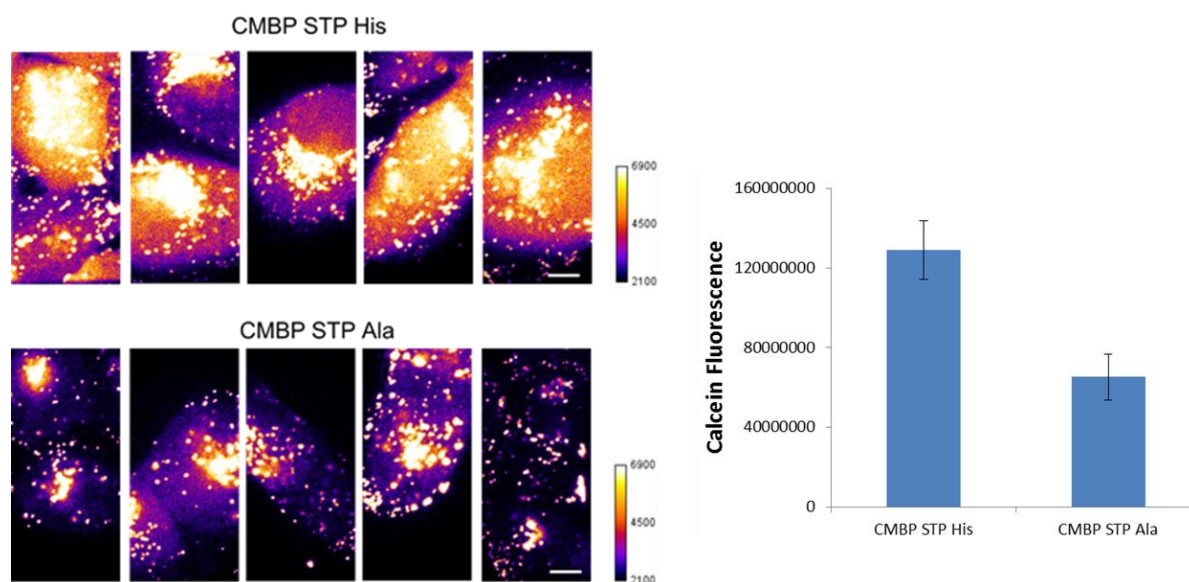


Figure A5. Calcein Release assay with hepatocyte growth factor receptor-targeted STP polyplexes. C-Met binding peptide (CMBP)-equipped polyplexes with **(A)** histidine as endosomal escape agent (CMBP STP His) or with **(B)** alanine substitution (CMBP STP Ala) were coincubated with 0.5 mg/ml calcein on transferrin receptor overexpressing DU145 cells. Calcein release from endosomes was imaged with 488 nm laser excitation after 20 hours of incubation by spinning disk confocal microscopy. Images of five representative cells are depicted, the fluorescence intensity is color coded with orange and white regions exhibiting highest calcein fluorescence. **(C)** Calcein fluorescence in the cytoplasm was quantified by digital image analysis. Mean values of all evaluated cells are presented (N=20 cells), the standard error is depicted by error bars. A significant increase in calcein release from endosomes is observed for the histidine analogue.

Bibliography

1. Richards, S. in *Scientist Magazine* (2012).
2. Nathwani, A.C. et al. Adenovirus-Associated Virus Vector–Mediated Gene Transfer in Hemophilia B. *New England Journal of Medicine* **365**, 2357-2365 (2011).
3. Gaspar, H.B. et al. Hematopoietic stem cell gene therapy for adenosine deaminase-deficient severe combined immunodeficiency leads to long-term immunological recovery and metabolic correction. *Science translational medicine* **3**, 97 (2011).
4. Porter, D.L., Levine, B.L., Kalos, M., Bagg, A. & June, C.H. Chimeric antigen receptor-modified T cells in chronic lymphoid leukemia. *The New England journal of medicine* **365**, 725-733 (2011).
5. Hacein-Bey-Abina, S. et al. LMO2-associated clonal T cell proliferation in two patients after gene therapy for SCID-X1. *Science* **302**, 415-419 (2003).
6. Mickler, F. M., Vachutinsky, Y., Oba, M., Miyata, K., Nishiyama, N., Kataoka, K., Bräuchle, C. and Ruthardt, N. Effect of integrin targeting and PEG shielding on polyplex micelle internalization studied by live-cell imaging. *Journal of Controlled Release* **156**, 364-373 (2011).
7. Zhu, C., Zheng, M., Meng, F., Mickler, F.M., Ruthardt, N, Zhu, X. and Zhong, Z. Reversibly Shielded DNA Polyplexes Based on Bioreducible PDMAEMA-SS-PEG-SS-PDMAEMA Triblock Copolymers Mediate Markedly Enhanced Nonviral Gene Transfection. *Biomacromolecules* **13**, 769-778 (2012).
8. Mickler, F.M., Möckl, L., Ruthardt, N., Ogris, M., Wagner, E. and Bräuchle, C. Tuning Nanoparticle Uptake: Live-Cell Imaging Reveals Two Distinct Endocytosis Mechanisms Mediated by Natural and Artificial EGFR Targeting Ligand. *Nano Letters* **12**, 3417-3423 (2012).
9. Albertazzi, L. , Mickler, F.M., Pavan, G.M., Giovanni M., Salomone, F., Bardi, G., Panniello, M., Amir, E., Kang, T., Killops, K.L., Bräuchle, C., Amir, R.J. and Hawker, C.J. Enhanced Bioactivity of Internally Functionalized Cationic Dendrimers with PEG Cores. *Biomacromolecules* **13**, 4089-4097 (2012).
10. Alberts, B. et al. *Molecular Biology of the Cell*, 4th edition. *New York: Garland Science* (2002).
11. Flotte, T.R. Gene therapy: the first two decades and the current state-of-the-art. *Journal of cellular physiology* **213**, 301-305 (2007).
12. Alton, E.W. et al. A randomised, double-blind, placebo-controlled phase IIB clinical trial of repeated application of gene therapy in patients with cystic fibrosis. *Thorax* (2013) doi: 10.1136/thoraxjnl-2013-203309.
13. Qian, C. & Prieto, J. Gene therapy of cancer: induction of anti-tumor immunity. *Cellular & molecular immunology* **1**, 105-111 (2004).
14. Guzman-Villanueva, D., El-Sherbiny, I.M., Herrera-Ruiz, D., Vlassov, A.V. & Smyth, H.D. Formulation approaches to short interfering RNA and MicroRNA: challenges and implications. *Journal of pharmaceutical sciences* **101**, 4046-4066 (2012).
15. Aboul-Fadl, T. Antisense oligonucleotides: the state of the art. *Current medicinal chemistry* **12**, 2193-2214 (2005).

BIBLIOGRAPHY

16. Ginn, S.L., Alexander, I.E., Edelstein, M.L., Abedi, M.R. & Wixon, J. Gene therapy clinical trials worldwide to 2012 - an update. *Journal of Gene Medicine* **15**, 65-77 (2013).
17. Shimamura, M. & Morishita, R. Naked plasmid DNA for gene therapy. *Current gene therapy* **11**, 433 (2011).
18. Giacca, M. & Zacchigna, S. Virus-mediated gene delivery for human gene therapy. *Journal of controlled release* **161**, 377-388 (2012).
19. Al-Dosari, M. & Gao, X. Nonviral Gene Delivery: Principle, Limitations, and Recent Progress. *The AAPS Journal* **11**, 671-681 (2009).
20. Akin, D. et al. Bacteria-mediated delivery of nanoparticles and cargo into cells. *Nature nanotechnology* **2**, 441-449 (2007).
21. Larocca, D., Jensen-Pergakes, K., Burg, M.A. & Baird, A. Receptor-targeted gene delivery using multivalent phagemid particles. *Molecular therapy* **3**, 476-484 (2001).
22. Byun, H.M. et al. Erythrocyte ghost-mediated gene delivery for prolonged and blood-targeted expression. *Gene therapy* **11**, 492-496 (2004).
23. Kim, S.H. et al. Exosomes derived from IL-10-treated dendritic cells can suppress inflammation and collagen-induced arthritis. *Journal of immunology* **174**, 6440-6448 (2005).
24. Khare, R., Chen, C.Y., Weaver, E.A. & Barry, M.A. Advances and future challenges in adenoviral vector pharmacology and targeting. *Current gene therapy* **11**, 241-258 (2011).
25. Maetzig, T., Baum, C. & Schambach, A. Retroviral protein transfer: falling apart to make an impact. *Current gene therapy* **12**, 389-409 (2012).
26. Meier, O. & Greber, U.F. Adenovirus endocytosis. *The Journal of Gene Medicine* **6**, S152-S163 (2004).
27. Kubo, Y., Hayashi, H., Matsuyama, T., Sato, H. & Yamamoto, N. Retrovirus entry by endocytosis and cathepsin proteases. *Advances in virology* **2012**, 640894 (2012).
28. Matrai, J., Chuah, M.K.L. & VandenDriessche, T. Recent Advances in Lentiviral Vector Development and Applications. *Molecular therapy* **18**, 477-490 (2010).
29. Itaka, K. & Kataoka, K. Recent development of nonviral gene delivery systems with virus-like structures and mechanisms. *European Journal of Pharmaceutics and Biopharmaceutics* **71**, 475-483 (2009).
30. Zuhorn, I.S., Engberts, J.B. & Hoekstra, D. Gene delivery by cationic lipid vectors: overcoming cellular barriers. *European Biophysical Journal* **36**, 349-362 (2007).
31. Crombez, L., Morris, M.C., Heitz, F. & Divita, G. A non-covalent peptide-based strategy for ex vivo and in vivo oligonucleotide delivery. *Methods in molecular biology* **764**, 59-73 (2011).
32. Duncan, R. The dawning era of polymer therapeutics. *Nature Reviews Drug Discovery* **2**, 347-360 (2003).
33. Gao, X., Kim, K.S. & Liu, D. Nonviral gene delivery: what we know and what is next. *The AAPS Journal* **9**, E92-104 (2007).
34. Russ, V. & Wagner, E. Cell and Tissue Targeting of Nucleic Acids for Cancer Gene Therapy. *Pharmaceutical Research* **24**, 1047-1057 (2007).
35. Molineux, G. Pegylation: engineering improved pharmaceuticals for enhanced therapy. *Cancer Treatment Reviews* **28** Suppl A, 13-16 (2002).

36. Edinger, D. & Wagner, E. Bioresponsive polymers for the delivery of therapeutic nucleic acids. *Wiley Interdisciplinary Reviews: Nanomedicine and Nanobiotechnology* **3**, 33-46 (2011).
37. Ferlay, J. et al. Estimates of worldwide burden of cancer in 2008: GLOBOCAN 2008. *International journal of cancer*. **127**, 2893-2917 (2010).
38. Weinberg, R.A. Cancer Biology and Therapy: the road ahead. *Cancer biology & therapy* **1**, 3 (2002).
39. Bucci, M.K., Bevan, A. & Roach, M. Advances in Radiation Therapy: Conventional to 3D, to IMRT, to 4D, and Beyond. *CA: A Cancer Journal for Clinicians* **55**, 117-134 (2005).
40. Chemotherapy Principles. *American Cancer Society*, www.cancer.org/treatment (2013).
41. Lane, D.P., Check, C.F. & Lain, S. p53-based cancer therapy. *Cold Spring Harbor perspectives in biology* **2**, 9, a001222 (2010).
42. Ochoa, M.C. et al. Interleukin-15 in gene therapy of cancer. *Current gene therapy* **13**, 15-30 (2013).
43. Persano, L., Crescenzi, M. & Indraccolo, S. Anti-angiogenic gene therapy of cancer: current status and future prospects. *Molecular aspects of medicine* **28**, 87-114 (2007).
44. Cowen, R.L. et al. Adenovirus vector-mediated delivery of the prodrug-converting enzyme carboxypeptidase G2 in a secreted or GPI-anchored form: High-level expression of this active conditional cytotoxic enzyme at the plasma membrane. *Cancer gene therapy* **9**, 897-907 (2002).
45. Dobson, J. Cancer therapy: A twist on tumour targeting. *Nature Materials* **9**, 95-96 (2010).
46. Zhang, J., Yang, P.L. & Gray, N.S. Targeting cancer with small molecule kinase inhibitors. *Nature Reviews Cancer* **9**, 28-39 (2009).
47. Di Fiore, P.P. et al. Overexpression of the human EGF receptor confers an EGF-dependent transformed phenotype to NIH 3T3 cells. *Cell* **51**, 1063-1070 (1987).
48. Daniels, T.R. et al. The transferrin receptor and the targeted delivery of therapeutic agents against cancer. *Biochimica et biophysica acta* **1820**, 291-317 (2012).
49. Kelemen, L.E. The role of folate receptor alpha in cancer development, progression and treatment: cause, consequence or innocent bystander? *International journal of cancer* **119**, 243-250 (2006).
50. Desgrosellier, J.S. & Cheresh, D.A. Integrins in cancer: biological implications and therapeutic opportunities. *Nature Reviews Cancer* **10**, 9-22 (2010).
51. Ohtsubo, K. & Marth, J.D. Glycosylation in cellular mechanisms of health and disease. *Cell* **126**, 855-867 (2006).
52. Baselga, J. & Albanell, J. Mechanism of action of anti-HER2 monoclonal antibodies. *Annals of oncology* **12**, S35-41 (2001).
53. Danhier, F., Feron, O. & Préat, V. To exploit the tumor microenvironment: Passive and active tumor targeting of nanocarriers for anti-cancer drug delivery. *Journal of Controlled Release* **148**, 135-146 (2010).
54. Liu, R., Kay, B.K., Jiang, S. & Chen, S. Nanoparticle Delivery: Targeting and Nonspecific Binding. *MRS Bulletin* **34**, 432-440 (2009).
55. Albini, A. & Sporn, M.B. The tumour microenvironment as a target for chemoprevention. *Nature Reviews Cancer* **7**, 139-147 (2007).

BIBLIOGRAPHY

56. Brower, V. Macrophages: Cancer Therapy's Double-Edged Sword. *Journal of the National Cancer Institute* **104**, 649-652 (2012).
57. Gialeli, C., Theocharis, A.D. & Karamanos, N.K. Roles of matrix metalloproteinases in cancer progression and their pharmacological targeting. *FEBS Journal* **278**, 16-27 (2011).
58. Siemann, D.W. The unique characteristics of tumor vasculature and preclinical evidence for its selective disruption by Tumor-Vascular Disrupting Agents. *Cancer treatment reviews* **37**, 63-74 (2011).
59. Maeda, H., Nakamura, H. & Fang, J. The EPR effect for macromolecular drug delivery to solid tumors: Improvement of tumor uptake, lowering of systemic toxicity, and distinct tumor imaging in vivo. *Advanced Drug Delivery Reviews* **65**, 71-79 (2013).
60. Choi, H.S. et al. Renal clearance of quantum dots. *Nature biotechnology* **25**, 1165-1170 (2007).
61. Taurin, S., Nehoff, H. & Greish, K. Anticancer nanomedicine and tumor vascular permeability; Where is the missing link? *Journal of Controlled Release* **164**, 265-275 (2012).
62. Bergers, G. & Benjamin, L.E. Tumorigenesis and the angiogenic switch. *Nature Reviews Cancer* **3**, 401-410 (2003).
63. Johannessen, T.C., Wagner, M., Straume, O., Bjerkvig, R. & Eikesdal, H.P. Tumor vasculature: the Achilles' heel of cancer? *Expert opinion on therapeutic targets* **17**, 7-20 (2013).
64. Lee, E.S., Gao, Z. & Bae, Y.H. Recent progress in tumor pH targeting nanotechnology. *Journal of Controlled Release* **132**, 164-170 (2008).
65. Sawant, R.M. et al. "SMART" drug delivery systems: double-targeted pH-responsive pharmaceutical nanocarriers. *Bioconjugate chemistry* **17**, 943-949 (2006).
66. Torchilin, V.P. Tat peptide-mediated intracellular delivery of pharmaceutical nanocarriers. *Advanced Drug Delivery Reviews* **60**, 548-558 (2008).
67. Li, S. Electroporation gene therapy: new developments in vivo and in vitro. *Current gene therapy* **4**, 309-316 (2004).
68. Escoffre, J.M., Zeghimi, A., Novell, A. & Bouakaz, A. In-vivo gene delivery by sonoporation: recent progress and prospects. *Current gene therapy* **13**, 2-14 (2013).
69. Kim, D.H. et al. Biofunctionalized magnetic-vortex microdiscs for targeted cancer-cell destruction. *Nature Materials* (2010).
70. Huff, T.B. et al. Hyperthermic effects of gold nanorods on tumor cells. *Nanomedicine* **2**, 125-132 (2007).
71. de Bruin, K.G., Fella, C., Ogris, M., Wagner, E., Ruthardt, N. and Bräuchle, C.. Dynamics of photoinduced endosomal release of polyplexes. *Journal of controlled release* **130**, 175-182 (2008).
72. Koontongkaew, S. The tumor microenvironment contribution to development, growth, invasion and metastasis of head and neck squamous cell carcinomas. *Journal of Cancer* **4**, 66-83 (2013).
73. Li, S.-D. & Huang, L. Pharmacokinetics and Biodistribution of Nanoparticles. *Molecular Pharmaceutics* **5**, 496-504 (2008).

74. Alexis, F., Pridgen, E., Molnar, L.K. & Farokhzad, O.C. Factors Affecting the Clearance and Biodistribution of Polymeric Nanoparticles. *Molecular Pharmaceutics* **5**, 505-515 (2008).
75. Davies, J.C. & Alton, E.W. Airway gene therapy. *Advances in genetics* **54**, 291-314 (2005).
76. Owens, D.E., 3rd & Peppas, N.A. Opsonization, biodistribution, and pharmacokinetics of polymeric nanoparticles. *International journal of pharmaceutics* **307**, 93-102 (2006).
77. Aderem, A. & Underhill, D.M. Mechanisms of phagocytosis in macrophages. *Annual review of immunology* **17**, 593-623 (1999).
78. Levchenko, T.S., Rammohan, R., Lukyanov, A.N., Whiteman, K.R. & Torchilin, V.P. Liposome clearance in mice: the effect of a separate and combined presence of surface charge and polymer coating. *International journal of pharmaceutics* **240**, 95-102 (2002).
79. Champion, J.A. & Mitragotri, S. Role of target geometry in phagocytosis. *Proceedings of the National Academy of Sciences of the United States of America* **103**, 4930-4934 (2006).
80. Tabata, Y. & Ikada, Y. Effect of the size and surface charge of polymer microspheres on their phagocytosis by macrophage. *Biomaterials* **9**, 356-362 (1988).
81. Korn, E.D. & Weisman, R.A. Phagocytosis of latex beads by *Acanthamoeba*. II. Electron microscopic study of the initial events. *The Journal of cell biology* **34**, 219-227 (1967).
82. Mahato, R.I. et al. Biodistribution and gene expression of lipid/plasmid complexes after systemic administration. *Human gene therapy* **9**, 2083-2099 (1998).
83. Pries, A.R. & Kuebler, W.M. Normal endothelium. *Handbook of experimental pharmacology*, 1-40 (2006).
84. Ludatscher, R.M. & Stehbens, W.E. Vesicles of fenestrated and non-fenestrated endothelium. *Zeitschrift fur Zellforschung und mikroskopische Anatomie (Vienna, Austria : 1948)* **97**, 169-177 (1969).
85. Greish, K. Enhanced permeability and retention (EPR) effect for anticancer nanomedicine drug targeting. *Methods in molecular biology* **624**, 25-37 (2010).
86. Huhn, D. et al. Polymer-coated nanoparticles interacting with proteins and cells: focusing on the sign of the net charge. *ACS Nano* **7**, 3253-3263 (2013).
87. Miller, N. Glybera and the future of gene therapy in the European Union. *Nature Reviews Drug Discovery* **11**, 419 (2012).
88. Stylianopoulos, T. et al. Diffusion of particles in the extracellular matrix: the effect of repulsive electrostatic interactions. *Biophysical Journal* **99**, 1342-1349 (2010).
89. Goodman, T.T., Olive, P.L. & Pun, S.H. Increased nanoparticle penetration in collagenase-treated multicellular spheroids. *International journal of nanomedicine* **2**, 265-274 (2007).
90. Almeida, J.P., Chen, A.L., Foster, A. & Drezek, R. In vivo biodistribution of nanoparticles. *Nanomedicine* **6**, 815-835 (2011).
91. Shi, Y. & Huang, G. Recent developments of biodegradable and biocompatible materials based micro/nanoparticles for delivering macromolecular therapeutics. *Critical reviews in therapeutic drug carrier systems* **26**, 29-84 (2009).
92. Mailänder, V. & Landfester, K. Interaction of Nanoparticles with Cells. *Biomacromolecules* **10**, 2379-2400 (2009).
93. Curry, F.E. & Adamson, R.H. Endothelial glycocalyx: permeability barrier and mechanosensor. *Annals of biomedical engineering* **40**, 828-839 (2012).

BIBLIOGRAPHY

94. Sarrazin, S., Lamanna, W.C. & Esko, J.D. Heparan sulfate proteoglycans. *Cold Spring Harbor perspectives in biology* **3**, 7, a004952 (2011).
95. Gratton, S.E.A. et al. The effect of particle design on cellular internalization pathways. *Proceedings of the National Academy of Sciences of the United States of America* **105**, 11613-11618 (2008).
96. Miller, C.R., Bondurant, B., McLean, S.D., McGovern, K.A. & O'Brien, D.F. Liposome-Cell Interactions in Vitro: Effect of Liposome Surface Charge on the Binding and Endocytosis of Conventional and Sterically Stabilized Liposomes†. *Biochemistry* **37**, 12875-12883 (1998).
97. Paris, S., Burlacu, A. & Durocher, Y. Opposing roles of syndecan-1 and syndecan-2 in polyethyleneimine-mediated gene delivery. *The Journal of biological chemistry* **283**, 7697-7704 (2008).
98. Hanzlikova, M. et al. Mechanisms of polyethylenimine-mediated DNA delivery: free carrier helps to overcome the barrier of cell-surface glycosaminoglycans. *Journal of Gene Medicine* **13**, 402-409 (2011).
99. Walkey, C.D. & Chan, W.C. Understanding and controlling the interaction of nanomaterials with proteins in a physiological environment. *Chemical Society reviews* **41**, 2780-2799 (2012).
100. Mirshafiee, V., Mahmoudi, M., Lou, K., Cheng, J. & Kraft, M.L. Protein corona significantly reduces active targeting yield. *Chemical communications (Cambridge, England)* **49**, 2557-2559 (2013).
101. Xu, Y.H., Richert, N., Ito, S., Merlino, G.T. & Pastan, I. Characterization of epidermal growth factor receptor gene expression in malignant and normal human cell lines. *Proceedings of the National Academy of Sciences of the United States of America* **81**, 7308-7312 (1984).
102. Ciardiello, F. et al. Differential expression of epidermal growth factor-related proteins in human colorectal tumors. *Proceedings of the National Academy of Sciences of the United States of America* **88**, 7792-7796 (1991).
103. Wieduwilt, M.J. & Moasser, M.M. The epidermal growth factor receptor family: Biology driving targeted therapeutics. *Cellular and Molecular Life Sciences* **65**, 1566-1584 (2008).
104. Chung, I. et al. Spatial control of EGF receptor activation by reversible dimerization on living cells. *Nature* **464**, 783-787 (2010).
105. Schlessinger, J. Ligand-Induced, Receptor-Mediated Dimerization and Activation of EGF Receptor. *Cell* **110**, 669-672 (2002).
106. Duan, L. et al. Cbl-mediated Ubiquitinylation Is Required for Lysosomal Sorting of Epidermal Growth Factor Receptor but Is Dispensable for Endocytosis. *The Journal of biological chemistry* **278**, 28950-28960 (2003).
107. Sorkin, A. & Carpenter, G. Interaction of activated EGF receptors with coated pit adaptins. *Science* **261**, 612-615 (1993).
108. Sorkin, A. & von Zastrow, M. Endocytosis and signalling: intertwining molecular networks. *Nature reviews. Molecular cell biology* **10**, 609-622 (2009).
109. Kaksonen, M., Toret, C.P. & Drubin, D.G. Harnessing actin dynamics for clathrin-mediated endocytosis. *Nature reviews. Molecular cell biology* **7**, 404-414 (2006).
110. Van Aelst, L. & D'Souza-Schorey, C. Rho GTPases and signaling networks. *Genes and Development* **11**, 2295-2322 (1997).

111. Roepstorff, K. et al. Differential Effects of EGFR Ligands on Endocytic Sorting of the Receptor. *Traffic* **10**, 1115-1127 (2009).
112. Herbst, J.J., Opresko, L.K., Walsh, B.J., Lauffenburger, D.A. & Wiley, H.S. Regulation of postendocytic trafficking of the epidermal growth factor receptor through endosomal retention. *The Journal of biological chemistry* **269**, 12865-12873 (1994).
113. Dinneen, J.L. & Ceresa, B.P. Continual Expression of Rab5(Q79L) Causes a Ligand-Independent EGFR Internalization and Diminishes EGFR Activity. *Traffic* **5**, 606-615 (2004).
114. Zwang, Y. & Yarden, Y. p38 MAP kinase mediates stress-induced internalization of EGFR: implications for cancer chemotherapy. *EMBO Journal* **25**, 4195-4206 (2006).
115. Norambuena, A. et al. Phosphatidic Acid Induces Ligand-independent Epidermal Growth Factor Receptor Endocytic Traffic through PDE4 Activation. *Molecular Biology of the Cell* **21**, 2916-2929 (2010).
116. Harris, M. Monoclonal antibodies as therapeutic agents for cancer. *Lancet Oncology* **5**, 292-302 (2004).
117. Noble, M.E.M., Endicott, J.A. & Johnson, L.N. Protein Kinase Inhibitors: Insights into Drug Design from Structure. *Science* **303**, 1800-1805 (2004).
118. Bhattacharyya, S., Bhattacharya, R., Curley, S., McNiven, M.A. & Mukherjee, P. Nanoconjugation modulates the trafficking and mechanism of antibody induced receptor endocytosis. *Proceedings of the National Academy of Sciences of the United States of America* **107**, 14541-14546 (2011).
119. Bunuales, M., Düzgünes, N., Zalba, S., Garrido, M.J. & de Ilarduya, C. Efficient gene delivery by EGF-lipoplexes in vitro and in vivo. *Nanomedicine* **6**, 89-98 (2011).
120. Zhao, R., Diop-Bove, N., Visentin, M. & Goldman, I.D. Mechanisms of Membrane Transport of Folates into Cells and Across Epithelia. *Annual Review of Nutrition* **31**, 177-201 (2011).
121. Weitman, S.D. et al. Distribution of the folate receptor GP38 in normal and malignant cell lines and tissues. *Cancer research* **52**, 3396-3401 (1992).
122. Anderson, R.G., Kamen, B.A., Rothberg, K.G. & Lacey, S.W. Potocytosis: sequestration and transport of small molecules by caveolae. *Science* **255**, 410-411 (1992).
123. Mayor, S., Rothberg, K.G. & Maxfield, F.R. Sequestration of GPI-anchored proteins in caveolae triggered by cross-linking. *Science* **264**, 1948-1951 (1994).
124. Sabharanjak, S., Sharma, P., Parton, R.G. & Mayor, S. GPI-anchored proteins are delivered to recycling endosomes via a distinct cdc42-regulated, clathrin-independent pinocytic pathway. *Developmental cell* **2**, 411-423 (2002).
125. Zhao, X., Li, H. & Lee, R.J. Targeted drug delivery via folate receptors. *Expert Opinion on Drug Delivery* **5**, 309-319 (2008).
126. Prior, R., Reifenberger, G. & Wechsler, W. Transferrin receptor expression in tumours of the human nervous system: relation to tumour type, grading and tumour growth fraction. *Virchows Archiv. A, Pathological anatomy and histopathology* **416**, 491-496 (1990).
127. Cheng, Y., Zak, O., Aisen, P., Harrison, S.C. & Walz, T. Structure of the human transferrin receptor-transferrin complex. *Cell* **116**, 565-576 (2004).
128. Ciechanover, A., Schwartz, A.L. & Lodish, H.F. Sorting and recycling of cell surface receptors and endocytosed ligands: the asialoglycoprotein and transferrin receptors. *Journal of cellular biochemistry* **23**, 107-130 (1983).

BIBLIOGRAPHY

129. Dautry-Varsat, A. Receptor-mediated endocytosis: the intracellular journey of transferrin and its receptor. *Biochimie* **68**, 375-381 (1986).
130. Legate, K.R., Wickstrom, S.A. & Fassler, R. Genetic and cell biological analysis of integrin outside-in signaling. *Genes and Development* **23**, 397-418 (2009).
131. Margadant, C., Monsuur, H.N., Norman, J.C. & Sonnenberg, A. Mechanisms of integrin activation and trafficking. *Current Opinion in Cell Biology* **23**, 607-614 (2011).
132. Carman, C.V. & Springer, T.A. Integrin avidity regulation: are changes in affinity and conformation underemphasized? *Current Opinion in Cell Biology* **15**, 547-556 (2003).
133. Takagi, J., Petre, B.M., Walz, T. & Springer, T.A. Global conformational rearrangements in integrin extracellular domains in outside-in and inside-out signaling. *Cell* **110**, 599-511 (2002).
134. Ali, O. et al. Cooperativity between Integrin Activation and Mechanical Stress Leads to Integrin Clustering. *Biophysical journal* **100**, 2595-2604 (2011).
135. Boettiger, D. Mechanical control of integrin-mediated adhesion and signaling. *Current Opinion in Cell Biology* **24**, 592-599 (2012).
136. Ezratty, E.J., Bertaux, C., Marcantonio, E.E. & Gundersen, G.G. Clathrin mediates integrin endocytosis for focal adhesion disassembly in migrating cells. *Journal of Cell Biology* **187**, 733-747 (2009).
137. Gu, Z., Noss, E.H., Hsu, V.W. & Brenner, M.B. Integrins traffic rapidly via circular dorsal ruffles and macropinocytosis during stimulated cell migration. *Journal of Cell Biology* **193**, 61-70 (2011).
138. Reardon, D.A., Nabors, L.B., Stupp, R. & Mikkelsen, T. Cilengitide: an integrin-targeting arginine-glycine-aspartic acid peptide with promising activity for glioblastoma multiforme. *Expert opinion on investigational drugs* **17**, 1225-1235 (2008).
139. Ziello, J.E., Huang, Y. & Jovin, I.S. Cellular endocytosis and gene delivery. *Molecular Medicine* **16**, 222-229 (2010).
140. Conner, S.D. & Schmid, S.L. Regulated portals of entry into the cell. *Nature* **422**, 37-44 (2003).
141. McMahon, H.T. & Boucrot, E. Molecular mechanism and physiological functions of clathrin-mediated endocytosis. *Nature reviews. Molecular cell biology* **12**, 517-533 (2011).
142. Pearse, B.M. Clathrin: a unique protein associated with intracellular transfer of membrane by coated vesicles. *Proceedings of the National Academy of Sciences of the United States of America* **73**, 1255-1259 (1976).
143. Ford, M.G.J. et al. Simultaneous Binding of PtdIns(4,5)P₂ and Clathrin by AP180 in the Nucleation of Clathrin Lattices on Membranes. *Science* **291**, 1051-1055 (2001).
144. Roux, A., Uyhazi, K., Frost, A. & De Camilli, P. GTP-dependent twisting of dynamin implicates constriction and tension in membrane fission. *Nature* **441**, 528-531 (2006).
145. Nelson, N. et al. The cellular biology of proton-motive force generation by V-ATPases. *The Journal of experimental biology* **203**, 89-95 (2000).
146. Maxfield, F.R. & McGraw, T.E. Endocytic recycling. *Nature reviews. Molecular cell biology* **5**, 121-132 (2004).
147. Luzio, J.P., Pryor, P.R. & Bright, N.A. Lysosomes: fusion and function. *Nature reviews. Molecular cell biology* **8**, 622-632 (2007).

148. Sahay, G., Alakhova, D.Y. & Kabanov, A.V. Endocytosis of nanomedicines. *Journal of controlled release* **145**, 182-195 (2010).
149. Tekle, C., Deurs, B., Sandvig, K. & Iversen, T.G. Cellular trafficking of quantum dot-ligand bioconjugates and their induction of changes in normal routing of unconjugated ligands. *Nano Letters* **8**, 1858-1865 (2008).
150. Parton, R.G. & Simons, K. The multiple faces of caveolae. *Nature reviews. Molecular cell biology* **8**, 185-194 (2007).
151. Schnitzer, J.E., Liu, J. & Oh, P. Endothelial caveolae have the molecular transport machinery for vesicle budding, docking, and fusion including VAMP, NSF, SNAP, annexins, and GTPases. *The Journal of biological chemistry* **270**, 14399-14404 (1995).
152. Kiss, A.L. & Botos, E. Endocytosis via caveolae: alternative pathway with distinct cellular compartments to avoid lysosomal degradation? *Journal of cellular and molecular medicine* **13**, 1228-1237 (2009).
153. Hansen, C.G., Bright, N.A., Howard, G. & Nichols, B.J. SDPR induces membrane curvature and functions in the formation of caveolae. *Nature cell biology* **11**, 807-814 (2009).
154. Mercer, J., Schelhaas, M. & Helenius, A. Virus entry by endocytosis. *Annual review of biochemistry* **79**, 803-833 (2010).
155. Doherty, G.J. & McMahon, H.T. Mechanisms of endocytosis. *Annual review of biochemistry* **78**, 857-902 (2009).
156. Lu, Y. & Low, P.S. Folate-mediated delivery of macromolecular anticancer therapeutic agents. *Advanced Drug Delivery Reviews* **54**, 675-693 (2002).
157. Kerr, M.C. & Teasdale, R.D. Defining macropinocytosis. *Traffic* **10**, 364-371 (2009).
158. Mercer, J. & Helenius, A. Virus entry by macropinocytosis. *Nature cell biology* **11**, 510-520 (2009).
159. Lechardeur, D. et al. Metabolic instability of plasmid DNA in the cytosol: a potential barrier to gene transfer. *Gene therapy* **6**, 482-497 (1999).
160. de Bruin, K., Ruthardt, N., von Gersdorff, K., Bausinger, R., Wagner, E., Ogris, M. and Bräuchle, C. Cellular dynamics of EGF receptor-targeted synthetic viruses. *Molecular therapy* **15**, 1297-1305 (2007).
161. Kamal, A. & Goldstein, L.S. Connecting vesicle transport to the cytoskeleton. *Current opinion in cell biology* **12**, 503-508 (2000).
162. Felgner, P.L. et al. Lipofection: a highly efficient, lipid-mediated DNA-transfection procedure. *Proceedings of the National Academy of Sciences of the United States of America* **84**, 7413-7417 (1987).
163. Jahn, R., Lang, T. & Südhof, T.C. Membrane Fusion. *Cell* **112**, 519-533 (2003).
164. Duzgunes, N. et al. Calcium- and magnesium-induced fusion of mixed phosphatidylserine/phosphatidylcholine vesicles: effect of ion binding. *Journal of Membrane Biology* **59**, 115-125 (1981).
165. Duzgunes, N., Wilschut, J., Fraley, R. & Papahadjopoulos, D. Studies on the mechanism of membrane fusion. Role of head-group composition in calcium- and magnesium-induced fusion of mixed phospholipid vesicles. *Biochimica et biophysica acta* **642**, 182-195 (1981).
166. Wilen, C.B., Tilton, J.C. & Doms, R.W. Molecular mechanisms of HIV entry. *Advances in experimental medicine and biology* **726**, 223-242 (2012).

BIBLIOGRAPHY

167. Connolly, S.A., Jackson, J.O., Jardetzky, T.S. & Longnecker, R. Fusing structure and function: a structural view of the herpesvirus entry machinery. *Nature reviews. Microbiology* **9**, 369-381 (2011).
168. Zuhorn, I.S. & Hoekstra, D. On the Mechanism of Cationic Amphiphile-mediated Transfection. To Fuse or not to Fuse: Is that the Question? *Journal of Membrane Biology* **189**, 167-179 (2002).
169. Zuhorn, I.S., Kalicharan, R. & Hoekstra, D. Lipoplex-mediated transfection of mammalian cells occurs through the cholesterol-dependent clathrin-mediated pathway of endocytosis. *The Journal of biological chemistry* **277**, 18021-18028 (2002).
170. Madani, F., Lindberg, S., Langel, U., Futaki, S. & Graslund, A. Mechanisms of cellular uptake of cell-penetrating peptides. *Journal of Biophysics* ,414729 (2011).
171. Green, M. & Loewenstein, P.M. Autonomous functional domains of chemically synthesized human immunodeficiency virus tat trans-activator protein. *Cell* **55**, 1179-1188 (1988).
172. Carney, R.P., Carney, T.M., Mueller, M. & Stellacci, F. Dynamic cellular uptake of mixed-monolayer protected nanoparticles. *Biointerphases* **7**, 17 (2012).
173. Verma, A. et al. Surface-structure-regulated cell-membrane penetration by monolayer-protected nanoparticles. *Nature Materials* **7**, 588-595 (2008).
174. Andreev, O.A. et al. Mechanism and uses of a membrane peptide that targets tumors and other acidic tissues in vivo. *Proceedings of the National Academy of Sciences of the United States of America* **104**, 7893-7898 (2007).
175. Andreev, O.A., Engelman, D.M. & Reshetnyak, Y.K. pH-sensitive membrane peptides (pHLIPs) as a novel class of delivery agents. *Molecular membrane biology* **27**, 341-352 (2010).
176. Varkouhi, A.K., Scholte, M., Storm, G. & Haisma, H.J. Endosomal escape pathways for delivery of biologicals. *Journal of Controlled Release* **151**, 220-228 (2011).
177. Lau, W.L., Ege, D.S., Lear, J.D., Hammer, D.A. & DeGrado, W.F. Oligomerization of fusogenic peptides promotes membrane fusion by enhancing membrane destabilization. *Biophysical Journal* **86**, 272-284 (2004).
178. Kwon, E.J., Bergen, J.M. & Pun, S.H. Application of an HIV gp41-derived peptide for enhanced intracellular trafficking of synthetic gene and siRNA delivery vehicles. *Bioconjugate chemistry* **19**, 920-927 (2008).
179. Spilsberg, B., Hanada, K. & Sandvig, K. Diphtheria toxin translocation across cellular membranes is regulated by sphingolipids. *Biochemical and biophysical research communications* **329**, 465-473 (2005).
180. Dempsey, C.E. The actions of melittin on membranes. *Biochimica et biophysica acta* **1031**, 143-161 (1990).
181. Wyman, T.B. et al. Design, synthesis, and characterization of a cationic peptide that binds to nucleic acids and permeabilizes bilayers. *Biochemistry* **36**, 3008-3017 (1997).
182. Zelphati, O. & Szoka, F.C., Jr. Mechanism of oligonucleotide release from cationic liposomes. *Proceedings of the National Academy of Sciences of the United States of America* **93**, 11493-11498 (1996).
183. Zuhorn, I.S. et al. Nonbilayer phase of lipoplex-membrane mixture determines endosomal escape of genetic cargo and transfection efficiency. *Molecular therapy* **11**, 801-810 (2005).

184. Boussif, O. et al. A versatile vector for gene and oligonucleotide transfer into cells in culture and in vivo: polyethylenimine. *Proceedings of the National Academy of Sciences of the United States of America* **92**, 7297-7301 (1995).
185. Rehman, Z.U., Hoekstra, D. & Zuhorn, I.S. On the Mechanism of Polyplex- and Lipoplex-Mediated Delivery of Nucleic Acids: Real-Time Visualization of Transient Membrane Destabilization Without Endosomal Lysis. *ACS Nano* , **7**, 3767-77, (2013).
186. Leroueil, P.R. et al. Nanoparticle Interaction with Biological Membranes: Does Nanotechnology Present a Janus Face? *Accounts of Chemical Research* **40**, 335-342 (2007).
187. Boe, S., Prasmickaite, L., Engesaeter, B. & Hovig, E. Light-directed delivery of nucleic acids. *Methods in molecular biology* **764**, 107-121 (2011).
188. Schlossbauer, A., Sauer, A. M., Cauda, V., Schmidt, A., Engelke, H., Rothbauer, U., Zolghadr, K., Leonhardt, H., Bräuchle, C., Bein, T.. Cascaded photoinduced drug delivery to cells from multifunctional core-shell mesoporous silica. *Advanced healthcare materials* **1**, 316-320 (2012).
189. Braun, G.B. et al. Laser-Activated Gene Silencing via Gold Nanoshell-siRNA Conjugates. *ACS Nano* **3**, 2007-2015 (2009).
190. Huth, S. et al. Interaction of polyamine gene vectors with RNA leads to the dissociation of plasmid DNA-carrier complexes. *The Journal of Gene Medicine* **8**, 1416-1424 (2006).
191. Hebert, E. Improvement of exogenous DNA nuclear importation by nuclear localization signal-bearing vectors: a promising way for non-viral gene therapy? *Biology of the Cell* **95**, 59-68 (2003).
192. Lam, A.P. & Dean, D.A. Progress and prospects: nuclear import of nonviral vectors. *Gene therapy* **17**, 439-447 (2010).
193. Rebuffat, A.G. et al. Gene delivery by a steroid-peptide nucleic acid conjugate. *FASEB journal* **16**, 1426-1428 (2002).
194. Brunner, S. et al. Cell cycle dependence of gene transfer by lipoplex, polyplex and recombinant adenovirus. *Gene therapy* **7**, 401-407 (2000).
195. Gao, W., Rzewski, A., Sun, H., Robbins, P.D. & Gambotto, A. UpGene: Application of a web-based DNA codon optimization algorithm. *Biotechnology progress* **20**, 443-448 (2004).
196. Mitsui, M. et al. Effect of the content of unmethylated CpG dinucleotides in plasmid DNA on the sustainability of transgene expression. *Journal of Gene Medicine* **11**, 435-443 (2009).
197. Yew, N.S. et al. Reduced inflammatory response to plasmid DNA vectors by elimination and inhibition of immunostimulatory CpG motifs. *Molecular therapy* **1**, 255-262 (2000).
198. Magnusson, T., Haase, R., Schleaf, M., Wagner, E. & Ogris, M. Sustained, high transgene expression in liver with plasmid vectors using optimized promoter-enhancer combinations. *The Journal of Gene Medicine* **13**, 382-391 (2011).
199. Manfredsson, F.P., Bloom, D.C. & Mandel, R.J. Regulated protein expression for in vivo gene therapy for neurological disorders: Progress, strategies, and issues. *Neurobiology of Disease* **48**, 212-221 (2012).
200. Harvey, D.M. & Caskey, C.T. Inducible control of gene expression: prospects for gene therapy. *Current opinion in chemical biology* **2**, 512-518 (1998).
201. Kole, R., Krainer, A.R. & Altman, S. RNA therapeutics: beyond RNA interference and antisense oligonucleotides. *Nature Reviews Drug Discovery* **11**, 125-140 (2012).

BIBLIOGRAPHY

202. Macrae, I.J. et al. Structural basis for double-stranded RNA processing by Dicer. *Science* **311**, 195-198 (2006).
203. Miele, E. et al. Nanoparticle-based delivery of small interfering RNA: challenges for cancer therapy. *International journal of nanomedicine* **7**, 3637-3657 (2012).
204. Krutzfeldt, J. et al. Silencing of microRNAs in vivo with 'antagomirs'. *Nature* **438**, 685-689 (2005).
205. Higuchi, Y., Kawakami, S. & Hashida, M. Strategies for in vivo delivery of siRNAs: recent progress. *BioDrugs : clinical immunotherapeutics, biopharmaceuticals and gene therapy* **24**, 195-205 (2010).
206. Koppelhus, U. & Nielsen, P.E. Cellular delivery of peptide nucleic acid (PNA). *Advanced Drug Delivery Reviews* **55**, 267-280 (2003).
207. Scholz, C. & Wagner, E. Therapeutic plasmid DNA versus siRNA delivery: Common and different tasks for synthetic carriers. *Journal of Controlled Release* **161**, 554-565 (2012).
208. Lv, H., Zhang, S., Wang, B., Cui, S. & Yan, J. Toxicity of cationic lipids and cationic polymers in gene delivery. *Journal of Controlled Release* **114**, 100-109 (2006).
209. van der Woude, I. et al. Novel pyridinium surfactants for efficient, nontoxic in vitro gene delivery. *Proceedings of the National Academy of Sciences of the United States of America* **94**, 1160-1165 (1997).
210. Zhi, D. et al. Synthesis and biological activity of carbamate-linked cationic lipids for gene delivery in vitro. *Bioorganic & medicinal chemistry letters* **22**, 3837-3841 (2012).
211. Godbey, W.T., Wu, K.K. & Mikos, A.G. Poly(ethylenimine)-mediated gene delivery affects endothelial cell function and viability. *Biomaterials* **22**, 471-480 (2001).
212. Kim, Y.H. et al. Polyethylenimine with acid-labile linkages as a biodegradable gene carrier. *Journal of controlled release* **103**, 209-219 (2005).
213. Petersen, H. et al. Polyethylenimine-graft-poly(ethylene glycol) copolymers: influence of copolymer block structure on DNA complexation and biological activities as gene delivery system. *Bioconjugate chemistry* **13**, 845-854 (2002).
214. Pouton, C.W. et al. Polycation-DNA complexes for gene delivery: a comparison of the biopharmaceutical properties of cationic polypeptides and cationic lipids. *Journal of controlled release* **53**, 289-299 (1998).
215. Guang Liu, W. & De Yao, K. Chitosan and its derivatives--a promising non-viral vector for gene transfection. *Journal of controlled release* **83**, 1-11 (2002).
216. Eliyahu, H. et al. Novel dextran-spermine conjugates as transfecting agents: comparing water-soluble and micellar polymers. *Gene therapy* **12**, 494-503 (2005).
217. Funhoff, A.M. et al. Polymer side-chain degradation as a tool to control the destabilization of polyplexes. *Pharmaceutical Research* **21**, 170-176 (2004).
218. Read, M.L. et al. Vectors based on reducible polycations facilitate intracellular release of nucleic acids. *Journal of Gene Medicine* **5**, 232-245 (2003).
219. Jiang, J., Zhang, L., Wu, M. & Zhang, X. Synthesis and characterization of a novel biodegradable amphiphilic MPEG-dendritic block copolymer containing (glycolic acid)-alt-(lactic acid) oligomer and glycerol. *Journal of controlled release* **152**, Suppl 1, e264-266 (2011).

220. Zamboni, W.C. et al. Best practices in cancer nanotechnology: perspective from NCI nanotechnology alliance. *Clinical cancer research* **18**, 3229-3241 (2012).
221. Harries, M., Ellis, P. & Harper, P. Nanoparticle albumin-bound paclitaxel for metastatic breast cancer. *Journal of clinical oncology* **23**, 7768-7771 (2005).
222. Robertson, D. Genentech's anticancer Mab expected by November. *Nature biotechnology* **16**, 615 (1998).
223. Wiseman, G.A. et al. Radioimmunotherapy of relapsed non-Hodgkin's lymphoma with zevalin, a 90Y-labeled anti-CD20 monoclonal antibody. *Clinical cancer research* **5**, 3281s-3286s (1999).
224. Bevacizumab. Anti-VEGF monoclonal antibody, avastin, rhumab-VEGF. *Drugs in R&D* **3**, 28-30 (2002).
225. Forssen, E.A. & Tokes, Z.A. Improved therapeutic benefits of doxorubicin by entrapment in anionic liposomes. *Cancer research* **43**, 546-550 (1983).
226. Gill, P.S. et al. Phase I/II clinical and pharmacokinetic evaluation of liposomal daunorubicin. *Journal of clinical oncology* **13**, 996-1003 (1995).
227. Venditto, V.J. & Szoka, F.C., Jr. Cancer nanomedicines: so many papers and so few drugs! *Advanced Drug Delivery Reviews* **65**, 80-88 (2013).
228. Service, R.F. Nanotechnology. Nanoparticle Trojan horses gallop from the lab into the clinic. *Science* **330**, 314-315 (2010).
229. Matsumura, Y. & Kataoka, K. Preclinical and clinical studies of anticancer agent-incorporating polymer micelles. *Cancer Science* **100**, 572-579 (2009).
230. Kay, M.A. State-of-the-art gene-based therapies: the road ahead. *Nature reviews. Genetics* **12**, 316-328 (2011).
231. Teichler Zallen, D. US gene therapy in crisis. *Trends in genetics : TIG* **16**, 272-275 (2000).
232. Fischer, A., Hacein-Bey-Abina, S. & Cavazzana-Calvo, M. 20 years of gene therapy for SCID. *Nature immunology* **11**, 457-460 (2010).
233. LeWitt, P.A. et al. AAV2-GAD gene therapy for advanced Parkinson's disease: a double-blind, sham-surgery controlled, randomised trial. *Lancet neurology* **10**, 309-319 (2011).
234. Cideciyan, A.V. et al. Vision 1 year after gene therapy for Leber's congenital amaurosis. *The New England journal of medicine* **361**, 725-727 (2009).
235. Lichtman, J.W. & Conchello, J.-A. Fluorescence microscopy. *Nature methods* **2**, 910-919 (2005).
236. Kirstein, J., Platschek, B., Jung, C., Brown, R., Bein, T. and Bräuchle, C. Exploration of nanostructured channel systems with single-molecule probes. *Nature Materials* **6**, 303-310 (2007).
237. Zürner, A., Kirstein, J., Doblinger, M., Bräuchle, C. and Bein, T. Visualizing single-molecule diffusion in mesoporous materials. *Nature* **450**, 705-708 (2007).
238. Kajihara, D. et al. FRET analysis of protein conformational change through position-specific incorporation of fluorescent amino acids. *Nature methods* **3**, 923-929 (2006).
239. Mickler, M., Hessling, M., Ratzke, C., Buchner, J. & Hugel, T. The large conformational changes of Hsp90 are only weakly coupled to ATP hydrolysis. *Nature structural & molecular biology* **16**, 281-286 (2009).

BIBLIOGRAPHY

240. Baumgärtel, V., Ivanchenko, S., Dupont, A., Sergeev, M., Wiseman, P. W., Kräusslich, H. G., Bräuchle, C. Müller, B. and Lamb, D. C. Live-cell visualization of dynamics of HIV budding site interactions with an ESCRT component. *Nature cell biology* **13**, 469-474 (2011).
241. Ruthardt, N., Lamb, D.C. and Bräuchle, C. Visualizing uptake and intracellular trafficking of gene carriers by single-particle tracking. *Topics in Current Chemistry* **296**, 283-304 (2010).
242. Seisenberger, G., Ried, M. U., Endress, T., Buning, H., Hallek, M. and Bräuchle, C. Real-time single-molecule imaging of the infection pathway of an adeno-associated virus. *Science* **294**, 1929-1932 (2001).
243. Stelzer Contrast, resolution, pixelation, dynamic range and signal-to-noise ratio: fundamental limits to resolution in fluorescence light microscopy. *Journal of Microscopy* **189**, 15-24 (1998).
244. Sluder, G. & Nordberg, J.J. in *Methods in Cell Biology*, Vol. Volume 81. (eds. S. Greenfield & E.W. David) 1-10 (Academic Press, 2007).
245. Bräuchle, C., Lamb, D.C. & Michaelis, J. *Single Particle Tracking and Single Molecule Energy Transfer*. (Wiley-VCH Verlag GmbH, 2009).
246. Yildiz, A. & Selvin, P.R. Fluorescence imaging with one nanometer accuracy: application to molecular motors. *Accounts of Chemical Research* **38**, 574-582 (2005).
247. Ruthardt, N., Lamb, D.C. & Brauchle, C. Single-particle tracking as a quantitative microscopy-based approach to unravel cell entry mechanisms of viruses and pharmaceutical nanoparticles. *Molecular therapy* **19**, 1199-1211 (2011).
248. Petty, H.R. Fluorescence microscopy: established and emerging methods, experimental strategies, and applications in immunology. *Microscopy research and technique* **70**, 687-709 (2007).
249. Rust, M.J., Bates, M. & Zhuang, X. Sub-diffraction-limit imaging by stochastic optical reconstruction microscopy (STORM). *Nature methods* **3**, 793-795 (2006).
250. Betzig, E. et al. Imaging intracellular fluorescent proteins at nanometer resolution. *Science* **313**, 1642-1645 (2006).
251. Willig, K.I., Rizzoli, S.O., Westphal, V., Jahn, R. & Hell, S.W. STED microscopy reveals that synaptotagmin remains clustered after synaptic vesicle exocytosis. *Nature* **440**, 935-939 (2006).
252. Lakowicz, J.R. *Principles of fluorescence spectroscopy*, Vol. 2nd edition. (1999).
253. Morrison, L.E. Basic principles of fluorescence and energy transfer. *Methods in molecular biology* **429**, 3-19 (2008).
254. Lakowicz, J.R. Fluorescence spectroscopic investigations of the dynamic properties of proteins, membranes and nucleic acids. *Journal of biochemical and biophysical methods* **2**, 91-119 (1980).
255. Haase, M., Hubner, C.G., Nolde, F., Mullen, K. & Basche, T. Photoblinking and photobleaching of rylene diimide dyes. *Physical chemistry chemical physics* **13**, 1776-1785 (2011).
256. Marks, K.M. & Nolan, G.P. Chemical labeling strategies for cell biology. *Nature methods* **3**, 591-596 (2006).
257. Lippincott-Schwartz, J. & Patterson, G.H. Development and Use of Fluorescent Protein Markers in Living Cells. *Science* **300**, 87-91 (2003).

258. Alivisatos, P. The use of nanocrystals in biological detection. *Nature biotechnology* **22**, 47-52 (2004).
259. Tsien, R.Y. THE GREEN FLUORESCENT PROTEIN. *Annual review of biochemistry* **67**, 509-544 (1998).
260. Giepmans, B.N., Adams, S.R., Ellisman, M.H. & Tsien, R.Y. The fluorescent toolbox for assessing protein location and function. *Science* **312**, 217-224 (2006).
261. Life Technologies, The Molecular Probes Handbook - A guide to fluorescent probes and labeling technologies, Vol. 11th edition. (2013).
262. Amblard, F., Cho, J.H. & Schinazi, R.F. Cu(I)-catalyzed Huisgen azide-alkyne 1,3-dipolar cycloaddition reaction in nucleoside, nucleotide, and oligonucleotide chemistry. *Chemical Reviews* **109**, 4207-4220 (2009).
263. Baskin, J.M. et al. Copper-free click chemistry for dynamic in vivo imaging. *Proceedings of the National Academy of Sciences of the United States of America* **104**, 16793-16797 (2007).
264. Miller, L.W. & Cornish, V.W. Selective chemical labeling of proteins in living cells. *Current opinion in chemical biology* **9**, 56-61 (2005).
265. Michalet, X. et al. Quantum Dots for Live Cells, in Vivo Imaging, and Diagnostics. *Science* **307**, 538-544 (2005).
266. Bucci, C. et al. The small GTPase rab5 functions as a regulatory factor in the early endocytic pathway. *Cell* **70**, 715-728 (1992).
267. Jun, M.E., Roy, B. & Ahn, K.H. "Turn-on" fluorescent sensing with "reactive" probes. *Chemical communications* **47**, 7583-7601 (2011).
268. Stephens, D.J. & Allan, V.J. Light microscopy techniques for live cell imaging. *Science* **300**, 82-86 (2003).
269. Billinton, N. & Knight, A.W. Seeing the wood through the trees: a review of techniques for distinguishing green fluorescent protein from endogenous autofluorescence. *Analytical biochemistry* **291**, 175-197 (2001).
270. Aubin, J.E. Autofluorescence of viable cultured mammalian cells. *The journal of histochemistry and cytochemistry* **27**, 36-43 (1979).
271. Dixit, R. & Cyr, R. Cell damage and reactive oxygen species production induced by fluorescence microscopy: effect on mitosis and guidelines for non-invasive fluorescence microscopy. *The Plant Journal* **36**, 280-290 (2003).
272. Hinterdorfer, P. & Van Oijen, A. Handbook of Single Molecule Biophysics. (Springer, 2009).
273. Shen, F., Hodgson, L. & Hahn, K. in Methods in Enzymology, Vol. Volume 414. (ed. I. James) 620-632 (Academic Press, 2006).
274. Kikuta, J. & Ishii, M. Recent advances in intravital imaging of dynamic biological systems. *Journal of pharmacological sciences* **119**, 193-197 (2012).
275. Conchello, J.-A. & Lichtman, J.W. Optical sectioning microscopy. *Nature methods* **2**, 920-931 (2005).
276. Gräf, R., Rietdorf, J. & Zimmermann, T. in Microscopy Techniques, Vol. 95. (ed. J. Rietdorf) 57-75 (Springer Berlin Heidelberg, 2005).

BIBLIOGRAPHY

277. Kaminskas, L.M. et al. The Impact of Molecular Weight and PEG Chain Length on the Systemic Pharmacokinetics of PEGylated Poly L-Lysine Dendrimers. *Molecular Pharmaceutics* **5**, 449-463 (2008).
278. Zhang, X. et al. Poly(ethylene glycol)-block-polyethylenimine copolymers as carriers for gene delivery: Effects of PEG molecular weight and PEGylation degree. *Journal of Biomedical Material Research* **84A**, 795-804 (2008).
279. Merkel, O.M. et al. Integrin $\alpha v \beta 3$ Targeted Gene Delivery Using RGD Peptidomimetic Conjugates with Copolymers of PEGylated Poly(ethylene imine). *Bioconjugate chemistry* **20**, 1270-1280 (2009).
280. Wang, T., Upponi, J.R. & Torchilin, V.P. Design of multifunctional non-viral gene vectors to overcome physiological barriers: dilemmas and strategies. *International journal of pharmaceutics* **427**, 3-20 (2012).
281. Oba, M., Fukushima, S., Kanayama, N., Aoyagi, K., Nishiyama, N., Koyama, H. and Kataoka, K. Cyclic RGD Peptide-Conjugated Polyplex Micelles as a Targetable Gene Delivery System Directed to Cells Possessing $\alpha v \beta 3$ and $\alpha v \beta 5$ Integrins. *Bioconjugate chemistry* **18**, 1415-1423 (2007).
282. Miyata, K., Kakizawa, Y., Nishiyama, N., Harada, A., Yamasaki, Y., Koyama, H. and Kataoka, K. Block Cationic Polyplexes with Regulated Densities of Charge and Disulfide Cross-Linking Directed To Enhance Gene Expression. *Journal of the American Chemical Society* **126**, 2355-2361 (2004).
283. Oba, M., Aoyagi, K., Miyata, K., Matsumoto, Y., Itaka, K., Nishiyama, N., Yamasaki, Y., Koyama, H. and Kataoka, K. Polyplex Micelles with Cyclic RGD Peptide Ligands and Disulfide Cross-Links Directing to the Enhanced Transfection via Controlled Intracellular Trafficking. *Molecular Pharmaceutics* **5**, 1080-1092 (2008).
284. Arap, W., Pasqualini, R. & Ruoslahti, E. Cancer Treatment by Targeted Drug Delivery to Tumor Vasculature in a Mouse Model. *Science* **279**, 377-380 (1998).
285. Rader, C., Popkov, M., Neves, J.A. & Barbas, C.F. Integrin $\alpha v \beta 3$ -targeted therapy for Kaposi's sarcoma with an in vitro-evolved antibody. *FASEB journal* **16**, 2000-2002 (2002).
286. Vachutinsky, Y., Oba, M., Miyata, K., Hiki, S., Kano, M., Nishiyama, N., Koyama, H., Miyazono, K., and Kataoka, K. Antiangiogenic gene therapy of experimental pancreatic tumor by sFlt-1 plasmid DNA carried by RGD-modified crosslinked polyplex micelles. *Journal of Controlled Release* **149**, 51-57 (2011).
287. Singh, R.D. et al. Selective Caveolin-1-dependent Endocytosis of Glycosphingolipids. *Molecular Biology of the Cell* **14**, 3254-3265 (2003).
288. Vercauteren, D. et al. The Use of Inhibitors to Study Endocytic Pathways of Gene Carriers: Optimization and Pitfalls. *Molecular therapy* **18**, 561-569 (2010).
289. Cheyne, R.B. & Moffitt, M.G. Self-Assembly of Polystyrene-block-Poly(Ethylene Oxide) Copolymers at the Air Water Interface: Is Dewetting the Genesis of Surface Aggregate Formation? *Langmuir* **22**, 8387-8396 (2006).
290. Hoenig, D. et al. Biophysical Characterization of Copolymer-Protected Gene Vectors. *Biomacromolecules* **11**, 1802-1809 (2010).
291. Kim, Y., Pyun, J., Frechet, J.M.J., Hawker, C.J. & Frank, C.W. The Dramatic Effect of Architecture on the Self-Assembly of Block Copolymers at Interfaces. *Langmuir* **21**, 10444-10458 (2005).
292. Kichler, A. Gene transfer with modified polyethylenimines. *Journal of Gene Medicine* **6**, S3-S10 (2004).

293. Piest, M. & Engbersen, J.F.J. Effects of charge density and hydrophobicity of poly(amido amine)s for non-viral gene delivery. *Journal of Controlled Release* **148**, 83-90 (2010).
294. Sancey, L. et al. Clustering and Internalization of Integrin $\alpha_v\beta_3$ With a Tetrameric RGD-synthetic Peptide. *Molecular therapy* **17**, 837-843 (2009).
295. Caswell, P.T., Vadrevu, S. & Norman, J.C. Integrins: masters and slaves of endocytic transport. *Nature Reviews Molecular Cell Biology* **10**, 843-853 (2009).
296. Roberts, M.S., Woods, A.J., Dale, T.C., van der Sluijs, P. & Norman, J.C. Protein Kinase B/Akt Acts via Glycogen Synthase Kinase 3 To Regulate Recycling of $\alpha_v\beta_3$ and $\alpha_5\beta_1$ Integrins. *Molecular Biology of the Cell* **24**, 1505-1515 (2004).
297. Woods, A.J., White, D.P., Caswell, P.T. & Norman, J.C. PKD1/PKC promotes $\alpha_v\beta_3$ integrin recycling and delivery to nascent focal adhesions. *EMBO Journal* **23**, 2531-2543 (2004).
298. Nishimura, T. & Kaibuchi, K. Numb Controls Integrin Endocytosis for Directional Cell Migration with aPKC and PAR-3. *Developmental cell* **13**, 15-28 (2007).
299. Galvez, B.G. et al. Caveolae Are a Novel Pathway for Membrane-Type 1 Matrix Metalloproteinase Traffic in Human Endothelial Cells. *Molecular Biology of the Cell* **15**, 678-687 (2004).
300. Shi, F. & Sottile, J. Caveolin-1-dependent β_1 integrin endocytosis is a critical regulator of fibronectin turnover. *Journal of Cell Science* **121**, 2360-2371 (2008).
301. Lakadamyali, M., Rust, M.J. & Zhuang, X. Ligands for Clathrin-Mediated Endocytosis Are Differentially Sorted into Distinct Populations of Early Endosomes. *Cell* **124**, 997-1009 (2006).
302. Cohen, R.N., van der Aa, M.A.E.M., Macaraeg, N., Lee, A.P. & Szoka Jr, F.C. Quantification of plasmid DNA copies in the nucleus after lipoplex and polyplex transfection. *Journal of Controlled Release* **135**, 166-174 (2009).
303. Schwake, G. et al. Predictive modeling of non-viral gene transfer. *Biotechnology and Bioengineering* **105**, 805-813 (2010).
304. Shayakhmetov, D.M., Eberly, A.M., Li, Z.-Y. & Lieber, A. Deletion of Penton RGD Motifs Affects the Efficiency of both the Internalization and the Endosome Escape of Viral Particles Containing Adenovirus Serotype 5 or 35 Fiber Knobs. *Journal of Virology* **79**, 1053-1061 (2005).
305. Chávez, A., Pujol, M., Haro, I., Alsina, M.A. & Cajal, Y. Membrane fusion by an RGD-containing sequence from the core protein VP3 of hepatitis A virus and the RGA-analogue: Implications for viral infection. *Biopolymers* **58**, 63-77 (2001).
306. Sauer, Anna M., Schlossbauer, Axel, Ruthardt, Nadia, Cauda, Valentina, Bein, Thomas and Bräuchle, Christoph. Role of Endosomal Escape for Disulfide-Based Drug Delivery from Colloidal Mesoporous Silica Evaluated by Live-Cell Imaging. *Nano Letters* **10**, 3684-3691 (2010).
307. Austin, C.D. et al. Oxidizing potential of endosomes and lysosomes limits intracellular cleavage of disulfide-based antibody-drug conjugates. *Proceedings of the National Academy of Sciences of the United States of America* **102**, 17987-17992 (2005).
308. Yang, J., Chen, H., Vlahov, I.R., Cheng, J.X. & Low, P.S. Evaluation of disulfide reduction during receptor-mediated endocytosis by using FRET imaging. *Proceedings of the National Academy of Sciences of the United States of America* **103**, 13872-13877 (2006).

BIBLIOGRAPHY

309. Ballantyne, A. & Dhillon, S. Trastuzumab Emtansine: First Global Approval. **73**, 755-65, *Drugs* (2013).
310. de Bruin, K. et al. Cellular Dynamics of EGF Receptor-Targeted Synthetic Viruses. *Molecular Therapy* **15**, 1297-1305 (2007).
311. Milane, L., Duan, Z. & Amiji, M. Development of EGFR-Targeted Polymer Blend Nanocarriers for Combination Paclitaxel/Lonidamine Delivery To Treat Multi-Drug Resistance in Human Breast and Ovarian Tumor Cells. *Molecular Pharmaceutics* **8**, 185-203 (2011).
312. Song, S. et al. Peptide ligand-mediated liposome distribution and targeting to EGFR expressing tumor in vivo. *International journal of pharmaceutics* **363**, 155-161 (2008).
313. Li, Z. et al. Identification and characterization of a novel peptide ligand of epidermal growth factor receptor for targeted delivery of therapeutics. *FASEB journal* **19**, 1978-85 (2005).
314. Schäfer, A., Pahnke, A., Schaffert, D., van Weerden, W. M., de Ridder, C. M. A., Rödl, W., Vetter, A., Spitzweg, C., Kraaij, R., Wagner, E. and Ogris, M. Disconnecting the Yin and Yang Relation of Epidermal Growth Factor Receptor (EGFR)-Mediated Delivery: A Fully Synthetic, EGFR-Targeted Gene Transfer System Avoiding Receptor Activation. *Human gene therapy* **22**, 1463-1473 (2011).
315. Abourbeh, G. et al. PolyIC GE11 polyplex inhibits EGFR-overexpressing tumors. *IUBMB Life* **64**, 324-330 (2012).
316. Klutz, K., Schaffert, D., Willhauck, M.J., Grunwald, G.K., Haase, R., Wunderlich, N., Zach, C., Gildehaus, F.J., Senekowitsch-Schmidtke, R., Goke, B., Wagner, E., Ogris, M., and Spitzweg, C. Epidermal Growth Factor Receptor-targeted 131I-therapy of Liver Cancer Following Systemic Delivery of the Sodium Iodide Symporter Gene. *Molecular therapy* **19**, 676-685 (2011).
317. Wagner, E. Strategies to Improve DNA Polyplexes for in Vivo Gene Transfer: Will "Artificial Viruses" Be the Answer? *Pharmaceutical Research* **21**, 8-14 (2004).
318. Schaffert, D., Kiss, M., Rödl, W., Shir, A., Levitzki, A., Ogris, M. and Wagner, E. Poly(I:C)-Mediated Tumor Growth Suppression in EGF-Receptor Overexpressing Tumors Using EGF-Polyethylene Glycol-Linear Polyethylenimine as Carrier. *Pharmaceutical Research* **28**, 731-741 (2011).
319. von Gersdorff, K., Ogris, M. & Wagner, E. Cryoconserved shielded and EGF receptor targeted DNA polyplexes: cellular mechanisms. *European Journal of Pharmaceutics and Biopharmaceutics* **60**, 279-285 (2005).
320. Levitzki, A.G.A. Tyrosine kinase inhibition: an approach to drug development. *Science* **267**, 1782-1788 (1995).
321. Song, W., Xuan, H. & Lin, Q. Epidermal growth factor induces changes of interaction between epidermal growth factor receptor and actin in intact cells. *Acta Biochimica et Biophysica Sinica* **40**, 754-760 (2008).
322. Magadala, P. & Amiji, M. Epidermal Growth Factor Receptor-Targeted Gelatin-Based Engineered Nanocarriers for DNA Delivery and Transfection in Human Pancreatic Cancer Cells. *The AAPS Journal* **10**, 565-576 (2008).
323. Nordberg, E. et al. Cellular studies of binding, internalization and retention of a radiolabeled EGFR-binding affibody molecule. *Nuclear Medicine and Biology* **34**, 609-618 (2007).

324. Klutz, K., Willhauck, M., Dohmen, C., Wunderlich, N., Knoop, K., Zach, C., Senekowitsch-Schmidtke, R., Gildehaus, F.J., Ziegler, S., Fürst, S., Göke, B., Wagner, E., Ogris, M. and Spitzweg, C. Image-guided tumor-selective radioiodine therapy of liver cancer following systemic nonviral delivery of the sodium iodide symporter gene. *Human gene therapy* **22**, 1563-1574 (2011).
325. Nie, Y., Schaffert, D., Rödl, W. , Ogris, M., Wagner, E. and Günther, M. Dual-targeted polyplexes: One step towards a synthetic virus for cancer gene therapy. *Journal of controlled release* **152**, 127-134 (2011).
326. Jing, F., Li, J., Liu, D., Wang, C. & Sui, Z. Dual ligands modified double targeted nano-system for liver targeted gene delivery. *Pharmaceutical biology* **51**, 643-649 (2013).
327. Kakimoto, S., Moriyama, T., Tanabe, T., Shinkai, S. & Nagasaki, T. Dual-ligand effect of transferrin and transforming growth factor alpha on polyethyleneimine-mediated gene delivery. *Journal of controlled release* **120**, 242-249 (2007).
328. Torrano, A. A., Blechinger, J., Osseforth, C., Argyo, C., Reller, A., Bein, T., Michaelis, J. and Bräuchle, C. A fast analysis method to quantify nanoparticle uptake on a single cell level. *Nanomedicine* (2013), doi: 10.2217/nnm.12.178
329. Miravete, M. et al. Renal tubular fluid shear stress promotes endothelial cell activation. *Biochemical and biophysical research communications* **407**, 813-817 (2011).
330. Kamioka, H. et al. Microscale fluid flow analysis in a human osteocyte canaliculus using a realistic high-resolution image-based three-dimensional model. *Integrative biology : quantitative biosciences from nano to macro* **4**, 1198-1206 (2012).
331. Kurbel, S., Kurbel, B., Dmitrovic, B. & Wagner, J. A model of hydraulic interactions in liver parenchyma as forces behind the intrahepatic bile flow. *Medical hypotheses* **56**, 599-603 (2001).
332. Cucina, A. et al. Shear stress induces changes in the morphology and cytoskeleton organisation of arterial endothelial cells. *European journal of vascular and endovascular surgery* **9**, 86-92 (1995).
333. Malek, A.M. & Izumo, S. Control of endothelial cell gene expression by flow. *Journal of biomechanics* **28**, 1515-1528 (1995).
334. Schneider, M.F. et al. An acoustically driven microliter flow chamber on a chip (muFCC) for cell-cell and cell-surface interaction studies. *Chemphyschem* **9**, 641-645 (2008).
335. Cho, E.C., Zhang, Q. & Xia, Y. The effect of sedimentation and diffusion on cellular uptake of gold nanoparticles. *Nature nanotechnology* **6**, 385-391 (2011).
336. Hinderliter, P.M. et al. ISDD: A computational model of particle sedimentation, diffusion and target cell dosimetry for in vitro toxicity studies. *Particle and fibre toxicology* **7**, 36 (2010).
337. Amir, R. J., Albertazzi, L., Willis, J., Khan, A., Kang, T., Hawker, C. J. Multifunctional trackable dendritic scaffolds and delivery agents. *Angewandte Chemie (International ed. in English)* **50**, 3425-3429 (2011).
338. Schaffert, D., Troiber, C., Salcher, E. E., Frohlich, T., Martin, I., Badgular, N., Dohmen, C., Edinger, D., Klager, R., Maiwald, G., Farkasova, K., Seeber, S., Jahn-Hofmann, K., Hadwiger, P. and Wagner, E. Solid-phase synthesis of sequence-defined T-, i-, and U-shape polymers for pDNA and siRNA delivery. *Angewandte Chemie (International ed. in English)* **50**, 8986-8989 (2011).
339. Wang, Y., Guo, R., Cao, X., Shen, M. & Shi, X. Encapsulation of 2-methoxyestradiol within multifunctional poly(amidoamine) dendrimers for targeted cancer therapy. *Biomaterials* **32**, 3322-3329 (2011).

BIBLIOGRAPHY

340. Cheng, Y., Xu, Z., Ma, M. & Xu, T. Dendrimers as drug carriers: applications in different routes of drug administration. *Journal of pharmaceutical sciences* **97**, 123-143 (2008).
341. Casley-Smith, J.R., Morgan, R.G. & Piller, N.B. Treatment of Lymphedema of the Arms and Legs with 5,6-Benzo-[alpha]-pyrone. *New England Journal of Medicine* **329**, 1158-1163 (1993).
342. Martin, I., Dohmen, C., Mas-Moruno, C., Troiber, C., Kos, P., Schaffert, D., Lächelt, U., Teixido, M., Günther, M., Kessler, H., Giral, E. and Wagner, E. Solid-phase-assisted synthesis of targeting peptide-PEG-oligo(ethane amino)amides for receptor-mediated gene delivery. *Organic & biomolecular chemistry* **10**, 3258-3268 (2012).
343. Nishiyama, N. et al. Photochemical enhancement of transgene expression by polymeric micelles incorporating plasmid DNA and dendrimer-based photosensitizer. *Journal of Drug Targeting* **14**, 413-424 (2006).
344. Maier, K. & Wagner, E. Acid-labile traceless click linker for protein transduction. *Journal of the American Chemical Society* **134**, 10169-10173 (2012).
345. Brissault, B. et al. Linear topology confers in vivo gene transfer activity to polyethylenimines. *Bioconjugate chemistry* **17**, 759-765 (2006).
346. Fallah, M.A. et al. Acoustic driven flow and lattice Boltzmann simulations to study cell adhesion in biofunctionalized microfluidic channels with complex geometry. *Biomicrofluidics* **4** (2010).
347. Franke, T., Abate, A.R., Weitz, D.A. & Wixforth, A. Surface acoustic wave (SAW) directed droplet flow in microfluidics for PDMS devices. *Lab on a chip* **9**, 2625-2627 (2009).

List of Abbreviations

AOTF	acousto optic tunable filter
CCD	charge coupled device
CME	clathrin mediated endocytosis
CpG	cytosine-phosphate-guanine
CML	chronic myelogenous leukemia
CMV	cytomegalovirus
CPP	cell-penetrating peptide
CT-B	cholera toxin-B
DNA	deoxyribonucleic acid
DOPC	1,2-dioleoyl-sn-glycero-3-phosphocholine
DOPE	1,2-Dioleoyl-sn-glycero-3-phosphoethanolamine
DOSPA	2,3-dioleyloxy- <i>N</i> -[2-(sperminecarboxamido)ethyl]- <i>N,N</i> -dimethyl-1-propanaminium trifluoroacetate
DOTAP	<i>N</i> -[1-(2,3-Dioleoyloxy)propyl]- <i>N,N,N</i> -trimethylammonium propane
DOTMA	<i>N</i> -[1-(2, 3-dioleyloxy)propyl]- <i>N,N,N</i> -trimethylammonium
DTT	dithiothreitol
ECM	extracellular matrix
EGF	epidermal growth factor
eGFP	enhanced green fluorescent protein
EGFR	epidermal growth factor receptor
EMCCD	electron multiplying charge coupled device
EPR	enhanced permeability and retention effect

ABBREVIATIONS

FBS	fetal bovine serum
FDA	US food and drug administration
FR	folate receptor
FRET	fluorescence resonance energy transfer
GEEC	GPI-enriched endocytic compartments
GFP	green fluorescent protein
GPI	glycosylphosphatidylinositol
His	histidine
HIV	human immunodeficiency virus
LaCer	lactosyl ceramide
LDL	low density lipoprotein
miRNA	micro ribonucleic acid
MMP	matrix metallo proteinase
mRNA	messenger ribonucleic acid
NLS	nuclear localization sequence
PAMAM	poly(amido amine)
PCFT	proton-coupled folate receptor
PDMAEMA	poly(2-(dimethylamino)ethyl methacrylate)
pDNA	plasmid deoxyribonucleic acid
PEG	polyethylene glycol
PEI	polyethylenimine
pHLIP	pH low integrating peptide
PI3	phosphatidylinositide-3
PKC	protein kinase C
PLA	polylactide
PLC	phospholipase C

PLGA	<i>poly(lactic-co-glycolic acid)</i>
PLL	poly-L-lysine
RGD	arginine-glycine-aspartate
RISC	RNA-induced silencing complex
RFC	reduced folate carrier
RLU	relative light unit
RNA	ribonucleic acid
SAW	surface acoustic wave
SCID	severe combined immunodeficiency
siRNA	small interfering RNA
STP	succinoyl tetraethylene pentamine
VEGF	vascular endothelial growth factor
WHO	world health organization
WGA	wheat germ agglutinin

List of Publications

Publications related to the thesis

Peer reviewed journals

- F.M. Mickler, L. Möckl, N. Ruthardt, M. Ogris, E. Wagner and C. Bräuchle, "Tuning Nanoparticle Uptake: Live-Cell Imaging Reveals Two Distinct Endocytosis Mechanisms Mediated by Natural and Artificial EGFR Targeting Ligand." *Nano Letters*, (2012), 12, 3417-3423
- F.M. Mickler, Y. Vachutinsky, M. Oba, K. Miyata, N. Nishiyama, K. Kataoka, C. Bräuchle and N. Ruthardt, "Effect of integrin targeting and PEG shielding on polyplex micelle internalization studied by live-cell imaging." *Journal of Controlled Release*, (2011), 156(3), 364-373
- C. Zhu, M. Zheng, F. Meng, F.M. Mickler, N. Ruthardt, X. Zhu and Z. Zhong, "Reversibly Shielded DNA Polyplexes Based on Bioreducible PDMAEMA-SS-PEG-SS-PDMAEMA Triblock Copolymers Mediate Markedly Enhanced Nonviral Gene Transfection." *Biomacromolecules*, (2012), 13, 769-778
- L. Albertazzi, F.M. Mickler, G.M. Pavan, F. Salomone, G. Bardi, M. Panniello, E. Amir, T. Kang, K. Killops, C. Bräuchle, R. J. Amir and C. J. Hawker. "Strong positive dendritic effects in the bioactivity of internally functionalized dendrimers with PEG cores", *Biomacromolecules* (2012), 13, 4089-4097
- U. Lächelt, P. Kos, F.M. Mickler, E. Salcher, W. Roedl, N. Badgajar, Naresh, C. Bräuchle and E. Wagner, "Fine-tuning of proton sponges by precise diaminoethanes and histidines in pDNA polyplexes." *Nanomedicine* (2013), accepted

Oral presentations

- "Drug and gene Delivery with "smart" nanoparticles and live cell imaging", MicroRNAs & Single Molecule Biology Europe - Symposium, 2011, Cambridge, UK
- "EGF receptor targeting of polyplexes with the short artificial peptide GE11 studied by live cell imaging", Annual Meeting of the German Society for Gene Therapy, 2010, Munich

Poster presentations

- F.M. Mickler, Y. Vachutinsky, L. Albertazzi, U. Lächelt, N. Ruthardt, Z. Zhong, C. Hawker, M. Ogris, K. Kataoka, E. Wagner and C. Bräuchle "Synthetic gene vectors for cancer therapy", Global Challenges and Opportunities for Nanotechnology – workshop organized by Swiss Nanoscience institute, ETH Zurich and CeNS, 2013, Venice, Italy
- F.M. Mickler, Y. Vachutinsky, M. Oba, N. Ruthardt, E. Wagner, M. Ogris, K. Kataoka and C. Bräuchle "Targeted delivery of gene vectors into cancer cells", CeNS (Center of NanoScience) workshop, 2011, Venice, Italy
- F.M. Mickler, N. Ruthardt, Y. Vachutinsky, M. Oba, K. Miyata, K. Kataoka and C. Bräuchle "Visualizing the effect of integrin targeting and surface shielding on gene vector uptake by live cell imaging", International Symposium Cellular Delivery of Therapeutic Macromolecules, 2010, Cardiff, UK
- F.M. Mickler, Y. Vachutinsky, M. Oba, N. Ruthardt, E. Wagner, M. Ogris, K. Kataoka and C. Bräuchle "Targeted delivery of gene vectors into cancer cells studied by live-cell imaging", 4th Annual Symposium on Nanobiotechnology, 2010, Munich.
- F.M. Mickler, N. Ruthardt, A. Sauer, M. Oba, K. Kataoka and C. Bräuchle "Internalization of Integrin-Receptor targeted Polyplex Micelles", 3th Annual Symposium on Nanobiotechnology at the University of California, Los Angeles, 2009, CA, USA.

Publications not related to this thesis (under my maiden name)

- H. Dietz, T. Bornschlöggl, R. Heym, F. König, and M. Rief, "Programming protein self-assembly with coiled coils" *New Journal of Physics*, (2007), 9, 424

Curriculum Vitae

Frauke Martina Mickler, nee König

Date of birth: 20th of April 1984

Place of birth: Braunschweig, Germany

Education

- 2009-2012 Doctorate studies in the group of Prof Bräuchle at the Physical Chemistry Department, Ludwig Maximilians University Munich, Germany
- 2006-2008 Master Studies in Biochemistry, Technical University of Munich, Germany
- 2003-2006 Bachelor studies in Molecular Biotechnology/Biochemistry, Technical University of Munich, Germany
- 1994-2003 Lauenburgische Gelehrtenschule Ratzeburg, Germany

Awards and scholarships:

- 2010-2012 Scholarship of the International Doctorate Program Nanobiotechnology (IDK-NBT, Elitenetwork of Bavaria)
- 2010-2012 Member in the graduate program of the Nanosystems Initiative Munich (NIM). Student Representative in the Student Board of NIM in 2011/2012.
- 2010 Society for Experimental Biology and Medicine (SEBM) International Prize (Europe), awarded for oral presentation at the Annual Conference of the German Society for Gene Therapy
- 2012 Center of Nanoscience (CeNS) Publication Award

Acknowledgements

I owe my deepest gratitude to many people without whom this dissertation would not have been possible.

First of all, I gratefully and sincerely thank my advisor Prof. Dr. Christoph Bräuchle for his guidance and continuous support during my Ph.D. study. I really appreciate that I had the chance to work in his group on an exciting research topic. His excellent organization and constant encouragement helped me to successfully proceed with my projects and to develop my own ideas.

It was a great privilege to cooperate with Prof. Dr. Ernst Wagner, PD. Dr. Manfred Ogris, Prof. Dr. Kazunori Kataoka, Prof. Dr. Zhiyuan Zhong, Prof. Dr. Craig Hawker and Dr. Roey Amir. I benefited a lot from their extensive knowledge and exchange of ideas during fruitful discussions.

I thank my second supervisor PD Dr. Manfred Ogris for his encouragement and support and for being always in good spirits. My appreciation is extended to Prof. Dr. Don Lamb and Prof. Dr. Jens Michaelis for inspiring discussions during our Monday morning seminars. My thanks also go to the reviewers of my thesis: Prof. Dr. Joachim Rädler, Prof. Dr. Christina Scheu and Prof. Dr. Achim Hartschuh.

I express my sincere gratitude to my co-advisor Dr. Nadia Ruthardt for teaching me the basics of live-cell imaging and paper writing as well as her scientific input during data discussion and the planning of experiments.

I am very grateful for the close collaboration with Ulrich Lächelt, Petra Kos, Dr. Christian Dohmen and Dr. Kevin Maier from the Wagner group, Dr. Yelena Vachutinsky from Kataoka group and Lorenzo Albertazzi from the Hawker group. Thank you for always providing me with fresh samples, for taking the time to answer my questions, discuss the data and for giving scientific input. It was a lot of fun to work with you!

I am thankful to Dr. Sergey Ivanchenko for his expert knowledge and help to set up and fix our microscope setups, and to Dr. Volodymyr Kudryavtsev, Adriano Torrano and Julia Blechinger for providing, explaining and debugging the data analysis software.

I thank Monika Franke and Jaroslava Obel for taking care of our cell cultures and seeding many hundred slices of cells over the years for me.

Many thanks to my students Sophia Betzler and Carola Braun, as well as my ex-students and now colleagues Ellen Broda and Leonhard Möckl who helped me with the experiments and were always very patient and hard-working.

I acknowledge the International Doctorate Program NanoBioTechnology (IDK), Nanosystems Initiative Munich (NIM) and the Center of Nanoscience (CeNS) for financial support, great workshops and the opportunity to meet many interdisciplinary researchers from all over the world. Special thanks to Marilena for always having an open ear for listening and helping all PhD students.

All members from AK Bräuchle, AK Lamb and AK Michaelis I would like to thank for a great atmosphere, relaxing coffee breaks, delicious cakes, nice smiles and discussions and being very helpful whenever needed. Especially I thank my colleagues and ex-colleagues Adam, Adriano, Aurelie, Bärbel, Ellen, Flo, Gregor, Jens, Leonhard, Martin, Niko, Robert, Stephan, Vroni and Wolffi. Special thanks to Meli, I really enjoyed to share exciting times with growing bellies with you. And to Moritz Ehrl for great advices and lots of fun during lunch and coffee breaks.

Three special girls have been always there to share happy and sad moments during my PhD life and have become true friends. A thousand thanks to Anna, Doro and Julia for all the good times and fun we had in and out of the lab!

I deeply thank my parents Regine and Frank, my sister Imke, my brother Jan as well as my grandparents Julie and Karl-Friedrich and my parents-in-law Reinhild and Otfried for their never-ending support, their trust and encouragement.

Above all, my thanks go to Moritz; I thank you for your loving me the way I am and for your optimism and encouragement. For being always by my side, supporting me wherever you can and being a great daddy.

Finally, I thank my son Lasse, who is very little yet but already has a big place in my heart.